School of Doctoral Studies in Biological Sciences

University of South Bohemia in České Budějovice

Faculty of Science

The role of electroactive organisms in biomineralization reactions involving transition metals, nitrogen and humic substances under suboxic/anoxic conditions

Ph.D. Thesis

MSc. Astolfo Valero

Supervisor: MSc, Daniel Petráš, Ph.D.

Institute of Soil Biology and Biogeochemistry

Biology Centre of the Czech Academy of Sciences

České Budějovice 2024

Annotation

Electroactive microorganisms sustain their respiratory metabolisms by retrieving or transferring electrons to extracellular conductive particles. Electroactive metabolisms based on iron respiration can trigger the precipitation of Fe(III)-oxyhydroxides or changes in their crystallinity. Iron biomineralization has a sound effect on the geochemical cycles of elements because it also influence the solubility of other elements such as phosphorus and arsenic. Thus, siderophile elements are removed from solution within precipitated particles or they are released back after mineral stabilization. However, major insights are often deduced by studying lab isolates of model microorganisms and using simplified substrates. This does not reflect environments where the presence of redox stratification boosts the overlapping of nitrogen- and iron-based metabolisms and interspecies interactions regarding thermodynamics constraints of minimal energetic loss for microbial respiration. For example, reactive nitrogen species (i.e., nitrate and ammonia) serve as alternative electron sources as sinks during iron biomineralization in nature. This can be also furthered by the presence of re-oxidable moieties of humic substances, which are used as electron shuttlers to reach extracellular materials. Therefore, this doctoral research aimed to describe how the availability of redox-reactive humic substances and reactive nitrogen species, as alternative electron donors or acceptors, affect electroactive metabolisms and linked iron biomineralization in the anoxic water column of a redox-stratified lake with high metal load (Lake Medard, NW Czech Republic). This was addressed by assessing the geochemical and hydrobiological features of the uppermost layers of sediment and the redox-stratified ferruginous water column of Lake Medard, and then, (ii) using the resulting dataset as input conditions in bioelectrochemical experiments to model the lake's biomineralization reactions by inducing microbe-mineral interactions under controlled electric potentials.

Declaration

This thesis originated from a partnership of Faculty of Science, University of South Bohemia, and Institute of Soil Biology and Biogeochemistry, Academy of Sciences of the Czech Republic, supporting doctoral studies in the Hydrobiology study program.

Acknowledgements

This thesis is dedicated **to my family**: my wife and baby Ka were the main support and biggest motivation to overcome the days when the road looked uphill. While support from my parents and mother in-law always pushed me forward.

I am really **grateful to**:

Dr Daniel Petráš for inviting me to be part of this scientific project, and believing in my skills to reach the goal line. All the learned lesson – in the bright but also in the no so good days – will go along with me during my career. "We need to stop the **tirar flechas and make it happen!** (and so we did it).

Dr Borovec and Dr Meador for integrating me in their research groups; as well as **Dr Jan and Dr Znachor** for their unvaluable help to collect samples from Lake Medard.

Dr Porcal, Dr Angel, Dr Syrová, and Dr Chroňaková for their scientific advice and cooperation; as well as **BSc Steenbergen, MSc. Umbría-Salinas, Dr Petrová, Dr Hubáček, Ing. Tomková** – and any member of the UPBB and HBU – who provided vital technical support during this research

Dr Lara-Rodríguez, Dr Pérez-Valera, and Dr Pires de Paula by being always available to address my dummy questions about microbiology

Dr Korth and Dr Harnisch for sharing their knowledge on the vast universe of bioelectrochemistry and how to culture unculturable microbes; as well as the members of their group at UFZ-Leipzig

Members of the Department of Ecosystem Biology and Student affairs, special mention to **Dr Vrba** and **Bc. Korcova**, for their inexhaustible patience and help during my doctoral studies

All colleagues and friends (**Bernard, Julián, Edu, Javi, Staní, Ana, and Nana**), who not only (make fun of) corrected my English but kindly provided the best antidote to bad days: food, pivo, and laughs.

List of papers and author's contribution

The thesis is based on the following papers (listed chronologically):

I.   Umbría-Salinas, K., **Valero, A.**, Jan, J., Borovec, J., Chrastný, V., Petrash, D. A. (2021). Redox-driven geochemical partitioning of metal(loid)s in the iron-rich anoxic sediments of a recently flooded lignite mine pit: Lake Medard, NW Czechia. Journal of Hazardous Materials Advances 3, 100009.
Valero A shares the main co-authorship and he performed samples collection, wet chemistry, data preparation and curation, and formal analysis. He also prepared the original draft and participated of review and editing of the manuscript. *His contribution was 30%.*

II.   Petrash, D. A., Steenbergen, I. G., **Valero, A.**, Meador, T. B., Pačes, T., Thomazo, C. (2022). Aqueous system-level processes and prokaryote assemblages in the ferruginous and sulfate-rich bottom waters of a post-mining lake. Biogeosciences 19 (6), 1723–1751 pp. (IF = 4.8)
Valero A. performed samples collection, wet chemistry, and data preparation and curation. *His contribution was 20 %.*

III.   **Valero, A.**, Jan, J., Petrash, D. A. (2023). Anaerobic dissolved As(III) removal from metal-polluted waters by cathode-stabilized Fe(III)-oxyhydroxides. Environmental Science: Water Research & Technology 9, 454 – 466 pp. (IF = 5.0).
Valero A. planed and conducted the bioelectrochemical experiments and performed data curation and formal analysis. He also prepared the original draft and participated in review and editing of the manuscript. *His contribution was 70%.*

IV.   **Valero, A.**, Petrash, D.A., Kuchenbuch, A., Korth, B. (2024). Enriching electroactive microorganisms from ferruginous lake waters – Mind the sulfate reducers! Bioelectrochemistry 157, 108661. (IF = 5.0)
Valero A. Planned and conducted the bioelectrochemical experiments and performed chemical analysis and data curation. He also prepared the original draft and participated in review and editing of the manuscript. *His contribution was 70%.*

Co-author agreement

Dr. Daniel Petráš, supervisor of this Ph.D. thesis lead author of paper II and co-author of papers I, III and IV, fully acknowledges the stated contribution of Valero A. to these manuscripts.

....

MSc., Daniel Petráš, Ph.D.

Table of contents

1.   Introduction

Diverse microbial respiratory pathways are driven by redox reactions that enable the breaking down of organic or inorganic substrates by coupling the oxidation of electron donors to the reduction of terminal electron acceptors (Borch et al., 2010; Melton et al., 2014). Also, several bacteria and archaea – termed as electroactive – sustain their metabolisms by transferring electrons to (electrogens or electricigens) or retrieving them (electrotrophs) from extracellular conductive particles such as minerals and electrodes (Fig. 1) (Lovley, 2022, 2012). Fe(III)-oxyhydroxides are among the most common terminal electron acceptors used by electroactive microorganisms (EAM) for organic matter oxidation because they are a more thermodynamically favourable electron sink under anoxic conditions than, for example, sulphur species (Kappler et al., 2021; Melton et al., 2014). Fe(III)-oxyhydroxides can undergo changes in their mineral array when used as terminal electron acceptor for microbial respiration, which in turn, can boost their capacity to sorb metals and nutrients or release them back to solution (Fig. 1a) (Borch et al., 2007; Muehe et al., 2013). Iron mineral transformation can also be furthered by the presence of alternative electron sources such as ammonia (Clément et al., 2005), or by the use of organic compounds as electron shuttlers like humic substances (Klüpfel et al., 2014). Thus, electron transfer from electroactive cells to conductive mineral particles has important effect on the dynamics of siderophile elements at the Earth' surface (Melton et al., 2014). However, mechanistic insights have been often reached by studying a few species of EAM under lab conditions and single substrates (Koch and Harnisch, 2016a; Lovley, 2012; Yee et al., 2020). Therefore, there is a lack of mechanistic insights on how extracellular electron transfer (EET) operates in nature, and its environmental importance is not fully understood (Koch and Harnisch, 2016a). This difference between lab conditions and nature is contrasting when considering environments with numerous electron sources and sinks, which can promote competition for available substrates and the overlapping of microbial respiratory pathways.

1.1. Electromicrobiology – a tool to assess extracellular electron transfer beyond model organisms

EET is performed by diverse microorganisms that have cell envelopes containing cytoplasmic membranes, which facilitate electron translocation from inner redox carriers to solid-state particles beyond the cell surface (Shi et al., 2016; Lovley and Holmes, 2021). Both electricigens and electrotrophs harness electrons from the extracellular environment by (i) direct contact via multiheme c-type cytochromes or protein nanowires (Shi et al., 2016; Lovley and Walker, 2019), or (ii) mediated by using redox-reactive electron shuttlers such as quinones and flavins (Fig. 1) (Marsili et al., 2008; Klüpfel et al., 2014). Alternative strategies to enhance direct and mediated EET include (i) the excretion of compounds to chelate and reduce Fe(III) (Taillefert et al., 2007), (ii) chemotaxis to migrate into zones with abundant conductive particles (Tremblay et al., 2012), (iii) the use of mineral networks as electron shuttlers to reach other cells (Kato et al., 2012), and (iv) production of micrometre-long conductive filaments of intracellular protein fibers arranged to interconnect hundreds of cells (Meysman et al., 2019).

Figure 1. Schematic representation of main mechanisms used by electroactive microorganisms (green ovals) to allocate electrons to conductive insoluble materials such as minerals (a) and electrodes (b). Direct electron transfer (yellow arrows) proceeds through c-type cytochromes (blue circles) or protein nanowires (yellow curves); while mediated electron transfer proceeds by using re-oxidable redox mediators as electron shuttlers (red arrows). Extracellular electron transfer to Fe(III)-oxyhydroxides (light brown) induces mineral stabilization within more crystalline phases (dark brown) and the release back to solution or scavenging of siderophile elements (green arrows).

Mechanisms used to reach minerals in nature are also used to interact with conductive electrodes (Fig. 1b). Hence, application of electrochemical approaches had advanced our understanding of how EET operate in natural and engineered environments (Lovley, 2012; Koch and Harnisch, 2016b; Lovley and Holmes, 2021). EAM isolation can proceed by inducing microbial-electrode interactions when applying a fixed electric potential (i.e., chronoamperometry) (Yee et al., 2020). Often, isolation of microorganisms (e.g., *Geobacter* spp.) occur on the surface of electrodes by forming thick biofilms of single or multiple electroactive species (Lovley, 2012; Koch and Harnisch, 2016b). In contrast, microbes relying on mediated EET (e.g., *Shewanella* spp.) remain in planktonic state (Marsili et al., 2008). After isolation of electroactive species, assessment of the cellular redox carriers (e.g., cytochromes) can proceed by sweeping electric potentials on a fixed range (i.e., cyclic voltammetry) (Harnisch and Freguia, 2012). On the other hand, microbe-electrode interactions furthered the development of bioelectrotechnologies with multiple applications such as the degradation of organic pollutants, energy production, synthesis of chemicals, bioremediation, and secondary metal recovery (Schröder et al., 2015).

1.2. Electroactivity in nature – how microbial competition for electron sources and sinks fuel Earth's biogeochemical cycles

EAM have not a unitary phylogenetic affiliation (Chabert et al., 2015; Koch and Harnisch, 2016a), and EET have been reported for species of iron reducers, both acidophilic and neutrophilic iron oxidizers, nitrate reducers, ammonia oxidizers, sulphate reducers, and methanogens (Koch and Harnisch, 2016a; Logan et al., 2019; Lovley and Holmes, 2021). Thereby, EAM are widely distributed at Earth' surface in environments with natural abundance of electron donors and acceptors such as sediments (Doyle et al., 2017; Armato et al., 2019), soils (Jiang et al., 2016; Wang et al., 2019), freshwater (Petrash et al., 2018; He et al., 2019), and seawater (Erable et al., 2010; Hidalgo et al., 2015). In Earth' surface, EAM display metabolic flexibility to couple organic matter remineralization with the use of several electron donors and acceptors (Lovley and Phillips, 1988; Lovley, 2022). Available electron sources and sinks are used following thermodynamics constraints of redox reactions that provide minimal energetic lost during microbial respiration (Helton et al., 2015).

Redox reactions occurring at the cell vicinities can induce micro-scale changes on the geochemical conditions at the cell milieu during remineralization, which promote the precipitation or transformation of minerals by microorganisms (Benzerara et al., 2011; Cosmidis and Benzerara, 2022). This process – termed biomineralization – can be detrimental to microbes because cell entombment reduce waste elimination and motility (Cosmidis and Benzerara, 2022), but in contrast, it can also be beneficial as biogenic minerals like magnetite work as electron storage or electron conductors to other microbial cells (Kappler et al., 2023). Biomineralization impact the dynamics of elements such as calcium, silicon, and sulphur (Benzerara et al., 2011; Cosmidis and Benzerara, 2022). However, it may be highlighted the significant influence on iron biogeochemical cycle (Melton et al., 2014; Bryce et al., 2018), which in turn, influence several environmental processes such as global carbon turnover, ocean productivity, pollutants recycling and greenhouse gas emissions (Kappler et al., 2021).

Iron biogeochemical cycle is controlled by redox reactions of the Fe(II)/Fe(III) redox pair that often overlap in nature (Kappler et al., 2021). For example, Fe(III) mineral particles precipitated by *Gallionella* spp. – after oxidizing Fe(II) and reducing nitrate – in dysoxic aquatic environments (Bryce et al., 2018), serve as terminal electron acceptors for organic matter oxidation by *Geobacter* spp. with a concurrent release of Fe(II) back to solution and stabilization of mixed-valence Fe(II,III)-oxyhydroxides (Fig. 2) (Melton et al., 2014; Kappler et al., 2021). Dissimilatory iron(III) reduction can be boosted by the presence of humic substances in redox boundaries by serving as electron shuttlers to foster long-range EET (Klüpfel et al., 2014; Sundman et al., 2020). Iron mineral stabilization also affects nutrients recycling because reactive nitrogen species (i.e., ammonium and nitrate) work as alternative electron donors or terminal electron acceptors for iron(III) dissimilatory reduction and ferrous iron(II) oxidation, respectively (Clément et al., 2005; Melton et al., 2014; Bryce et al., 2018). On the other hand, changes in the mineral array during the stabilization of Fe(III)-oxyhydroxides provide actives sites able to sorb oxyanions (e.g., phosphate and arsenite) (Borch et al., 2007; Muehe et al., 2013). While stabilized mixed valence Fe(II,III)-oxyhydroxides (e.g., magnetite) can behave as energy storage (Shi et al., 2016; Kappler et al., 2023), and impact carbon recycling by acting as electric conductive particles to facilitate syntrophic interactions between iron-reducers and methanogens in anoxic environments (Rotaru et al., 2018).
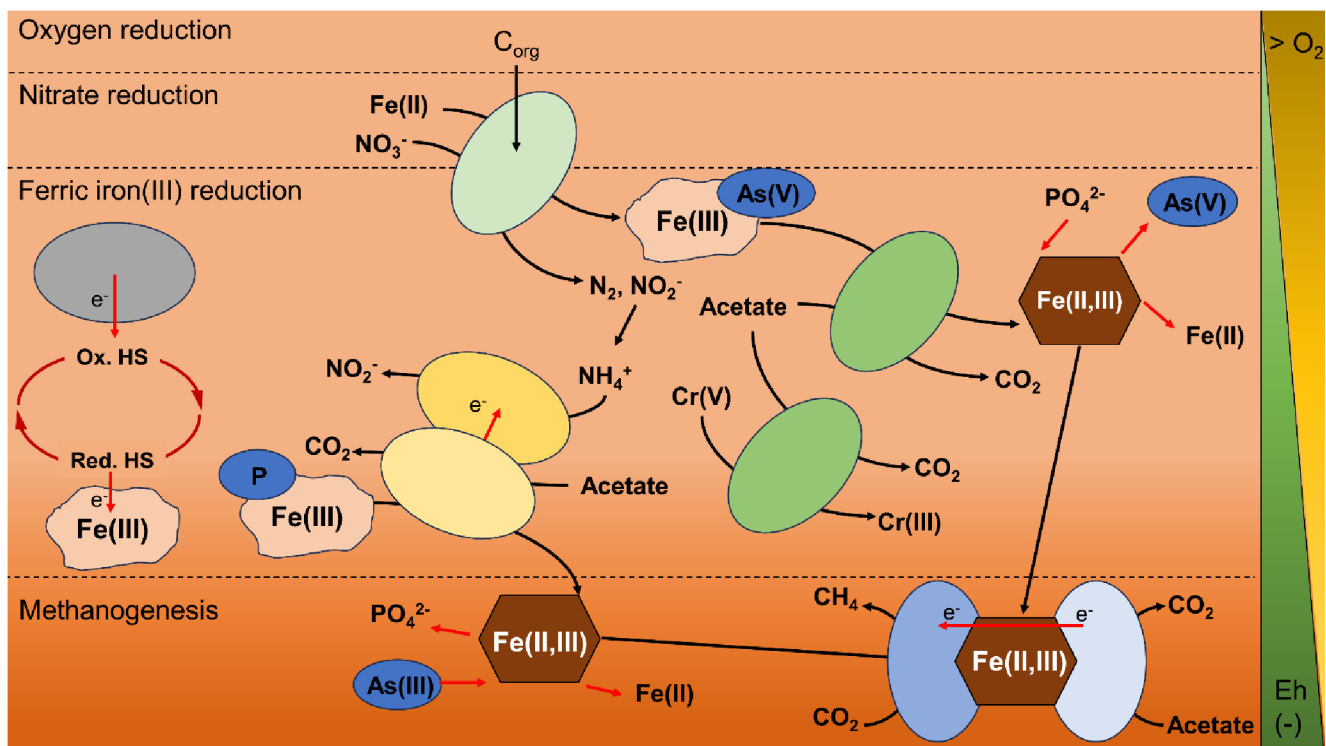
3

Figure 2. Scheme depicting how the overlapping of microbial respiratory metabolisms drives elemental cycling (brown polygons) under environmental gradients of dissolved oxygen (O_2) and redox potential (Eh). Concomitant iron biomineralization occurs through ferrous iron(II) oxidation (light green ovals), ferric iron(III) and metal dissimilatory reduction (dark green ovals), iron-ammox (yellow ovals), methanogenesis (blue ovals), and re-oxidation of humic substances derivatives (HS, grey ovals).

However, insights on EET involving iron biomineralization reaction were mainly gained through the study of model electroactive species (e.g., from the Geobacteraceae family) (Lovley, 2012; Koch and Harnisch, 2016b), which are often isolated under lab conditions and using simplified growth media with restricted substrates (Yee et al. 2020). This could limit the discovery of mechanistic insights reflecting nature because EET is controlled by thermodynamics constraints of minimal energetic loss and environmental redox potential (Helton et al., 2015; Korth and Harnisch, 2019). Moreover, as respiratory metabolisms can overlap due to microbial competition for available substrates (Melton et al., 2014; Helton et al., 2015; Kappler et al., 2021), there is a lack of mechanistic insights for microorganisms merely identified as electroactive or that alternatively perform EET as an adaptative surviving strategy under stress situations (i.e., non-conventional EAM) (Koch and Harnisch, 2016b; Aiyer and Doyle, 2022).

1.3. Lake Medard – Czech model environment to study biomineralization reactions

Metabolic flexibility to use a plethora of electron sources and sinks and adaptiveness to perform EET allow EAM flourishment in complex environments such as intertidal sediments (Doyle et al., 2017), deep-ocean hydrothermal vents (Kawaichi et al., 2018), and ferruginous lakes (Petrash et al., 2018). These environments highlight by the occurrence of microbe-mineral interactions promoted by the abundance of redox-reactive minerals and dissolved redox mediators. But among others, ferruginous lakes can be considered ideal systems to explore how EET operates because they commonly exhibit marked redox-stratification in their water column. This allows the study of biogeochemical processes that mimic those occurring in sediments but in a resolution of meters rather than mm to cm (Lambrecht et al., 2018; Petrash et al., 2018; Berg et al., 2019).

Czech Republic has an outstanding ferruginous waterbody, Lake Medard (50∘10′45″N, 12∘35′45″E), an oligotrophic lake formed after the flooding of a former open-cast lignite mine. This meromictic lake (i.e., not seasonal mixing of the entire water column) displays a dysoxic hypolimnion ranging from 44 to 48 m depth and a chemically differentiated anoxic ferruginous monimolimnion (Fig. 3a and 3b). Lake Medard exhibits high dissolved sulphate concentrations (19 ± 2 mM) coupled to low dissolved hydrogen sulphide contents (<0.3 µM) (Petrash et al., 2018). Elements like nickel and arsenic are recycled through microbial iron and carbon turnover fuelled by a moderated rise in the bioavailability of volatile fatty acids (e.g., acetate and formate) in the monimolimnion (Fig. 3c) (Petrash et al., 2018). A significant abundance of iron-reducing electroactive species (e.g., *Geobacter* spp. and *Rhodoferax* spp.) is observed in the bottom waters as the response to linked biotic and abiotic reactions driving iron and carbon turnover, which in turn impact the interlinked iron, carbon, nitrogen, and phosphorus recycling (Petrash et al. 2018).

Electroactive species are suggested to control element dynamics by using extracellular iron particles as terminal electron acceptors, which is fuelled by the capacity of the microbiome to (i) shift between nitrogen- to iron-based metabolisms and to (ii) use re-oxidable humic substances as electron shuttlers to reach conductive particles. Thereby, the study of microbe-mineral interactions occurring in the monimolimnion of our natural laboratory can bring paramount insights into how competition for alternative electron donors and acceptors could impact iron biomineralization in redox-stratified ferruginous lakes. This has been addressed in a few research efforts (e.g., see Berg et al., 2019; Sánchez-España et al., 2020); but EET mechanisms were barely explored and hence there is still plenty of room for improvement. Alternatively, unravelling the EET mechanisms of Lake Medard can shed light on the ecological role of understudied or yet-to-known electroactive species (Aiyer and Doyle, 2022). Also, the unveiling of novel EET mechanisms in aqueous systems with high metal loads, could aid in the designing of new bioelectrotechnologies (e.g., for secondary metal recovery) or to anticipate metal dynamics over potential management scenarios of water reservoirs under more realistic conditions.
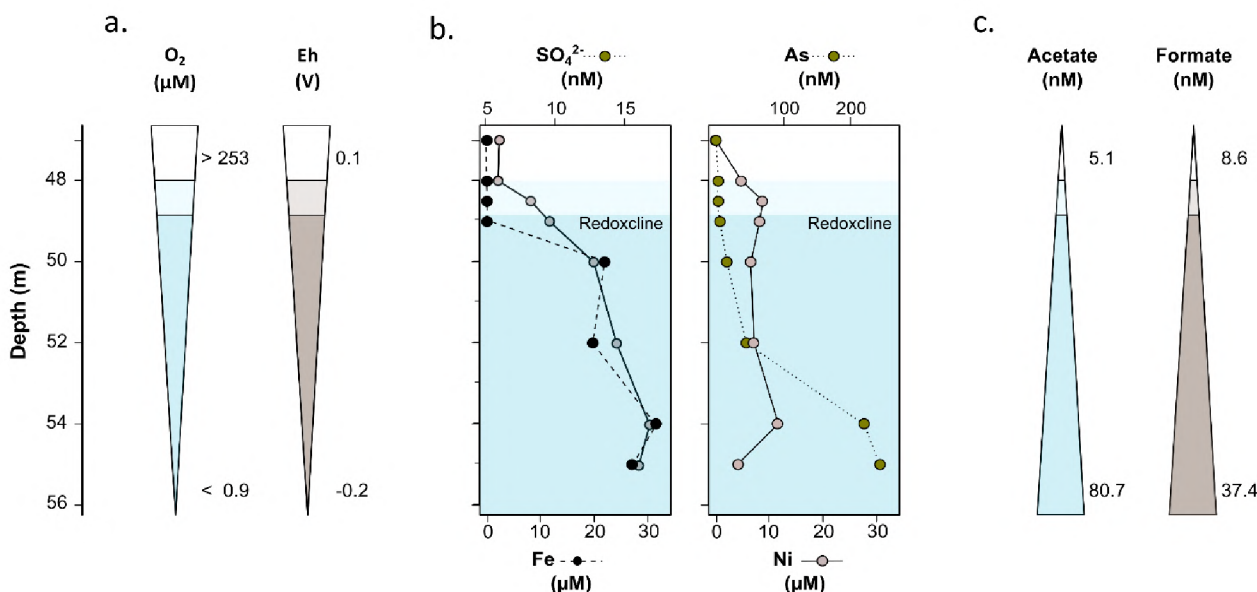
Figure 3. In-depth gradients of redox potential (Eh) and dissolved oxygen (O₂) in the hypolimnion of Lake Medard (a), which influence the interlinked biogeochemical cycles of siderophile elements such as iron, sulphur, nickel, and arsenic (b) and the bioavailability of labile carbon sources (e.g.,. acetate and formate) for microbial respiration (c). Data from ion content was extracted from Petrash et al. 2022 (Paper II). Figure was extracted from the Supplementary Electronic Information of Valero et al. 2024 (Paper IV).

1.4.   Research goal and hypothesis

The overarching goal of this doctoral research was: *"to investigate the influence of controlled electric potentials on the presence and activity of redox-reactive humic substances and reactive nitrogen species. This to understand their effect on electroactive metabolisms and the biomineralization of iron, phosphorus, and arsenic in the anoxic water column of Lake Medard, located northwest of the Czech Republic."*

This was addressed by studying the monimolimnion of Lake Medard by hydrogeochemical, hydrobiological, and electromicrobiology approaches. For this, the research goal was branched into three different working hypothesis:

(i)   *Interactions between electroactive microbial communities, thriving in the ferruginous hypolimnion of Lake Medard, have a broad influence on the amorphous-to-crystalline transformation of Fe(III)-bearing minerals*

6

(ii)   As nitrate is depleted at Lake Medard monimolimnion, a switch from nitrogen- to iron-based electroactive metabolism is boosted by a microbial preference for re-oxidable humic substances as alternative electron acceptor to reach and stabilize Fe(III)-oxyhydroxides

(iii)   Extracellular electron transfer involving humic substances and ferric iron(III) drives the scavenging of dissolved phosphate and arsenate from the hypolimnion by facilitating their co-precipitation within stabilized Fe(II,III)-oxyhydroxides.

Hypothesis were individually addressed by using the geochemical and hydrochemical characterization of the sediment's uppermost layers and the water column to assess the physic-chemical conditions and redox reactions occurring at Lake Medard's monimolimnion (Paper I). These insights were then informed by datasets of 16s rRNA amplicon sequencing to potentially link respiratory pathways and concomitant biomineralization reactions with members of the microbiome (Paper II). Afterwards, biomineralization reactions occurring at the monimolimnion were modelled by using the resulting dataset as input conditions for bioelectrochemical experiments that induced microbe-mineral interactions under controlled electric potentials and with the presence of humic substances and reactive nitrogen species (Papers III and IV).

2. Results

2.1. Summary results from Paper I

This paper assessed the geochemical partitioning of redox-reactive metal(loid)s in surface bottom sediments (0 to 8 cm depth) of Lake Medard by applying a chemical sequential extraction targeting reactive Fe and Mn minerals. These minerals were selected as they could act as terminal electron acceptors or provide dissolved phosphorus or metals when microbially reduced. Thus, they could support electroactive metabolisms in Lake Medard's monimolimnion. Spectrometric analysis showed that siderophile elements (e.g., As, V, and lanthanides) are bonded to highly reactive and easily reducible mineral phases (e.g., carbonates and poorly crystalline oxyhydroxides, respectively). Calculation of enrichment factors highlighted that such siderophile elements are accumulated over local and world-wide background values. Sediment characterization was further informed by X-ray diffraction analysis, which featured the presence of (i) poorly-crystalline particles exported from the redoxcline to the sediment-water interface and (ii) minerals equilibrated at deepest layers (up to 8 cm depth) from authigenic phases precipitated at the former mine pit. On the other hand, rare earth element systematics suggest that swift oscillations on redox potential (ca. 150 mV) generate metal(loid)s co-precipitation within highly reactive mineral phases in the monimolimnion. Overall, these results suggest that (i) metal(loid)s are released to the sediment porewater after reductive dissolution of reactive mineral phases; and (ii) their removal from the anoxic water column, by co-precipitating withing Fe(III)-oxyhydroxides, could be key factors controlling substrate availability for electroactive microorganisms at the sediment-water interface.

2.2. Summary results from Paper II

This peer-reviewed publication evaluated different biogeochemical processes occurring in the anoxic bottom waters of Lake Medard and their link to specific functionalities of the planktonic prokaryote community. Insights were informed by combining in-depth profiles of bioactive ions with relative amplicon abundances of the planktonic microbiome. This approach highlighted a compartmentalization of the planktonic microbiome thorough the monimolimnion based on microbial respiratory metabolisms involving chemical species of carbon, nitrogen, phosphorus, sulphur, iron, and manganese. Compartmentalized microorganisms likely affect carbon and siderophile elements turnover by exploiting an increasing availability of volatile fatty acids with water column depth. Accordingly, microaerophilic iron oxidizer–nitrate reducer community (e.g., *Gallionella* spp.) are suggested to biomineralize amorphous iron and manganese aggregates near the hypolimnion. Aggregates are exported then to the sediment-water interface and likely reductively dissolved or stabilized by electroactive metal reducers (e.g., *Rhodoferax* and *Geobacter* spp.) thriving near the bottom. 16Ss rRNA gene amplicon dataset also pointed out the genetic potential for microbial sulphate reduction at the sediment-water interface. In contrast, isotopes ratios of $\delta^{18}O$, $\delta^{34}S$ and $\delta^{56}Fe$ from the anoxic sediment pile (up to 8 cm depth) indicate an active co-recycling of iron and sulphur but with incomplete sulphate reduction. This suggest that concentration gradients of bioactive ions are impacted by bioenergetic considerations given the (i) continuous abundance of Fe(II)/Fe(III) redox pair as substrate for abundant iron oxidizer and reducers; and the (ii) occurrence of a cryptic sulphur cycle with generation and consumption of intermediate species. Overall, these results emphasise the

potential role of electroactive microorganisms over biomineralization reactions governing the interlinked biogeochemical cycling of carbon, nitrogen, phosphorus, sulphur, iron, and manganese.

2.3. Summary results from Paper III

This research effort focused on the modelling of iron biomineralization reactions controlling the interlinked cycling of nutrients and metals in the anoxic monimolimnion of Lake Medard as described in Paper II (topic 2.2). For this, graphite rod electrodes were poised as electron donors into anoxic ferruginous solutions mimicking our model site. Electrode-microbe interactions were induced in solutions inoculated with *Geobacter* spp., a model iron-reducing electroactive bacteria, which are naturally abundant near the sediment-water interface of Lake Medard. Experimental solutions contained environmentally relevant concentrations of ferrous iron(II), reactive nitrogen species (i.e., nitrate and ammonium), and humic substances which matched dataset from sediment-water interface described in Papers I and II (topic 2.1 & 2.2). These chemical species were selected because they are thought to control the niche compartmentalization of electroactive metabolisms in our model site described in Paper II (topic 2.2). In addition, arsenite was amended to explore how the biomineralization of Fe(III)-oxyhydroxides influence the immobilization of this and other oxyanions with analogous geochemical behaviour (e.g., phosphate) at the sediment-water interface.

Electrochemical and spectrometric analyses indicated that the generation of a reductive milieu at the surface of cathodes supported microbial electrotophy by providing electrons for carbon and nitrogen assimilation from acetate and ammonium, respectively. Electrotophy prompted variable ferrous iron(II) and arsenite concentration trends depending on the presence or absence of amended substrates. This, in turn, drove the formation of mineral aggregates entombing microbial cells as highlighted by SEM microphotographs.

Characterization of the microbial-mineral aggregates, by *in situ* μXRD and μXRF synchrotron-based analyses, highlighted that experimentally-precipitated FeOOH scavenged arsenic within reactive surfaces. Immobilization was fostered by the presence of ammonium as nitrogen source and oxidized humic substance derivatives, which worked as redox shuttlers for the partial reduction of ferric iron(III) by cells of *Geobacter* sp. This increased arsenite removal from solution operated by mediated EET even under elevated competing levels of phosphate, an oxyanion with analogous siderophile behaviour. In contrast, lack of humic derivatives promoted the formation of bacterial–mineral networks, which likely triggered long distance electron transfer mechanisms between cells due to absence of microbial biofilms. Accumulation of microbial-mineral networks, in turn, fostered the stabilization of amorphous ferrihydrite and augmented ferrous iron(II) immobilization. Consequently, iron species outcompeted arsenic oxyanions for available active sites on the reactive mineral surfaces.

As experimental solutions contained environmentally relevant contents of chemical species found in the bottom waters of Lake Medard, the described mechanisms is not only relevant to arsenic but also to phosphorus and another siderophile elements with analogous geochemical behaviour. Overall, these results pointed out the *Geobacter*'s preference for re-oxidable humic substances over nitrate as terminal electron acceptor to drive biomineralization reactions involving iron and siderophile elements (e.g., arsenic and phosphorus) in the bottom waters of Lake Medard and analogous ferruginous settings.

2.4. Summary results from Paper IV

This paper aimed to expand our insights on EET by stimulating the electroactivity of microbial species naturally thriving at the monimolimnion of our model site. For this, graphite rod were poised as terminal electron acceptor in bioelectrochemical systems inoculated with anoxic water from Lake Medard and amended with volatile fatty acids (i.e., acetate and formate) as carbon and electron sources. Experimental conditions drove the enrichment of electroactive planktonic cells capable of mediated EET rather than culturing them in thicker biofilms covering the surface of electrodes. Low electrogenesis (j = ~ 5 μA cm^{-2}) mainly relied on a microbial preference for formate over acetate as carbon and electron sources, but it was not sustainable on time (< 30 days). Yeast extract was alternatively amended to surge electroactivity as it contains redox shuttlers, but in spite of decreasing lag phase, electrogenesis was not augmented. Addition of other redox mediators (e.g., riboflavin and humic substances) produced no appreciable current increase. Mediated EET to electrodes was likely enhanced by flavin-type compounds from yeast extract amendments but not by other exogenous compounds such as humic substances derivatives.

16Ss rRNA gene amplicon sequencing analyses showed that enriched bacterial community varied depending on the substrate composition. However, enriched microbiome was mainly comprised of sulphate- (e.g., *Desulfatomaculum* spp.) and nitrate-reducing bacteria (*Stenotrophomonas* spp.). Harvesting of electroactive planktonic cells also resulted in the enrichment of different bacterial communities composed of iron-reducers (e.g., *Klebsiella* spp.) and fermenters (e.g., *Paeniclostridium* spp.). Scanning electron microscopy and energy-dispersive X-ray spectroscopy exhibited that microbial-mineral interactions induced the precipitation of sulphur and iron-rich organomineral aggregates on the surface of electrodes.

Altogether these results suggest that electroactive species capable of adaptive EET could also drove biomineralization reactions in the monimolimnion of Lake Medard. This also illustrate that nutrients and metals cycling are likely fostered by interspecies interactions, and they could be stimulated by an rise of labile carbon sources in the water column.

Paper I

Redox-driven geochemical partitioning of metal(loid)s in the iron-rich anoxic sediments of a recently flooded lignite mine pit: Lake Medard, NW Czechia

Umbría-Salinas K., **Valero A.**, Jan J., Borovec J., Chrastný V., Petrash D. A.

Redox-driven geochemical partitioning of metal(loid)s in the iron-rich anoxic sediments of a recently flooded lignite mine pit: Lake Medard, NW Czechia

Karelys Umbría-Salinas [a,*], Astolfo Valero [a,b,*], Jiří Jan [a], Jakub Borovec [a,b], Vladislav Chrastný [c], Daniel A. Petrash [a,d]

[a] Biology Centre CAS, Soil and Water Research Infrastructure, Na Sádkách 7, 370 05 České Budějovice, Czech Republic
[b] University of South Bohemia, Faculty of Science, Branisovská 1645/31a, 370 05 České Budějovice, Czech Republic
[c] Department of Environmental Geosciences, Faculty of Environmental Sciences, Czech University of Life Sciences Prague, Kamýcká 129, 165 21 Prague 6, Czech Republic
[d] Department of Environmental Geochemistry and Biogeochemistry, Czech Geological Survey, 152 00 Prague 5, Czech Republic

ARTICLE INFO

ABSTRACT

We evaluated the geochemical partitioning of Fe, Mn, As, V, and REE in sediments of a recently flooded open-cast lignite mine to interpret their response to recently established anoxia, and minor variations in the redox potential of its ferruginous bottom water column. Results from a sequential extraction scheme targeting reactive Fe mineral phases are combined with an assessment of sediment enrichment factors and REE systematics. Across the sediment pile metal(loid)s are being released from pre-existing authigenic phases as minor shifts in redox potential induce elemental immobilisation through co-precipitation with Fe into mineral phases of diverse reactivity. REE systematics confirms that minor oscillations in the water column's redox state can trigger swift changes in the speciation of the redox-sensitive elements. The observed metal(loid)s enrichment in the sediments can either be considered an ecological risk, if a management scenario involving solely recreational purposes is conceived, but it can also be seen as a feasible source of critical metals (e.g., REE and V) that are amenable to sustainable, secondary metal recovery endeavours. By anticipating the fate of redox-sensitive metal(loid)s in our study site, we provide parameters useful to delineate management programmes of this and similar post-mining lakes.

1. Introduction

Post-mining lakes result from water filling of former open-cast mines after mining operations cease (Gammons et al., 2009). Flooding either proceeds artificially (e.g., by deviating nearby river waters for reclamation purposes), or naturally by runoff and groundwater infilling (Schultze et al., 2017). Many coal and lignite mines are now post-mining lakes (Denimal et al., 2005; Schultze et al., 2010; Petrash et al., 2018), and their number is expected to increase as coal mining and coal-powered energy generation are progressively phased out worldwide.

The hydrochemistry of lignite post-mining lakes usually reflects the effects of weathering on Fe-sulphides, Fe-hydrous sulphates, and to a lesser extent aluminosilicate and sometimes carbonate phases comprising the outcropping, coal seam-associated facies and/or the former mine spoils (Denimal et al., 2005; Schultze et al., 2010). In their early stage, which could last up to 100 yrs., post-mining lakes tend to be meromic-

tic since density stratification between upper and bottom waters prevents seasonal mixing of the water column (Boehrer and Schultze, 2008; Schultze et al., 2010). Density stratification generates a permanent chemical boundary zone, known as the chemocline, that separates an oxygenated and seasonally mixed mixolimnion (upper waters) from an anoxic monimolimnion (Boehrer and Schultze, 2008). The chemocline exhibits marked activity gradients of redox-sensitive elements (Sánchez-España et al., 2020).

Post-mining lakes can slowly evolve towards holomictic conditions (Schutlze et al., 2010) which is followed by the solubilisation of high loads of potentially toxic metalloids–such as As–from the Fe(III)-oxyhydroxides that often comprise their sediments (Azcue and Nriagu, 1993; Tabelin et al., 2020). The leaching of potentially toxic metal(loid)s is probably the greatest impediment against efforts to develop complex ecological networks that could allocate safe use of these sites for recreational purposes (e.g., Otchere et al., 2004; Brázová et al., 2021).

---

* Corresponding authors.
E-mail addresses: karelys.umbria@bc.cas.cz (K. Umbría-Salinas), astolfo.valero@bc.cas.cz (A. Valero).

Conversely, controlled scavenging of critical transition metals such as rare earth elements (REE) from the redox stratified water column, for example through emerging methods for secondary biotechnological recovery (Thompson et al., 2017; Hua et al., 2019), would secure a supply of these metals. Establishing post-mining lakes as a secondary source of valuable trace metals would be crucial to a circular economic model for the redevelopment of coal-mining districts in countries such as Australia, Czech Republic, Germany, and Poland, amongst others with heavy economic reliance on coal.

Despite their relevance, there is a lack of studies showing how short-term development of contrasting physicochemical conditions in the water column of recent post-mining lakes affects the solid-state geochemical partitioning of metal(loid)s. Anticipating the fate of these elements as drastic changes of the bottom water column's redox state proceeds is of concern for management scenarios of post-mining lakes (e.g., Jakob-Tatapu et al., 2021; Woon et al., 2021).

Here we examine depth variations in the concentrations and redox behaviour of Fe, Mn, As, REE, and V in recent lacustrine sediments collected from a former open-cast lignite mine that was flooded between 2008 and 2015 (Lake Medard, NW Czech Republic). This recently flooded post-mining lake features oligotrophic and meromictic conditions, enrichment in dissolved SO_4^{-2}, Fe(II), and other metal(loid)s in its bottom water column (Petrash et al., 2018). At the sediment-water interface (SWI), Fe-oxyhydroxides formed at the chemocline have accumulated together with weathered minerals derived from a carbonate-rich Miocene claystone (Petrash et al., 2018).

To assess the response of Lake Medard sediments to the recently established bottom water anoxia, we evaluated the short-term geochemical partitioning of redox-sensitive metal(loid)s into reactive Fe minerals that occur to a depth of 18 cm in the sediment pile. Arsenic was selected as a proxy for the fate of redox-sensitive pollutants of concern; Mn was considered to better assess the redox behaviour of Fe, whilst V and REE were evaluated as proxies for economically valuable critical transition metal recovery.

We combined a sequential extraction protocol that targeted Fe mineral phases with diverse crystallinity and redox reactivity (e.g., ferrihydrite, lepidocrocite, goethite, and siderite), with Enrichment Factor (EF) and REE systematics (e.g., Bau and Möller, 1993). The approach applied here permits anticipating the redox dynamics of the metals of interest over potential variations of physicochemical parameters. Therefore, results from this research could be applied to improve the decision-making process of remediation and/or management programmes of post-mining lakes featuring similar hydrochemical and geological contexts.

2. Methods

2.1. Study area

Lake Medard (50°10′45″N, 12°35′45″E) is an engineered oligotrophic lake located in the Karlovy Vary region (NW Czech Republic; Fig. 1). It was formed by the flooding of a former open-cast lignite mine – known as Medard-Libík – with water from the nearby Ohře river between 2008 and 2015. It has an elongate surface area of ca. 4.93 km^2, with maximum central and eastern water column depths of ca. 60 m. Currently, the lake receives influx from one acidic surface drainage (Jozef creek; hereafter referred to as JC) that is rich in sulphate (SO_4^{2-}), Fe(II), and other metals (Petrash et al., 2018). After water infilling, continuous hydrochemical monitoring of key physicochemical parameters (i.e., dissolved oxygen, Eh, pH, conductivity, and temperature) of the newly formed oligotrophic lacustrine system has consistently shown the establishment of meromictic conditions. Accordingly, the bottom water column features a dysoxic hypolimnion and an anoxic ferruginous monimolimnion, with high dissolved SO_4^{-2} (19 ± 2 mM) but low dissolved hydrogen sulphide concentrations (< 0.3 μM; Petrash et al., 2018).

2.2. Sample collection

Two undisturbed sediment cores were retrieved from the lake bottom at ca. 55m depth in the central area. The sampling campaigns were carried out in November 2019 (S_1), and December 2020 (S_2). Before sediment sampling, we measured the conductivity, pH, Eh, dissolved oxygen (O_2), and temperature of the bottom water column from 47 m depth down to about 1 m above the anoxic SWI. Also, the bottom water column (monimolimnion, 50 to 56 m), and the Jozef creek waters were sampled. At the lab, core slicing was performed at 2 cm resolution and up to 18 cm (S_1) and 8 cm depth (S_2). For further details see Supplementary Material 1 (Appendix A, SM1.1).

2.3. Powder X-ray diffraction analysis

The mineralogy of the sediments was determined by a powder diffractometer (D8 ADVANCE, Bruker) equipped with a CuKα anode, using a 2Θ range of 4–80°, a step size of 0.015°, and a count time of 0.8 s /step. Semi-quantitative phase analysis was performed following the Rietveld method (Post and Bish, 1989). See Appendix A, SM1.2 for further details.

2.4. Chemical analyses

2.4.1. Organic matter, total organic carbon, total nitrogen, and total sulphur content determination

Sediment aliquots (100 mg) were digested using cold 10% HCl for 24 h to dissolve the carbonate fractions before determining the total organic carbon (TOC) and nitrogen (TN) content using a CHNS/O elemental analyser (Flash Smart, Thermo Fisher Scientific). Variability of the elemental concentration data obtained was between 0.21 and 0.37% for TOC, and 0.02 to 0.05% for TN, based on repeated analyses ($n = 12$) of the stream sediment certified reference material STDS-1 (Canadian Centre for Mineral and Energy Technology) and the peat soil standard SC2351 (Sercon).

2.4.2. Trace metals and rare earth elements content determination

A modified sequential extraction scheme was applied to dissolve Fe-bearing mineral phases of variable redox reactivity (e.g., Poulton and Canfield, 2005; Claff et al., 2010). Sediment aliquots (100 mg), corresponding to each of the sub-sampled depths, were chemically leached (10 mL of each of the extractants) to determine the geochemical partitioning–exchangeable metallic cations (M_{EX}), metal(loid)s bonded to carbonate minerals (M_{CARB}), metal(loid)s bonded to easily reducible Fe-oxyhydroxides (M_{ERO}), and metal(loid)s bonded to reducible and highly crystalline Fe-oxyhydroxides (M_{RO})– of Fe, Mn, V, As, and REE in the sediment pile. The metal(loid)s extracted by the applied sequential scheme are bound to the highly redox-reactive Fe pool of the sediments (i.e., after Poulton and Canfield, 2005). As such, any residual Fe-binding phases, most likely comprised of silicates, can be regarded as unreactive towards dissolved sulphide on the time scales encountered in post-mining lake sediments (Canfield et al., 1992; Raiswell and Canfield, 1996). Details on the sequential extraction scheme are provided in Appendix A, SM1.3.

Each extract was analysed for metal(loid)s (Al, Fe, Mn, V, and As), and REE (La, Ce, Pr, Nd, Sm, Eu, Gd, Tb, Dy, Ho, Er, Tm, and Yb) concentrations via quadrupole inductively coupled plasma mass spectrometry (Xseries II, Thermo Scientific) at the Czech University of Life Sciences, Prague. As an internal standard, we used ^{115}In at 1 μgL^{-1} concentration. Also, to achieve optimal analytical conditions for REE, the instrument was tuned to reach a CeO/Ce ratio < 1.5%. A five-point calibration curve was performed by using dilutions of single-element standards for ICP (Certipur®) and REE mix for ICP-MS (TraceCERT®) with concentrations of 0, 1, 10, 20, and 50 μgL^{-1}. The variability of the elemental concentration data was less than 10%. This is based on analyses of replicates ($n = 3$) for each extractant and element.
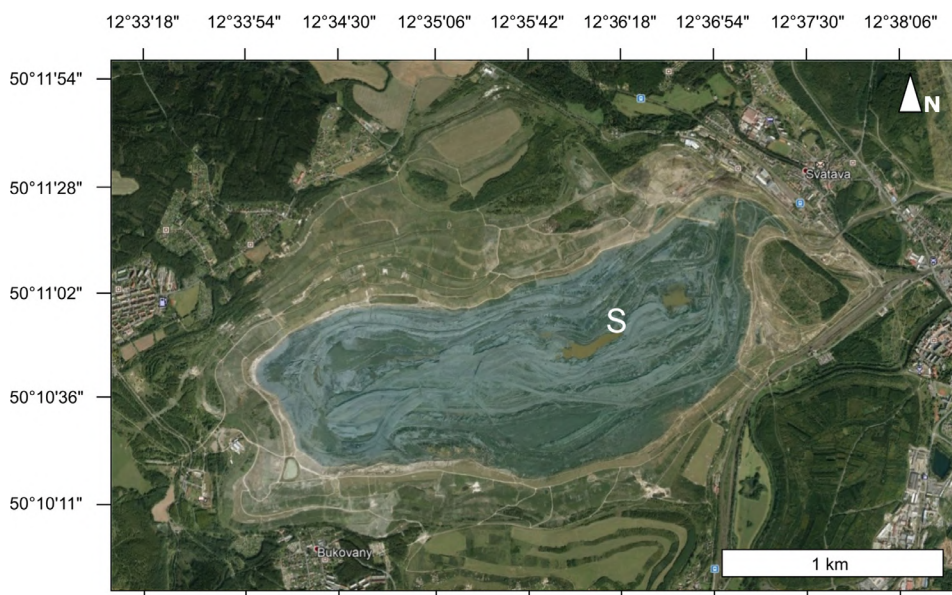
Fig. 1. Post-mining lake Medard (Karlovy Vary region, NW Czech Republic; blue area) formed after flooding of the Medard-Libík lignite mine (background). Brown areas indicate past pit lakes, and are the current deepest and permanently redox stratified depressions of the artificial lake bed. "S" indicates the central sampling location. Satellite imagery was extracted from Google Earth® in June 2021.

The water sample concentrations of the same elements listed above were determined by using High-Resolution ICP-MS (Thermo Scientific Element2) at the Pôle Spectrométrie Océan in Brest, France. The instrument was tuned to minimize oxide production, and mixed mono-elemental Pr-Nd, Ba-Ce, and Sm-Tb solutions were analysed to quantify potential oxide interferences prior to the analyses, which were negligible. Calibration was performed against multi-element solutions and analysed in the same session as unknowns to monitor accuracy (better than 5% for REE, and 10% for the other elements of interest).

2.5. Data treatment

2.5.1. Metal enrichment determinations

For assessing differential accumulation of the metal(loid)s in the lake sediment profiles examined here, we estimated the Enrichment Factors (EFs; Appendix A, SM1.4), considering the total concentrations (bulk extractable pool) and discrete background values of relevance (e.g., Dendievel et al., 2020). These background values included the metal content of world average shale (WAS) and carbonate (WAC) (Turekian and Wedepohl, 1961), and concentrations reported for the claystone lithology of the Sokolov basin (i.e., Miocene Cypris Fm.; Kříbek et al., 1998), which is the source of detrital material that accumulated in the abandoned lignite mine prior to and during flooding. By evaluating the respective extractant concentrations with regard to the former background values, we estimated the relative sediment enrichment/depletion in the Fe-oxyhydroxides ($M_{ERO} + M_{RO}$) and carbonate (M_{CARB}) fractions.

To obtain a broader estimation on whether a redox-sensitive metal(loid) of interest is significantly enriched in our post-mining lacustrine sediment profiles, we evaluated the obtained dataset using average elemental concentrations of the overlying O_2-depleted water column (50 to 55 m depth; Appendix A, ST1) to calculate relative enrichments. Besides, we also evaluated the sediment's relative enrichment by using elemental concentrations of the surficial Jozef creek water (Fig. 3b). JC is thought representative of the hydrochemistry of the mine's runoff waters before the flooding of the former mine pit. It is used primarily as a reference to the aqueous elemental partitioning that would have governed mineralisation reactions that proceeded in the sediments before the flooding and the establishment of the anoxic sediment-water interface in the current post-mining lake. Details on the mineralogy that was in equilibrium with the mining-impacted water bodies (preceding river water infilling) are available in Murad and Rojík (2003, 2005).

2.5.2. Rare earth elements anomalies and fractionation

Rare earth elements anomalies (i.e., relative enrichment regarding selected neighbouring elements within the group) were calculated (Eq (2) and (3), Appendix A, SM1.5) to distinguish the geochemical behaviour of lanthanides that could reflect variations in environmental redox conditions in the sediment profile (Shields and Stille, 2001; Hannigan et al., 2010). See Appendix A, SM1.5 for further details. Besides, the REE fractionation degree (i.e., light REE vs. heavy REE) was calculated by following Nance and Taylor (1976); Eq (4), Appendix A, SM1.5).

2.5.3. Statistical analyses

Normality of data distribution was evaluated by the Shapiro-Wilk test at the 95% significance level. When necessary, i.e., for elements exhibiting relatively low concentrations, data were plotted using a log-scale. Statistically relevant differences were evaluated by the t-test ($p < 0.05$)–for each fraction and total (bulk) and considering the two sampling periods. Data processing was performed with the software R Foundation for Statistical Computing (Vienna, Austria; R Core Team, 2016).

2.5.4. Potential metal(loid) release from the reactive sediments

By using the average elemental concentrations, the sediment characteristics (e.g., density and porosity), and the area of Lake Medard where O_2-depleted conditions are prevalent (Fig. 1) we estimated the potential of the reactive mineral phases to release As, V, and REE from the sediment pile to 8 cm depth. The utilised considerations are described in Appendix A, SM1.6. This approach also allowed us to determine the potential concentrations of metal(loid)s that would establish in the monimolimniom as a latent source of pollution or as an economically feasible resource of critical metals.

3. Results and discussion

3.1. Sediment-water interface characterisation

The pH values in both sampling periods, S_1 and S_2, displayed only minor variability. Despite the lack of mixing, the Eh of the monimolimnion increased by S_2 vs. S_1 (i.e., −80 vs. −192 mV, respectively). This change in redox potential was consistent with a shift in the depth of the chemocline to 52 m (S_2) from 48 m depth (S_1). This shift is interpreted to be linked to less groundwater recharge as the three months

Table 1

Concentration values of TOC, TN contents, and C/N ratios in the sediment cores. The values corresponding to the first sampling period (S_1; November 2019) are listed first; followed by the second period (S_2; December 2020). The range of semi-quantitative (XRD) mineralogical abundances in the sediments is also listed.

Sampling	Depth (cm)	TOC (%)	TN (%)	C/N
S_1	0–2	5.13	0.31	16.55
	2–4	3.93	0.20	19.65
	4–6	3.73	0.19	19.63
	6–8	3.70	0.17	21.76
	8–10	1.36	0.04	34.00
	10–12	1.34	0.03	44.67
	12–14	4.29	0.05	85.80
	14–16	1.73	0.03	57.67
	16–18	1.57	0.02	78.50
S_2	0–2	4.69	0.28	16.88
	2–4	3.93	0.23	17.17
	4–6	3.68	0.22	16.62
	6–8	4.09	0.14	29.28

Semi-quantitative phase analysis (range wt.%): kaolinite 66.0–68.5, quartz 8.0–9.0, mica 2.0–3.0, plagioclase 1.0–2.5, K-feldspar 3.0–6.0, gypsum 2.5–3.5, anatase 5.0–5.5, rutile 0.5–1.0, analcime 1.0–2.0, siderite 2.0–3.0, pyroxene 3.0.
Variability (%): TOC = 0.21 (S_1), 0.37 (S_2); TN = 0.02 (S_1), 0.05% (S_2).

preceding our 2020 sampling (S_2), were on average, considerably drier than the previous year, when S_1 took place (i.e., 77% less precipitation according to the records of the Czech Hydrometeorological Institute 2021). Less precipitation before S_2 diminished the recharge of salts dissolved by fluid-rock interaction in the bedrock and underlying crystalline lithologies, which are known to host epithermal fracture mineralisation (Pačes and Šmejkal, 2004). Decreased dissolution of subsurface salts caused the monimolimnion waters to become less dense. In turn, this triggered an increase in the depth of the mixolimnion and shifted the chemocline (e.g., Boehrer and Schultze, 2006). Consistent with this interpretation, there was a decrease in the monimolimnion's conductivity from 6,808 µScm^{-1} during S_1 to 2,607 µScm^{-1} during S_2. More recent hydrochemical monitoring of the water column (early May 2021) showed that such conditions were short-lived, as redox parameters resembling S_1 were re-established only five months after S_2 (Appendix A, ST2).

Despite increased redox potential of the monimolimnion during S_2, the bottom sediments remained under oxygen-depleted conditions and the overlaying waters displayed dissolved O_2 concentrations between 0.1 and 1.4 mg L^{-1}. XRD analyses (Appendix A, SF1) of the sediments showed that rutile (TiO_2), siderite ($FeCO_3$), gypsum ($CaSO_4 \bullet 2H_2O$), and in lower abundance pyrite (FeS_2) are phases present within a clayey sediment matrix that is composed mainly of kaolinite (Table 1).

FeOOH polymorphs (i.e., lepidocrocite and goethite) have accumulated as heterogeneous mineral clusters embedded in an organic clay-rich matrix. Amorphous precursors to these authigenic Fe(III) mineral phases are formed at the chemocline, from where they are exported to the anoxic SWI and stabilised (Petrash et al., 2018). Underlying the recent sediments are detrital materials derived from a weathered claystone (Cypris Fm.; Kříbek et al., 1998). These sediments also contained at some point, a secondary mine-drainage precipitated mineralogy that included jarosite ($Fe_3(SO_4)_2(OH)_6$; which occurs at more acidic spring sources), schwertmannite ($XFe_8O_8(OH)_6SO_4$), ferrihydrite, and goethite (Murad and Rojík, 2003; 2005). The oxyhydroxysulphate phases likely behaved as powerful scavengers for As(III) in solution leading to As(III)-enriched precipitates (Paikaray et al., 2017). When we compared our XRD analyses (Appendix A, SF1) with previously reported diffraction data of pit lake sediments (Murad and Rojík, 2003; 2005), it could be

observed that the oxyhydroxysulphates have undergone complete dissolution under the physicochemical conditions governing the anoxic deep water/sediments examined here, thus releasing both As and sulphate. Their alteration products (i.e., the Fe-oxyhydroxides polymorphs) exhibit contrasting crystallinities and presumably much lower redox reactivities towards As (Park et al., 2018), and, as discussed below, occur at variable abundances in the now ferruginous sediment pile.

The total organic carbon and total nitrogen contents were higher in the uppermost layer (0–2 cm) and decreased towards the bottom (Table 1). In detail, the C:N ratio ranged from 16 to 30 from 0 to 8 cm, and below this section ranged between 34 and 86 (S_1). These results indicate that N has accumulated in the upper sediments following flooding, and despite the lake's current oligotrophic nature (Vejřík et al., 2017). A significant downcore increase in the C:N ratio reveals depletion of N in the lower sediment organic reservoir and reflects an increase in the proportion of refractory OC derived from lignite.

3.2. Trace metals fractionation in surface sediments

Table 2 shows the total concentration at each depth for each element extracted in our four sequential steps for both sampling periods. We refer hereafter to these total concentrations as the highly reactive pool of any given metal (M_{HR}), and these values were used for normalisation purposes as well as for enrichment factor calculations (Appendix A, SM1.4). The Al_{HR} pool, and Fe_{HR} increased with increasing depth (Table 2). At 8 cm depth, however, an abrupt change in the prevailing trends occurred, and Al_{HR} and Fe_{HR} decreased two- and four-fold, respectively. On the other hand, compared with S_1, Mn_{HR} increased two-fold (to reach 809.2 mg kg^{-1}) in S_2 between 0–2 cm and 4–6 cm. Although it must also be noted that Mn_{HR} shows a decreasing downcore trend both in S_1 and S_2. The As_{HR} and V_{HR} peaked at the 6–8 cm depth interval, whereas the summatory of all the lanthanides (ΣREE) also increased with increasing depth in both periods (Table 2). Below we summarise and compare the partitioning trends of the elements under consideration.

3.2.1. Iron

Fe partitioning in S_1 was principally controlled by the easily reducible Fe-oxyhydroxides fraction (Fe_{ERO}), which accounted for 22.0 to 70.1% of the Fe_{HR} pool (Appendix A, SF2a) and displayed a higher abundance below 10 cm depth. Conversely, in the core collected in S_2 the total Fe_{HR} was principally related to the carbonates fraction (Fe_{CARB}), which ranged from 44.8 to 53.8%. Despite changes in the Fe reactivity trends in S_1 when compared to S_2, only exchangeable Fe (Fe_{EX}) showed a significant difference ($p > 0.05$) between both sampling periods. This is thought to be related to an enhanced reductive dissolution of Fe(III)-oxyhydroxides in the S_1 period, which released additional dissolved Fe(II). Throughout its reoxidation and subsequent precipitation as newly formed poorly crystalline Fe-oxyhydroxides, Fe(II) solubilised from the Fe_{EX} fraction as a response to slight variations in the physicochemical conditions of the water column, which contributes significantly to the internal (bottom water) Fe-cycling (Davison, 1993; Nealson et al., 2002).

3.2.2. Manganese

The summatory of Mn_{EX}, Mn_{CARB}, and Mn_{ERO} represented from 84.2 to 93.3% of the total Mn_{HR} pool in S_1 samples, whereas Mn_{RO} accounted for only 6.7 to 15.8% (Appendix A, SF2b). Our results indicate that at the top of the core, the Mn_{HR} is mostly comprised of the more reactive (weakly bonded) fraction, while downcore it appears rather to be bonded to less reactive phases. This suggests that, at the SWI, Mn could be readily available to be utilised as an alternative terminal electron acceptor to further fuel Fe(III)-based anaerobic microbial respiration pathways (Davison, 1993; Nealson et al., 2002). These pathways may in turn lead to subsequent stabilisation of Fe(II,III)-oxyhydroxides, and induce the co-precipitation of V, As, and REE (Sundman et al., 2020; Kontny et al., 2021). By S_2, the Mn_{HR} pool was found to have increased two-fold (Table 2), and all of the assessed fractions, except for Mn_{EX},

Table 2
Total elemental concentration (in mg kg⁻¹) of the highly reactive pool of metal(loid)s extracted in both sampling periods.

Sampling	Depth (cm)	Al	Fe	Mn	V	As	La	Ce	Pr	Nd	Sm	Eu	Gd	Tb	Dy	Ho	Er	Tm	Yb	ΣREE
S_1	0–2	5011.6	14,228.1	402.2	69.9	49.4	4.9	7.3	2.4	8.9	1.5	0.4	1.5	0.2	0.9	0.1	0.4	0.04	0.4	28.9
	2–4	8276.6	26,377.2	362.5	110.9	64.9	13.3	19.9	4.2	16.8	3.2	0.8	3.3	0.4	2.1	0.4	0.5	0.1	0.9	66.5
	4–6	9573.7	26,947.1	250.5	98.8	61.2	13.9	21.6	4.9	19.5	3.5	1.0	3.6	0.5	2.4	0.4	0.5	0.1	0.9	73.4
	6–8	9961.8	51,295.3	314.8	145.8	123.8	23.9	29.6	6.0	23.5	4.1	1.2	4.5	0.6	2.9	0.6	0.6	0.2	1.1	99.7
	8–10	4162.8	11,978.3	299.7	120.2	41.2	15.2	23.5	5.2	21.2	4.4	1.0	4.1	0.5	2.7	0.5	1.1	0.1	0.9	80.5
	10–12	2874.1	12,197.3	353.2	63.8	45.2	17.6	23.3	5.2	21.1	4.2	1.0	3.9	0.5	2.4	0.4	0.9	0.1	0.8	81.5
	12–14	3177.8	14,494.8	380.1	51.6	45.4	21.0	30.0	7.3	29.8	5.9	1.4	5.5	0.7	3.2	0.6	1.3	0.1	1.0	108.0
	14–16	3874.1	12,062.3	305.9	68.7	59.4	17.1	25.6	5.9	24.5	4.7	1.2	4.6	0.6	2.7	0.5	1.0	0.1	0.8	89.6
	16–18	3731.2	13,022.6	340.1	71.7	63.8	18.2	26.4	6.0	24.2	4.7	1.2	4.4	0.6	2.6	0.5	0.9	0.1	0.8	90.8
S_2	0–2	4120.3	21,862.5	809.2	110.2	37.5	8.1	22.9	1.3	10.4	2.0	0.5	2.1	0.2	1.3	0.2	0.7	0.1	0.6	50.4
	2–4	4698.2	22,797.2	452.1	173.6	25.9	8.1	25.8	1.6	12.0	2.3	0.6	2.4	0.2	1.5	0.3	0.7	0.0	0.7	56.3
	4–6	3824.1	23,567.3	504.6	93.2	20.1	10.6	27.8	1.6	12.8	2.3	0.6	2.5	0.3	1.6	0.3	0.8	0.0	0.8	62.2
	6–8	7631.3	49,364.8	323.0	383.5	55.8	21.0	47.1	2.6	21.7	4.0	1.1	4.3	0.4	2.4	0.4	1.1	0.1	1.1	107.3

Variability range (%) (S_1 and S_2): Al, V, Mn, Fe = [4.4 to 9.0]; As = [8.3 to 10.6]; REE = [1.5 to 10.8].

exhibited statistically significant differences ($p < 0.05$) with regard to S_1. The Mn_{HR} pool was then dominated by Mn_{CARB}, which accounted for up to 79.8% of the total Mn extracted (Appendix A, SF2b), and it showed even higher values at the top of the sediment pile.

3.2.3. Vanadium

Partitioning of V was variable along the sediment profile. In S_1, the summatory of V_{ERO} (81.0%) and V_{RO} (16.7%) represented up to 97.7% of the V_{HR} pool at the top of the core (Appendix A, SF2c). V_{ERO} decreased downcore, but a marked abundance peak is observed between 6 and 10 cm. The V_{CARB} fraction was not detected in the SWI. Analogously, in S_2, V was mostly bonded to Fe-oxyhydroxides of diverse crystallinity, which together accounted for 97.9% of the V_{HR} pool. However, in S_2 the V content bound to reducible, more crystalline Fe-oxyhydroxides increased up to 20-fold throughout the entire sediment profile, when compared to the first sampling. Thus, the V_{RO} fraction exhibited significant differences between periods ($p < 0.05$).

3.2.4. Arsenic

As partitioned quite differently downcore when compared to the other elements with siderophile affinity also evaluated here (Appendix A, SF2d). In the S_1 period, at the SWI, As bonded to easily reducible and highly crystalline Fe-oxyhydroxides, accounting for up to 83.4% of As_{HR} pool. However, the element was principally bound to As_{RO}, with concentrations between 30.8 and 45.0% from the top of the core to 8 cm depth. Below this depth, As was dominated by the exchangeable fraction, which displayed increasing downcore concentrations from 39.8% at 8 cm to 71.8% at the bottom. In our second sampling, As was principally associated with the As_{ERO} fraction, which bound 61.5 to 79.9% of the As_{HR}, and displayed peak concentrations at the 4–6 cm interval. The As_{CARB} decreased from 38.5 to 3.4% with increasing depth. Besides, As_{EX} and As_{RO} concentrations were mostly below the detection limit ($< DL$). Despite the described variations in the As reactivity trends, this element did not show significant differences ($p > 0.05$) between sampling periods in any of the assessed fractions. However, given that As_{EX} was $< D.L$ in the second sampling, we infer that highly mobile As co-precipitated with Fe into the dominant Fe(II,III)-oxyhydroxide and, to a lower extent, carbonate phases.

3.2.5. Rare earth elements

Fig. 2e shows the geochemical partitioning of REE. In our S_1 sampling, REE_{ERO} and REE_{RO} fractions accounted for between 53.3 and 99.6% of the REE_{HR}, respectively (Appendix A, SF2e). In contrast, REE bound to carbonates dominated the sediment's REE pool in S_2, when this fraction accounted for 47.8 to 52.9% of the REE_{HR}. Also in S_2 the REE_{RO} represented $< 5.0\%$ of the highly reactive pool. Thus, as described for As above, lanthanides were released after the dissolution of easily reducible Fe-oxyhydroxides, and then, trapped within newly formed crystalline Fe-bearing mineral phases (e.g., Hua et al., 2019).

3.2.6. Trace metal(loid)s remobilisation in the sediment pile

Overall, the geochemical partitioning of the studied elements (Appendix A, SF3) allowed us to determine that at the SWI (0–2 cm), the Fe, V, As, REE, and Mn were principally related to poorly crystalline reducible Fe-oxyhydroxides and to a lesser extent to crystalline phases. Differently to other elements, Mn and As were also weakly sorbed onto the surfaces of discrete Fe-bearing mineral phases (i.e., M_{EX} fraction). From 2 to 8 cm, siderite exerts a more significant role controlling the fate of REE and Mn. This assumption is based on our XDR analyses, which showed siderite as the only detectable carbonate mineral (2.0–3.0 wt. %). The control exerted by siderite over REE and Mn appears to intensify when slight variations in the environmental redox state occur, such as observed in S_2, when the proportion of metals bonded to Fe-carbonates increased substantially. This was also the case for As, which seems to rapidly adsorb onto the surfaces of siderite as a response to dysoxic conditions in the SWI (i.e., S_2).

Below 8 cm, Fe, Mn, REE, and to a lesser degree the V content appears to be strongly controlled by Fe-oxyhydroxides transformations, whereas As continues to be mostly weakly bonded onto mineral surfaces (Appendix A, SF3). The behaviour of As is not surprising given that its oxyanions – arsenate and arsenite – easily adsorb onto reducible oxyhydroxides (Dixit and Hering, 2003), carbonates (Wang et al., 2021), and/or green rust (Perez et al., 2021). Despite variations in the geochemical partitioning trends of the metal(loid)s under examination, the bulk sediment M_{HR} pool did not present significant differences between sampling periods ($p > 0.05$). Therefore, we infer that the slight variation in the redox state of the overlying water column that we registered between S_2 and S_1 (i.e., −80 and −192 mV, respectively), is sufficient to trigger the release of redox-sensitive metals from the sediment reactive mineral phases (see Zhang et al., 2014). For most metals, this release is followed by their subsequent co-precipitation with Fe either into poorly crystalline oxyhydroxide or recrystallised carbonates. To shed further light on the mobility and partitioning of the metals of interest, in the following section we considered their bulk vs. fraction specific enrichment trends.

3.3. Trace metal(loid)s enrichment

The calculated enrichment factors are displayed in Fig. 3. Except for Mn, Ce, and Ho, most elements showed relative enrichment when the carbonate and the combined Fe-oxyhydroxide fractions are compared to world average carbonate (WAC) and shale (WAS) (Fig. 3a). Regarding Fe, its EF values (EF_{Fe}) ranged from 5 to 10, indicating acute enrichment with regard to all of the background values. Conversely, the EF_{Mn} only shows acute enrichment when normalised with regard to the Sokolov claystone. V could either be moderately (WAC and Sokolov claystone) or acutely enriched (WAS). The ΣREE in the carbonate fraction, as Mn, did not display enrichment (WAC), but the combined oxy-
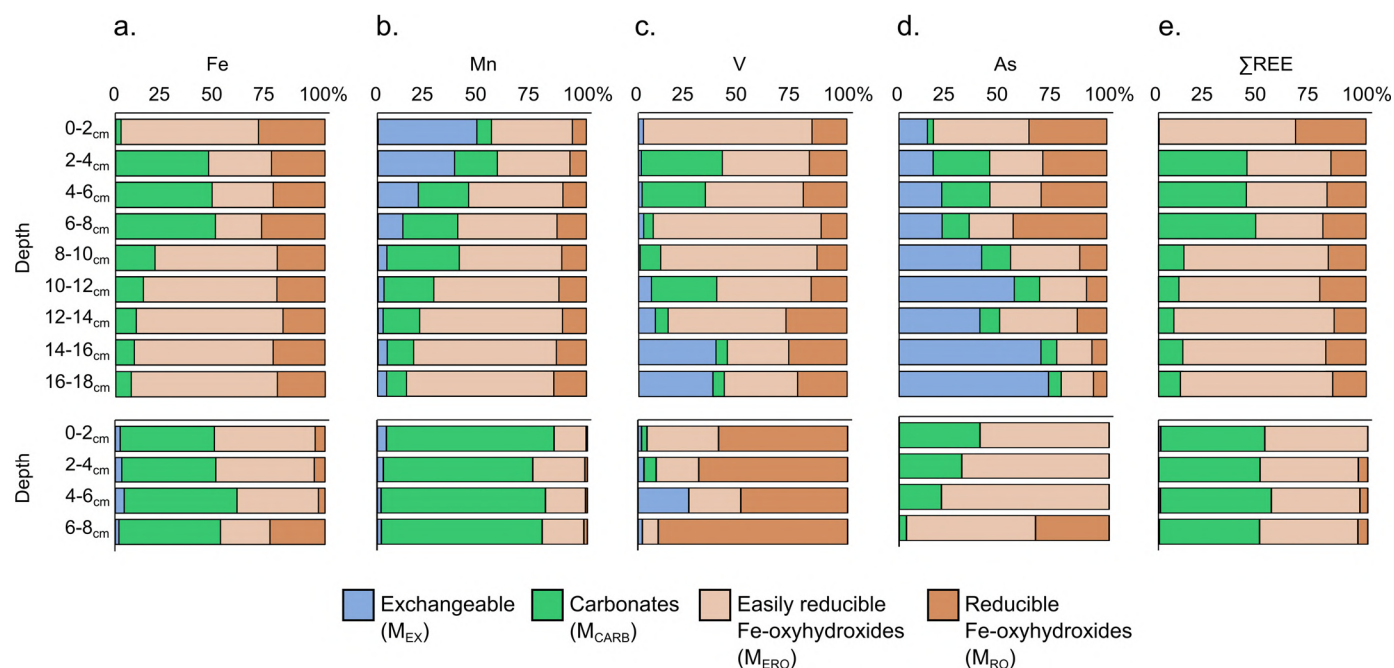
Fig. 2. Depth metal concentration profiles of highly reactive fractions in the lacustrine sediments of Lake Medard. The upper part shows concentration values corresponding to the first sampling (S_1; November 2019), while the lower part corresponds to the second sampling (S_2; December 2020).

hydroxide pool and the bulk sediments are acutely enriched when compared to both WAS and the Sokolov claystone (Fig. 3a). Lastly, As displayed an acute enrichment according to all backgrounds as its EF values ranged between 30 and 55. The EF values for the fractions that dominated the geochemical partitioning of the metals -i.e., carbonates and Fe-oxyhydroxides - are summarised in Appendix A, ST3.

When we compared the Fe-oxyhydroxide phases to WAS, all metals presented EF values equivalent to those calculated using the M_{HR} pool, except for Mn that showed higher EFs. Contrastingly, higher EF values regarding WAC are observed for all the metals under consideration, with As showing the most acute enrichment. In addition, V and the lanthanides revealed higher values downcore for both fractions, whereas EF values for Fe_{CARB}, Mn_{CARB}, and As_{CARB} were higher at the top of the sediment core. These data suggest that effectively, Fe-bearing carbonates and Fe-oxyhydroxides of diverse crystallinity re-immobilise redox-reactive metal(loid)s in the most recent lacustrine sediments (i.e., above 8 cm). Some of these metal(loid)s are likely being leached and sourced from alteration products of the former mine bedrock (below 8 cm depth), from where they can diffuse upwards to the now anoxic lake floor. Also, groundwater inflow carrying dissolution products may be important, as reported in other lignite post-mining lakes (e.g., Denimal et al., 2005). Accordingly, it is plausible that groundwater replenishment causes the bottom water column to exhibit variable conductivities but a prevalent circumneutral pH (~7.2) despite its rather high sulphate content, which contrasts with what has been observed in acidic post-mining lakes not affected by carbonate dissolution and groundwater influx (cf. Schultze et al., 2010). Finally, the EF_{Fe}, EF_{Mn}, and EF_V were higher in S_2 than in S_1 cores, while the EF_{As} and $EF_{\Sigma REE}$ were lower in the second sampling (Appendix A, ST4). This result confirms that slight Eh variations (i.e., from anoxic to dysoxic conditions) of the SWI, can lead to mineral transformations that allocate remobilisation of Fe and Mn, triggering the release of As, V, and lanthanides.

3.4. Potential lake management scenarios

Due to the metal-polluted nature of the lacustrine sediment under examination, in this section, we assess the potential of the reactive mineral phases to release As and accumulate V and REE. Also, by using equilib-

rium modelling generated by the Geochemist's Workbench™ software as supporting information (Bethke et al., 2021; Appendix A, SF4 and SF5), we speculate on how these latent metal loads would alter the hydrochemistry of the bottom waters.

3.4.1. Latent sediment metalloid accumulations: as pollution and an environmental risk

Regarding As, we estimate that the recent sediments, to a depth of 8 cm, have accumulated between 22.9 and 45.5 mgkg^{-1} of this element; mostly into the more reactive binding phases (i.e., As_{EX} and As_{ERO}). The current sinks of As could change, however, since meromictic post-mining lakes that have sulphate-rich waters, such as Lake Medard, could transition towards euxinia (i.e., free dissolved hydrogen sulphide; Meyer and Kump, 2008; van de Velde et al., 2021). The establishment of euxinia in the bottom water column would induce As(III) immobilisation through its co-precipitation with Fe(II) into (arseno)pyrite (Telfeyan et al., 2017; Appendix A, SF4 and SF5). Yet, the stabilisation of pyrite from metastable mackinawite (FeS)-like precursors appears to be at present hindered by the general lack of labile organic matter in the oligotrophic lake, and the sediment pyrite abundance is < 0.5 wt. % (Table 1).

The reduction of poorly crystalline Fe-oxyhydroxides and their subsequent stabilisation as more crystalline oxyhydroxide phases does exert a major control over the fate of As in the present-day anoxic lacustrine system. In addition, percolation of anoxic waters into the porewater system appears to promote the leaching of weakly bound As stocks (Fig. 2d). Hence, should the current ferruginous but not euxinic conditions prevail at the monimolimnion, the reductive dissolution of reducible Fe(III)-oxyhydroxide sinks has the potential to solubilise between 1.8 and 3.3 tons of As, i.e., by only considering the exchangeable and poorly crystalline oxyhydroxides fractions to a depth of 8 cm. These latent As levels would then accumulate in the monimolimnion to levels that represent an ecological risk.

Slight dissolved O$_2$ oscillations at the SWI observed during S_2 have proven to be instrumental for significant As remobilisation. More prevalent oxygenation of the bottom water column, such as in the event of holomixis, would thus increase the dissolved As concentrations of the monimolimnion to up to 0.73 mg L^{-1}, which would represent a 1.9-fold increase in its current average concentrations (i.e., 0.37 ± 0.17 mgL^{-1},
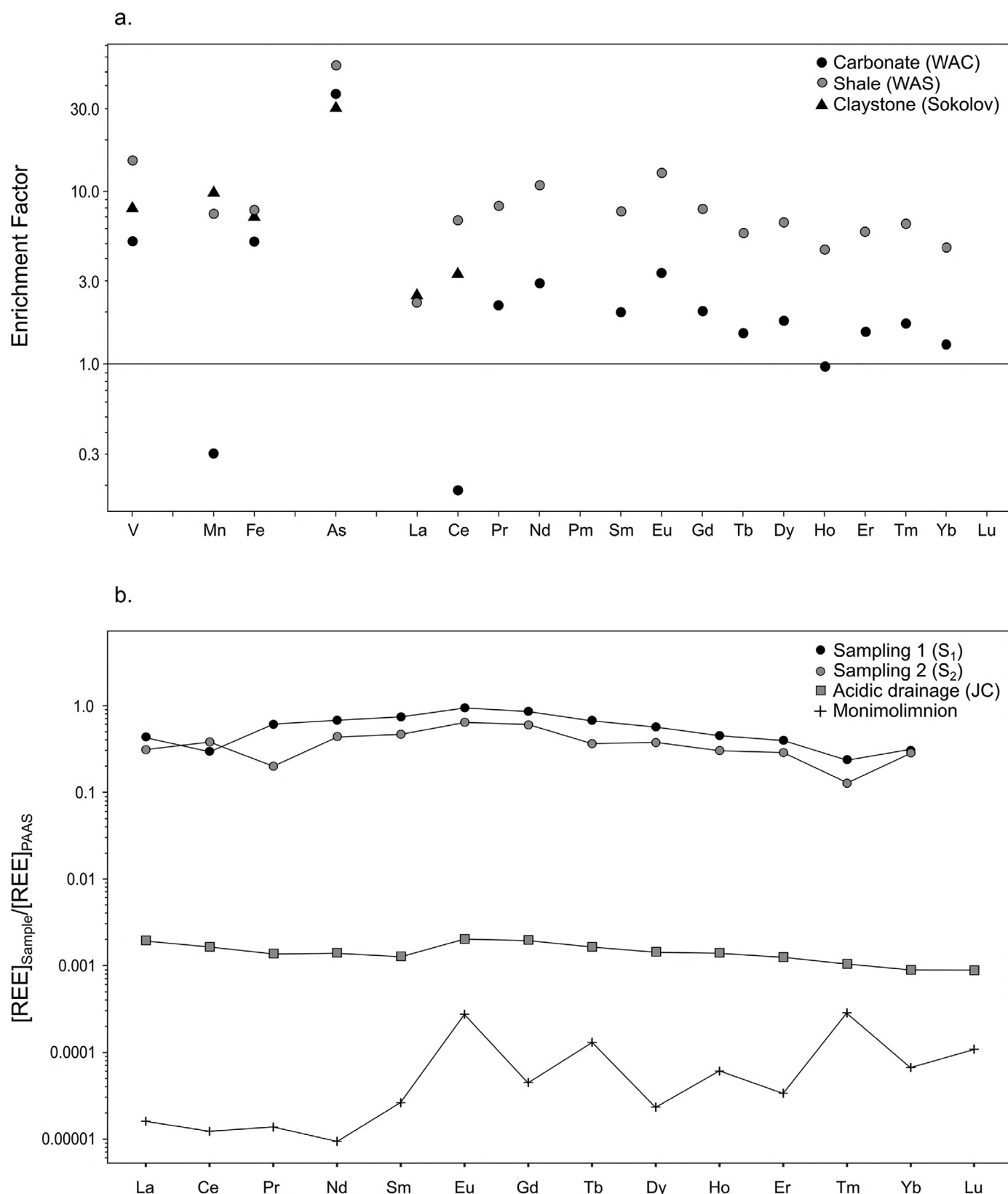
a.

b.

Fig. 3. Relative enrichment in the post-mining lacustrine sediment profiles, using the mean values between both sampling periods, and considering the average concentration from the core. The figure shows (a) the calculated enrichment factor (EF, Eq. (4)) normalising the total concentrations of the highly reactive (M_{HR}) pool with regard to: (i) world average carbonate (WAC, ●; Turekian and Wedepohl, 1961); (ii) shale (WAS, ◐; Turekian and Wedepohl, 1961); and (iii) the local claystone lithology of the Sokolov basin (Miocene Cypris Fm., ▲; Kříbek et al., 1998), and (b) the Post-archean Australian shale (PAAS) REE abundance patterns (S_1 ● and S_2 ▲) sampling. For comparison purposes, we also plotted the PAAS-normalised patterns of the O_2-depleted water column (monimolimnion ◐), and the acidic drainage (JC ■). See text for details.

Appendix A, ST1). Currently, the monimolimnion's As concentrations are already considerably higher than the existing European thresholds for groundwater values (i.e., between 7.5 to 12 μgL^{-1}, Directive 2000/60/EC; European Community, 2000). In the foreseen transition to episodic holomixis, dissolved As levels would decrease to 27.7 μg L^{-1} in the entire water column, which would be 2-fold higher than the aforementioned thresholds.

Under anoxic (ferruginous) conditions, the more mobile and toxic As(III) is expected to prevail (Smedley and Kinniburgh, 2002; Jiang et al., 2009). This is an environmental concern since As(III) can affect proteins and enzymes and thus, propitiate cell damage (Duker et al., 2005). The sediment's latent As concentrations can therefore be seen as an ecological risk to efforts to develop complex ecological networks such as ongoing fish introduction (e.g., Vejřík et al., 2017; Brázová et al., 2021) since the metalloid bioaccumulates in fish livers and gills (Kumari et al., 2017).

3.4.2. Latent sediment metal accumulations: economic secondary recovery feasibility

The fate of lanthanides in the sediment pile is governed by reactions transforming poorly crystalline Fe-oxyhydroxides (Fig. 2e). Co-precipitation of REE with Fe into more crystalline oxyhydroxides appears to be a crucial process controlling the fraction-specific lanthanide enrichment in our sediment pile. The enrichment of REE in the sediments would have initiated even before the former mine was flooded, REE enrichment in the now anoxic lake sediments is up to 100 times higher than those measured in the Jozef creek (Fig. 3b).

The REE-enriched sediments represent an outstanding secondary source of REE to the water column since their Post archean Australian Shale (PAAS)-normalised concentrations are up to 10^4 times higher than those in the anoxic bottom waters (Fig. 3b). Likewise, the REE content of the anoxic sediments in Medard is 10^6 times higher than the concentrations reported for seawater (Fig. 3b) and is within the range observed in deep-sea sediments (e.g., Milinovic et al., 2021). These latter reservoirs have been considered as alternative yet still technologically challenging sources of REE (Milinovic et al., 2021).

Analogous to our calculations for As, but considering the total highly reactive pool, we estimate that the recent sediments (up to 8 cm depth) have REE contents that would become economically feasible. For example, considering that the recent upper anoxic sediment pile has accumulated 283 kg of Gd, which at the time of writing this article has a market value of 16,456 € kg^{-1}. Then, it could be estimated that the first 8 cm of the post-mining lake sediments contain a recoverable Gd accumulation with a value of up to €4.7 M. Similarly, the first 8 cm of these sediments contain a V accumulation equivalent to 7730 kg, which at the current market price of €26.5 kg^{-1} would have a value of €204 k should an 80% recovery efficiency be achieved. The figures given above can be expected to increase significantly due to a global supply shortage of such critical metals, increasing demand, a lack of substitutes, and mounting geopolitical pressures. Although these figures are broad and currently speculative, the calculations above highlight the possibility of developing post-mining lakes, such as Medard, as secondary sources of valuable metals.

An inexpensive and green alternative to recover such elements from solution is emerging in the increasing application of bioelectrochemical systems (BES) that use microorganisms as biocatalysts to recover valuable dissolved resources efficiently and sustainably from wastewaters (Chatterjeea et al., 2019). BES can be optimised for high-efficiency metal removal and/or recovery (Wang and He, 2020), and the fundamentals behind a foreseen, economically feasible deployment of up-scaled BES in post-mining lakes are being actively investigated.

3.5. The fate of redox-sensitive metals as revealed by the REE systematics

We explored to what extent short-lived redox variations were recorded by the REE systematics of the Fe-rich lacustrine sediments under examination, as a gauge for sediment transformation under suboxic conditions. As described in Section 3.2.6, most REE (except for Ce) displayed lesser concentrations in S$_2$ (Table 2), which implies that the slightly increased redox potentials of the water column triggered lanthanides remobilisation (Fig. 2e). Also, in S$_1$, the sediments below 2 cm, exhibited 3 times higher REE concentrations than the sediments near the SWI, which confirms the assertion above.

The average PAAS-normalised REE abundance patterns during both of the sampling periods are shown in Fig. 4. The sediment REE content displayed a more variable behaviour in the uppermost sediment layers (black line, Fig. 4a) than below this zone (grey shadowed line, Fig. 4a). This implies that redox-sensitive metals–such as cerium–in recently deposited sediments are more prone to be influenced by minor shifts in the physicochemical conditions of the bottom waters. Also, the heavy rare earth elements (HREE) patterns from both sampling periods were similar, but the light rare earth elements (LREE) patterns varied. In S$_1$ (Fig. 4a), an enrichment in LREE is consistent with La$_N$/Yb$_N$ > 1 (Appendix A, ST5). This LREE enrichment has been described as a signature of lignite weathering in other post-mining lake systems located in Central Europe (Bozau et al., 2004; 2008). Only LREE bonded to carbonates are depleted (i.e., La$_N$/Yb$_N$ < 1; Appendix A, ST5). This may be due to a stronger affinity of carbonate towards HREE (Bozau et al., 2008; Laveuf and Cornu, 2009). An enrichment in the so-called MREE: i.e., Nd and Tb (Fig. 4), is reflected by La$_N$/Sm$_N$ ratios < 1 (Appendix A, ST5). A similar MREE enrichment was also observed by Bozau et al. (2008) when studying other post-mining lakes more strongly influenced by acidic drainages.

Based on the variability of the abundance patterns of LREE between sampling periods, we evaluated the Ce and Eu anomalies to determine if such variability corresponds to changes in the redox potentials of the overlying waters. The S$_1$ bulk sediment showed a negative Ce anomaly (Ce/Ce* range between 0.45 and 0.61 mean = 0.56; Appendix A, ST5) that is indicative of a relative depletion of Ce(III) (Fig. 4a). The later results from the reduction of Ce(IV) that solubilises trivalent Ce from the sediments (e.g., Haley et al., 2004). Under laboratory conditions, Nedel et al. (2010) demonstrated that cerium is absorbed into easily reducible Fe(III)-oxyhydroxides and can be readily released into solution as the oxyhydroxides stabilise to more crystalline phases. In contrast, the Ce/Ce* values from S$_2$ ranged between 1.39 and 1.64 (mean = 1.53; Appendix A, ST5), and the PAAS-normalised REE abundance pattern (Fig. 4b) depicted a positive Ce anomaly, which is likely related to the establishment of less reducing conditions in the SWI (Manoj and Kawsar, 2020) by the time of our 2020 sampling. Although the redox potential difference in the overlying water column was not so marked between sampling periods, and the SWI remained under suboxic conditions, the change in bottom water Eh that we recorded in S$_2$ appears to have been sufficient to stimulate further precipitation of poorly crystalline Fe(III)-oxyhydroxides while also favouring the oxidation of Ce(III) in solution and its subsequent immobilisation as Ce(IV) in the metastable mineral array of newly formed or altered phases (cf. Nedel et al., 2010).

We also evaluated the Eu anomaly, Eu/Eu*, but the values obtained in both sampling periods and for each fraction (mean = 0.1; Appendix A, ST5) indicate no occurrence of Eu anomalies in the sediment. Contrary to Ce, the observed changes in the environmental redox state were not sufficient to trigger Eu(III) release from Fe(III)-oxyhydroxide sinks nor its accumulation by co-precipitation within other mineral phases. This is not an unexpected result because europium could remain in solution as Eu(II) under circumneutral and highly reductive conditions. In this regard, it behaves as Fe(II) (MacRae et al., 1992; Tostevin et al., 2016). Besides, MacRae et al. (1992) estimated that detection of an Eu anomaly in recent sediments could be delayed by up to 10^3 years. Thus, the short-term redox variations targeted here do not produce significant changes in Eu speciation in the lacustrine sediment pile.

Relative enrichments of Ce are traditionally thought to be a very sensitive proxy to minimal variability in O$_2$ levels in the water column
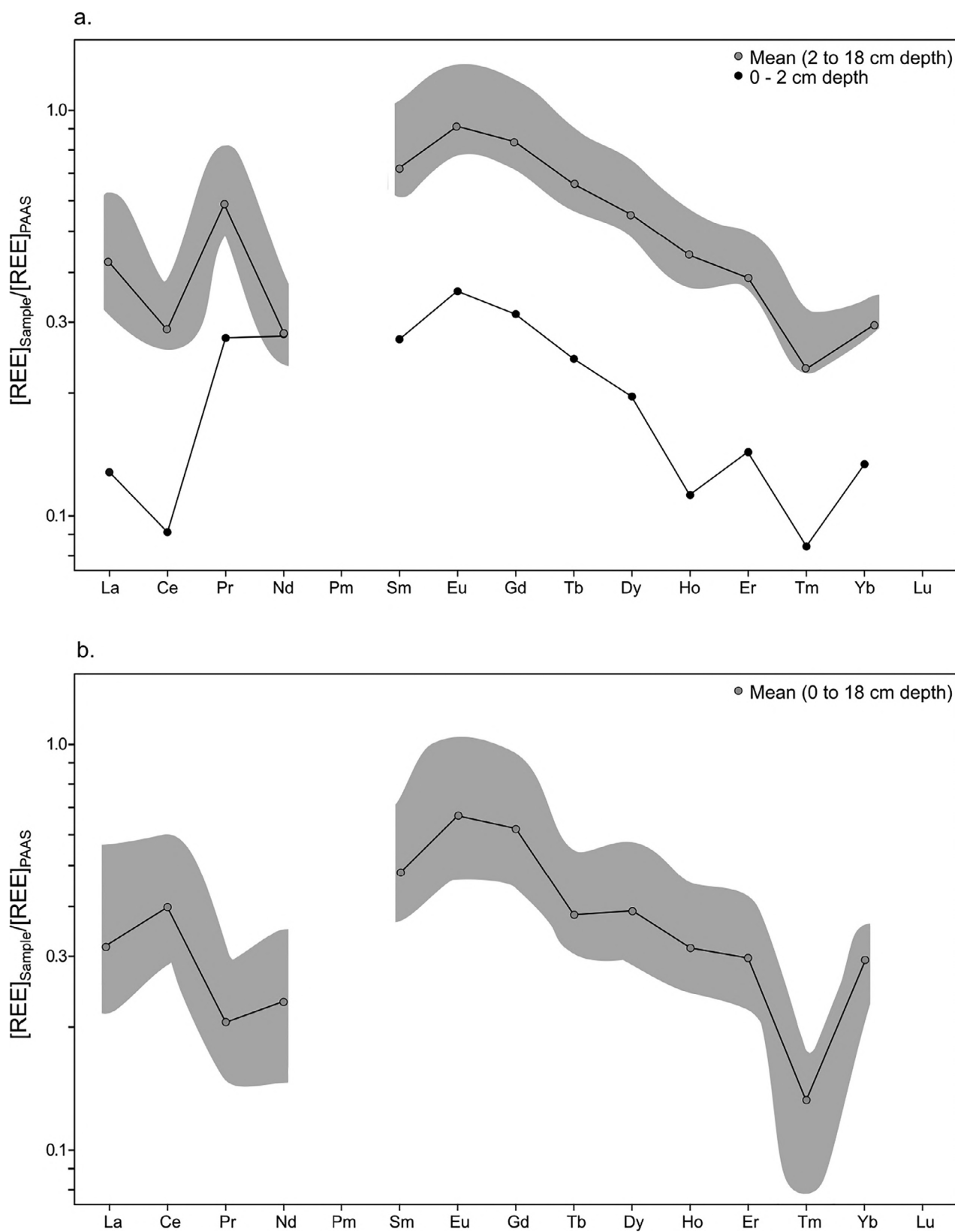
Fig. 4. Scatter plot displaying the average PAAS-normalised REE abundance patterns of sediments collected in (a) S_1; and (b) S_2. Black line indicates the obtained pattern by using concentrations from 0 to 2 cm depth by S1 (●), and from 2 to 18 cm depth by S_1 and 0 to 18 cm depth by S_2 (◉), with the grey shadow portraying the range of average concentrations.
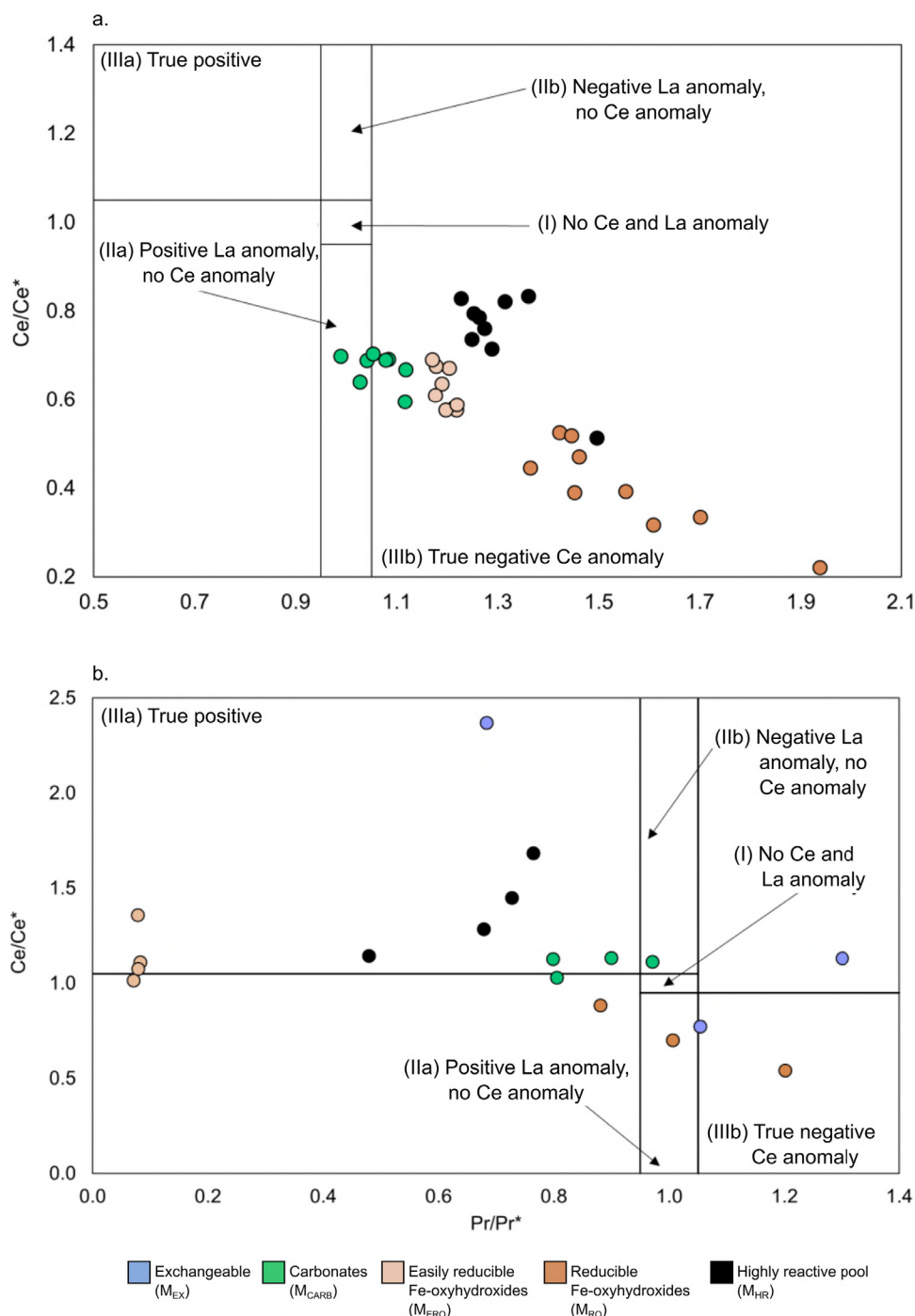
Fig. 5. PAAS-normalised Ce/Ce* vs. Pr/Pr* cross-plot. The diagram helps in elucidating whether true La and Ce anomalies exist in the discrete reactive phases evaluated here.

(Tostevin et al., 2016). However, an environmental interpretation based on REE scatter plots alone could be inconclusive or lead to misinterpretations (Shields and Stille, 2001; Tostevin et al., 2016). For example, La enrichment in the system can lead to uncertainties in whether a Ce anomaly exists (Shields and Stille, 2001). Accordingly, a cross-plot of Pr/Pr* and Ce/Ce* values, as described by Bau and Dulski (1996), allowed us to confirm the occurrence of true negative (by S_1; Fig. 5a), and true positive (by S_2; Fig. 5b), Ce anomalies for all the reactive fractions, except for a few Ce_{CARB} and Ce_{RO} extractions from S_1 and S_2, respectively. These fractions, however, exert little control over the geochemical partitioning of Ce.

To conclude on the value of REE systematics as applied here, it effectively serves as a gauge for short-term variations in the monimolimnion's redox state and reveals that, under suboxic conditions, transient shifts in the order of 100 mV are sufficient to propitiate significant changes in speciation in redox-sensitive Ce but not Eu. These speciation shifts may also affect other redox-sensitive metal(loid)s that in the recent sediments evaluated here are bound to solid phases with variable reactivity/crystallinity. Furthermore, should periodical redox state changes develop (e.g., seasonal holomixis), we determined that such changes would be swiftly recorded by the Ce anomaly of the sediments. Therefore, this parameter can be useful to gauge minor changes in the redox dynamics of the system and predict the behaviour of other metal(loid)s in lacustrine environments in general. This also applies to other post-mining lakes with similar hydrogeochemical features that could be the subject of economically feasible secondary recovery endeavours. Finally, the

application of REE systematics also pinpoints the fact that oxygenation of the monimolimnion of post-mining lake systems could be relevant to the remobilisation of REE from the sediment pile to favour their technologically controlled scavenging from the water column, as discussed in Section 3.4.

4. Conclusions

The post-mining Lake Medard acts as a large-scale incubation experiment, useful to further understand the evolution of aqueous-mineral equilibrium as a response to drastic changes in redox state. Thus, the analysis of geochemical partitioning of redox-sensitive metal(loid)s with reactive Fe phases revealed that the sediments of this system have equilibrated to recently established bottom water anoxia but respond swiftly to transient shifts of the bottom water column towards low-oxygen conditions. These shifts appear to be linked to changes in salinity arising from seasonal hydrological variability and its effects on groundwater flow. A sequential extraction protocol that targeted Fe mineral phases with diverse crystallinity and redox reactivity shows that As, V, and lanthanides are released from authigenic minerals formed under oxic conditions in the bottom of the former mine pit, with recycling of these elements likely occurring at the chemocline. Accordingly, these elements are being immobilised anew either by their co-precipitation within Fe-oxyhydroxides of variable crystallinity or incorporation into Fe-carbonate phases distributed at a fluctuating abundance across the sediment pile.

Enrichment factors showed that the recent lacustrine sediments are moderately to acutely enrich in As, V, and lanthanides regarding world average and local backgrounds. The application of REE systematics to the post-mining lake sediment was helpful to gauge the extent to which minor oscillations in the bottom water column's redox state produce significant changes in speciation of the redox-sensitive metal(loid)s evaluated here. Therefore, the approach applied here permits anticipating the fate of metals of interest (i.e., pollutants or critical transition metals) over potential variations of physicochemical parameters resulting from future managment strategies. Predicting the evolution of the lacustrine sediment mineral equilibrium phases would be of great concern for potential management scenarios of the understudied post-mining lake. For example, progressive mobilisation of labile As, due to seasonal oxygenation of the water column, would impede management scenarios involving the introduction of freshwater biota and thus, the establishment of complex ecological networks. Contrastingly, controlled scavenging of lanthanides and V, by propitiating their co-precipitation in Fe mineral phases, would make it plausible to envision post-mining lakes as secondary sources of critical transition metals.

Importantly, a sound understanding of the redox dynamics of lignite-derived post-mining lakes is not only relevant to the system under examination, but also to analogous anthropogenic environments whose numbers can be expected to increase as coal-powered generation is being phased out. Similar to Lake Medard, some of these post-mining lakes might either represent an ecological risk due to their monimolimnion metalloid pollutant load but may as well be amenable to secondary metal recovery endeavours. Therefore, results from this research could be applied to the decision-making process of remediation and/or managment programmes of post-mining lakes featuring similar hydrochemical and geological contexts.

Declaration of Competing Interest

The authors declare that they have no competing financial interests or personal relationships that could influence their study.

CRediT authorship contribution statement

Karelys Umbría-Salinas: Conceptualization, Methodology, Formal analysis, Investigation, Data curation, Writing – original draft, Visualiza-

tion. **Astolfo Valero:** Conceptualization, Methodology, Formal analysis, Investigation, Data curation, Writing – original draft. **Jiří Jan:** Methodology, Resources. **Jakub Borovec:** Methodology, Resources. **Vladislav Chrastný:** Formal analysis, Resources. **Daniel A. Petrash:** Conceptualization, Investigation, Resources, Data curation, Writing – original draft, Writing – review & editing, Supervision, Project administration, Funding acquisition.

Supplementary materials

Supplementary material associated with this article can be found, in the online version, at doi:10.1016/j.hazadv.2021.100009.

References

Azcue, J.M., Nriagu, J.O., 1993. Arsenic forms in mine-polluted sediments of Moira Lake, Ontario. Environ. Int. 19 (4), 405–415. doi:10.1016/0160-4120(93)90131-Z.

Bau, M., Möller, P., 1993. Rare earth element systematics of the chemically precipitated component in early precambrian iron formations and the evolution of the terrestrial atmosphere-hydrosphere-lithosphere system. Geochim. Cosmochim. Acta 57 (10), 2239–2249. doi:10.1016/0016-7037(93)90566-F.

Bau, M., Dulski, P., 1996. Distribution of yttrium and rare-earth elements in the Penge and Kuruman iron-formations, transvaal supergroup, South Africa. Precambrian Res. 79 (1–2), 37–55. doi:10.1016/0301-9268(95)00087-9.

Bethke, C.M., Farrell, B., Sharifi, M., 2021. GWB Reaction Modeling Guide. Aqueous Solutions LLC, IL USA, pp. 1–219.

Brázová, T., Šalamún, P., Miklisová, D., Šestinová, O., Findoráková, L., Hanzelová, V., Oros, M., 2021. Transfer of heavy metals through three components: sediments, plants and fish in the area with previous mining activity. Bull. Environ. Contam. Toxicol. 106, 485–492. doi:10.1007/s00128-021-03114-w.

Boehrer, B., Schultze, M., 2006. On the relevance of meromixis in mine pit lakes. In: Barnhisel, RI (Ed.), Proceedings, 7th international conference on acid rock drainage (ICARD). American Society of Mining and Reclamation, St Louis, pp. 200–213. doi:10.21000/JASMR06020200.

Boehrer, B., Schultze, M., 2008. Stratification of lakes. Rev. Geophys. 46 (2), RG2005. doi:10.1029/2006RG000210.

Bozau, E., Leblanc, M., Seidel, J.L., Stärk, H.J., 2004. Light rare earth elements enrichment in an acidic mine lake (Lusatia, Germany). J. Appl. Geochem. 19 (3), 261–271. doi:10.1016/S0883-2927(03)00150-1.

Bozau, E., Göttlicher, J., Hans-Joachim, S., 2008. Rare earth element fractionation during the precipitation and crystallisation of hydrous ferric oxides from anoxic lake water. J. Appl. Geochem. 23 (12), 3473–3486. doi:10.1016/j.apgeochem.2008.08.007.

Canfield, D., Raiswell, R., Bottrell, S., 1992. The reactivity of sedimentary iron minerals toward sulfide. Am. J. Sci. 292, 659–683. doi:10.2475/ajs.292.9.659.

Chatterjeea, P., Dessì, P., Kokko, M., Lakaniemi, A.-M., Lens, P., 2019. Selective enrichment of biocatalysts for bioelectrochemical systems: a critical review. Renew. Sustain. Energy Rev. 109, 10–23. doi:10.1016/j.rser.2019.04.012.

Czech Hydrometeorological Institute, 2021 Monthly sums of territorial precipitation from 1961 to 2021. Available online: https://www.chmi.cz/historicka-data/pocasi/uzemni-srazky?l=en (accessed on 08 June 2021).

Claff, S., Sullivan, L., Burton, E., Bush, R., 2010. A sequential extraction procedure for acid sulfate soils: partitioning of iron. Geoderma 155 (3–4), 224–230. doi:10.1016/j.geoderma.2009.12.002.

Davison, W., 1993. Iron and manganese in lakes. Earth Sci. Rev. 34 (2), 119–163. doi:10.1016/0012-8252(93)90029-7.

Dendievel, A.E., Mourier, B., Dabrin, A., Delile, H., Coynel, A., Gosset, A., Liber, Y., Berger, J.F., Bedell, J.P., 2020. Metal pollution trajectories and mixture risk assessed by combining dated cores and subsurface sediments along a major European river (Rhône River, France). Environ. Int. 144, 106032. doi:10.1016/j.envint.2020.106032.

Denimal, S., Bertrand, C., Mudry, J., Paquette, Y., Hochart, M., Steinmann, M., 2005. Evolution of the aqueous geochemistry of mine pit lakes –Blanzy–Montceau-les-Mines coal basin (Massif Central, France): origin of sulfate contents; effects of stratification on water quality. J. Appl. Geochem. 20 (5), 825–839. doi:10.1016/j.apgeochem.2004.11.015.

Dixit, S., Hering, J., 2003. Comparison of arsenic(V) and arsenic(III) sorption onto iron oxide minerals: implications for arsenic mobility. Environ. Sci. Technol. 37 (18), 4182–4189. doi:10.1021/es030309t.

Duker, A.A., Carranza, E.J.M., Hale, M., 2005. Arsenic geochemistry and health. Environ. Int. 31 (5), 631–641. doi:10.1016/j.envint.2004.10.020.

European Community, 2000. Directive 2000/60/EC of the European Parliament and of the Council of 23 October 2000 establishing a framework for Community action in the field of water policy. OJEC 43, 1–72.

Gammons, C.H., Harris, L.N., Castro, J.M., Cott, P.A., Hanna, B.W., 2009. Creating lakes from open pit mines: processes and considerations–with emphasis on northern environments. Can. J. Fish. Aquat. 2826, 106.

Haley, B.A., Klinkhammer, G.P., McManus, J., 2004. Rare earth elements in pore waters of marine sediments. Geochim. Cosmochim. Acta 68 (6), 1265–1279. doi:10.1016/j.gca.2003.09.012.

Hannigan, R., Dorval, E., Jones, C., 2010. The rare earth element chemistry of estuarine surface sediments in the Chesapeake Bay. Chem. Geol. 272 (1–4), 20–30. doi:10.1016/j.chemgeo.2010.01.009.

Hua, J., Liu, C., Li, F., Zhu, Z., Wei, Z., Chen, M., Gao, T., Qiu, G., 2019. Effects of Rare Earth Elements' Physicochemical Properties on their stabilization during the Fe(II)aq-induced phase transformation of Ferrihydrite. ACS Earth Space Chem. 3 (6), 895–904. doi:10.1021/acsearthspacechem.8b00201.

Jacob-Tatapu, K.J., Albert, S., Grinham, A., 2021. Sediment arsenic hotspots in an abandoned tailings storage facility, Gold Ridge Mine, Solomon Islands. Chem. 269, 128756. doi:10.1016/j.chemosphere.2020.128756.

Jiang, J., Bauer, I., Paul, A., Kappler, A., 2009. Arsenic redox changes by microbially and chemically formed semiquinone radicals and hydroquinones in a humic substance model quinone. Environ. Sci. Technol. 43, 3639–3645. doi:10.1021/es803112a.

Kontny, A., Schneider, M., Eiche, E., Neumann, T., 2021. Iron mineral transformations and their impact on As (im)mobilization at redox interfaces in As-contaminated aquifers. Geochim. Cosmochim. Acta 296 (1), 189–209. doi:10.1016/j.gca.2020.12.029.

Kříbek, B., Strand, M., Boháček, Z., Sýkorová, I., Čejkac, J., Sobalík, Z., 1998. Geochemistry of Miocene lacustrine sediments from the Sokolov Coal Basin (Czech Republic). Int. J. Coal Geol. 37 (3–4), 207–233. doi:10.1016/S0166-5162(98)00002-0.

Kumari, B., Kumar, V., Sinha, A.K., Ahsan, J., Ghosh, A.K., Wang, H., DeBoeck, G., 2017. Toxicology of arsenic in fish and aquatic systems. Environ. Chem. 15, 43–64. doi:10.1007/s10311-016-0588-9.

Laveuf, C., Cornu, S., 2009. A review on the potentiality of rare earth elements to trace pedogenetic processes. Geoderma 154 (1–2), 1–12. doi:10.1016/j.geoderma.2009.10.002.

MacRae, N.D., Nesbitt, H.W., Kronberg, B.I., 1992. Development of a positive Eu anomaly during diagenesis. Earth Planet. Sci. Lett. 109 (3–54), 585–591. doi:10.1016/0012-821X(92)90116-D.

Manoj, M.C., Kawsar, M., 2020. Metal contamination assessment in a sediment core from Vagamon Lake, southwest India: natural/anthropogenic impact. Environ. Nanotechnol. Monit. 14, 100362. doi:10.1016/j.enmm.2020.100362.

Meyer, K.M., Kump, L.R., 2008. Oceanic euxinia in earth history: causes and consequences. Annu. Rev. Earth Planet. Sci. 36 (1), 251–288. doi:10.1146/annurev.earth.36.031207.124256.

Milinovic, J., Rodrigues, F.J.L., Barriga, F.J.A.S., Murton, B.J., 2021. Ocean-floor sediments as a resource of rare earth elements: an overview of recently studied sites. Minerals 11 (2), 142. doi:10.3390/min11020142.

Murad, E., Rojík, P., 2003. Iron-rich precipitates in a mine drainage environment: influence of pH on mineralogy. Am. Mineral. 88 (11–12), 1915–1918. doi:10.2138/am-2003-11-1234.

Murad, E., Rojík, P., 2005. Iron mineralogy of mine-drainage precipitates as environmental indicators: review of current concepts and a case study from the Sokolov Basin, Czech Republic. Clays Clay Miner 40 (4), 427–440. doi:10.1180/0009855054040181.

Nance, W.B., Taylor, S.R., 1976. Rare earth elements patterns and crustal evolution – I. Australian post-Archean sedimentary rocks. Geochim. Cosmochim. Acta 40 (12), 1539–1551. doi:10.1016/0016-7037(76)90093-4.

Nealson, K.H., Belz, A., McKee, B., 2002. Breathing metals as a way of life: geobiology in action. Antonie Van Leeuwenhoek 81, 215–222. doi:10.1023/A:1020518818647.

Nedel, S., Dideriksen, K., Christiansen, B.C., Bovet, N., Stipp, S.L.S., 2010. Uptake and release of cerium during Fe-oxide formation and transformation in Fe(II) solutions. Environ. Sci. Technol. 44 (12), 4493–4498. doi:10.1021/es9031503.

Otchere, F.A., Veiga, M.M., Hinton, J.J., Farias, R.A., Hamaguchi, R., 2004. Transforming open mining pits into fish farms: moving towards sustainability. Nat. Resour. Forum 28 (3), 216–223. doi:10.1111/j.1477-8947.2004.00091.x.

Pačes, T., Šmejkal, V., 2004. Magmatic and fossil components of thermal and mineral waters in the Eger River continental rift (Bohemian massif, central Europe). In: Wanty, R.B., Seal, II, R.R. (Eds.), Water-Rock Interaction. Taylor and Francis Group, London, AA. Balkema Publishers ISBN 167-172.

Paikaray, S., Schröder, C., Peiffer, S., 2017. Schwertmannite stability in anoxic Fe(II)-rich aqueous solution. Geochim. Cosmochim. Acta 217 (15), 292–305. doi:10.1016/j.gca.2017.08.026.

Park, S., Lee, J.-.H., Shin, T.J., Hur, H.-.G., Kim, M.G., 2018. Adsorption and incorporation of arsenic to biogenic lepidocrocite formed in the presence of ferrous iron during denitrification by *Paracoccus denitrificans*. Environ. Sci. Technol. 52 (17), 9983–9991. doi:10.1021/acs.est.8b02101.

Perez, J.P.H., Schiefler, A.A., Rubio, S.N., Reischer, M., Overheu, N.D., Benning, L.G., Tobler, D.J., 2021. Arsenic removal from natural groundwater using 'green rust': solid phase stability and contaminant fate. J. Hazard. Mater. 401 (5), 123327. doi:10.1016/j.jhazmat.2020.123327.

Petrash, D.A., Jan, J., Sirová, D., Osafo, N.O-A., Borovec, J., 2018. Iron and nitrogen cycling, bacterioplankton community composition and mineral transformations involving phosphorus stabilisation in the ferruginous hypolimnion of a post-mining lake. Environ. Sci. Process Impacts 20 (10), 1414–1426. doi:10.1039/C8EM00328A.

Post, J., Bish, D., 1989. Rietveld refinement of crystal structures using powder X-ray diffraction data. Rev. Mineral. Geochem. 20 (1), 277–308. doi:10.1515/9781501509018-012.

Poulton, S.W., Canfield, D.E., 2005. Development of a sequential extraction procedure for iron: implications for iron partitioning in continentally derived particulates. Chem. Geol. 214 (3–4), 209–221. doi:10.1016/j.chemgeo.2004.09.003.

Raiswell, R., Canfield, D., 1996. Rates of reaction between silicate iron and dissolved sulfide in Peru Margin sediments. Geochim. Cosmochim. Acta 60, 2777–2788. doi:10.1016/0016-7037(96)00141-X.

Sánchez-España, J., Yusta, I., Illin, A., van der Graaf, C., Sánchez-Andrea, I., 2020. Microbial geochemistry of the acidic Saline Pit Lake of Brunita Mine (La Unión, SE Spain). Mine Water Environ. 39, 535–555. doi:10.1007/s10230-020-00655-0.

Shields, G., Stille, P., 2001. Diagenetic constraints on the use of cerium anomalies as palaeoseawater redox proxies: an isotopic and REE study of Cambrian phosphorites. Chem. Geol. 175 (1–2), 29–48. doi:10.1016/S0009-2541(00)00362-4.

Schultze, M., Pokrandt, K.-.H., Hille, W., 2010. Pit lakes of the Central German lignite mining district: creation, morphometry and water quality aspects. Limnologica 40 (2), 148–155. doi:10.1016/j.limno.2009.11.006.

Schultze M., Boehrer B., Wendt-Potthoff K., Sánchez-España J., Castendyk D., 2017. Meromictic pit lakes: case studies from Spain, Germany and Canada and general aspects of management and modelling. In: Gulati R., Zadereev E., Degermendzhi A. (eds) Ecology of Meromictic Lakes. Ecological Studies (Analysis and Synthesis), vol 228. Springer, Cham 10.1007/978-3-319-49143-1_9

Smedley, P.L., Kinniburgh, D.G., 2002. A review of the source, behaviour and distribution of arsenic in natural waters. J. Appl. Geochem. 17 (5), 517–568. doi:10.1016/S0883-2927(02)00018-5.

Sundman, A., Vitzthum, A.-.L., Adaktylos-surber, K., …, Byrne, J.M., 2020. Effect of Fe-metabolizing bacteria and humic substances on magnetite nanoparticle reactivity towards arsenic and chromium. J. Hazard. Mater. 384 (15), 121450. doi:10.1016/j.jhazmat.2019.121450.

Tabelin, C.B., Corpuz, R.D., Igarashi, T., …, Hiroyoshi, N., 2020. Acid mine drainage formation and arsenic mobility under strongly acidic conditions: importance of soluble phases, iron oxyhydroxides/oxides and nature of oxidation layer on pyrite. J. Hazard. Mater. 399 (15), 122844. doi:10.1016/j.jhazmat.2020.122844.

Telfeyan, K., Breaux, A., Kim, J., Cable, J.E., Koller, A.S., Grimm, D.A., Johannesson, K.H., 2017. Arsenic, vanadium, iron, and manganese biogeochemistry in a deltaic wetland, southern Louisiana, USA. Mar. *Chem.* 192, 32–48. doi:10.1016/j.marchem.2017.03.010.

Thompson, V.S., Gupta, M., Jin, H., 2017. Techno-economic and life cycle analysis for bioleaching rare-earth elements from waste materials. ACS Sustain. Chem. Eng. 6 (2), 1602–1609. doi:10.1021/acssuschemeng.7b02771.

Tostevin, R., Shields, G.A., Tarbuck, G.M., He, T., Clarkson, M.O., Wood, R.A., 2016. Effective use of cerium anomalies as a redox proxy in carbonate-dominated marine settings. Chem. Geol. 438 (2), 146–162. doi:10.1016/j.chemgeo.2016.06.027.

Turekian, K.K., Wedepohl, K.H., 1961. Distribution of the elements in some major units of the earth's crust. Geol. Soc. Am. Bull. 72 (2), 175–192 doi:10.1130/0016-7606(1961)72[175:DOTEIS]2.0.CO;2.

van de Velde, S.J., Reinhard, C.T., Ridgwell, A., Meysman, F.J.R., 2021. Bistability in the redox chemistry of sediments and oceans. Proc. Natl. Acad. Sci. U.S.A. 117, 33043–33050. doi:10.1073/PNAS.2008235117.

Vejřík, L., Vejříková, I., Blabolil, P., …, Čech, M., 2017. European catfish (*Silurus glanis*) as a freshwater apex predator drives ecosystem via its diet adaptability. Sci. Rep. 7, 15970. https://www.nature.com/articles/s41598-017-16169-9.

Wang, Z., He, Z., 2020. Frontier review on metal removal in bioelectrochemical systems: mechanisms, performance, and perspectives. J. Hazard. Mater. Lett. 1, 100002. doi:10.1016/j.hazl.2020.100002.

Wang, M., Wu, S., Guo, J., Liao, Z., Yang, Y., Chen, F., Zhu, R., 2021. Immobilization and migration of arsenic during the conversion of microbially induced calcium carbonate to hydroxylapatite. J. Hazard. Mater. 412, 125261. doi:10.1016/j.jhazmat.2021.125261.

Woon, S.H.J., Srinuansom, K., Chuah, C.J., Ramchunder, S.J., Promya, J., Ziegler, A.D., 2021. Pre-closure assessment of elevated arsenic and other potential environmental constraints to developing aquaculture and fisheries: the case of the Mae Moh mine and power plant, Lampang, Thailand. Chem. 269, 128682. doi:10.1016/j.chemosphere.2020.128682.

Zhang, C., Yu, Z.-.G., Zeng, G.-.M., …, Hu, L., 2014. Effects of sediment geochemical properties on heavy metal bioavailability. Environ. Int. 73, 270–281. doi:10.1016/j.envint.2014.08.010.

Paper II

Aqueous system-level processes and prokaryote assemblages in the ferruginous and sulfate-rich bottom waters of a post-mining lake.

Petrash D. A., Steenbergen I. M., **Valero A.**, Meador T. B., Pačes T., Thomazo C.

Biogeosciences

Open Access

EGU

Research article

Aqueous system-level processes and prokaryote assemblages in the ferruginous and sulfate-rich bottom waters of a post-mining lake

Daniel A. Petrash[1,2], Ingrid M. Steenbergen[1,3], Astolfo Valero[1,3], Travis B. Meador[1,3], Tomáš Pačes[2], and Christophe Thomazo[4,5]

[1]SoWa Research Infrastructure, Biology Centre of the Czech Academy of Sciences, České Budějovice, 370 05, Czechia
[2]Department of Environmental Geochemistry and Biogeochemistry, Czech Geological Survey, Prague, 152 00, Czechia
[3]Department of Ecosystem Biology, University of South Bohemia, České Budějovice, 370 05, Czechia
[4]UMR CNRS 6282 Biogéosciences, University of Burgundy, Dijon, 21000, France
[5]Institut Universitaire de France, Paris, 75000, France

Correspondence: Daniel A. Petrash (daniel.petras@geology.cz)

Abstract. In the low-nutrient, redox-stratified Lake Medard (Czechia), reductive Fe(III) dissolution outpaces sulfide generation from microbial sulfate reduction (MSR) and ferruginous conditions occur without quantitative sulfate depletion. The lake currently has marked overlapping C, N, S, Mn and Fe cycles occurring in the anoxic portion of the water column. This feature is unusual in stable, natural, redox-stratified lacustrine systems where at least one of these biogeochemical cycles is functionally diminished or undergoes minimal transformations because of the dominance of another component or other components. Therefore, this post-mining lake has scientific value for (i) testing emerging hypotheses on how such interlinked biogeochemical cycles operate during transitional redox states and (ii) acquiring insight into redox proxy signals of ferruginous sediments underlying a sulfatic and ferruginous water column. An isotopically constrained estimate of the rates of sulfate reduction (SRRs) suggests that despite high genetic potential, this respiration pathway may be limited by the rather low amounts of metabolizable organic carbon. This points to substrate competition exerted by iron- and nitrogen-respiring prokaryotes. Yet, the planktonic microbial succession across the nitrogenous and ferruginous zones also indicates genetic potential for chemolithotrophic sulfur oxidation. Therefore, our SRR estimates could rather be portraying high rates of anoxic sulfide oxidation to sulfate, probably accompanied by microbially induced disproportionation of S intermediates. Near and at the anoxic sediment–water interface, vigorous sulfur cycling can be fuelled by ferric and manganic particulate matter and redeposited siderite stocks. Sulfur oxidation and disproportionation then appear to prevent substantial stabilization of iron monosulfides as pyrite but enable the interstitial precipitation of microcrystalline equant gypsum. This latter mineral isotopically recorded sulfur oxidation proceeding at near equilibrium with the ambient anoxic waters, whilst authigenic pyrite sulfur displays a 38 ‰ to 27 ‰ isotopic offset from ambient sulfate, suggestive of incomplete MSR and open sulfur cycling. Pyrite-sulfur fractionation decreases with increased reducible reactive iron in the sediment. In the absence of ferruginous coastal zones today affected by post-depositional sulfate fluxes, the current water column redox stratification in the post-mining Lake Medard is thought relevant for refining interpretations pertaining to the onset of widespread redox-stratified states across ancient nearshore depositional systems.

1 Introduction

The biogeochemical reactions governing the distinctive redox structure of modern permanently stratified lakes have been studied, for the most part, in natural settings featuring relatively high dissolved iron but low sulfate concentrations (Swanner et al., 2020). Improved by insights from laboratory experiments (e.g., Konhauser et al., 2007; Rasmussen et al., 2015; Jiang and Tosca, 2019), geochemical and mi-

25

crobiological analyses made in such lacustrine systems have provided us with an empirical framework to interpret modern iron biomineralization mechanisms and, by analogy, similar processes that determined a secular trend in the stratigraphic distribution of iron formations in the Precambrian.

Lakes that display permanent stagnation and marked redox gradients in their water column are termed meromictic. Meromictic lakes featuring ferruginous conditions in their water columns (i.e., $[Fe^{2+}] > [H_2S/HS^-]$ and $[Fe^{2+}] > [NO_3^-/NO_2^-]$) are relevant to deciphering the environmental significance of specific chemical and isotopic signals recorded in iron-rich deposits and to advance paleoenvironmental interpretations of redox-stratified oceans, such as those prevalent during the Precambrian (Canfield et al., 2018) or intermittently developed during the Phanerozoic (Crowe et al., 2008; Walter et al., 2014; Posth et al., 2014; Lambrecht et al., 2018; Canfield et al., 2018; Swanner et al., 2020; Reershemius and Planavsky, 2021).

Ferruginous water columns that also contain elevated dissolved sulfate concentrations are not uncommon in acidic shallow pit lakes (e.g., Denimal et al., 2005; Trettin et al., 2007) and have also been reported in pH-neutralized post-mining lakes (McCullough and Schultze, 2018). Lake Medard, in NW Czechia (Fig. 1), belongs to this latter group. The newly formed lake features low nutrient contents (i.e., it is oligotrophic), and its temperature-, redox- and salinity-stratified water column (Fig. 2a) remains unmixed throughout the year. Given its recent water-filling history – completed in 2016 – and the fact that its ferruginous bottom waters contain up to 21 mM of dissolved sulfate (Petrash et al., 2018), this oligotrophic lake can be considered a large-scale incubation experiment featuring an imbalanced sulfatic transition between aqueous ferruginous and euxinic redox states. The latter redox state is defined by an abundance of dissolved sulfide able to titrate dissolved Fe^{2+} out from solution (Scholz, 2018; van de Velde et al., 2021).

Here we combined spectroscopic analyses of the hypoxic (i.e., 2.0 to 0.2 $mg\,O_2\,L^{-1}$), nitrogenous and ferruginous, and ultimately anoxic ($< 0.03\,mg\,O_2\,L^{-1}$) ferruginous and sulfatic bottom water column of Lake Medard. System-level processes that can be linked to specific planktonic prokaryote functionalities were interpreted. For this aim, isotope ratios of carbon and oxygen in dissolved inorganic carbon, sulfur and oxygen in dissolved sulfate, and concentration profiles of bioactive ions and volatile fatty acids (VFAs) were measured together with a 16S rRNA gene amplicon sequence profile. Amplicon gene sequencing informed our ecological and biogeochemical interpretations despite quantitative biases that are inherent in this type of data (Salcher, 2014; Piwosz et al., 2020). To complement our interpretations, we also conducted mineralogical analyses and a mineral-calibrated wet chemical speciation study of reactive Fe and Mn pools in the upper anoxic sediments. Using these data, we developed a mechanistic model that assesses the potential regulatory roles of prokaryotes over the geochemical gradients detected in the
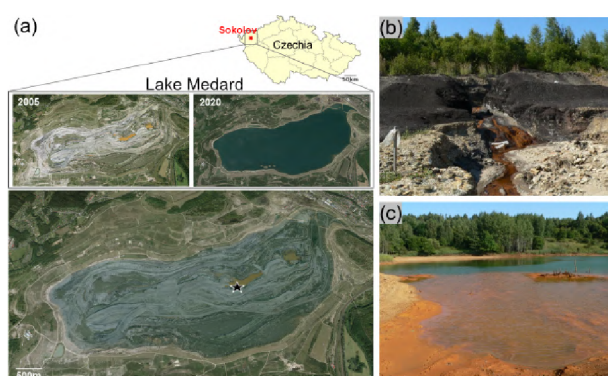
Figure 1. The area now occupied by the post-mining Lake Medard was previously an open-cast coal mine near Sokolov, NW Czechia. Upon mine abandonment, the deepest parts of the open-cast mine became shallow acidic pit lakes and are now the lake depocentres. The deeper zone of the lake now features ferruginous and sulfate-rich aqueous conditions, but the pH is circumneutral. The star marks the central sampling location in a recent lake imagery superimposed on the 2005 mine-pit imagery (a). The mine pit had important fluxes of solutes linked to pyrite oxidation in exploited coal seams and their associated pyrite-bearing lithologies (b–c). These fluxes may still affect the hydrochemistry of the present-day lacustrine system; i.e., solutes are currently sourced from now submerged lithologies that also bear pH-neutralizing carbonates (Appendix A). Imagery dates 19 May 2020 (© CNES/Airbus) and 1 January 2004 (© GEODIS Brno). Historical photographic record by courtesy of the Czech Geological Survey.

water column and their influence over interlinked biogeochemical cycling involving reactive minerals. Consumption and replenishment of iron, sulfur (S), carbon (C), nitrogen (N) and manganese (Mn) across the redoxcline and near the anoxic sediment–water interface (SWI) are presented as a set of geochemical reactions. These reactions differentiate distinctive niches where a phylogenetically and metabolically diverse planktonic microbial community induce vigorous elemental recycling.

Our observations in this unique lake are thought relevant since analogue aqueous-level system processes would have also operated in some ancient ferruginous coastal settings. Lake Medard could therefore offer valuable information to further understand early diagenetic signals resulting from analogue microbial ecosystem dynamics. When preserved in the rock record, such signals could be elusive and reflective, for instance, of ferruginous nearshore facies affected by continental sulfate delivery during shallow burial. In this regard, our research furthers understanding of the cryptic S cycle under ferruginous conditions unaccompanied by quantitative dissolved sulfate exhaustion.

2 Study site

Reclamation (flooding) of land occupied by the decommissioned Medard open-cast lignite mine in the Sokolov mining district of Karlovy Vary, northwest Czechia, led to the ca. $4.9\,km^2$ ($\sim 60\,m$ max. depth) post-mining Lake Medard (Fig. 1a; $50°10'41''$ N, $12°35'46''$ E). The lake was filled with waters diverted for reclamation purposes from the nearby river Eger (Ohře). The filling of the former open-cast mine pit with river water started in 2010 and was reportedly completed by 2016 (Kovar et al., 2016). During closure and abandonment of the former mine pit, dissolved iron and sulfate – the latter derived from pyrite oxidation – leached towards initially shallow ephemeral and acidic pit lakes formed as surficial and groundwater filled the mine pit (Fig. 1b–c). In these mining-impacted brines, metastable Fe(III) oxyhydroxides and Fe(III) oxyhydroxysulfates precipitated (Murad and Rojík, 2005). Runoff also affected the hydrochemistry of the ensuing shallow pit lake (Fig. 1b–c) by carrying solutes sourced from weathered Miocene tuffaceous and carbonate-rich lacustrine claystones associated with the mined coal seam. These lithological units were described by Kříbek et al. (2017).

At present, Lake Medard exhibits density, temperature and marked redox stratification in its hypolimnion that is hypoxic (0.2 to $0.03\,mg\,O_2\,L^{-1}$) to anoxic (Fig. 2a) and ferruginous (Petrash et al., 2018). Water–rock interactions down to the underlying granitic basement also influence the hydrochemistry of the modern lake. Percolation and subsurface flow of meteoric water cause dissolution of fault-related thenardite (Na_2SO_4) accumulations. Thenardite dissolution and groundwater reflux introduce significant loads of isotopically heavy sulfate into the present-day hydrological system (Pačes and Šmejkal, 2004). Additional details on the geological framework of the area and its influence over the hydrochemistry of the post-mining lake are in Appendix A.

Water column stratification was already observed in 2009, when environmental monitoring of the shallow pit lake formed after decommissioning of the dewatering wells took place (e.g., Medová et al., 2015). In the current deep post-mining lake, both abiotic and microbially mediated precipitation of poorly crystalline iron minerals – i.e., amorphous ferric hydroxide ($Fe(OH)_3$) and metastable nanocrystalline ferrihydrite ($Fe_2O_3 \cdot (H_2O)_n$) – occurs near the pelagic redoxcline (i.e., the redox transition between low dissolved oxygen and anoxic waters, Fig. 2a), from where these solid phases are exported to the SWI (Petrash et al., 2018). Mineral equilibrium reactions at the SWI proceed mostly within the nitrogenous to ferruginous redox potentials (Eh) and at a circumneutral to moderately alkaline pH. Stability diagrams showcasing the predicted stability of S and Fe species in the bottom waters of Lake Medard are shown in Fig. B1 (Appendix B). The stability diagrams show that the current physicochemical conditions of the bottom sulfatic waters favour colloidal Fe(III)-oxyhydroxide formation, but ferruginous monimolimnial waters also occur.

3 Methods

3.1 Water sampling and analyses

3.1.1 Physicochemical parameter measurements and water column sampling

A water quality monitoring and profiling probe (YSI 6600 V2-2) was used – prior to sampling – to measure conductivity, temperature, O_2 concentrations, pH and Eh in the stratified portion of the water column of Lake Medard (from 47 to 55 m depth) in its central location (Fig. 1a, star). The probing resolution was 1 m above and below the O_2 minimum zone and 0.5 m at the redoxcline. Based on the profiles, water column samples ($n = 8$; four replicates) were collected (in November 2019) using a Ruttner sampler with a capacity of 1.7 L. Flushing and rinsing of the sampling device with distilled water (dH_2O) were performed between samples. A total of eight samples were taken at depths of 47, 48, 48.5, 49, 50, 52, 54 and 55 m. Replicate samples were taken at depths of 47, 48.5, 50 and 54 m below the lake water surface. On aliquots of our water samples, we performed (i) prokaryote DNA extraction followed by MiSeq Illumina 16S rRNA gene amplicon sequencing; (ii) mass determinations of cations (iron, manganese, potassium, sodium, magnesium and calcium); (iii) high-pressure liquid chromatography for concentrations of chlorine, sulfate, nitrate, ammonium and phosphate anions, and VFA abundances; (iv) measurement of dissolved inorganic carbon and methane concentrations; (v) isotope ratio analyses of $\delta^{13}C$ in total dissolved inorganic carbon and methane; and (vi) isotope ratio analyses of $\delta^{34}S$ and $\delta^{18}O$ values in dissolved sulfate. Details on these analyses follow.

3.1.2 Environmental microbial DNA sampling

For each DNA sampling depth, an aliquot of 1 L was transferred to polyethylene (PET) bottles using a hand pump connected to sterile a Sterifil® aseptic system loaded with sterile cellulose nitrate Whatman® MicroPlus-21 ST filters (0.45 µm cutoff, 47 mm diameter). The filters were separated from the filtrating apparatus using a pair of sterilized tweezers (70 % ethanol and Bunsen burner) and transferred into sterile 2 mL Cryotube vials (Thermo Scientific). These were stored in liquid N_2 for transport to the lab, where DNA extraction from the biomass collected on the filters took place. After each sample collection, the filtration apparatus was rinsed three times with dH_2O and a new filter was carefully placed onto the apparatus. Samples for 16 S rRNA gene analyses were collected from the two redox compartments of the lake: the hypoxic hypolimnion and anoxic monimolimnion.
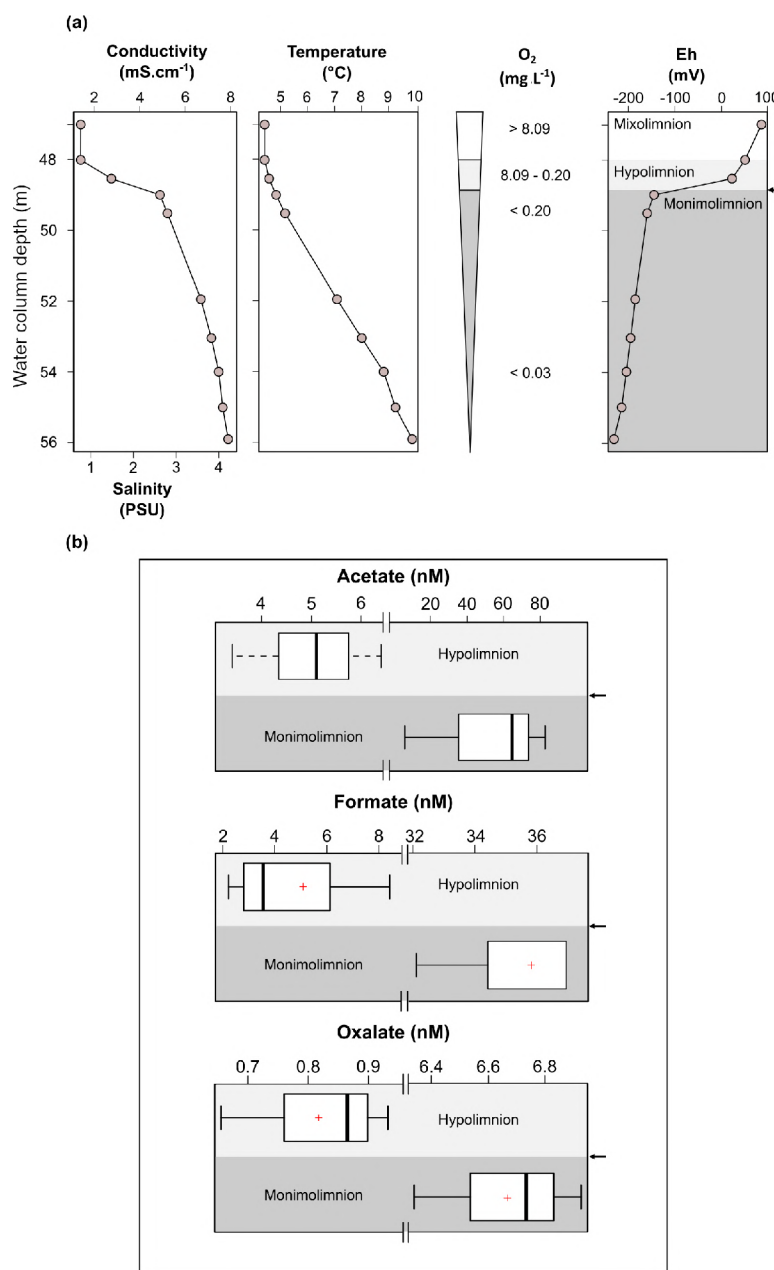
Figure 2. Physicochemical parameters in the dysoxic to anoxic waters of Lake Medard in its central sampling location, which has a maximum depth of 56 m **(a)**, and concentration range of acetate, formate and oxalate quantified in the dysoxic ($n = 4$; < 48 depth) and anoxic ($n = 3$; 54–55 m depth) waters of Lake Medard **(b)**. The arrow shows the redoxcline.

The rinsing water (1 L) prior to the second-last sampling (52 m) was used as a control.

3.1.3   Microbiome profile

DNA was extracted from the water filters described above using a Quick-DNA Soil Microbe Kit (Zymo Research) according to the manufacturer's instructions. A total of 11 water replicates (i.e., 47 to 54 m depth and replicates) were eval-

uated. The DNA extracted from these samples was ≥ 6 ng as per Qubit dsDNA BR fluorometric assays (Life Technologies) and below limits of quantification ($< LQs$) for the control (i.e., nucleic acids < 0.2 ng). DNA integrity was assessed by agarose gel (2 %) electrophoresis.

A two-step PCR protocol targeting the small subunit 16S rRNA gene in bacteria and archaea was conducted using the universal primer combinations 341F/806R (CCTAYGGGR-

BGCASCAG and GGACTACNNGGGTATCTAAT) and 519F/915R (CAGCCGCCGCGGTAA and GTGCTCCC-CCGCCAATTCCT), respectively. The samples were sequenced on the MiSeq Illumina platform. The 16Ss rRNA gene amplicon datasets were analyzed with a pipeline consisting of an initial step where all reads passing the standard Illumina chastity filter (PF reads) were demultiplexed according to their index sequences. This was followed by a primer clipping step in which the target forward and reverse primer sequences for bacteria and archaea were identified and clipped from the starts of the raw forward and reverse reads. Only read pairs exhibiting forward and reverse primer overlaps were kept for merging by using FLASH 2.2.00 (Magoč and Salzberg, 2011). This yielded a total of 1 799 339 high-quality sequence reads, with an average length after processing of 412 bp.

Sequence features (herein described as representative operational taxonomic units, OTUs) were clustered using QIIME 2 (VSEARCH cluster-features-de-novo option; Rognes et al., 2016). To assign taxonomic information to each OTU, we performed DC-MegaBLAST alignments of cluster-representative sequences regarding the NCBI sequence database (release 10 October 2019). A taxonomic assignment for each OTU was then transferred from the set of best-matching reference sequences (lowest common taxonomic unit of all best hits). Hereby, a sequence identity of > 70 % across at least ≥ 80 % of the representative sequence was a minimal requirement when considering reference sequences. We assigned significant tentative correspondence of OTUs to reference species provided that identity thresholds ≥ 97 % of the V3–V4 hypervariable region for bacteria and V4–V5 for archaea were meet. Further processing of OTUs and taxonomic assignments (75.8 % of the sequences after chimera detection and filtering; Edgar et al., 2011) and read abundance estimation for all detected OTUs were performed using the QIIME 2 software package (version 1.9.1, Caporaso et al., 2010). Abundances of bacterial and archaeal taxonomic units were normalized using lineage-specific copy numbers of the relevant marker genes to improve estimates (Angly et al., 2014). The microbial sequence data for this study (lengths ≥ 402 bp) were deposited in the European Nucleotide Archive (ENA) at EMBL-EBI under accession number PRJEB47217.

3.1.4 Cation concentration analyses

For cation concentration analyses, aliquots of 15 mL were filtered using sterile, high-flow, 28 mm diameter, polyethersulfone (PES) filters to remove particles > 0.22 μm and then placed in acid-cleaned, PET centrifuge tubes. The aliquots were acidified using concentrated trace metal grade HNO_3. At the lab these water aliquots were digested with trace metal grade HNO_3 (8 N) and were sent for analyses at the Pôle Spectrométrie Océan at IUEM in Brest, France. A Thermo Element 2 high-resolution inductively coupled plasma mass

spectrometer set to solution mode was used. The data were calibrated against multi-element standards at concentrations that were measured repeatedly throughout the session. Multi-element solutions were measured at the beginning, end and twice in the middle of the sequence, and a $5 \mu g L^{-1}$ standard was further repeated after every five samples throughout the sequence. Additionally, 5 ppb indium (In) was added directly to the 2 % HNO_3 diluent employed to prepare all standard solutions and was used to monitor signal stability and correct for instrumental drift across the session. Each sample and standard were bracketed by a rinse composed of the same diluent (i.e., the 2 % HNO_3 with In), for which data were also acquired to determine the method detection limit. Relative standard deviations (2σ level) were better than 0.01 % for Fe and Mn, and between 0.001 % and 0.002 % for other analyzed elements, e.g., K, Na, Mg and Ca, concentrations of which were used for aqueous-mineral equilibrium modelling (Appendix A, also Supplement 1 – PHREEQC modelling input/results).

3.1.5 Ions, ammonia and VFA concentration analyses

Alkalinity (i.e., the capacity of water to neutralize free hydrogen ions, H^+) was measured as HCO_3^- via acidometric titration of filtered water samples. The titrations were conducted on board immediately upon sample collection by using 0.16 N sulfuric acid cartridges on a digital titrator (Hach).

Ions, ammonia and VFA concentrations were measured in filtered, unacidified water sample aliquots via high-pressure liquid chromatography (HP-LC). For these analyses we used an ICS-5000 + Eluent Generator (Dionex), with conductivity detection application and suppression. Analytes were separated using Dionex IonPac AS11-HC-4 μm (anions, VFAs) and IonPac CS16-4 μm (ammonium) columns (2 × 250 mm in size). The flow rate was 0.36 mL min^{-1}; run time was 65 min for anions and VFAs and 17 min for ammonium. Potassium hydroxide was the eluent for inorganic anions and monovalent organic acids; methanesulfonic acid was the eluent for ammonium ion detection/quantification. A combined stock calibration standard solution featuring environmentally relevant anion ratios was used for determining concentrations and was prepared from corresponding analytical reagent grade salts. To optimize and calibrate the method for VFA analyses and determine the limits of detection, we used stock mixtures of IC grade formate, oxalate, acetate, lactate, pyruvate and butyrate standards for preparing our working saline stock solutions. Detection limits were better than 60 ppb for lactate and oxalate and 200 ppb for pyruvate, formate and acetate. Recoveries, based on standards, exceed 80 % for all analytes reported. The ion concentration measurements have an error (2σ) < 20 % based on replicate analyses.

3.1.6 Dissolved (in)organic carbon and methane

Aliquots of the lake water collected were immediately transferred from the sampler to pre-cleaned – i.e., rinsed three times with ddH$_2$O and oven-dried at 550 °C – 12 mL glass exetainer septum-capped vials (Labco), pre-filled with He(g) and 1 mL NaCl oversaturated solution (40 %) for CH$_4$ or 1 mL 85 % phosphoric acid for ΣCO$_2$. On board, the vials were filled with $\sim$ 11 mL water samples using a syringe connected to 15 cm PES tube that was introduced from below into the sampler to prevent diffusion of atmospheric gases into the exetainer vials.

A dissolved inorganic carbon (ΣCO$_2$) concentration profile was produced using a peak area calibration curve obtained on a MAT253 Plus isotope ratio mass spectrometer (IR-MS; Thermo Scientific). The same instrument was used for determining isotope ratios of ΣCO$_2$ (δ^{13}C$_{\Sigma CO_2}$, δ^{18}O$_{\Sigma CO_2}$) and methane (δ^{13}C$_{CH_4}$) and for a rough estimation of the CH$_4$ concentrations at the monimolimnion. In brief, CO$_2$ (or CH$_4$) is purged from the headspace of the exetainer vials and then the gas passes through a Nafion water trap and into a sample loop PoraPLOT-Q column (0.32 mm i.d.) cooled in liquid N$_2$; with He as the carrier gas. The sample gases are then separated via a Carboxen PLOT 1010 (0.53 mm i.d.; Supelco) held at 90 °C with a flow rate of 2.2 mL min^{-1} and transferred via a ConFlo IV interface to the instrument. For methane, prior to transfer to the IR-MS, the sample is transferred via a multi-channel device to a nickel oxide conversion reactor tube with copper oxide as a catalyst (1000 °C). The δ^{13}C values obtained relative to CO$_2$ working gas are then corrected for linearity and normalized to laboratory working standards calibrated against CO$_2$ evolved from the international standard IAEA-603.

The concentration measurements have an error (1σ) < 4 % for ΣCO$_2$ and < 25 % for CH$_4$. Isotope data are expressed in delta notation: $\delta = R_{\text{sample}}/R_{\text{standard}} - 1$, where R is the mole ratio of ^{13}C/^{12}C or ^{18}O/^{16}O and is reported in units per mil (‰). The δ^{13}C data are reported vs. the Vienna Pee Dee Belemnite (V-PDB) standard. The δ^{18}O data are reported vs. the international Vienna Standard Mean Ocean Water (V-SMOW) standard. The reproducibility of the δ^{13}C$_{DIC}$ and δ^{13}C$_{CH_4}$ measurements was better than ± 0.05‰ and ± 0.3‰ (1σ), respectively, based on replicates for reported values of the standard materials and the samples. Reproducibility of δ^{18}O$_{\Sigma CO_2}$ measurements was better than 0.4‰. DOC was analyzed in untreated samples by catalytic combustion at 680 °C (Shimadzu 5000A) with a detection limit of $\sim$ 0.05 mg L^{-1}.

3.1.7 Dissolved sulfur analyses

For measuring dissolved acid-volatile sulfur (AVS) in the monimolimnion (i.e., HS$^-$, intermediate sulfur species, H$_2$S and the aqueous FeS clusters; Rickard and Morse, 2005), 500 mL aliquots of water samples collected at the 52–54 m depth interval were transferred to PET sample bottles pre-filled with 2 mL of 1 M Zn acetate and then 50 mL of 5 M NaOH was added. The combined concentrations of AVS bound into the ZnS precipitates were spectrophotometrically determined in an acidified solution of phenylenediamine and ferric chloride by using a Specord 210 UV/Vis (Analytik). The detection limit of the method is ≥ 0.25 μM.

As for cation analyses, 1 L aliquots of the filtered water samples were intended for sulfate S and O isotope analyses. These samples were acidified to a pH $\sim$ 3 with 6 N reagent grade HCl. Also, to oxidize and degas dissolved organic matter, we added 6 mL of hydrogen peroxide (H$_2$O$_2$) 6 % and heated the samples (90 °C) until clear (i.e., 1 to 3 h). Dissolved sulfate was then precipitated as purified baryte (BaSO$_4$) by using a saturated BaCl$_2$ solution. Accordingly, after heating, $\sim$ 5 mL of 10 % BaCl$_2$ was added to the water samples that were then allowed to cool down overnight. An additional 1 mL of BaCl$_2$ solution was added the next day to ensure that all possible BaSO$_4$ precipitated. The precipitates were then collected on pre-weighed membrane filters, rinsed thoroughly using deionized water, stored in plastic petri dishes and dried in a desiccator using a sulfate-free desiccant; the dry BaSO$_4$ powder was scraped into clean vials; weighted; and stored until shipped to the Biogéosciences Laboratory, Dijon, France, for isotope analysis.

Each purified BaSO$_4$ sample was analyzed for δ^{34}S$_{SO_4}$ and δ^{18}O$_{SO_4}$. Samples were measured on a vario PYRO cube elemental analyzer (Elementar) in line with a 100 IR-MS (IsoPrime) in continuous-flow mode. The SO$_4^{2-}$ isotope data are expressed in the delta notation: $\delta \equiv R_{\text{sample}}/R_{\text{standard}} - 1$, where R is the mole ratio reported in units per mil (‰) vs. the Vienna Canyon Diablo Troilite (V-CDT) and V-SMOW standards for ^{34}S/^{32}S and ^{18}O/^{16}O, respectively. Analytical errors are better than ± 0.4‰ (2σ) based on replicate analyses of the international baryte standard NBS-127, which was used for data correction via standard–sample–standard bracketing. International standards IAEA-S-1, IAEA-S-2 and IAEA-S-3 were used for calibration with a cumulative reproducibility better than 0.3‰ (1σ).

3.2 Sediment samples

We also sampled the upper anoxic sediment column to a depth of $\sim$ 8 cm. The mineralogy of these fine-grained sediments (silt to clay in size) was qualitatively and semi-quantitatively assessed via X-ray diffraction (XRD). The δ^{34}S and δ^{18}O of gypsum (CaSO$_4 \cdot$ 2H$_2$O), δ^{13}C of siderite (FeCO$_3$), and δ^{34}S isotope values of pyrite (FeS$_2$) from these sediments were also measured and reported as described

above using the delta notation: $\delta = R_{\text{sample}}/R_{\text{standard}} - 1$, where R is the mole ratio. Scanning electron microscopy aided by electron dispersive spectrometry (SEM-EDS) was used for textural analyses focused on the S- and/or Fe-bearing phases. In addition, a sequential extraction scheme (after Poulton et al., 2004; Goldberg et al., 2012) was conducted to characterize the sedimentary partitioning of reactive Fe and Mn fractions. Details on these analyses follow.

3.3 Sampling

Replicate sediment cores (~ 16 cm in length) were collected with a messenger-activated gravity corer attached to 20 cm long polycarbonate tubes (5 cm in diameter). The cores were immediately sealed upon retrieval with butyl rubber stoppers, preserving about 3 cm of anoxic lake water. The head water showed no signs of oxidation (i.e., no reddish hue observed) upon transport – within about 6 h of collection – to the lab. The sediment pile was extruded and sectioned at 2 cm intervals. Surfaces of the silty clayey sediment in contact with the core liner were scrapped to remove potential contamination from the lake water and to minimize smearing effects. The sediment subsamples were rapidly frozen using liquid N_2 and then stored at $-18\,^{\circ}$C until freeze-dried. We interrogated the upper part of the sediment pile to a depth of 8 cm (i.e., two replicate samples per depth, two cores).

3.3.1 Mineralogy

The mineralogy of the sediment was determined, semi-quantitatively, via X-ray diffraction (XRD). Powder XRD data were collected on a D8 Advance powder diffractometer (Bruker) with a LYNXEYE XE detector, under a Bragg–Brentano geometry and Cu K_1 radiation ($\lambda = 1.5405$ Å). Collection in the 2Θ range 4–80° was performed using 0.015° step-size increments and 0.8 s collection time per step size. Qualitative phase analyses were performed by comparison with diffraction patterns from the PDF-2 database. A semi-quantitative phase analysis was performed by the Rietveld refinement method (Post and Bish, 1989), as implemented in the computer code TOPAS 5 (Bruker). The crystal structures of the mineral phases used for refinement were obtained from the Inorganic Crystal Structure Database (ICSD). During Rietveld refinement, only the scale factors, unit-cell parameters and size of coherent diffracting domains were refined. A correction for preferred orientation was applied for selected mineral phases (i.e., K-feldspar, mica, gypsum).

The abundance of sedimentary Fe- and Mn-bearing phases was established by applying a sequential extraction scheme aiming to quantify the contribution of the operationally defined reactive pool capable of reacting after reductive dissolution with sulfide (after Poulton and Canfield, 2005). A wet chemical extraction scheme was applied to liberate (i) the fraction of total acid-volatile sulfur (AVS) in the sediment, which might consist of mackinawite, a portion of greigite,

and a (usually) unknown yet typically negligible fraction of pyrite (Rickard and Morse, 2005), and (ii) chromium-reducible sulfur (CRS), consisting primarily in pyrite but also in the sediment intermediate sulfur compounds (Canfield et al., 1986). AVS was extracted with cold concentrated HCl for 2 h. Then, the resulting hydrogen sulfide concentration (i.e., between 0.004 wt % and 0.036 wt %) was precipitated as Ag_2S by using a 0.3 M $AgNO_3$ solution. Subsequently, CRS was liberated using a hot and acidic 1.0 M $CrCl_2$ solution (Canfield et al., 1986). The resulting H_2S was trapped as Ag_2S. Mass balance after gravimetric quantification was used to calculate the amount of AVS and CRS. Concentration analyses of Fe and Mn dissolved in each of these extracts were conducted via ICP-MS measurements (XSERIES II, Thermo Scientific) at the Department of Environmental Geosciences, Czech University of Life Sciences, Prague.

3.3.2 Sedimentary geochemistry and stable S, O and C isotope analyses

Aliquots of the sediment samples were analyzed for total S (S_{tot}) concentration using a CS analyzer (Eltra GmbH). The detection limit was 0.01 wt % for S_{tot}. The relative errors using the reference material (CRM 7001) was ± 2 % for S_{tot}.

Total S for δ^{34}S determination was extracted in the form of $BaSO_4$ from the sediments. To evaluate the S and sulfate-O isotope ratios of gypsum ($\delta^{34}S_{\text{gy}}$), first the heavy mineral fraction of the samples, which includes pyrite, was excluded by using 1,1,2,2-tetrabromoethane ($\rho = 2.95$). The gypsum was then dissolved in ddH_2O to extract sulfate. The free sulfate obtained was precipitated as $BaSO_4$ as described above (Sect. 3.1.7). The $BaSO_4$ was then converted to SO_2 by direct decomposition mixed with V_2O_5 and SiO_2 powder and combusted at 1000 °C under vacuum (10^{-2}–10^{-3} mbar); mass spectroscopic measurements of the evolved SO_2 were conducted on a Finnigan MAT 251 IR-MS dedicated to S isotope determinations. The results are expressed in delta notation and reported against the V-CDT and V-SMOW standards. The accuracy of the measurements was determined via international standards, with reproducibility better than 0.2 ‰.

The IR-MS instrument used to evaluate the isotope ratios of dissolved sulfate was also used for determining the δ^{34}S of pyrite in the upper anoxic sediments. Prior to analyses, an AVS/CRS wet chemical extraction scheme similar to the one described above was applied. After centrifugation, the Ag_2S precipitate was washed several times with ddH_2O and oven-dried at 50 °C for 48 h. The pyrite δ^{34}S measurements were performed on SO_2 molecules via combustion of ~ 500 mg of silver sulfide homogeneously mixed with an equal amount of WO_3 using a vario PYRO cube (Elementar) connected online via an open split device to the IR-MS. International standards (IAEA-S-1, IAEA-S-2, IAEA-S-3) were used for calibration. Isotope results are reported in the delta notation against the V-CDT standard. Analytical reproducibility was better than 0.5 ‰ based on replicates for standard materials and samples.

The isotope ratios of carbonate in the sediment fraction were evaluated – after removal of organic carbon with H_2O_2 – by implementing the method described by Rosenbaum and Sheppard (1986). These were measured using a DELTA V mass spectrometer (Thermo Fisher Scientific) coupled with an EA-1108 elemental analyzer (Fisons). The same instrument was used for measuring the sediment $\delta^{13}C_{org}$. For this purpose, the samples where finely milled, place in tin (Sn) capsules and oxidized to CO_2 at 1040 °C in the elemental analyzer. The reproducibility of the isotope measurements for organic C was better than $\pm 0.12‰$ and better than $\pm 0.1‰$ for both carbon and oxygen isotopes of siderite. For siderite, the accuracy of the measurement was monitored by analyses of the IAEA NBS-18 ($\delta^{13}C = -5.014‰$; $\delta^{18}O = -23.2‰$) and two in-house standards; the long-term reproducibility is better than 0.05‰ for $\delta^{13}C$ and 0.1‰ for $\delta^{18}O$.

3.3.3 Textural features

For SEM of the sediments, we used a MIRA3 GMU scanning electron microscope (Tescan) combined with a NordlysNano electron backscattering diffraction (EBSD) system for semi-quantitative chemical petrography and a Magellan 400 (FEI) for higher-resolution imaging in secondary electron mode.

4 Results and discussion

4.1 Bottom water column stratification and dissolved oxygen levels

Physicochemical parameters measured in the dysoxic to anoxic waters at the time of sampling are shown in Fig. 2a. Profiling of these parameters was consistent with several previous and subsequent probe monitoring measurements in the meromictic post-mining lake (e.g., Petrash et al., 2018). The pH in the hypolimnion was ~ 8.2 and decreased moderately downwards, reaching 7.4 ± 0.2 units near the anoxic SWI. Simultaneous reactions involving dissolution, anoxic re-oxidation and (re)precipitation of reactive minerals could be responsible for this moderate pH decrease (see Soetaert et al., 2007). These reactions are considered in subsequent sections of this work.

Conductivity exhibited a steep gradient at ca. 48 m depth that flattens with increasing depth. Temperature increased gradually towards the bottom. The zone in the water column where these gradients concur is referred to as the hypolimnion. Increased conductivities within the hypolimnion of post-mining lakes, such as that examined here, could result from the legacy of the former mine drainage and/or from groundwater inflow (e.g., Denimal et al., 2005; Schultze et al., 2010).

Salinity was directly derived by using the measured conductivity values (after Hambright et al., 1994). It increased 3-fold from the hypolimnion downwards (Fig. 2a). This could result from recharge of groundwater carrying high loads of dissolved salts and/or from the lack of mixing of the legacy mine-impacted pit lake waters with those now comprising the mixolimnion. The temperature gradient, on the other hand, is a consequence of limited seasonal vertical heat exchange between the density-stratified water column and the mixolimnion (Boehrer and Schultze, 2008).

Molecular oxygen (O_2) from the mixolimnion cannot be replenished below the density-stratified and thermally stratified bottom waters, and O_2 dropped rapidly within the 48 to 49 m depth interval of the water column from about 8.1 to ~ 0.2 mg L^{-1}. The deepest part of the lake is anoxic (Fig. 2a). At this level, the Eh shifts from > 100 mV at the lower mixolimnion to negative values down to ≤ -230 mV near the SWI. The dysoxic, nitrogenous zone of the water column is referred to as the hypolimnion; it contains a sharp redox boundary zone referred to as the redoxcline. Below the redoxcline lies the monimolimnion which becomes anoxic (ferruginous) towards the SWI (Fig. 2a).

The hydrochemically different monimolimnion persists in the deepest depressions of the lakebed throughout the year, although with slight variations in the monitored Eh and pH ranges that could be accompanied by minor (± 1 m) shifts in the vertical position of the redoxcline. In this study, we focused on the central part of the lake as it exhibited the broadest Eh range in its bottom water column (Fig. 2a). Details on the eastern and western sampling locations are available in a descriptive study by Petrash et al. (2018). Short-lived changes in redox potential of about 150 mV in the bottom water column were recently considered by Umbría-Salinas et al. (2021). These changes have effects on water column speciation (Fig. B1, Appendix B) and affect the partitioning of several redox-sensitive metals that bind to reactive iron phases in the upper sediments (Umbría-Salinas et al., 2021, for details).

4.2 Dissolved carbon concentrations and $\delta^{13}C$ isotope values

4.2.1 Dissolved organic carbon (DOC)

The average of measured DOC concentration in the sampled waters is 1050 ± 500 µM. This range of values was higher than observed in the bottom waters of meromictic lakes such as Matano (< 100 µM; Crowe et al., 2008) or Pavin (300 ± 100 µM; Viollier et al., 1995). DOC is generally comprised of relatively high molecular weight organic compounds (not quantified here), such as cellular exudates from living and senescent planktonic microorganisms (e.g., algae, protists, bacteria) and their degradation products. Probably also present in solution are soluble humic substances (HSs) derived from the biological breakdown of refractory organic matter (e.g., lignite particles) in the sediment (Petrash et al., 2018). VFAs are linear short-chain aliphatic mono-carboxylate compounds produced during anaerobic degradation of the organic compounds referred to above. They serve

as C sources and electron donors for planktonic microbial heterotrophy and were therefore quantified here. VFAs in the bottom waters were at nanomolar concentrations that are reflective of the general scarcity of labile organic substrates. A 6- to 10-fold increase in concentrations of acetate, oxalate and formate occurred towards the increasingly saline and O_2-depleted waters. Concentrations of lactate, propionate, and butyrate could be detected at similar nanomolar magnitudes in the mixolimnion (not shown), but in the monimolimnion these VFAs were exhausted, i.e., below the LQ.

4.2.2 Total dissolved inorganic carbon

The concentrations of total dissolved inorganic carbon (i.e., $\Sigma CO_2 = H_2CO_3 + HCO_3^- + CO_3^{2-}$) ranged from 1.9 to 9.8 mM and increased downwards (Fig. 3a). This parameter positively correlated with alkalinity, which ranged from 1.8 to 2.9 meq L^{-1}. Total dissolved inorganic carbon exhibited lower $\delta^{13}C$ values at the anoxic monimolimnion, and [ΣCO_2] values were inversely correlated with the $\delta^{13}C$ values (Table 1; Fig. 3a–b). The $\delta^{13}C$ values are in the range +0.2 to −4.1 and were inversely correlated with the dissolved sulfate concentrations [SO_4^{2-}] too (Table 1), whilst [SO_4^{2-}] and [ΣCO_2] were directly correlated (Fig. 3b–c). From these observations, an increased ΣCO_2-to-alkalinity ratio is consistent with heterotrophy exceeding gross primary production (for example from chemo- and photoautotrophy). But admixture of the lake's monimolimnion with groundwater carrying geogenic CO_2 could also alter the ΣCO_2 / alkalinity balance. A contribution of organically derived CO_2 is evident as per $\delta^{13}C$ data, yet it could be argued that in the monimolimnion, sulfate reduction has only a moderate impact on alkalinity generation. Although speculative, it is possible that microbial sulfate reduction (MSR) is responsible for the observed lactate depletion. Therefore, the complete (to CO_2) and incomplete (to acetate) oxidation of lactate by MSR could be a factor contributing to the slight decrease in pH in the monimolimnion (see Gallagher et al., 2012).

The CO_2 source flux at the lake floor was estimated using a two-component mixing model that considers the $\delta^{13}C$ values in sedimentary carbonates and organic matter. An input to our model is the isotope values of the sedimentary organic matter ($\delta^{13}C = -27.9 \pm 0.1\,‰$; $n = 6$) and those of (bi)carbonate ions derived from the dissolution of carbonate phases near the SWI and below (Table 1). For the latter, a minor contribution of ΣCO_2 evolved from the oxidation of methane (mean $\delta^{13}C_{CH_4} \approx -67‰$; Table 1) might also be possible and was considered. This methane diffuses throughout the anoxic sediments to the bottom water column. To account for the reactive C of the sedimentary carbonates, we used the $\delta^{13}C$ mean values in the anoxic sediments (+6.4 ± 0.3‰), which are within the range reported for carbonates in the lignite-associated lithologies ($\delta^{13}C$ range +1.7‰ to +13.4‰; median +9.8‰; Šmejkal, 1978, 1984). Our sed-

Table 1. Measured concentrations and isotopic ratios in the O_2-depleted bottom water column of the central sampling location (from 47 to 55 m depth below the surface), Lake Medard.

Depth	pH	Eh	O_2	Conductivity	ΣCO_2*			CH_4		[NO_3^-]	[NH_4^+]	[Fe^{2+}]	[PO_4^{-3}]	[Mn^{2+}]	SO_4^{2-}		
m		mV	mg L^{-1}	µS cm^{-1}	mM	$\delta^{13}C^a$ ‰V-PDB	$\delta^{18}O^b$ ‰V-PDB	µM	$\delta^{13}C^c$ ‰V-PDB	µM	µM	µM	µM	µM	mM	$\delta^{34}S^d$ ‰V-CDT	$\delta^{18}O^e$ ‰V-SMOW
47	8.1	85.9	8.0	1394	n.d.	n.d.	n.d.	n.d.	n.d.	23.8±0.5	3.4±0.4	<0.07	<1.78	0.3±0.01	6.0±0.8	10.9±0.1	2.4±0.1
48	8.1	88.4	8.0	1409	1.9±0.1	+0.2±0.05	13.2±0.2	n.d.	n.d.	24.5±0.5	5.2±0.5	<0.07	9.1±1.8	0.4±0.01	5.9±0.8	13.5±0.07	2.6±0.1
48.5	7.8	−36.4	3.7	3143	3.5±0.2	−0.1	13.1	n.d.	n.d.	26.0±0.5	15.4±0.5	<0.07	1.0±0.2	19.9±0.4	8.3±0.8	11.3±0.03	2.4±0.4
49	7.8	−145.1	0.9	4871	7.5±0.1	−2.1±0.03	14.2±0.1	n.d.	n.d.	19.8±1.2	34.5±9.3	<0.07	3.8±0.8	20.1±0.4	9.6±1.6	11.5±0.1	3.9±0.1
50	7.7	−159.9	0.1	5197	5.9±0.1	−2.7±0.1	12.7±0.4	3.0±0.6	−68.0	17.5±1.2	68.7±9.3	22.8±0.4	10.1±1.0	30.6±0.5	12.8±1.6	12.1±0.1	3.5±0.3
52	7.7	−185.3	0.07	6661	9.8±0.2	−2.5±0.1	13.8±0.2	7.0±1.3	−68.2	18.7±0.2	87.3±14.7	20.5±2.3	11.7±2.3	14.6±0.3	14.4±0.7	12.5±0.1	3.7±0.2
54	7.7	−204.6	0.06	7440	9.0±0.2	−3.9±0.4	13.2±1.1	1.9±0.3	−66.4	18.3±0.2	134.5±14.7	32.7±6.5	19.9±4.0	13.7±0.2	16.8±0.7	13.3±0.1	4.0±0.4
55	7.7	−214.8	0.03	7618	n.d.	n.d.	n.d.	6.8±0.7	−67.2	17.9±0.2	127.7±14.7	28.1±5.6	28.1±5.6	11.1±0.2	16.0±0.7	n.d.	n.d.

* $\Sigma CO_2 = H_2CO_3 + HCO_3^- + CO_3^{2-}$. ^{a} 0.05 precision of the isotopic values reported (here and for all following footnotes, based on repeated measurements of analytical standards; better than 2σ in ‰). ^{b} 0.4 precision.
^{c} 0.9 precision. ^{d} 0.1 precision. ^{e} 0.4 precision. n.d.– not determined.
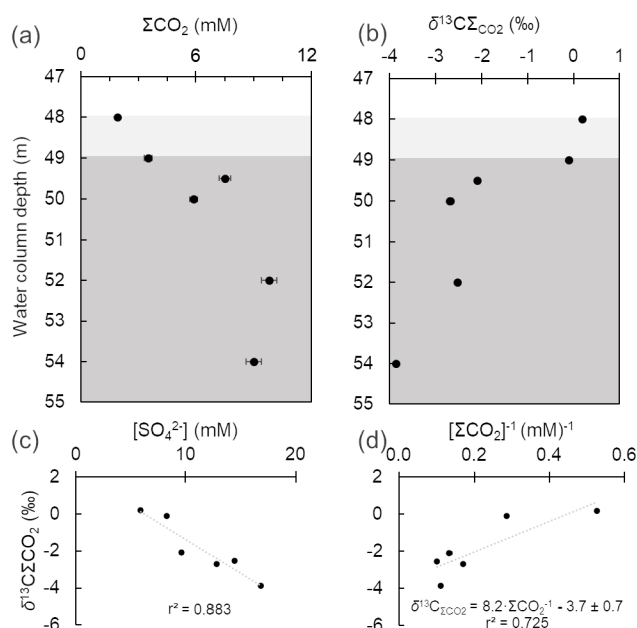
Figure 3. Depth-dependent variation in total dissolved inorganic carbon (ΣCO_2) **(a)** and its $\delta^{13}C$ **(b)** in the oxygen-depleted bottom water column of Lake Medard (centre). Background grey colour code as in Fig. 2. There is negative correlation ($r^2 = 0.883$) between the $\delta^{13}C$ values and dissolved SO_4^{2-} concentrations **(c)**. A Keeling-style plot (ΣCO_2 vs. $\delta^{13}C_{\Sigma CO_2}$) was used to deduce the isotopic C signature of the combined CO_2 flux at the sediment water interface, i.e., the intercept **(d)**.

iment's $\delta^{13}C$ mean value likely fingerprints siderite, which was the only carbonate phase detected via XRD. Yet, other relatively more soluble carbonate phases, such as dolomite and calcite, might be present in small proportions at the lake floor because they occur with siderite in the claystone sediment source. These would account for only ≤ 0.2 wt % (i.e., the LQ of our semi-quantitative XRD analyses). The range of estimated isotopic C values of the CO_2 flux from the sediments to the water column is between -3.0‰ and -4.2‰ (Fig. 3d). The contributions of CO_2 derived from OM degradation, carbonate mineral dissolution and any plausible methanotrophic activity thus produce isotopic C values in the lake bottom water's ΣCO_2 that match those of magmatic-derived CO_2 emissions (Weinlich et al., 1999; Dupalová et al., 2012).

The mixing factor in a simple linear mixing model was calculated after Phillips and Gregg (2001). Accordingly, it could be established that dissolution of sedimentary carbonates contributes 70 ± 5 % of the dissolved inorganic carbon, with the remaining fraction being CO_2 from organic matter heterotrophy (35 % to 25 %). The influence of isotopically light CO_2 derived from the oxidation of diffused methane is negligible, and any contribution of CO_2 from the magmatic source cannot be estimated because of the similar iso-

topic values. The implication for environmental/early diagenetic interpretations of this approach is that if siderite is formed in the lake sediments, it displays a significant $\delta^{13}C$ offset (i.e., between $+9.1$‰ and $+10.9$‰) from the values of the ΣCO_2 reservoir of the lake's floor. Alternatively, siderite could rather be a redeposited mineral sourced from the Miocene claystone lithology that provided detrital material to the mine spoils and modern lake system. We will revisit siderite under Sect. 4.6.1.

4.3 Nitrogen, iron and sulfur species in water column with functional annotations on the planktonic prokaryote community

4.3.1 Nitrogen species transformations and the N-utilizing prokaryotes

Dissolved nitrate (NO_3^-) concentrations across the dysoxic hypolimnion were approximately 25 μM and decrease about 28 % towards the anoxic monimolimnion. This decrease is accompanied by an increase in ammonium from 16 μM to up to 142 μM (Table 1; Fig. 4a). Similar behaviour of reactive N species was described in other ferruginous water columns (e.g., Michiels et al., 2017; Lambrecht et al., 2018).

The relative abundance of 16S rRNA gene sequences that can be ascribed to N-utilizing planktonic prokaryotes (Fig. 4d) indicates that *Nitrosomonas*-like species (95 % to 98 % gene similarity) are in the dysoxic hypolimnion at a low normalized abundance which increases at the redoxcline. Here *Nitrosomonas*-like species may conduct the first and rate-limiting step in nitrification, i.e., NH_3 oxidation (Lehtovirta-Morley, 2018). The second nitrification step, nitrite oxidation to NO_3^-, could be exerted predominantly by species exhibiting similarity (98 % gene sequence) to *Candidatus* (*Ca.*) Nitrotoga (98 % gene sequence similarity). *Ca.* Nitrotoga was detected in all our samples but exhibited a higher normalized abundance (up to 9 %) at the redoxcline (Fig. 4d).

Among the relatively abundant, NH_3-oxidizing microbes detected is an archaeon related to *Nitrosarchaeum koreense* (97 %–98 % gene similarity). This archaeon has higher normalized abundances in the ferruginous waters below the redoxcline (Fig. 4d, also Supplement 2 – Krona chart). Its distribution across the redox gradient is at odds with the fact that *N. koreense* has been previously suggested to be an aerobe (Jung et al., 2018). Similarly, members of the *Candidatus* Nitrosocaldaceae family (similarity 78 %–82 % in 387 bp) appeared to be present in the anoxic zone of the water column, despite the best-studied member of this family, *Ca.* Nitrosocaldus, being reported as displaying an aerobic lifestyle (de la Torre et al., 2008). The archaeal family has heterogeneous metabolic capabilities and is capable of oxidizing ammonia to nitrite (Luo et al., 2021). Our observation could make the case for niche differentiation linked to high loads of dissolved metal concentrations conferring a competitive
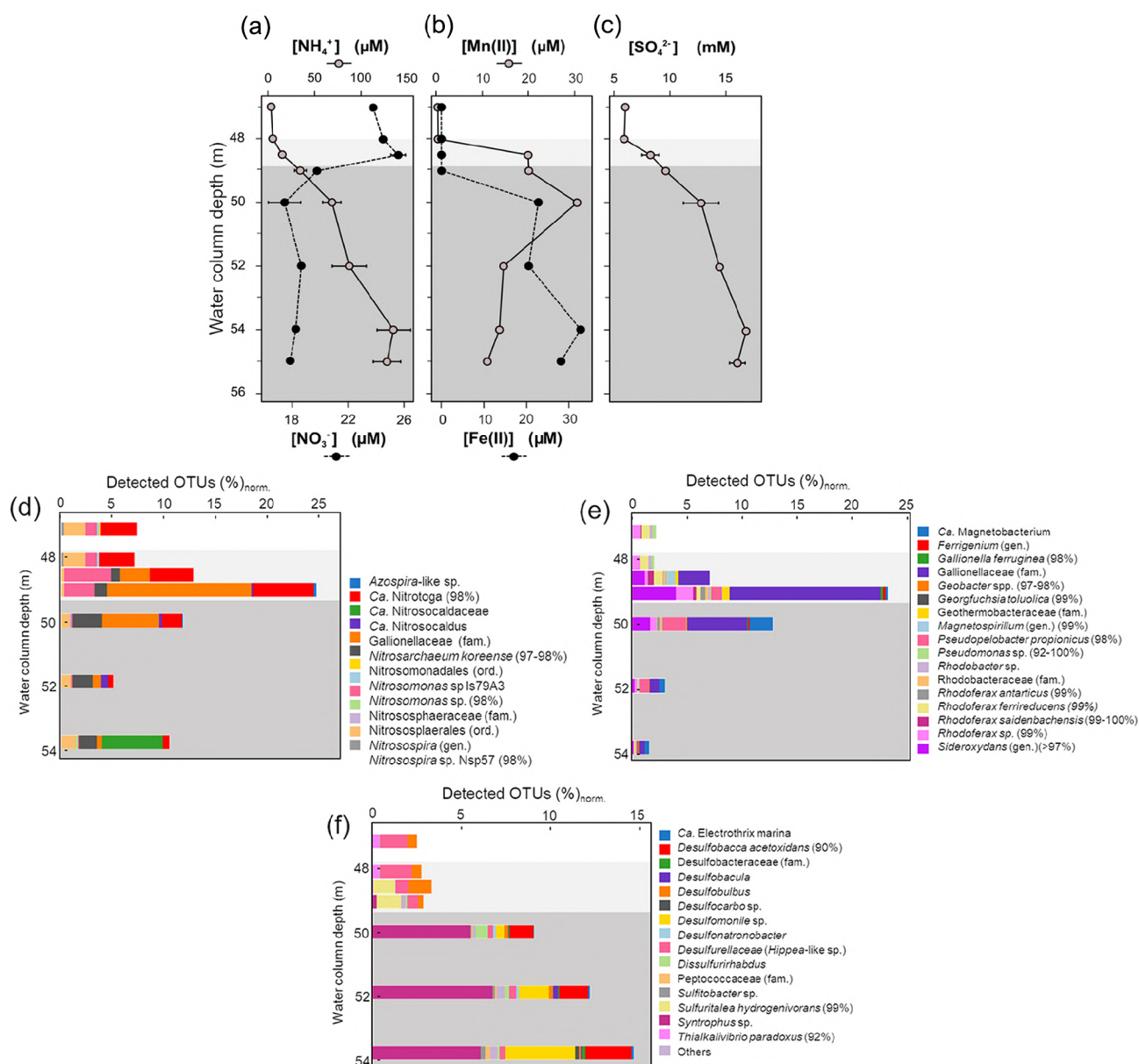
Figure 4. Measured dissolved concentrations of nitrate and ammonia **(a)**, manganous manganese and ferrous iron **(b)**, and sulfate **(c)** in the bottom water column of Lake Medard (central sampling location). The right-side panels show the corresponding, normalized abundance of putative planktonic nitrogen **(d)**, iron **(e)**, and sulfur-utilizing **(f)** prokaryotes. Sequences were classified based on best BLAST (basic local alignment search tool) hit results, and bacteria/archaea were identified based on phylogenetic affiliations. Normalization was with regard to total amplicon reads in each sample. Grey background colours are based on the Eh profile (Fig. 2) and here also indicate redox-stratified niches. The sequences were deposited in the European Nucleotide Archive EMBL-EBI (PRJEB47217).

advantage to these archaea (e.g., Gwak et al., 2019). Alternatively, the NH$_3$-oxidizing archaea detected predominantly in the ferruginous waters possess a yet to be explored tolerance to anoxia (see Mußmann et al., 2011). For instance, *Ca.* Nitrosocaldus encodes a pyruvate : ferredoxin oxidoreductase that is rather uncommon among aerobic ammonia oxidizers (Daebeler et al., 2018), but it is encoded by most

anaerobes able to catalyze the decarboxylation of pyruvate to form acetyl coenzyme A (Chabrière et al., 1999).

The maximal relative abundance of an *Azospira*-like microorganism (95 % similarity) coincides with the peak of relative abundance of members of the Gallionellaceae family at 49 to 50 m depth (Fig. 4d, Supplement 2). Like *Gallionella* spp., *Azospira* also possess dissimilatory N- and Fe-based

metabolisms capable of yielding dinitrogen (N_2) (Mattes et al., 2013). N_2 production probably accounts for a fraction of the apparent nitrogen loss observed when the dissolved reactive NH_4^+ and NO_3^- levels are compared across their counter-gradients (Table 1; Fig. 4a). Nitrite (NO_2^-), an intermediate between NO_3^- and NH_4^+, can also accumulate. Yet, concentration profiles of such an intermediate remain to be accurately resolved in the increasingly saline (high-chlorine) bottom water column of Lake Medard.

When contrasted, the counter-gradients of reactive nitrogen species and those of other dissolved bioactive chemical species suggest that while metabolizing nitrogen, the planktonic prokaryote community could also impact the cycles of Fe and S (e.g., Jewell et al., 2016, 2017; Starke et al., 2017). These cycles in the aqueous system under consideration are likely interlinked throughout microbial mediation in the generalized Reactions (R1)–(R3), but note that intermediate NO_2^- may as well act as a relevant Fe(II) oxidant in this O_2-depleted system (Klueglein et al., 2014):

$$10Fe^{2+} + 2NO_3^- + 24H_2O \rightarrow 10Fe(OH)_3 + N_2 + 18H^+, \quad (R1)$$

$$NO_3^- + 8Fe^{2+} + 21H_2O \rightarrow NH_4^+ + 8Fe(OH)_3 + 14H^+, \quad (R2)$$

$$5HS^- + 8NO_3^- \rightarrow 5SO_4^{2-} + 4N_2 + 3OH^- + H_2O. \quad (R3)$$
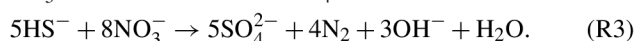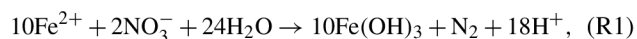
Reaction (R1) proceeds mixotrophically, usually requiring a favourable organic co-substrate, whereas Reactions (R2) and (R3) likely proceed under the influence of chemolithotrophic Fe(II)- and/or S-oxidizing nitrate reducers. Due to energetic considerations, these microorganisms are known for having metabolic advantages under ferruginous conditions over solely denitrifying organisms (see Robertson and Thamdrup, 2017). Reaction (R3) is known to proceed at rather low sulfide levels (Brunet and Garcia-Gil, 1996; Barnard and Russo, 2009), such as those characterizing the monimolimnion of our study site ($\leq 0.3\,\mu M$).

In the following section, to further investigate details on the microbial ecology of the bottom ferruginous waters of Lake Medard, we consider the concentration profiles of dissolved Fe and Mn along the redoxcline. Concentrations of these dissolved metals are operationally defined as the combined ionic and colloidal fractions that passed the $0.22\,\mu m$ cutoff of membrane filters. By co-evaluating the dissolved Fe and Mn concentration trends, we pursue further insight into the mechanism procuring and/or consuming these metals in the stratified water column (Davison, 1993). A 16S rRNA gene abundance profile of known iron-utilizing prokaryotes also permitted inferences about which members of the microbial community could be exerting a direct dissimilatory (catabolic) or indirect (via electron transfer) control over the concentration trends of these metals across the redox gradient.

4.3.2 Dissolved divalent manganese and iron and the Fe-utilizing prokaryotes

Dissolved manganese concentrations ([Mn]) peaked at about 50 m depth (Table 1). Below this depth, [Mn] showed a steady decrease (Fig. 4b). This trend indicates that in the water column the 50 m depth acts as a point source of Mn(II) (Davison, 1993). Divalent iron is also present at a similar concentration magnitude at this depth (Fig. 4b; Table 1), and it can readily act as a reductant of most particulate Mn(IV) settling down from the mixolimnion (Lovley and Phillips, 1988; Myers and Nealson, 1988); see Reaction (R4):

$$2Fe^{2+} + MnO_2 + 1.5H_2O \rightarrow$$
$$Fe_2O_3 \cdot 0.5H_2O + Mn^{2+} + 2H^+. \quad (R4)$$
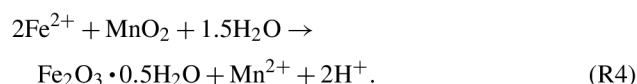
Accordingly, a substantial fraction of the Fe(II) diffusing upwards from the monimolimnion could be re-oxidized or cycled back to Fe(III) within the peak zone of Mn(IV) reduction at 50 m depth (Fig. 4b). Mn(II) yielded during iron oxidation can then be transported both upwards and downwards away from the 50 m depth source point by eddy diffusion (Fig. 4b; Davison, 1993). The internal bottom water column cycling of iron also reflects the concentration gradient of dissolved phosphate (Table 1). Solubilization of this oxyanion is thought to be regulated by reduction of its particulate Fe(III) sinks. Upward diffusion, however, allows for dissolved phosphate to be re-complexed back onto ferrihydrite-like phases that precipitate above the redoxcline, where its concentrations decrease (Table 1).

Contrary to Mn, dissolved Fe concentration ([Fe]) increased steadily downwards, and its global maximum is reached at about 54 m depth in the monimolimnion (Table 1). Immediately below this depth, [Fe] decreases by about 14 %. This decrease can be consistently observed in other anoxic zones of the lake (Petrash et al., 2018) and hints at Fe(II) and reduced S co-precipitation as metastable acid-volatile monosulfide (FeS; e.g., mackinawite). The dissimilar distribution of divalent Fe and Mn in the bottom water column (Fig. 4b) reflected reductive dissolution being much more effective for the sinking manganic particulate than for ferric particulate matter.

Our planktonic prokaryote analysis showed that above the redoxcline the relative abundance and taxonomic richness of known iron-respiring prokaryotes were low and dominated by species closely related to the β-proteobacterium *Rhodoferax* (99 %–100 % gene similarity) (Fig. 4e, Supplement 2). Other sequences that can be functionally affiliated to Fe(III) reduction in the dysoxic hypolimnion included a bacterium with between 92 % and 100 % gene similarity to unclassified *Pseudomonas* spp. (Fig. 4e). *Pseudomonas* could grow by coupling the oxidation of hydrogen (or nitrite) to the reduction of Fe(III) (Lovley et al., 2004). Bioutilization of manganese by *Pseudomonas* species – in both oxidation and reduction reactions – has also been reported (e.g., Tebo

et al., 2005; Geszvain et al., 2011; Lovley, 2013; Wright et al., 2018). Other bacteria that may influence the aqueous manganese cycling to indirectly affect that of dissolved iron belong to the family Hyphomicrobiaceae (e.g., Northup et al., 2003; Spilde et al., 2005). Three OTUs with significant homology to purportedly Mn(II)-oxidizing members of the family (*Hyphomicrobium hollandicum*, *H.* sp. KC-IT-W2 and *Devosia* sp.) exhibited maximal relative abundances above the redoxcline but were notably absent from deeper moni-molimnial waters (Supplement 2).

As previously mentioned, we detected a sharp increase in the relative number of microaerophilic Fe(II)-oxidizing *Gallionella* species at the redoxcline and immediately below it. They accounted for up to $\sim 24\%$ of the total normalized gene reads (Fig. 5b). The increase in relative abundance of *Gallionella* spp. coincided with an increase in sequences related to *Sideroxydans* spp. (Fig. 4e). These latter microaerophiles can also use Fe(II) as an energy source for chemolithotrophic growth with CO_2 as the sole carbon source (Emerson and Moyer, 1997). Other different physiological groups of putative Fe(II)-oxidizing microorganisms detected above- and near-redoxcline samples including anoxygenic phototrophic and nitrate-reducing species (*Magnetospirillum* and *Ferrigenium*; Fig. 4e, Supplement 2) and *Azospira*-like species (Khalifa et al., 2018; Mattes et al., 2013; Dziuba et al., 2016).

Prokaryotes that can adapt their metabolic strategies to the less pronounced geochemical gradients prevailing at the monimolimnion became predominant below the redoxcline. Among them is a bacterium distantly related (89 % identity in 399 bp) to *Candidatus* Magnetobacterium (Lin et al., 2014), whose relative abundance substantially increases at the 50 m depth (Fig. 4e). At this level, our gene sequence reads also included an OTU closely related to *Georgfuchsia toluolica*, a strictly anaerobic β-proteobacterium capable of degrading aromatic compounds with either Fe(III) or NO_3^- as electron acceptors (Weelink et al., 2009). HSs derived from lignite degradation contain abundant aromatic compounds (Wang et al., 2017).

Towards the SWI, important members of the Fe-respiring community were those from the family Geobacteraceae, which can use insoluble Fe(III) and/or Mn(IV) as electron acceptors and acetate, formate, alcohols, aromatics and dihydrogen (H_2) as electron donors (Weber et al., 2006; Lovley and Holmes, 2022). The abundance of *Geobacter* species peaked around the maximum of Fe(III) reduction within the monimolimnion, at about 54 m depth. Here, acetate availability is also relatively high (Fig. 2b). The relative proportion of *Geobacter* spp. increased in parallel with that of their phylogenetically associated *Pseudopelobacter propionicus*, which is a fermentative acetogen that can only indirectly mediate Fe(III) reduction. A possible ecological interaction between *P. propionicus* and *Geobacter* species at the interface of redox boundaries in sedimentary environments has been already reported by Holmes et al. (2007) and Butler et al. (2009).

4.3.3 Dissolved sulfate and the S-utilizing prokaryotes

The dissolved sulfate concentration ($[SO_4^{2-}]$) changed at the redoxcline, where it increased from 6.0 to 16.8 mM (Fig. 4c). At the lower monimolimnion, a decrease in $[SO_4^{2-}]$ coincided with a decrease in [Fe(II)] (Table 1; Fig. 4b–c). In the lower monimolimnion, we detected an increase in the number of taxonomic groups and relative abundances of known sulfate reducers (Fig. 4f). Their by-product sulfide, however, does not accumulate in the ambient waters ($[H_2S + HS^-] \leq 0.30\,\mu M$). The lack of substantial dissolved sulfide towards the SWI and the similar hydrochemical responses of both Fe(II) and $[SO_4^{2-}]$ could be considered circumstantial evidence for FeS precipitation, with other evidence being residual δ^{56}Fe values that increased across the redoxcline and towards the SWI (Petrash et al., 2022). Additional insight into this and other mechanisms of sulfate turnover operating in the water column was sought by evaluating the distribution of S-utilizing prokaryotes.

Our 16S rRNA gene analyses (Fig. 4f; also Supplement 2) revealed a rather low number of taxonomic groups of sulfur-respiring bacteria at the dysoxic hypolimnion. Here OTU assignments show mostly a few uncultured members of the newly proposed order Desulfobulbales of the phylum Desulfobacterota (previously δ-proteobacteria; Waite et al., 2020; Ward et al., 2021) (Fig. 4f). Some species within Desulfobulbales require intermediate S or thiosulfate for heterotrophic growth but can also gain energy from pyruvate fermentation (Flores et al., 2012). *Desulfobulbus* spp. can perform dissimilatory sulfate reduction via the incomplete oxidation of lactate, but *D. propionicus* is known for efficiently conducting disproportionation of elemental sulfur (Lovley and Phillips, 1994). Pyruvate, as lactate, was found below our detection limits across the bottom water column, where sequences distantly related to *D. propionicus* (91 % similarity in 428 bp) appeared to be particularly abundant (Fig. 4f; Supplement 2). Probably important for the microbial sulfur cycling at this level of the water column is also a γ-proteobacterium from the order Chromatiales that has 92 % gene identity in 424 bp with *Thioalkalivibrio paradoxus* (Fig. 4f). *T. paradoxus* is a chemolithoautotrophic sulfur-oxidizing bacterium that can use both reduced and intermediate S compounds for C fixation (Berben et al., 2015).

There were gene sequences that could be confidently ascribed to the facultative S-utilizing autotroph *Sulfuritalea hydrogenivorans* (3 OTUs with $\geq 97\%$ identity in 424 bp) at the redoxcline. The abundance of *S. hydrogenivorans* increased in parallel to a decrease in the *T. paradoxus*-like bacterium, which suggests that the latter may be at a disadvantage and limited by organic C fixation under the specific hydrochemical conditions prevailing at the redoxcline. Such conditions may include, for instance, an abundance of aqueous intermediate S species. Under such conditions, *S. hydrogenivorans* can outcompete the *T. paradoxus*-like bacterium by oxidizing, under denitrifying conditions, thiosulfate ($S_2O_3^{2-}$), S^0
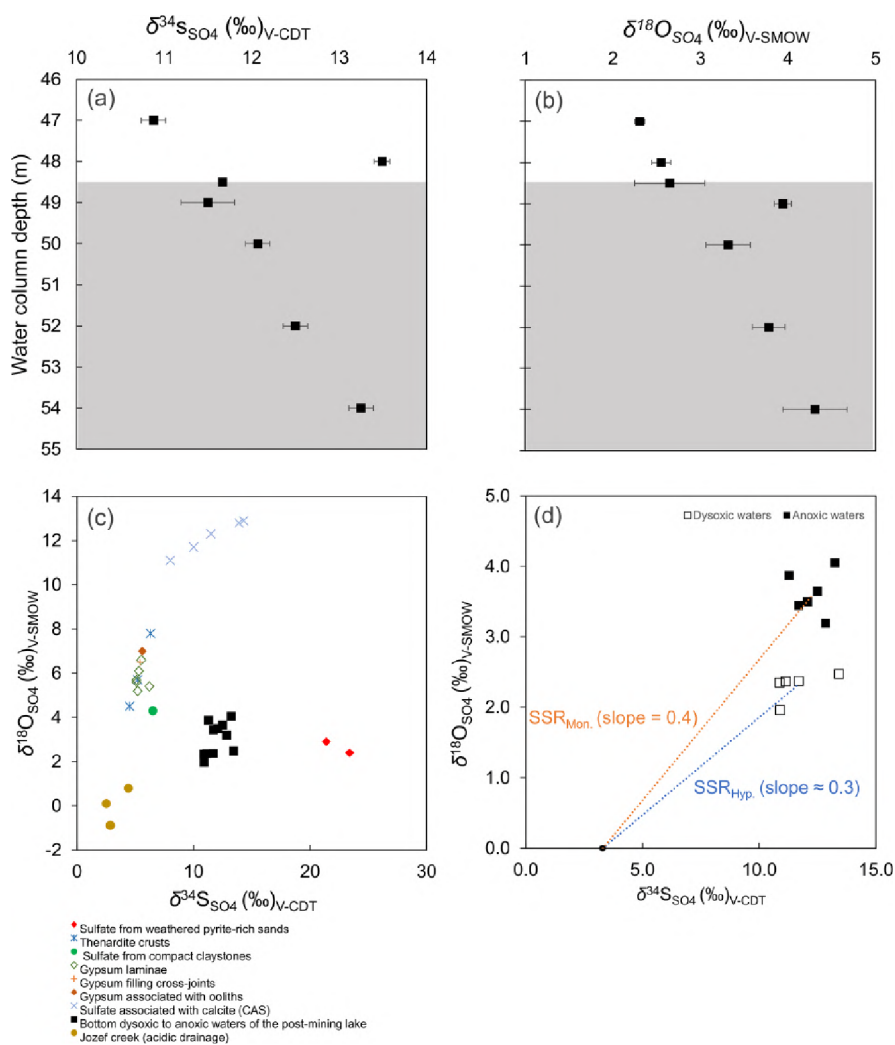
Figure 5. The bottom water column $\delta^{18}O_{SO_4}$ and $\delta^{34}S_{SO_4}$ values **(a–b)**. Grey background colour code as in Fig. 2. Also, a cross-plot of these values in the water column vs. those of all possible sources of dissolved SO_4^{2-} to the modern lacustrine system **(c)**. The coupled sulfur and oxygen isotope-constrained slopes of the linear regressions provide a rough estimation of the sulfate reduction rate (SRR) **(d)**. The regressions considered the $\delta^{18}O_{SO_4}$ and $\delta^{34}S_{SO_4}$ of the acidic drainage to be the initial isotope composition of dissolved sulfate immediately after flooding (see text for details).

and/or H_2 for C fixation (Kojima and Fukui, 2011; Kojima et al., 2014).

At the redoxcline, the relative abundance of species distantly related to fully sequenced Desulfobulbales also increased to $\sim 1.7\%$ (Fig. 4f). Below the redoxcline, our genomic data revealed a progressive development of a more diverse sulfur-respiring bacterial population (Fig. 4f). This was dominated by many relatively rare taxa and a few abundant lineages (Supplement 2) and has a punctuated dominance of species distantly related to *Desulfobacca acetoxidans* (90% identity in 432 bp). *D. acetoxidans* oxidizes acetate using sulfate or sulfite (SO_3^{2-}) or $S_2O_3^{2-}$ as electron acceptors but not S^0 (Oude Elferink et al., 1999). The *D. acetoxidans*-like prokaryote first appeared at 49 m depth but became

dominant towards the SWI, together with *Desulfomonile*-related species (96% identity in 432 bp). *Desulfomonile*-related species could be also responsible for the previously noticed pyruvate depletion, but here they may be also thriving chemolithoautotrophically with $S_2O_3^{2-}$ as the terminal electron acceptor (DeWeerd et al., 1990; Sun et al., 2001). Other prokaryotes probably gain energy out of intermediate S disproportionation in the anoxic monimolimnion. These may include uncultured species distantly related to *Desulfatibacillum* and *Dissulfurirhabdus* (2 OTUs with 87% identity in 428 bp). The presence of the genus *Sulfitobacter* across the aqueous redox gradient and into the monimolimnion (Fig. 4f) points to continuous genetic potential for chemolithotrophic sulfur oxidation across the entire bottom water column.

4.4 δ^{34}S and δ^{18}O isotope values of dissolved sulfate

4.4.1 A proxy for disproportionation

Water column $\delta^{18}O_{SO_4}$ values ranged from $+2.0\,‰$ to $+4.0\,‰$, with corresponding $\delta^{34}S_{SO_4}$ values ranging between $+10.9\,‰$ and $+13.4\,‰$ (Table 1; Fig. 5a–b). The depth profiles of these isotopes in the water column reveal that dissolved sulfate in the anoxic monimolimnion is enriched in ^{18}O (Fig. 5a–b) relative to the dysoxic waters. Despite the moderate decrease in $[SO_4^{2-}]$ towards the SWI (Fig. 4c), no significant sulfur isotope fractionation was registered. The $\delta^{34}S_{SO_4}$ values were only weakly correlated with $[SO_4^{2-}]$ ($r^2 = 0.16$).

The ambient bottom waters had a narrow $\delta^{18}O_{H_2O}$ range of values: $-6.1\,‰$ to $-6.7\,‰$. This is consistent with ongoing meteoric water–rock interactions and rather limited evaporation effects (cf. Noseck et al., 2004; Pačes and Šmejkal, 2004; Dupalová et al., 2012). By applying the expression first proposed by Taylor et al. (1984a) to relate the δ^{18}O values of dissolved SO_4^{2-} and those of ambient waters, we deduced that the oxygen isotope effect ($^{18}\varepsilon_{SO_4\text{-amb. wat.}}$) in our bottom waters ranged between $+9.3\,‰$ and $+10.7\,‰$. This range was calculated under the assumption that equilibrium of oxygen isotope exchange between cell-internal sulfur compounds and ambient water dominates over kinetic oxygen isotope fractionation (Fritz et al., 1989; Brunner et al., 2005). The estimated $^{18}\varepsilon_{SO_4\text{-amb. wat.}}$ is within the range experimentally derived by Brunner et al. (2005) while using similarly ^{18}O-depleted ambient waters. It is also within the range observed in studies of S disproportionation reactions generally proceeding under anoxic conditions (e.g., Böttcher et al., 2001, 2005). Yet, it is lower than $^{18}\varepsilon_{SO_4\text{-amb. wat.}}$ values reported by Bottrell and Newton (2006) in biotic experiments with excess reactive Fe(III) species – i.e., $+16.1\,‰$ to $+17.5\,‰$. Therefore, our $^{18}\varepsilon_{SO_4\text{-amb. wat.}}$ could result from the superimposition of the isotope signals of sulfate reduction, sulfide re-oxidation and intermediate sulfur disproportionation. It follows that the sulfur disproportionation in the bottom waters of Lake Medard most likely results from multiple biologically mediated reactions involving not only reactive iron but also reducible Mn stocks in the sediments (Böttcher et al., 2001). As further discussed below, the anoxic sediments contain a low – i.e., compared with Fe(III)-counterparts – yet still measurable abundance of Mn(IV) (Table 2).

A microbially mediated/induced sulfur disproportionation mechanism fuelled by reactive iron forms present in the sediments also involves Mn(IV)–Mn(III) reduction and is consistent with formation of FeS in the monimolimnion. This mechanism can be described by the following reactions (Reactions R5–R7, after Thamdrup et al., 1993; Böttcher and Thamdrup, 2001):

Table 2. Partitioning of reactive iron and manganese species in the lacustrine sediments (0–8 cm depth).

Depth	FeHR*					FeT	FeHR/FeT	Fepy/FeHR	MnHR*					MnT
(cm)	Exch.	Fe(II)$_{CO_3}$	Poorly cryst. Fe$_{ox}$	Cryst. Fe$_{ox}$	Fe(II)$_{py}$				Exch.	Mn(II)$_{CO_3}$	Poorly cryst. Mn$_{ox}$	Cryst. Mn$_{ox}$	Mn(II)$_{py}$	
0–2	14.7±2.4	283.2±45.3	302.8±48.3	29.6±4.7	189.9±3.6	1024.4±6.2	0.80	0.23	1.0±0.1	18.9±1.5	3.6±0.3	≤0.15	≤0.02	23.7±0.4
2–4	20.3±3.2	294.7±47.2	308.6±49.4	33.7±5.4	224.6±2.4	1067±10.5	0.83	0.25	3.8±0.3	9.4±0.8	3.3±0.3	≤0.16	≤0.03	13.2±0.2
4–6	28.8±4.6	365.7±58.5	263.6±42.2	21.5±21.5	128.9±2.9	1142±10.9	0.71	0.16	2.7±0.2	11.6±0.9	2.8±0.2	≤0.13	≤0.03	14.8±0.2
6–8	24.4±3.9	689.3±110.3	335.7±53.7	373.7±59.8	117.9±4.2	2097±22.8	0.73	0.08	1.2±0.3	7.3±0.6	1.9±0.2	≤0.17	≤0.02	9.5±0.1

* Sediment density is estimated at 2.71 g L^{-1} with a porosity of 40%; error in the measurement ($n = 4$) is ±16% [Fe] and ±8% [Mn]; in µmol cm^{-3}.

$$3S^0 + 2FeOOH \rightarrow SO_4^{2-} + 2FeS + 2H^+, \qquad (R5)$$

$$4S^0 + 4H_2O + 3FeCO_3 \rightarrow$$
$$\qquad SO_4^{2-} + 3FeS + 2H^+ + 3H_2CO_3 , \qquad (R6)$$

$$3S^0 + Mn_3O_4 + 2H^+ \rightarrow SO_4^{2-} + 2HS^- + 3Mn^{2+}. \qquad (R7)$$
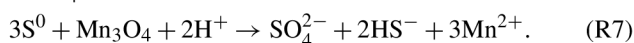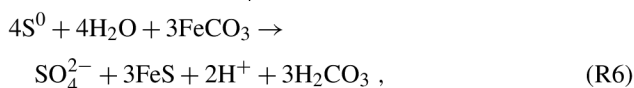
Although not shown in the rather simplified reaction set listed above, S^0 may well be a different intermediate sulfur species such as $S_2O_3^{2-}$ and/or SO_3^{2-} (e.g., Holmkvist et al., 2011). The intracellular isotope exchange of sulfite with anoxic ambient waters has been proven to produce an oxidized SO_4^{2-} product that is enriched in ^{18}O relative to precursory thiosulfate and/or sulfite. This enrichment displays only a minor change, if any, in its corresponding S isotope composition (e.g., Böttcher et al., 2005; Johnston et al., 2014; Bertran et al., 2020; see Table 1). In line with this assertion, at the monimolimnion there is negligible sulfur isotope fractionation accompanying the recorded fractionation of oxygen. Yet, our data recorded a small but significant reverse sulfur isotope effect ($+2.2‰$) at the upper hypolimnion (Fig. 5a, 48 m depth). This isotope effect could be ascribed to either abiotic or biotic oxidation processes of intermediate S species occurring at that level of the water column (see Zerkle et al., 2016, their Table 1).

4.4.2 Insights into intermediate sulfur oxidation

A cross-plot of the $\delta^{34}S_{SO_4}$-vs.-$\delta^{18}O_{SO_4}$ values along the redoxcline as well as those of all the possible geogenic sources of sulfate entering the lake system (see also Appendix B, Fig. B2) is shown in Fig. 5c. Analysis shows that the $\delta^{34}S_{SO_4}$ values of the redox-stratified Lake Medard fingerprint a mixed geogenic-sulfate source. Figure 5d offers further detail and linear regressions of the covariation in the $\delta^{34}S_{SO_4}$-vs.-$\delta^{18}O_{SO_4}$ cross-plot. The slopes of such linear regressions can be used to roughly estimate sulfate reduction rates (SRRs; after Böttcher et al., 2001, and Brunner et al., 2005, among others). For assessing our SRR, it is reasonable to assume that the initial S and O isotope composition linked to dissolved sulfate was within the range of the modern nearby acidic drainage (i.e., $+2.9 \pm 0.1‰$ for $\delta^{34}S_{SO_4}$; $0.0 \pm 0.5‰$ for $\delta^{18}O_{SO_4}$) and similar to the initial composition of sulfate in the pit lake prior to reclamation/flooding (Fig. B2, Appendix B). The residual isotope composition would then be that of dissolved sulfate in the bottom anoxic waters.

In agreement with the lack of accumulation of sulfide in the monimolimnion, our SRR estimation is consistent with slow gross but not net SO_4^{2-} reduction (see Böttcher et al., 2004). The SRR is apparently slower at the monimolimnion (i.e., higher slope) than in the hypolimnion. This is at odds, however, with the higher taxonomic abundance of sulfate reducers that we detected near the SWI (Fig. 4f). The decrease

in dissolved sulfate concentration (Table 1) does not lower the slope of the linear regression. It means that the sulfur isotope ratio of dissolved sulfate evolves more slowly relative to the corresponding change in the oxygen isotope ratio. This result is likely due to sulfate regeneration through microbial sulfide oxidation, with oxygen isotope exchange with ambient water occurring via an intracellular oxidation step of intermediate sulfur (Böttcher et al., 2005; Bertran et al., 2020). Under the low organic substrate availability characterizing the bottom waters examined here (Fig. 2b), sulfate reducers capable of disproportionation (e.g., bacteria from the order Desulfobulbales) can maintain intracellular concentrations of sulfite. This manifested geochemically as the rapid change in water column $\delta^{18}O_{SO_4}$ (Böttcher et al., 2005; Antler et al., 2013).

4.5 Insights from solid-phase analyses

4.5.1 Semi-quantitative X-ray diffraction

XRD analyses of the anoxic sediments show that most detrital minerals were sourced from the Miocene claystone lithology (Appendix A). These detrital phases include kaolinite, quartz, K-feldspar, the TiO_2 polymorphs rutile and anatase, and analcime ($NaAlSi_2O_6 \cdot H_2O$). Minor constituents of the anoxic lake sediments that can also be quantified include gypsum, siderite and pyrite. Gypsum and siderite were in similar abundances in the upper anoxic sediments ($\sim 3\,wt\%$ to $4\,wt\%$), whereas pyrite accounts for a maximum of $0.5\,wt\%$ of their total mineralogy (Fig. 6a). Given that the diffraction peaks of major and minor mineral sediment constituents mask those of Fe(III) and Mn(IV) oxyhydroxides, the abundances of these reactive phases were determined through a sequential extraction scheme that also targets Fe(II)- and Mn(II)-bearing carbonates.

4.5.2 Sequential extractions of reactive iron

The relative concentrations of highly reactive Fe-bearing species (Fe_{HR}) in the upper anoxic sediment pile are displayed in Fig. 6b. The Fe_{HR} sediment pool is defined as that capable of reacting (upon reductive dissolution) with dissolved sulfide to precipitate metastable FeS, which can later be stabilized to pyrite (Canfield and Berner, 1987; Canfield, 1989). We also report here Fe(II) bound to the pyrite fraction (Fe_{py}) and the total iron (Fe_T) in the sediments (Poulton and Canfield, 2005).

Our Fe_{HR} was dominated by poorly crystalline phases (Feh), such as ferrihydrite and/or lepidocrocite (γ-FeOOH). These Fe_{HR} mineral fractions were followed in abundance by those of Fe(II)-bearing carbonates (FeC) (Fig. 6b; Table 2). A significant increase in the FeC is observed with increasing depth (Fig. 6b). This may be indicative of partial dissolution of some Fe(II)-bearing carbonates at the SWI or the result of soluble Fe(II)-binding reactive carbonates deeper
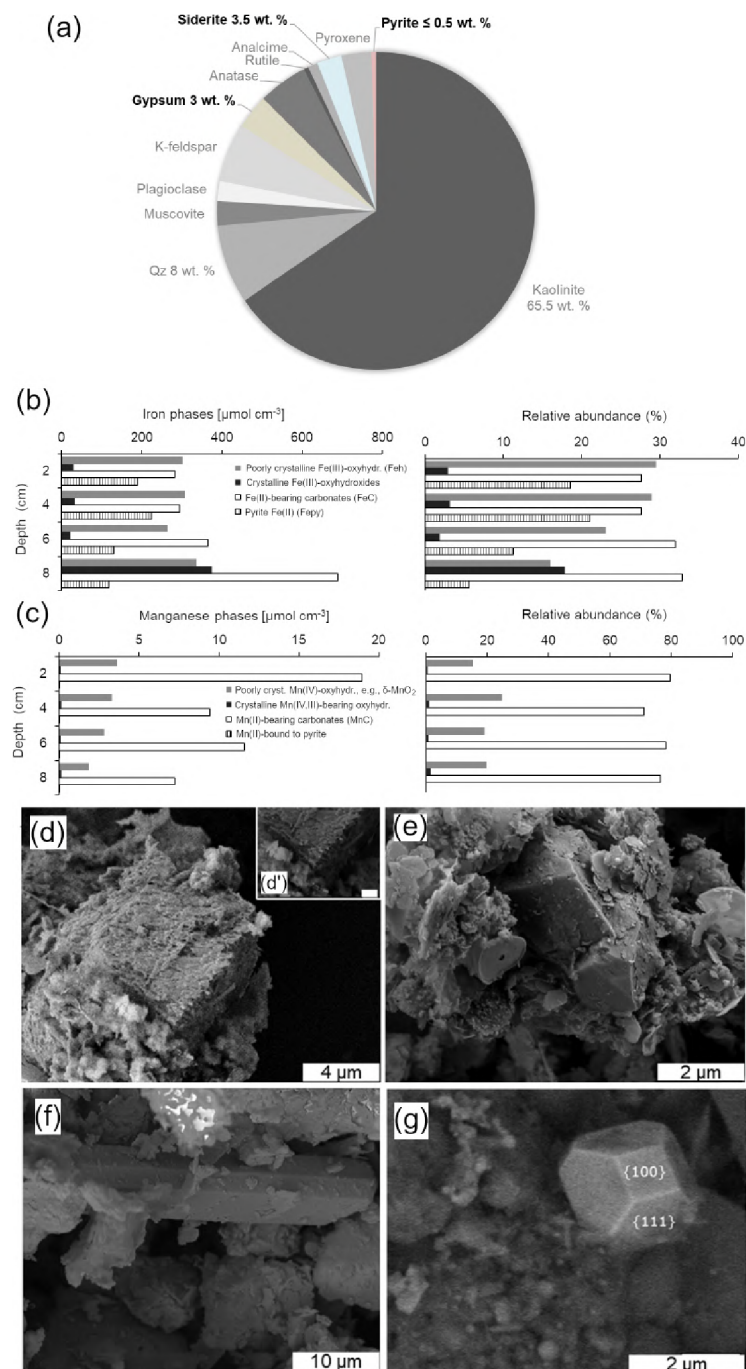
Figure 6. Representative semi-quantitative mineralogical analysis of the upper sediment (0 to 8 cm depth): the XRD data **(a)** show that the sediments are dominated by aluminosilicates and contain gypsum, siderite and pyrite. Results from sequential extraction of iron **(b)** and manganese **(c)** portray changes in partitioning of these metals in reactive oxyhydroxide, carbonate and sulfide solid phases with increasing sediment depth. SEM-EDS analyses of rhombohedral siderite in the **(d)** 0–4 and **(e)** 4–8 cm sediment depth intervals. This carbonate mineral displayed corroded surfaces near the SWI. The textures of microcrystalline equant gypsum **(f)** and truncated octahedral microcrystalline pyrite **(g)** are also shown (see text for details).

into the sedimentary pile. To clarify this matter, we discuss the petrographic features and C isotope values of siderite in Sect. 4.6.1.

Absolute Fe(III) concentrations ascribed to Feh phases increase towards the bottom of our 8 cm depth core, but their abundance, relative to total iron, decreases downwards (Table 2). The extraction step for Feh also extracts Fe(II) bound to monosulfides (Kostka et al., 1995; Scholz and Neumann, 2007). These metastable phases yielded ≤ 0.04 wt % according to our acid-volatile sulfur (AVS) extraction. However, possible rapid oxidation of AVS particles during sampling of the sediments makes it challenging to assess their actual abundance and mineralogy (Schoonen, 2004). It thus appears that the Feh abundance at the top of the sediments (Fig. 6b) is mostly comprised of poorly crystalline oxyhydroxide.

The iron extracted from crystalline Fe(III)-bearing phases (such as goethite) increased from 2.7 ± 0.4 % in the first 6 cm to up to 17.8 % of the Fe$_T$ at the 6 to 8 cm interval (Table 2). Fe concentrations bound to pyrite (Table 2; Fig. 6b) constituted up to ~ 21 % of the Fe$_T$ in the upper sediments (i.e., ~ 0.8 bulk wt %) and showed a general downward decreasing trend contrasting with that of crystalline Fe(III)-bearing phases. From these observations, the 0 to 6 cm depth interval is confidently considered recent anoxic lake deposition, whilst below 6 cm are sediments that were deposited in the shallow pit lake now undergoing alteration under the redox dynamics of the present-day lacustrine system.

The Fe$_{Py}$/Fe$_{HR}$ ratio in the 8 cm long sediment profile accounts for the extent to which the Fe pool was pyritized. The ratio is < 0.35 and decreases downwards (Table 2). When considering that the corresponding Fe$_{HR}$/Fe$_T$ ratios were consistently ≥ 0.71, the results from our sequential extraction scheme applied to iron are consistent with a persistent ferruginous but not euxinic redox state of the now anoxic sediments (Poulton and Canfield, 2011). Variability in Fe$_{py}$/Fe$_{HR}$ and Fe$_{HR}$/Fe$_T$ with depth of the sediments reflects the redox dynamics after flooding and establishment of a chemically distinct monimolimnion.

From combining results from Fe$_{HR}$ partitioning in the sediments (Table 2) and the dissolved Mn(II) and Fe(II) concentration trends (Fig. 4b), we can now strengthen an earlier deduction that Fe(II) sourced from reductive dissolution processes in the upper sediments diffuses upwards, where it rapidly reacts with residual O$_2$ in the vicinity of the redoxcline to form metastable Fe(III)-bearing particulate phases. Most of the iron in such amorphous to nanocrystalline ferrihydrite-like aggregates are deposited on the lake's anoxic floor. From the anoxic floor, iron is resolubilized back into the monimolimnion. Yet a fraction of it stabilizes upon burial as goethite (α-FeOOH) or is bound to the surfaces of reactive carbonates. Another fraction is pyritized through reactions involving elemental sulfur and/or polysulfide near the SWI (Fig. 6b) (Schoonen, 2004, for details). Indeed, we observed that in the upper sediment the partitioning of the reactive iron into these minerals can be swiftly altered by short-lived variations (± 150 mV) in the redox potential of the bottom water column. Variations in the relative proportions of reactive iron minerals also control the distribution of siderophile redox-sensitive elements in the sediment pile (Umbría-Salinas et al., 2021).

4.5.3 Sequential extractions of reactive Mn-bearing phases

Results from our extraction scheme applied to Mn (i.e., after Slomp et al., 1997; Van Der Zee and Van Raaphorst, 2004) show that the Mn$_{HR}$ pool in the anoxic sediment was dominated by Mn(II)-bearing carbonates (MnC) (Fig. 6c; Table 2). The carbonates were relatively more abundant at the SWI but, in contrast to FeC, showed no clearly defined concentration trend in the upper sediments (Table 2; Fig. 6b–c). A declining trend downwards is clear for the proportions of easily reducible Mn(IV) bound to poorly crystalline phases, such as δ-MnO$_2$. These were extracted by diluted HCl (Fig. 6c; Table 2) (Slomp et al., 1997). Reducible Mn associated with more crystalline oxyhydroxide forms is extracted by dithionite (Canfield et al., 1993), but concentrations of this fraction might be sourced from crystalline Fe(III) oxyhydroxides that can either sorb Mn(II) or structurally incorporate Mn(III) (Namgung et al., 2020). Irrespective of its source, the highly crystalline Mn-bearing fraction in our sediment comprises ≤ 0.2 wt % of Mn$_T$ (Table 2). The concentrations of Mn(II) bound to sulfides accounted for ≤ 0.03 wt % of the total Mn extracted (Fig. 6c; Table 2). From the analyses of the partitioning of reactive Mn species, we can thus confirm that under the anoxic conditions currently prevailing in the bottom waters and anoxic SWI of Lake Medard, a minor, yet still important, fraction of reducible Mn$_{HR}$ can be exported from the water column and can participate, together with the reactive forms of iron, in the internal cycle of S (e.g., Reaction R7).

4.6 Insights from siderite, gypsum and pyrite analyses

4.6.1 Siderite

Siderite accounts for up to 3.5 wt % of the total mineralogy of the anoxic lacustrine sediment where it occurs as dispersed fine crystalline rhombohedra. Siderite displays corroded surfaces towards the SWI. This textural feature cannot be observed in crystals at the 4 to 8 cm depth interval (Fig. 6d–e). This is consistent with results from the sequential iron extraction scheme (see above) indicative of Fe carbonate likely undergoing recrystallization and/or growth in the deeper part of the examined sediment pile but partial dissolution towards the SWI, despite its low supersaturation in the monimolimnion ($\Omega_{sid.} = \log \mathrm{IAP} \cdot (\log K_{SP})^{-1} = 1.1$; Supplement 1).

The siderite is enriched in ^{13}C by around $+9$ ‰ (mean δ^{13}C value of siderite is $+6.4 \pm 0.3$ ‰) relative to ΣCO$_2$ of

the bottom water column (Table 1). The mean $\delta^{13}C$ value of the mineral is, however, within the range of $\delta^{13}C$ isotope values reported by Šmejkal (1978) for carbonates of the Cypris claystone. Also, the mean $\delta^{18}O$ values ($+25.7 \pm 1.7\%$) of siderite are within the range observed in Miocene claystone carbonates, which are comprised also of dolomite and calcite (Šmejkal, 1978, 1984). From combining the average isotopic values and textural features of siderite in our anoxic sediments, the mineral can then be considered a seeded (detrital) phase also sourced from the claystone. Siderite seeds were probably redeposited first in the mine spoils and then in the floor of the post-mining lake, together with aluminosilicates and other major and minor mineral phases, during the lake's flooding stage (2008–2016) or thereafter.

4.6.2 Gypsum

Gypsum has a relative abundance of ca. 3 wt %. It displays a microcrystalline {010}-dominated platy shape (Fig. 6f). This is an equilibrium morphology corresponding to a rather low supersaturation (e.g., Simon et al., 1965; van der Voort and Hartman, 1991; Massaro et al., 2010; Rodríguez-Ruiz et al., 2011). This soluble mineral is not thermodynamically predicted by the aqueous-mineral equilibrium modelling of the monimolimnion water (i.e., $\Omega_{gy} = -2.3$; Supplement 1). However, a low-saturation state ($0 < \Omega_{gy} < 1$) that would allow for gypsum formation must exist in the upper sediment pore spaces, for instance, where Ca^{2+} ion activities are locally increased by carbonate dissolution.

Gypsum precipitation under low-saturation states can probably occur as the result of short-lived, climatically constrained changes in the precipitation–dissolution environment of the upper sediment pile (see Umbria-Salinas et al., 2021). The isotope values of the sulfate moiety in the authigenic gypsum ($\delta^{34}S_{gy}$ and $\delta^{18}O_{gy}$) provide further insight into the significance of this phase within the internal sulfur cycle and early diagenetic context of the system under consideration. The $\delta^{34}S_{gy}$ isotope values ranged from -13.9% to -9.6%. Accordingly, gypsum shows ^{34}S depletion of -17.8% to -11.6% relative to dissolved SO_4^{2-} in the ambient anoxic waters (Table 1). The $\delta^{18}O_{gy}$ values range from $+5.1\%$ to $+6.3\%$ (V-SMOW). In consequence, the sulfate in gypsum is ^{18}O-enriched by $+1.4\%$ to $+2.6\%$ as compared with the mean $\delta^{18}O_{SO_4}$ of the monimolimnion (Table 1). This magnitude of isotope ^{18}O enrichment of gypsum sulfate appears consistent with the range observed when sulfate is derived from pyrite that is oxidized by ferric iron in aqueous anaerobic experiments (e.g., Taylor et al., 1984b; Toran and Harris, 1989; Balci et al., 2007).

A net O_2 neutral reaction that also (i) accounts for significant iron sulfide oxidation, (ii) accounts for the localized presence of corroded siderite in the upper sediment, (iii) involves chemolithoautotrophic fixation of CO_2 and (iv) produces an isotopically light gypsum-sulfate could therefore be

written as follows (Reaction R8):

$$3Fe^{32}S + 3CaCO_3 + FeCO_3 + 14H_2O \rightarrow$$

$$4FeOOH + 3Ca^{32}SO_4 \cdot 2H_2O + 4CH_2O. \quad \text{(R8)}$$
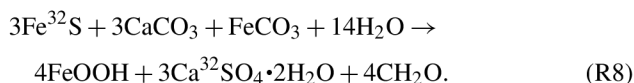
Reaction (R8) assumes that the acidity produced by the oxidation of pyrite and its precursors is neutralized by a 3 : 1 dissolution of calcium to iron carbonate phases in the upper anoxic sediments. The Ca^{2+} ions released by carbonate dissolution can then co-precipitate with the porewater SO_4^{2-} ions to form gypsum. The mineral is ^{34}S-depleted compared to sulfate dissolved in the monimolimnion, but it reflects the $\delta^{18}O$ signature of the ambient anoxic water.

4.6.3 Pyrite

Pyrite accounted for ≤ 0.5 wt % of the total XRD-estimated mineralogy of the sediments and occurs as finely dispersed single octahedral crystals that are up to 2 μm in size and exhibit {111} and {100} truncations (Fig. 6g). This morphology is often seen to develop under sulfide-limited conditions in synthetic experiments (e.g., Barnard and Russo, 2009). From the morphology of pyrite and because its $\delta^{34}S$ isotope values differ considerably from those of weathered pyrite in the coal-seam-associated lithology (Bouška et al., 1997; Appendix B, Fig. B2), this mineral is more probably authigenic in origin. It must have formed locally within the anoxic sediments at low supersaturation and with nucleation itself depleting the availability of reactants (i.e., S^{2-} species) required for further nuclei formation (Rickard and Morse, 2005), hence, its dispersed, fine crystalline occurrence.

The $\delta^{34}S$ isotope values of the finely dispersed pyrite crystals are operationally defined as those of the bulk sediment CRS pool (Canfield et al., 1986). In the upper anoxic sediments, this CRS pool became ^{34}S-enriched with depth. Accordingly, in the 0 to 4 cm depth pyrite has $\delta^{34}S_{CRS}$ isotope values of $-34.7 \pm 0.4\%$. At 4 to 8 cm sediment depth, however, it is relatively ^{34}S-enriched ($\delta^{34}S_{CRS} = -23.9 \pm 0.9\%$).

Pyrite captures the isotopic signature of dissolved sulfide in its local precipitation environment, and near the SWI this mineral appears to have recorded an isotopic offset ($^{34}\varepsilon_{CRS-SO_4}$) of around 38‰ relative to the $\delta^{34}S_{SO_4}$ of the monimolimnion. This magnitude of apparent fractionation could be ascribed to incomplete microbial sulfate reduction, within open-system oxidative sulfur cycling (Johnston et al., 2005; Zerkle et al., 2016). It may well point to our biogenic pyrite resulting from the activity of bacteria capable of fully oxidizing the organic substrates scarcely available (Canfield, 2001; Brüchert, 2004), which could explain the observed depletion of lactate and pyruvate in the bottom water column. Limited microbial sulfate reduction is consistent with the fact that pyrite in the modern lacustrine sediments precipitates without triggering sulfate or divalent iron exhaustion (Scholz, 2018; Canfield, 2001).

Approximately 10‰ ^{34}S isotope enrichment in authigenic pyrite at the bottom of our section hints at an additional heavy

CRS formation mechanism being more active deeper within the anoxic sediment pile. It could also be the case that the $\delta^{34}S_{SO_4}$ values in porewaters in equilibrium with the heavier pyrite are evolved because of variable fractionations associated with MSR (Canfield, 2001; Brüchert, 2004). The $\delta^{34}S$ values of pyrite from the lower part of the cores also exhibit a narrower difference when compared with those coexisting with authigenic gypsum as shown in Fig. B2 (Appendix B). We can attribute these results to a greater abundance of highly reactive Feh phases capable of oxidizing monosulfide (Table 2) in the lower part of the cores investigated.

The CRS pool also includes the sediment's S^0 fraction (Canfield et al., 1986), and given that S^0 derived from the chemolithotrophic oxidation of sulfide is relatively ^{34}S-enriched (e.g., Zerkle et al., 2016; Pellerin et al., 2019), we suggest that ^{34}S enrichment in gypsum in the bottom sediments fingerprints isotopically heavier S^0 comprising an evolved CRS pool. This interpretation is consistent not only with the decreased proportions of Fe_{py} in the lower part of the sediment pile (Table 2) but also with microbial disproportionation-induced fractionations (e.g., Canfield, 2001; Böttcher et al., 2005; Pellerin et al., 2019).

4.7 The imbalanced aqueous redox system in Lake Medard – synthesis

The newly formed Lake Medard has overlapping S, N, Fe and C cycles occurring in the anoxic portion of the water column. This is unusual in natural, redox-stabilized meromictic lakes where at least one of these cycles is functionally diminished or undergoes minimal redox transformations. Alternation of two bistable states could be the case in natural aqueous systems that can be rendered ferruginous, and this alternation is largely controlled by shifts in the prevailing trophic state. Accordingly, ferruginous conditions occur in low-productivity, organic-poor systems, whilst euxinic conditions would dominate in high-productivity, organic-rich systems where production of sulfide depletes dissolved sulfate and may titrate out dissolved iron (van de Velde et al., 2021; Antler et al., 2019).

The redox-stratified Lake Medard demonstrates that ferruginous conditions can develop without substantial sulfate consumption (see Scholz, 2018, and references therein). Our geochemical model on this imbalanced redox system confers a major role to a planktonic prokaryote community that is, to some extent, compartmentalized in the bottom water column, where it mediates in the interlinked C, N, S, and Fe and Mn species transformations occurring across the redoxcline (Fig. 7). These transformations involve a cryptic sulfur cycle with generation and consumption of sulfur intermediates and exert an influence on the concentration gradients of other dissolved bioactive species, such as phosphate. The internal P cycling occurring below the redoxcline (Fig. 7) can in fact render the entire water column oligotrophic (Petrash et al., 2018).

Towards the hypolimnion, particulate matter formation involves a microaerophilic iron oxidizer–nitrate reducer community (e.g., Gallionellaceae). These members of the community could be hypothesized as promoters of a continuous amorphous iron aggregate precipitation and export down to the ferruginous SWI, where these aggregates stabilize and/or are reductively dissolved by iron reducers (e.g., *Geobacter* spp.). In the sediment, stocks of pre-existing siderite and recently stabilized oxyhydroxides fuel anaerobic oxidation and disproportionation of by-product sulfide from MSR. In consequence, the SRR estimate based on coupled stable oxygen and sulfur isotopes indicates no net sulfate reduction, despite increased genetic potential for this pathway, as deducted from analysis, and concomitant evidence for dissolved SO_4^{2-} consumption likely involving metastable FeS formation in the monimolimnion. We are furthering the study of the interplay between Fe and S cycles in the O_2-depleted water column by bridging our $\delta^{34}S$ data with $\delta^{56}Fe$ measurements. The combined results support an active vigorous co-recycling of these elements below the redoxcline (Petrash et al., 2022). Accordingly, an increase in the relative proportion of dissolved ^{56}Fe near the lakebed ($\delta^{56}Fe = +0.12 \pm 0.05\,‰$) can be ascribed to precipitation of monosulfides, whilst precipitation of oxyhydroxides at the redoxcline leads to depletion of ^{56}Fe ($\delta^{56}Fe = -1.77 \pm 0.03$) in the residual dissolved Fe(II) (cf. Busigny et al., 2014).

The $\delta^{34}S_{CRS}$ values in the upper part of the sediment pile were consistent with incipient and incomplete MSR-induced fractionation, yet MSR is not accompanied by dissolved sulfate depletion because of low organic substrate availability and due to bioenergetic considerations given by the presence of dissimilatory iron reducers and an abundance of Fe(III) substrates. Importantly, the $\delta^{34}S_{CRS}$ of the CRS pool at the lower sediment pile likely incorporates ^{34}S from intermediate sulfur. Finally, acidity generated by anaerobic S oxidation reactions proceeding near and at the SWI is neutralized by partial carbonate dissolution, which in turn provides Ca^{2+} ions for interstitial microcrystalline gypsum precipitation. This gypsum's $\delta^{34}S$ values fingerprint intermediate sulfur disproportionation. Redeposited siderite, although experiencing dissolution at the SWI, may be undergoing recrystallization and growth below $\sim 4\,cm$ sediment depth, such as evidenced by increased FeC contents and the absence of corroded siderite crystal surfaces in the lower part of the sedimentary section examined here.

4.8 Relevance for deep-time paleoceanographic and/or diagenetic interpretations

The current lake system provides the opportunity to investigate biogeochemical controls active under a transitional state between nitrogenous and sulfidic conditions. This state cannot be observed in the scarce examples of redox-stratified
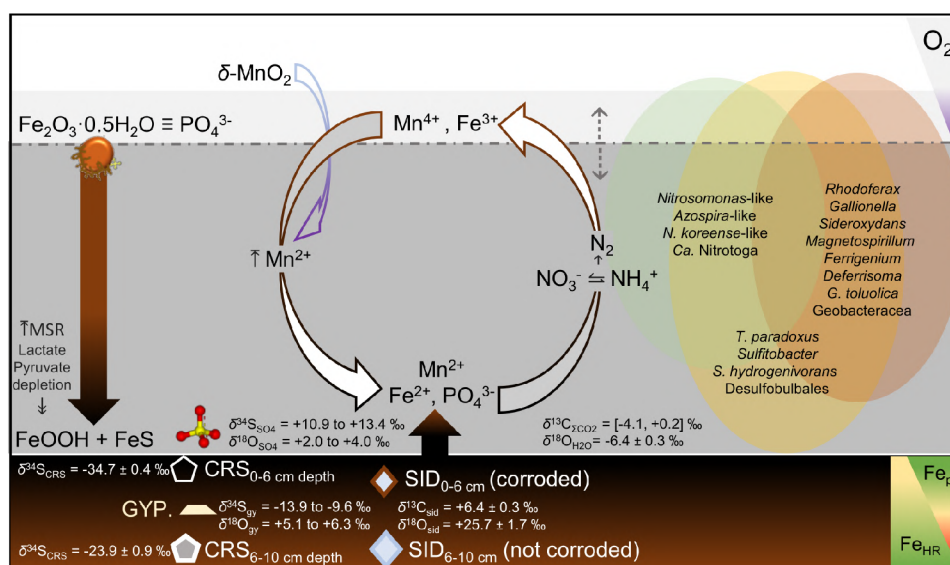
Figure 7. Scheme summarizing the speciation and stable isotopes ranges of sulfur-bearing phases (pyrite, S^0: CRS; gypsum: GYP; siderite: SID) and the biogeochemical cycling mechanisms likely operating in the redox-stratified Lake Medard and its SWI. (Background colours as in Fig. 2.) The prokaryote groups depicted represent nitrate-, iron- and sulfur-utilizing species identified via 16S rRNA gene amplicon sequencing (see text for details).

euxinic marine basins existing today (i.e., Black Sea, Cariaco Basin; Meyer and Kump, 2008) or in the few natural mesotrophic to eutrophic ferruginous lakes presumedly analogues to ancient redox-stratified oceans (see Koeksoy et al., 2016). Similar transitional redox states would have been more prevalent at times with decreased Phanerozoic seawater sulfate concentrations and diminished shuttling of Fe(II) to sediments. Together these factors would have enabled more widespread ferruginous conditions (Reershemius and Planavsky, 2021) that transiently encompassed the water column of Mesozoic epicontinental seas (Petrash et al., 2016; Bauer et al., 2022). Therefore, the link between the biogeochemical controls operating in the water column of our study site and the mineral equilibrium conditions prevailing near and at its anoxic SWI may be relevant for studying elusive shallow burial diagenetic signals developed in fluid-buffered sediments and also for unravelling overprinting of redox proxies in carbonates altered in redox-stratified coastal aquifers (Petrash et al., 2021).

In deeper geological time, the increased delivery of continental sulfate to Precambrian sediments containing not only iron oxyhydroxides but also siderite probably triggered early diagenetic reactions similar to those reported here (e.g., Bachan and Kump, 2015). Comparable diagenetic hydrochemical conditions would have also arisen when transgressions of basinal ferruginous seawater affected evaporitic facies buried by coastal progradation. In this scenario, the low preservation potential of gypsum would have hindered direct interpretations of any possible isotopic offset recorded by its more stable replacive phases (e.g., silicified Fe dolomite).

Although gypsum is rarely preserved in Proterozoic shallow-marine successions (but see Blättler et al., 2018), pseudomorphic carbonates after this mineral are volumetrically important in many Precambrian peritidal facies. In such facies, primary gypsum was often replaced by a metastable early diagenetic phase (e.g., Philippot et al., 2009). In a modern thrombolite-forming environment, Petrash et al. (2012) describe the early replacement of gypsum initially by metastable aragonite. This produces Sr carbonate signals in pseudomorphic calcite replacing aragonite that depart from the Sr content of the ambient water and, by analogy, can disguise an ancient primary gypsum mineralogy. Similarly to Sr, the structurally substituted sulfate in the carbonate lattice (CAS) of Proterozoic peritidal carbonates (i.e., as a putative proxy for contemporary seawater sulfate) can also be altered early during diagenesis and now exhibits isotope signals incompatible with those of coexisting pyrite (Blättler et al., 2020). The $\delta^{34}S$ values of these phases – if formed contemporaneously – would be expected to be similar as per the low dissolved sulfate levels generally ascribed to Proterozoic open oceans (e.g., $< 400\,\mu M$; Fakhraee et al., 2019). An explanation for such a discrepancy is that the CAS and pyrite S isotope proxies recorded the pore fluid signal of diagenetically evolved sulfate in Precambrian (e.g., Rennie and Turchyn, 2014; Li et al., 2015), and some Phanerozoic evaporitic/stromatolitic facies (e.g., Thomazo et al., 2019). Conversely, a similar inconsistency could arise when transient out-of-equilibrium water column conditions equivalent to those currently prevailing in Lake Medard ensued from early diagenesis; i.e., (i) dissolved Fe^{2+}

is amongst the dominant redox species, (ii) substantial dissolved sulfate and solid-phase sulfate are present, (iii) the oxidized Fe_{HR} sediment stocks buffer dissolved sulfide accumulation, and (iv) dissolution of redeposited carbonates buffers the system with regard to acidity generated by anoxygenic oxidative reactions.

5 Conclusions

We investigated biomineralization reactions occurring and prokaryotes thriving in the ferruginous and sulfate-rich water column of a post-mining lake. For this purpose, we considered the pools and fluxes of iron, manganese, carbon, nitrogen and sulfur in the bottom redox-stratified water column and upper reactive sediments (Fig. 7). Discrete spectroscopic datasets were combined with a 16S rRNA gene-aided inference of the planktonic prokaryote community structure to unravel the mechanisms procuring and/or consuming bioactive nitrogen, iron and sulfur species in the redox-stratified ecosystem. Integration of these datasets provides evidence for niche differentiation, but despite marked redox gradients in the water column, we observed sustained genetic potential for anoxygenic sulfide oxidation and intermediate sulfur disproportionation. The processes were further substantiated by using sulfate S and O isotope systematics. Microbe–mineral interactions near the anoxic sediment–water interface modulate the aqueous equilibrium of both reactive authigenic and redeposited Fe- and Mn-bearing phases. A vigorous anoxic sulfide oxidation pathway is coupled to the reduction and solubilization of the ferric and manganic particulate stocks of the lacustrine sediment (Fig. 7).

Dissolved sulfate need not be quantitatively depleted for the establishment of ferruginous conditions in the water column. The aqueous-system-scale reactions currently proceeding in the redox-stratified water column and upper anoxic sediments of Lake Medard are relevant for describing transient redox-imbalanced stages between nitrogenous and ferruginous conditions that developed in low-productivity water columns of ancient nearshore marine settings featuring decreased but not exhausted sulfate levels. These could have produced some of the conflicting isotope signatures often described for coexisting phases of interest as paleoredox proxies, e.g., carbonates and sulfides. The effects in the geochemical record of analogue imbalanced states are yet to be fully accounted for. Further studies in the ferruginous artificial lacustrine system targeted here can provide a more complete picture depicting processes recorded by conflicting proxies in several key, well-preserved Precambrian and Phanerozoic shallow-marine facies.

Appendix A: Geological background

The northwest Bohemia region (Czechia) was an intracontinental basin comprised of peatlands, isolated ephemeral lakes and peat bogs by the late Eocene. This lowland landscape developed and expanded in association with subsidence in the Eger rift (Dèzes et al., 2004). By the Oligocene, the lowlands extended over an area $> 1000\,km^2$ along the Sokolov and Most basins (Matys Grygar et al., 2014). Thus, organic-rich peatlands now encompass lignite seams that correlate across the Czech–German boundary and towards Polish Silesia. The extended wetlands along the Eger continental rift turned, by the beginning of the Miocene, into a large playa lake affected by exhalative hydrothermal inputs (Pačes and Šmejkal, 2004) and episodically by alkaline volcanism (Ulrych et al., 2011). The paleolake deposits recorded the last interval of the syn-rift sedimentation and consist of 70–120 m thick carbonate-rich, kaolinitic coal-bearing claystone with several horizons of tuff material. These deposits are lithostratigraphically referred to as the Cypris Formation (Kříbek et al., 1998, 2017) and now outcrop in elevated areas of the Sokolov mining district, where they overlie the coal seams that were exploited to exhaustion in the former Medard opencast mine. Percolation of waters from the Miocene paleolake produced epithermal mineral salt deposits. Efflorescences of thenardite (Na_2SO_4) are associated with fluid flow along faults and fractures (Šmejkal, 1978). Modern hydrological processes, including groundwater infiltration (Rapantová et al., 2012; Kovar et al., 2016), introduce dissolved sulfate (and iron) into the modern hydrological system (Pačes and Šmejkal, 2004). A 3-year monitoring survey (2007–2010) of dissolved sulfate and iron concentrations in the watershed now occupied by the post-mining lake (Supplement 3 – hydrochemical contours) explains the spatial (and temporal) concentration variabilities seen as bottom water concentrations of these ions were measured and compared across the lake's central W–E axis. For example, western Medard has consistently higher Fe(II) contents matching the dissolved iron gradients observed in the watershed. Conversely, dissolved SO_4^{2+} increases towards the east (Petrash et al., 2018; Supplement 3).

The Miocene Cypris claystone and Quaternary alluvium – comprised of material derived from this unit – function as the main source of sediments to the modern post-mining lacustrine system. The mineral assemblage of the stratigraphic unit includes kaolinite, K-feldspar, quartz, rutile and anatase, and gypsum. It also contains analcime ($NaAlSi_2O_6$), weathered pyrite, carbonates (calcite, Fe dolomite and siderite) and greigite (Fe_3S_4) (Murad and Rojík, 2003, 2005).

Organic matter content in the Cypris claystone exhibits variability that records discontinuous development of widespread anoxia across the paleolake, accompanied also by shifts in salinity and alkalinity. This paleoenvironmental setting promoted lacustrine authigenic carbonate deposition (Kříbek et al., 2017). Overall, the authigenic mineral assemblage, elemental concentration trends, and heavy O and S isotopic signatures of secondary sulfate minerals of the Cypris claystone (Fig. B2, Appendix B) indicate precipitation in a large saline playa paleolake in which the oxidative weath-

ering of sulfides, volcanic exhalations and meteoric water–rock interactions imparted a major geochemical imprint that is superimposed onto that of the episodic changes in the paleolake's redox conditions (Šmejkal, 1978; Pačes and Šmejkal, 2004). A compilation of the δ^{34}S of the sulfate sourced largely from the Miocene claystone is shown in Fig. B2. As discussed in the main text, dissolved sulfate of the modern redox-stratified Lake Medard's waters fingerprints these sources.

Appendix B: Figures B1 and B2
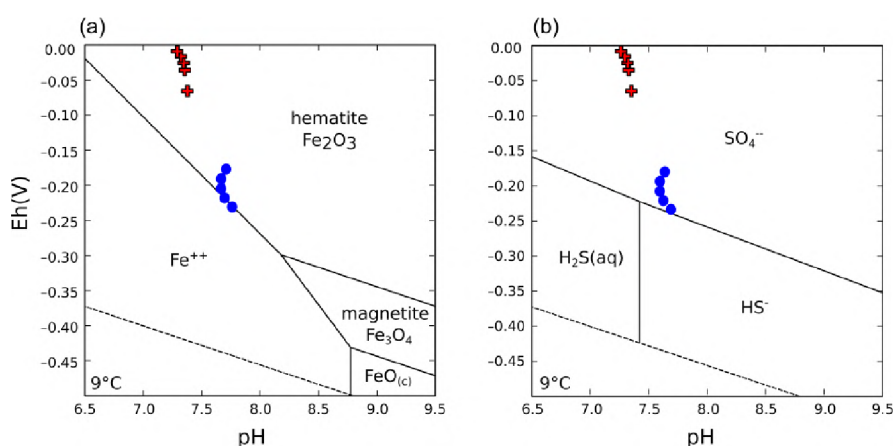
Figure B1. Pourbaix diagrams of the thermodynamically stable Fe and S phases in the bottom waters of Lake Medard at the time of sampling (dots). Also shown are modelling results of Eh–pH parameters measured when the redoxcline shifted downwards and mean monimolimnion's Eh transiently changed from < -200 to -80 mV (crosses). Variation in these physicochemical parameters coincides with seasonal hydrological dynamics of the local watershed and its effects over groundwater influx. Seasonal, short-lived shifts in conditions at the monimolimnic ferruginous waters favour Fe(III)-oxyhydroxide precipitation. Produced using the free Community Edition of The Geochemist's Workbench[®].
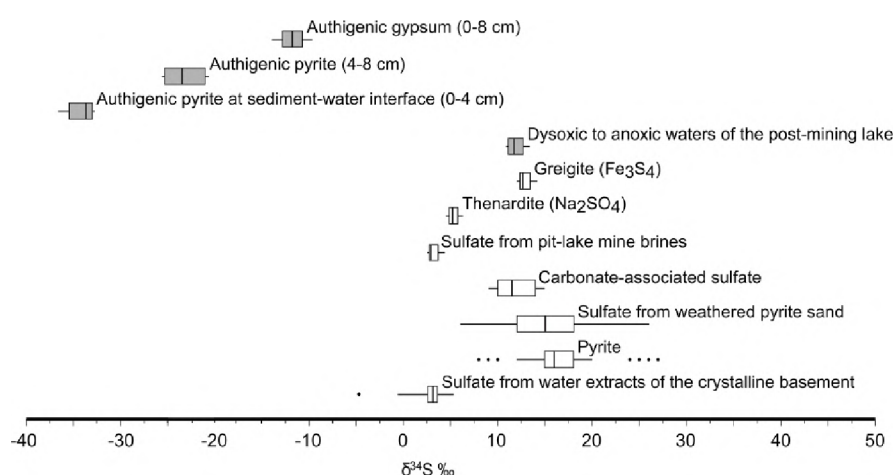
Figure B2. A comparison of the ranges of reported δ^{34}S values of potential sources of oxidized sulfur to Lake Medard (after Šmejkal, 1978; Krs et al., 1990, for greigite); the ranges of sulfate-rich bottom water column and authigenic gypsum and pyrite in the upper anoxic sediments (this work) are also shown (filled boxes).

References

Angly, F. E., Dennis, P. G., Skarshewski, A., Vanwonterghem, I., Hugenholtz, P., and Tyson, G. W.: CopyRighter: a rapid tool for improving the accuracy of microbial community profiles through lineage-specic gene copy number correction, Microbiome, 2, 1–13, 2014.

Antler, G., Turchyn, A. V., Rennie, V., Herut, B., and Sivan, O.: Coupled sulfur and oxygen isotope insight into bacterial sulfate reduction in the natural environment, Geochim. Cosmochim. Ac., 118, 98–117, 2013.

Antler, G., Mills, J. V., Hutchings, A. M., Redeker, K. R., and Turchyn, A. V.: The sedimentary carbon-sulfur-iron interplay – a lesson from East Anglian salt marsh sediments, Front. Earth Sci., 7, 140, https://doi.org/10.3389/feart.2019.00140, 2019.

Bachan, A. and Kump, L. R.: The rise of oxygen and siderite oxidation during the Lomagundi event, P. Natl. Acad. Sci. USA, 112, 6562–6567, 2015.

Balci, N., Shanks, W. C., Mayer, B., and Mandernack, K. W.: Oxygen and sulfur isotope systematics of sulfate produced by bacterial and abiotic oxidation of pyrite, Geochim. Cosmochim. Ac., 71, 3796–3811, 2007.

Barnard, A. S. and Russo, S. P.: Modelling nanoscale FeS_2 formation in sulfur-rich conditions, J. Mater. Chem., 19, 3389–3394, 2009.

Bauer, K. W., Bottini, C., Katsev, S., Jellinek, M., Francois, R., Erba, E., and Crowe, S. A.: Ferruginous oceans during OAE1a and collapse of the marine sulfate pool, Earth Planet. Sc. Lett., 578, 117324, https://doi.org/10.1016/j.epsl.2021.117324, 2022.

Berben, T., Sorokin, D. Y., Ivanova, N., Pati, A., Kyrpides, N., Goodwin, L. A., Woyke, T., and Muyzer, G.: Complete genome sequence of *Thioalkalivibrio paradoxus* type strain ARh 1T, an obligately chemolithoautotrophic haloalkaliphilic sulfur-oxidizing bacterium isolated from a Kenyan soda lake, Stand. Genomic Sci., 10, 105, https://doi.org/10.1186/s40793-015-0097-7, 2015.

Bertran, E., Waldeck, A., Wing, B. A., Halevy, I., Leavitt, W. D., Bradley, A. S., and Johnston, D. T.: Oxygen isotope effects during microbial sulfate reduction: applications to sediment cell abundances, ISME J., 14, 1508–1519, 2020.

Blättler, C. L., Claire, M. W., Prave, A. R., Kirsimäe, K., Higgins, J. A., Medvedev, P. V., Romashkin, A. E., Rychanchik, D. V., Zerkle, A. L., Paiste, K., Kreitsmann, T., Millar, I. L., Hayles, J. A., Bao, H., Turchyn, A. V., Warke, M. R., and Lepland, A.: Two-billion-year-old evaporites capture Earth's great oxidation, Science, 360, 320–323, 2018.

Blättler, C. L., Bergmann, K. D., Kah, L. C., Gómez-Pérez, I., and Higgins, J. A.: Constraints on Meso- to Neoproterozoic seawater from ancient evaporite deposits, Earth Planet. Sc. Lett., 532, 115951, https://doi.org/10.1016/j.epsl.2019.115951, 2020.

Boehrer, B. and Schultze, M.: Stratification of lakes, Rev. Geophys., 46, RG2005, https://doi.org/10.1029/2006RG000210, 2008.

Böttcher, M. E. and Thamdrup, B.: Anaerobic sulfide oxidation and stable isotope fractionation associated with bacterial sulfur disproportionation in the presence of MnO_2, Geochim. Cosmochim. Ac., 65, 1573–1581, 2001.

Böttcher, M. E., Thamdrup, B., and Vennemann, T. W.: Oxygen and sulfur isotope fractionation during anaerobic bacterial disproportionation of elemental sulfur, Geochim. Cosmochim. Ac., 65, 1601–1609, 2001.

Böttcher, M. E., Hespenheide, B., Brumsack, H. J., and Bosselmann, K.: Stable isotope biogeochemistry of the sulfur cycle in modern marine sediments, Isotopes Environ. Health Stud., 40, 267–283, 2004.

Böttcher, M. E., Thamdrup, B., Gehre, M., and Theune, A.: $^{34}S/^{32}S$ and $^{18}O/^{16}O$ fractionation during sulfur disproportionation by *Desulfobulbus propionicus*, Geomicrobiol. J., 22, 219–226, 2005.

Bottrell, S. H. and Newton, R. J.: Reconstruction of changes in global sulfur cycling from marine sulfate isotopes, Earth-Sci. Rev., 75, 59–83, 2006.

Bouška, V., Pešek, J., and Žák, K.: Values of $\delta^{34}S$ in iron disulphides of the North Bohemian Lignite Basin, Czech Republic, Geol. Soc. Lond. Spec. Publ., 125, 261–267, 1997.

Brüchert, V.: Physiological and ecological aspects of sulfur isotope fractionation during bacterial sulfate reduction, Spec. Pap. Geol. Soc. Am., 379, 1–16, 2004.

Brunet, R. C. and Garcia-Gil, L. J.: Sulfide-induced dissimilatory nitrate reduction to ammonia in anaerobic freshwater sediments, FEMS Microbiol. Ecol., 21, 131–138, 1996.

Brunner, B., Bernasconi, S. M., Kleikemper, J., and Schroth, M. H.: A model for oxygen and sulfur isotope fractionation in sulfate during bacterial sulfate reduction processes, Geochim. Cosmochim. Ac., 69, 4773–4785, 2005.

Busigny, V., Planavsky, N. J., Jézéquel, D., Crowe, S., Louvat, P., Moureau, J., Viollier, E., and Lyons, T. W.: Iron isotopes in an Archean ocean analogue, Geochim. Cosmochim. Ac., 133, 443–462, 2014.

Butler, J. E., Young, N. D., and Lovley, D. R.: Evolution from a respiratory ancestor to fill syntrophic and fermentative niches: comparative genomics of six Geobacteraceae species, BMC Genomics, 101, 1–10, 2009.

Canfield, D. E.: Reactive iron in marine sediments, Geochim. Cosmochim. Ac., 53, 619–632, 1989.

Canfield, D. E.: Biogeochemistry of Sulfur Isotopes, Rev. Mineral. Geochem., 43, 607–636, 2001.

Canfield, D. E. and Berner, R. A.: Dissolution and pyritization of magnetite in anoxic marine sediments, Geochim. Cosmochim. Ac., 51, 645–659, 1987.

Canfield, D. E., Raiswell, R., Westrich, J. T., Reaves, C. M., and Berner, R. A.: The use of chromium reduction in the analysis of reduced inorganic sulfur in sediments and shales, Chem. Geol., 54, 149–155, 1986.

Canfield, D. E., Thamdrup, B., and Hansen, J. W.: The anaerobic degradation of organic matter in Danish coastal sediments: Iron reduction, manganese reduction, and sulfate reduction, Geochim. Cosmochim. Ac., 57, 3867–3883, 1993.

Canfield, D. E., Zhang, S., Wang, H., Wang, X., Zhao, W., Su, J., Bjerrum, C. J., Haxen, E. R., and Hammarlund, E. U.: A Mesoproterozoic iron formation, P. Natl. Acad. Sci. USA, 115, E3895–E3904, https://doi.org/10.1073/pnas.1720529115, 2018.

Caporaso, J. G., Kuczynski, J., Stombaugh, J., Bittinger, K., Bushman, F. D., Costello, E. K., Fierer, N., Pa, A. G., Goodrich, J. K., Gordon, J. I., Huttley, G. A., Kelley, S. T., Knights, D., Koenig, J. E., Ley, R. E., Lozupone, C. A., McDonald, D., Muegge, B. D., Pirrung, M., Reeder, J., Sevinsky, J. R., Turnbaugh, P. J., Walters, W. A., Widmann, J., Yatsunenko, T., Zaneveld, J., and Knight, R.: QIIME allows analysis of high-throughput community sequencing data, Nat. Methods, 7, 335–336, 2010.

Davison, W.: Iron and manganese in lakes, Earth Sci. Rev., 34, 119–163, 1993.

Chabrière, E., Charon, M. H., Volbeda, A., Pieulle, L., Hatchikian, E. C., and Fontecilla-Camps, J. C.: Crystal structures of the key anaerobic enzyme pyruvate:ferredoxin oxidoreductase, free and in complex with pyruvate, Nat. Struct. Biol., 62, 182–190, 1999.

Crowe, S. A., O'Neill, A. H., Katsev, S., Hehanussa, P., Haffner, G. D., Sundby, B., Mucci, A., and Fowle, D. A.: The biogeochemistry of tropical lakes: A case study from Lake Matano, Indonesia, Limnol. Oceanogr., 53, 319–331, 2008.

Daebeler, A., Herbold, C. W., Vierheilig, J., Sedlacek, C. J., Pjevac, P., Albertsen, M., Kirkegaard, R. H., de la Torre, J. R., Daims, H., and Wagner, M.: Cultivation and genomic analysis of "Candidatus Nitrosocaldus islandicus," an obligately thermophilic, ammonia-oxidizing thaumarchaeon from a hot spring biofilm in Graendalur valley, Iceland, Front. Microbiol., 9, 193, https://doi.org/10.3389/fmicb.2018.00193, 2018.

de la Torre, J. R., Walker, C. B., Ingalls, A. E., Könneke, M., and Stahl, D. A.: Cultivation of a thermophilic ammonia oxidizing archaeon synthesizing crenarchaeol, Environ. Microbiol., 10, 810–818, 2008.

Denimal, S., Bertrand, C., Mudry, J., Paquette, Y., Hochart, M., and Steinmann, M.: Evolution of the aqueous geochemistry of mine pit lakes – Blanzy-Montceau-les-Mines coal basin (Massif Central, France): Origin of sulfate contents; effects of stratification on water quality, Appl. Geochem., 20, 825–839, 2005.

DeWeerd, K. A., Mandelco, L., Tanner, R. S., Woese, C. R., and Suflita, J. M.: *Desulfomonile tiedjei* gen. nov. and sp. nov., a novel anaerobic, dehalogenating, sulfate-reducing bacterium, Arch. Microbiol., 1541, 23–30, 1990.

Dèzes, P., Schmid, S. M., and Ziegler, P. A.: Evolution of the European Cenozoic Rift System: interaction of the Alpine and Pyrenean orogens with their foreland lithosphere, Tectonophysics, 389, 1–33, 2004.

Dupalová, T., Sracek, O., Vencelides, Z., and Žák, K.: The origin of thermal waters in the northeastern part of the Eger Rift, Czech Republic, Appl. Geochem., 27, 689–702, 2012.

Dziuba, M., Koziaeva, V., Grouzdev, D., Burganskaya, E., Baslerov, R., Kolganova, T., Chernyadyev, A., Osipov, G., Andrianova, E., Gorlenko, V., and Kuznetsov, B.: *Magnetospirillum caucaseum* sp. Nov., *Magnetospirillum marisnigri* sp. Nov. and *Magnetospirillum moscoviense* sp. Nov., freshwater magnetotactic bacteria isolated from three distinct geographical locations in European Russia, Int. J. Syst. Evol. Micr., 66, 2069–2077, 2016.

Edgar, R. C., Hass, B. J., Clemente, J. C., Quince, C., and Knight, R.: UCHIME improves sensitivity and speed of chimera detection, Bioinformatics, 27, 2194–2200, 2011.

Emerson, D. and Moyer, C.: Isolation and characterization of novel iron-oxidizing bacteria that grow at circumneutral pH, Appl. Environ. Microb., 63, 4784–4792, 1997.

Fakhraee, M., Hancisse, O., Canfield, D. E., Crowe, S. A., and Katsev, S.: Proterozoic seawater sulfate scarcity and the evolution of ocean–atmosphere chemistry, Nat. Geosci., 125, 375–380, 2019.

Flores, G. E., Hunter, R. C., Liu, Y., Mets, A., Schouten, S., and Reysenbach, A. L.: *Hippea jasoniae* sp. nov. and *Hippea alviniae* sp. nov., thermoacidophilic members of the class Deltaproteobacteria isolated from deep-sea hydrothermal vent deposits, Int. J. Syst. Evol. Microbiol., 62, 1252–1258, 2012.

Fritz, P., Basharmal, G. M., Drimmie, R. J., Ibsen, J., and Qureshi, R. M.: Oxygen isotope exchange between sulphate and water during bacterial reduction of sulphate, Chem. Geol. Isot. Geosci. Sect., 79, 99–105, 1989.

Gallagher, K. L., Kading, T., Braissant, O., Dupraz, C., and Visscher, P. T.: Inside the alkalinity engine: The role of electron donors in the organomineralization potential of sulfate-reducing bacteria, Geobiology, 10, 518–530, 2012.

Geszvain, K., Yamaguchi, A., Maybee, J., and Tebo, B. M.: Mn(II) oxidation in *Pseudomonas putida* GB-1 is influenced by flagella synthesis and surface substrate, Arch. Microbiol., 193, 605–614, 2011.

Goldberg, T., Archer, C., Vance, D., Thamdrup, B., McAnena, A., and Poulton, S. W.: Controls on Mo isotope fractionations in a Mn-rich anoxic marine sediment, Gullmar Fjord, Sweden, Chem. Geol., 296–297, 73–82, 2012.

Gwak, J.-H., Jung, M.-Y., Hong, H., Kim, J.-G., Quan, Z.-X., Reinfelder, J. R., Spasov, E., Neufeld, J. D., Wagner, M., and Rhee, S.-K.: Archaeal nitrification is constrained by copper complexation with organic matter in municipal wastewater treatment plants, ISME J., 142, 335–346, 2019.

Hambright, K. D., Gophen, M., and Serruya, S.: Influence of long-term climatic changes on the stratification of a subtropical, warm monomictic lake, Limnol. Oceanogr., 39, 1233–1242, 1994.

Holmes, D. E., O'Neil, R. A., Vrionis, H. A., N'Guessan, L. A., Ortiz-Bernad, I., Larrahondo, M. J., Adams, L. A., Wards, J. A., Nicoll, J. S., Nevin, K. P., Chavan, M. A., Johnson, J. P., Long, P. E., and Lovley, D. R.: Subsurface clade of Geobacteraceae that predominates in a diversity of Fe(III)-reducing subsurface environments, ISME J., 1, 663–677, 2007.

Holmkvist, L., Ferdelman, T. G., and Jørgensen, B. B.: A cryptic sulfur cycle driven by iron in the methane zone of marine sediment (Aarhus Bay, Denmark), Geochim. Cosmochim. Ac., 75, 3581–3599, 2011.

Jewell, T. N. M., Karaoz, U., Brodie, E. L., Williams, K. H., and Beller, H. R.: Metatranscriptomic evidence of pervasive and diverse chemolithoautotrophy relevant to C, S, N and Fe cycling in a shallow alluvial aquifer, ISME J., 10, 2106–2117, 2016.

Jewell, T. N. M., Karaoz, U., Bill, M., Chakraborty, R., Brodie, E. L., Williams, K. H., and Beller, H. R.: Metatranscriptomic analysis reveals unexpectedly diverse microbial metabolism in a biogeochemical hot spot in an alluvial aquifer, Front. Microbiol., 8, 40, https://doi.org/10.3389/fmicb.2017.00040, 2017.

Jiang, C. Z. and Tosca, N. J.: Fe(II)-carbonate precipitation kinetics and the chemistry of anoxic ferruginous seawater, Earth Planet. Sc. Lett., 506, 231–242, 2019.

Johnston, D. T., Farquhar, J., Wing, B. A., Kaufman, A., Canfield, D. E., and Habicht, K. S.: Multiple sulfur isotope fractionations in biological systems: a case study with sulfate reducers and sulfur disproportionators, Am. J. Sci., 305, 645–660, 2005.

Johnston, D. T., Gill, B. C., Masterson, A., Beirne, E., Casciotti, K. L., Knapp, A. N., and Berelson, W.: Placing an upper limit on cryptic marine sulphur cycling, Nature, 513, 530–533, 2014.

Jung, M.-Y., Islam, M. A., Gwak, J.-H., Kim, J.-G., and Rhee, S.-K.: *Nitrosarchaeum koreense* gen. nov., sp. nov., an aerobic and mesophilic, ammonia-oxidizing archaeon member of the phylum Thaumarchaeota isolated from agricultural soil, Int. J. Syst. Evol. Micr., 68, 3084–3095, 2018.

Khalifa, A., Nakasuji, Y., Saka, N., Honjo, H., Asakawa, S., and Watanabe, T.: *Ferrigenium kumadai* gen. Nov., sp. nov., a microaerophilic iron-oxidizing bacterium isolated from a paddy field soil, Int. J. Syst. Evol. Micr., 68, 2587–2592, 2018.

Klueglein, N., Zeitvogel, F., Stierhof, Y. D., Floetenmeyer, M., Konhauser, K. O., Kappler, A., and Obst, M.: Potential Role of Nitrite for Abiotic Fe(II) Oxidation and Cell Encrustation during Nitrate Reduction by Denitrifying Bacteria, Appl. Environ. Microb., 80, 1051–1061, 2014.

Koeksoy, E., Halama, M., Konhauser, K. O., and Kappler, A.: Using modern ferruginous habitats to interpret Precambrian banded iron formation deposition, Int. J. Astrobiol., 15, 205–217, 2016.

Kojima, H. and Fukui, M.: *Sulfuritalea hydrogenivorans* gen. nov., sp. nov., a facultative autotroph isolated from a freshwater lake, Int. J. Syst. Evol. Micr., 61, 1651–1655, 2011.

Kojima, H., Watanabe, T., Iwata, T., and Fukui, M.: Identification of major planktonic sulfur oxidizers in stratified freshwater lake, PLoS One, 9, e93877, https://doi.org/10.1371/journal.pone.0093877, 2014.

Konhauser, K. O., Amskold, L., Lalonde, S. V., Posth, N. R., Kappler, A., and Anbar, A.: Decoupling photochemical Fe(II) oxidation from shallow-water BIF deposition, Earth Planet. Sc. Lett., 258, 87–100, 2007.

Kostka, J. E., Luther, G. W., and Nealson, K. H.: Chemical and biological reduction of Mn (III)-pyrophosphate complexes: Potential importance of dissolved Mn (III) as an environmental oxidant, Geochim. Cosmochim. Ac., 59, 885–894, 1995.

Kovar, P., Kalibova, J., and Bacinova, H.: Computing hydrological balance in the Medard Mining Pit with the help of the water balance conceptual model, J. Civ. Environ. Eng., 6, 5, https://doi.org/10.4172/2165-784X.1000250, 2016.

Kříbek, B., Strnad, M., Boh\'{a}ˆcek, Z., Sýkorová, I., Čejka, J., and Sobalík, Z.: Geochemistry of Miocene lacustrine sediments from the Sokolov Coal Basin (Czech Republic), Int. J. Coal Geol., 37, 207–233, 1998.

Kříbek, B., Knésl, I., Rojík, P., Sýkorová, I., and Martínek, K.: Geochemical history of a Lower Miocene Lake, the Cypris Formation, Sokolov Basin, Czech Republic, J. Paleolimnol., 58, 169–190, 2017.

Krs, M., Krsová, M., Pruner, P., Zeman, A., Novák, F., and Jansa, J.: A petromagnetic study of Miocene rocks bearing micro-organic material and the magnetic mineral greigite (Sokolov and Cheb basins, Czechoslovakia), Phys. Earth Planet. In., 63, 98–112, 1990.

Lambrecht, N., Wittkop, C., Katsev, S., Fakhraee, M., and Swanner, E. D.: Geochemical Characterization of Two Ferruginous Meromictic Lakes in the Upper Midwest, USA, J. Geophys. Res.-Biogeo., 123, 3403–3422, 2018.

Lehtovirta-Morley, L. E.: Ammonia oxidation: Ecology, physiology, biochemistry and why they must all come together, EMS Microbiol. Lett., 365, fny058, https://doi.org/10.1093/femsle/fny058, 2018.

Li, C., Planavsky, N. J., Love, G. D., Reinhard, C. T., Hardisty, D., Feng, L., Bates, S. M., Huang, J., Zhang, Q., Chu, X., and Lyons, T. W.: Marine redox conditions in the middle Proterozoic ocean and isotopic constraints on authigenic carbonate formation: Insights from the Chuanlinggou Formation, Yanshan Basin, North China, Geochim. Cosmochim. Ac., 150, 90–105, 2015.

Lin, W., Deng, A., Wang, Z., Li, Y., Wen, T., Wu, L.-F., Wu, M., and Pan, Y.: Genomic insights into the uncultured genus *Candidatus* Magnetobacterium in the phylum Nitrospirae, ISME J., 812, 2463–2477, 2014.

Lovley, D.: Dissimilatory Fe(III)- and Mn(IV)-Reducing prokaryotes, in: The Prokaryotes: Prokaryotic Physiology and Biochemistry, Springer, Berlin, Heidelberg, 287–308, 2013.

Lovley, D. R. and Holmes, D. E.: Electromicrobiology: the ecophysiology of phylogenetically diverse electroactive microorganisms, Nat. Rev. Microbiol., 20, 5–19, https://doi.org/10.1038/s41579-021-00597-6, 2022.

Lovley, D. R. and Phillips, E. J. P.: Manganese inhibition of microbial iron reduction in anaerobic sediments, Geomicrobiol. J., 6, 145–155, 1988.

Lovley, D. R. and Phillips, E. J. P.: Novel processes for anaerobic sulfate production from elemental sulfur by sulfate-reducing bacteria, Appl. Environ. Microb., 60, 2394–2399, 1994.

Lovley, D. R., Holmes, D. E., and Nevin, K. P.: Dissimilatory Fe(III) and Mn(IV) reduction, Adv. Microb. Physiol., 49, 219–286, 2004.

Luo, Z. H., Narsing Rao, M. P., Chen, H., Hua, Z. S., Li, Q., Hedlund, B. P., Dong, Z. Y., Liu, B. B., Guo, S. X., Shu, W. S., and Li, W. J.: Genomic insights of *Candidatus* Nitrosocaldaceae based on nine new metagenome-assembled genomes, including *Candidatus* Nitrosothermus gen nov. and two new species of *Candidatus* Nitrosocaldus, Front. Microbiol., 11, https://doi.org/10.3389/fmicb.2020.608832, 2021.

Magoč, T. and Salzberg, S.: FLASH: Fast length adjustment of short reads to improve genome assemblies, Bioinformatics, 27, 2957–2963, 2011.

Massaro, F. R., Rubbo, M., and Aquilano, D.: Theoretical Equilibrium Morphology of Gypsum (CaSO$_4 \cdot$2H$_2$O). 1. A Syncretic Strategy to Calculate the Morphology of Crystals, Cryst. Growth Des., 10, 2870–2878, 2010.

Mattes, A., Gould, D., Taupp, M., and Glasauer, S.: A novel autotrophic bacterium isolated from an engineered wetland system links nitrate-coupled iron oxidation to the removal of As, Zn and S, Water. Air. Soil Poll., 224, 1–15, 2013.

Matys Grygar, T., Mach, K., Schnabl, P., Pruner, P., Laurin, J., and Martinez, M.: A lacustrine record of the early stage of the Miocene Climatic Optimum in Central Europe from the Most Basin, Ohře (Eger) Graben, Czech Republic, Geol. Mag., 151, 1013–1033, 2014.

McCullough, C. D. and Schultze, M.: Engineered river flow-through to improve mine pit lake and river values, Sci. Total Environ., 640–641, 217–231, https://doi.org/10.1016/J.SCITOTENV.2018.05.279, 2018.

Meyer, K. M. and Kump, L. R.: Oceanic euxinia in Earth history: Causes and consequences, Annu. Rev. Earth Planet. Sc., 36, 251–288, 2008.

Medová, H., Přikryl, I., Zapomnělová, E., and Pechar, L.: Effect of Postmining waters on cyanobacterial photosynthesis, Water Environ. Res., 87, 180–190, 2015.

Michiels, C. C., Darchambeau, F., Roland, F. A. E., Morana, C., Llirós, M., García-Armisen, T., Thamdrup, B., Borges, A. V., Canfield, D. E., Servais, P., Descy, J. P., and Crowe, S. A.: Iron-dependent nitrogen cycling in a ferruginous lake and the nutrient status of Proterozoic oceans, Nat. Geosci., 10, 217–221, https://doi.org/10.1038/ngeo2886, 2017.

Murad, E. and Rojík, P.: Iron-rich precipitates in a mine drainage environment: Influence of pH on mineralogy, Am. Mineral., 88, 1915–1918, 2003.

Murad, E. and Rojík, P.: Iron mineralogy of mine-drainage precipitates as environmental indicators: review of current concepts and a case study from the Sokolov Basin, Czech Republic, Clay Miner., 40, 427–440, 2005.

Mußmann, M., Brito, I., Pitcher, A., Damsté, J. S. S., Hatzenpichler, R., Richter, A., Nielsen, J. L., Nielsen, P. H., Müller, A., Daims, H., Wagner, M., and Head, I. M.: *Thaumarchaeotes* abundant in refinery nitrifying sludges express amoA but are not obligate autotrophic ammonia oxidizers, P. Natl. Acad. Sci. USA, 108, 16771, https://doi.org/10.1073/pnas.1106427108, 2011.

Myers, C. R. and Nealson, K. H.: Microbial reduction of manganese oxides: Interactions with iron and sulfur, Geochim. Cosmochim. Acta, 52(11), 2727–2732, doi:10.1016/0016-7037(88)90041-5, 1988.

Namgung, S., Guo, B., Sasaki, K., Lee, S. S., and Lee, G.: Macroscopic and microscopic behaviors of Mn(II) (ad)sorption to goethite with the effects of dissolved carbonates under anoxic conditions, Geochim. Cosmochim. Ac., 277, 300–319, 2020.

Northup, D. E., Barns, S. M., Yu, L. E., Spilde, M. N., Schelble, R. T., Dano, K. E., Crossey, L. J., Connolly, C. A., Boston, P. J., Natvig, D. O., and Dahm, C. N.: Diverse microbial communities inhabiting ferromanganese deposits in Lechuguilla and Spider Caves, Environ. Microbiol., 5, 1071–1086, https://doi.org/10.1046/j.1462-2920.2003.00500.x, 2003.

Noseck, U., Brasser, T., Rajlich, P., Laciok, A., and Hercik, M.: Mobility of uranium in tertiary argillaceous sediments – A natural analogue study, Radiochim. Acta, 92, 797–803, 2004.

Oude Elferink, S. J. W. H., Akkermans-van Met, W, M., Bogte, J. J., and Stams, A. J. M.: *Desulfobacca acetoxidans* gen. nov., sp. nov., a novel acetate-degrading sulfate reducer isolated from sulfidogenic granular sludge, Int. J. Syst. Bacteriol., 49, 345–350, 1999.

Pačes, T. and Šmejkal, V.: Magmatic and fossil components of thermal and mineral waters in the Eger River continental rift (Bohemian massif, central Europe), in: Water-Rock Interaction, Proc. 11th International Symposium, edited by: Wanty, R. B. and Seal II, R. R., Taylor and Francis Group, London, 167–172, 2004.

Pellerin, A., Antler, G., Holm, S. A., Findlay, A. J., Crockford, P. W., Turchyn, A. V., Jørgensen, B. B., and Finster, K.: Large sulfur isotope fractionation by bacterial sulfide oxidation, Sci. Adv., 5, eaaw1480, https://doi.org/10.1126/sciadv.aaw1480, 2019.

Petrash, D. A., Gingras, M. K., Lalonde, S. V., Orange, F., Pecoits, E., and Konhauser, K. O.: Dynamic controls on accretion and lithification of modern gypsum-dominated thrombolites, Los Roques, Venezuela, Sediment. Geol., 245–246, 29–47, 2012.

Petrash, D. A., Gueneli, N., Brocks, J. J., Méndez-Dot, J. A., González-Arismendi, G., Poulton, S. W., and Konhauser, K. O.: Black shale deposition and early diagenetic dolomite cementation during Oceanic Anoxic Event 1: The mid-Cretaceous Maracaibo Platform, Northwestern South America, Am. J. Sci., 316, 669–711, 2016.

Petrash, D. A., Jan, J., Sirová, D., Osafo, N. O.-A., and Borovec, J.: Iron and nitrogen cycling, bacterioplankton community composition and mineral transformations involving phosphorus sta-

bilisation in the ferruginous hypolimnion of a post-mining lake, Environ. Sci.-Proc. Imp., 20, 1414–1426, 2018.

Petrash, D. A., Bialik, O. M., Staudigel, P. T., Konhauser, K. O., and Budd, D. A.: Biogeochemical reappraisal of the freshwater–seawater mixing-zone diagenetic model, Sedimentology, 68, 1797–1830, 2021.

Petrash, D. A. Steenbergen, I. M., Valero, A., Meador, T. B., Lalonde, S. V., and Thomazo, C.: Disentangling the overlapping zonation of dissimilatory iron and sulfate reduction in a carbonate-buffered sulfate-rich and ferruginous lake water column, Geophys. Res. Abstr., EGU22-183, EGU General Assembly 2022, Vienna, Austria, 2022.

Philippot, P., Van Kranendonk, M., Van Zuilen, M., Lepot, K., Rividi, N., Teitler, Y., Thomazo, C., Blanc-Valleron, M. M., Rouchy, J. M., Grosch, E., and de Wit, M.: Early traces of life investigations in drilling Archean hydrothermal and sedimentary rocks of the Pilbara Craton, Western Australia and Barberton Greenstone Belt, South Africa, C. R. Palevol., 8, 649–663, 2009.

Phillips, D. L. and Gregg, J. W.: Uncertainty in source partitioning using stable isotopes, Oecologia, 127, 171–179, 2001.

Piwosz, K., Shabarova, T., Pernthaler, J., Posch, T., Šimek, K., Porcal, P., and Salcher, M. M.: Bacterial and Eukaryotic Small-Subunit Amplicon Data Do Not Provide a Quantitative Picture of Microbial Communities, but They Are Reliable in the Context of Ecological Interpretations, mSphere 5, e00052-20 https://doi.org/10.1128/mSphere.00052-20, 2020.

Post, J. and Bish, D.: Rietveld refinement of crystal structures using powder X-ray diffraction data, Rev. Mineral. Geochem., 20, 277–308, 1989.

Posth, N. R., Canfield, D. E., and Kappler, A.: Biogenic Fe(III) minerals: From formation to diagenesis and preservation in the rock record, Earth-Sci. Rev., 135, 103–121, 2014.

Poulton, S. W. and Canfield, D. E.: Development of a sequential extraction procedure for iron: Implications for iron partitioning in continentally derived particulates, Chem. Geol., 214, 209–221, 2005.

Poulton, S. W. and Canfield, D. E.: Ferruginous Conditions: A Dominant Feature of the Ocean through Earth's History, Elements, 7, 107–112, 2011.

Poulton, S. W., Krom, M. D., and Raiswell, R.: A revised scheme for the reactivity of iron (oxyhydr)oxide minerals towards dissolved sulfide, Geochim. Cosmochim. Ac., 68, 3703–3715, 2004.

Rapantová, N., Krzeszowski, Ś., Grmela, A., and Wolkersdorfer, C.: Quantitative Assessment of Mine Water Sources Based on the General Mixing Equation and Multivariate Statistics, Mine Water Environ., 31, 252–265, 2012.

Rasmussen, B., Krapež, B., Muhling, J. R., and Suvorova, A.: Precipitation of iron silicate nanoparticles in early Precambrian oceans marks Earth's first iron age, Geology, 43, 303–306, 2015.

Reershemius, T. and Planavsky, N. J.: What controls the duration and intensity of ocean anoxic events in the Paleozoic and the Mesozoic?, Earth-Sci. Rev., 221, 103787, https://doi.org/10.1016/j.earscirev.2021.103787, 2021.

Rennie, V. C. F. and Turchyn, A. V.: The preservation of $\delta^{34}S_{SO_4}$ and $\delta^{18}O_{SO_4}$ in carbonate-associated sulfate during marine diagenesis: A 25 Myr test case using marine sediments, Earth Planet. Sc. Lett., 395, 13–23, 2014.

Rickard, D. and Morse, J. W.: Acid volatile sulfide (AVS), Mar. Chem., 97, 141–197, 2005.

Rognes, T., Flouri, T., Nichols, B., Quince, C., and Mahé, F.: VSEARCH: a versatile open-source tool for metagenomics, PeerJ, 4, e2584, https://doi.org/10.7717/peerj.258, 2016.

Robertson, E. K. and Thamdrup, B.: The fate of nitrogen is linked to iron(II) availability in a freshwater lake sediment, Geochim. Cosmochim. Ac., 205, 84–99, 2017.

Rodríguez-Ruiz, I., Van Driessche, A. E. S., Veesler, S., García-Ruiz, J. M., and IUCr: Nucleation of gypsum at low supersaturations, Acta Crystallogr. A, 67, 461–462, https://doi.org/10.1107/S0108767311088386, 2011.

Rosenbaum, J. and Sheppard, S. M. F.: An isotopic study of siderites, dolomites and ankerites at high temperatures, Geochim. Cosmochim. Ac., 50, 1147–1150, 1986.

Salcher, M. M.: Same but different: Ecological niche partitioning of planktonic freshwater prokaryotes, J. Limnol., 73, 74–87, 2014.

Scholz, F.: Identifying oxygen minimum zone-type biogeochemical cycling in Earth history using inorganic geochemical proxies, Earth-Sci. Rev., 184, 29–45, 2018.

Scholz, F. and Neumann, T.: Trace element diagenesis in pyrite-rich sediments of the Achterwasser lagoon, SW Baltic Sea, Mar. Chem., 107, 516–532, 2007.

Schoonen, M.: Mechanisms of sedimentary pyrite formation, in: Sulfur biogeochemistry – Past and present, Geological Society of America Special Paper 379, edited by: Amend, J. P., Edwards, K. J., and Lyons, T. W., Geological Society of America, Boulder, Colorado, 117–134, https://doi.org/10.1130/0-8137-2379-5.117, 2004.

Schultze, M., Pokrandt, K. H., and Hille, W.: Pit lakes of the Central German lignite mining district: Creation, morphometry and water quality aspects, Limnologica, 40, 148–155, 2010.

Simon, B., Bienfait, M., and IUCr: Structure et mécanisme de croissance du gypse, Acta Cryst., 19, 750–756, 1965.

Slomp, C. P., Malschaert, J. F. P., Lohse, L., and Van Raaphorst, W.: Iron and manganese cycling in different sedimentary environments on the North Sea continental margin, Cont. Shelf Res., 17, 1083–1117, 1997.

Šmejkal, V.: Oxygen isotopic composition of sulphates from some mineral waters and mine waters in western Bohemia, in: Isotope hydrology, 1978: Proceedings of IAEA, Vienna, International symposium on isotope hydrology; Neuherberg, Germany, 19–23 June 1978, IAEA-SM-228/4, 83–97, ISBN 92-0-040179-1, 1978.

Šmejkal, V.: Isotopic composition of carbonates and differences in deposition environment during the Miocene lacustrine sedimentation in the Krusne Hory graben, Zentralinstitut für Isot. und Strahlenforschung, Leipzig, 84, 372–379, ISSN 0323-8776, 1984.

Soetaert, K., Hofmann, A. F., Middelburg, J. J., Meysman, F. J. R., and Greenwood, J.: The effect of biogeochemical processes on pH, Mar. Chem., 105, 30–51, 2007.

Spilde, M. N., Northup, D. E., Boston, P. J., Schelble, R. T., Dano, K. E., Crossey, L. J., and Dahm, C. N.: Geomicrobiology of cave ferromanganese deposits: A field and laboratory investigation, Geomicrobiol. J., 22, 99–116, https://doi.org/10.1080/01490450590945889, 2005.

Starke, R., Müller, M., Gaspar, M., Marz, M., Küsel, K., Totsche, K. U., von Bergen, M., and Jehmlich, N.: *Candidate* Brocadiales dominates C, N and S cycling in anoxic groundwater of a

pristine limestone-fracture aquifer, J. Proteomics, 152, 153–160, https://doi.org/10.1016/j.jprot.2016.11.003, 2017.

Sun, B., Cole, J. R., and Tiedje, J. M.: *Desulfomonile limimaris* sp. nov., an anaerobic dehalogenating bacterium from marine sediments, Int. J. Syst. Evol. Microbiol., 51, 365–371, 2001.

Swanner, E. D., Lambrecht, N., Wittkop, C., Harding, C., Katsev, S., Torgeson, J., and Poulton, S. W.: The biogeochemistry of ferruginous lakes and past ferruginous oceans, Earth-Sci. Rev., 211, 103430, https://doi.org/10.1016/j.earscirev.2020.103430, 2020.

Taylor, B. E., Wheeler, M. C., and Nordstrom, D. K.: Isotope composition of sulphate in acid mine drainage as measure of bacterial oxidation, Nature, 308, 538–541, 1984a.

Taylor, B. E., Wheeler, M. C., and Nordstrom, D. K.: Stable isotope geochemistry of acid mine drainage: Experimental oxidation of pyrite, Geochim. Cosmochim. Ac., 48, 2669–2678, 1984b.

Tebo, B. M., Johnson, H. A., McCarthy, J. K., and Templeton, A. S.: Geomicrobiology of manganese(II) oxidation, Trends Microbiol., 13, 421–428, 2005.

Thamdrup, B., Finster, K., Hansen, J. W., and Bak, F.: Bacterial disproportionation of elemental sulfur coupled to chemical reduction of iron or manganese, Appl. Environ. Microb., 59, 101–108, https://doi.org/10.1128/aem.59.1.101-108.1993, 1993.

Thomazo, C., Brayard, A., Elmeknassi, S., Vennin, E., Olivier, N., Caravaca, G., Escarguel, G., Fara, E., Bylund, K. G., Jenks, J. F., Stephen, D. A., Killingsworth, B., Sansjofre, P., and Cartigny, P.: Multiple sulfur isotope signals associated with the late Smithian event and the Smithian/Spathian boundary, Earth-Sci. Rev., 195, 96–113, 2019.

Toran, L. and Harris, R. F.: Interpretation of sulfur and oxygen isotopes in biological and abiological sulfide oxidation, Geochim. Cosmochim. Ac., 53, 2341–2348, 1989.

Trettin, R., Gläser, H. R., Schultze, M., and Strauch, G.: Sulfur isotope studies to quantify sulfate components in water of flooded lignite open pits – Lake Goitsche, Germany, Appl. Geochem., 22, 69–89, 2007.

Ulrych, J., Dostal, J., Adamović, J., Jelínek, E., Špaček, P., Hegner, E., and Balogh, K.: Recurrent Cenozoic volcanic activity in the Bohemian Massif (Czech Republic), Lithos, 123, 133–144, 2011.

Umbría-Salinas, K., Valero, A., Jan, J., Borovec, J., Chrastný, V., and Petrash, D. A.: Redox-driven geochemical partitioning of metal(loid)s in the iron-rich anoxic sediments of a recently flooded lignite mine pit: Lake Medard, NW Czechia, J. Hazard. Mater. Adv., 3, 100009, https://doi.org/10.1016/j.hazadv.2021.100009, 2021.

van der Voort, E. and Hartman, P.: The habit of gypsum and solvent interaction, J. Cryst. Growth, 112, 445–450, 1991.

Van Der Zee, C. and Van Raaphorst, W.: Manganese oxide reactivity in North Sea sediments, J. Sea Res., 52, 73–85, 2004.

van de Velde, S. J., Reinhard, C. T., Ridgwell, A., and Meysman, F. J. R.: Bistability in the redox chemistry of sediments and oceans, P. Natl. Acad. Sci. USA, 117, 33043–33050, 2021.

Viollier, E., Jézéquel, D., Michard, G., Pèpe, M., Sarazin, G., and Alberic, P.: Geochernical study of a crater lake (Pavin Lake, France): Trace-element behaviour in the monimolimnion, Chem. Geol., 125, 61–72, 1995.

Waite, D. W., Chuvochina, M., Pelikan, C., Parks, D. H., Yilmaz, P., Wagner, M., Loy, A., Naganuma, T., Nakai, R., Whitman, W. B., Hahn, M. W., Kuever, J., and Hugenholtz, P.: Proposal to reclassify the proteobacterial classes Deltaproteobacteria and Oligoflexia, and the phylum Thermodesulfobacteria into four phyla reflecting major functional capabilities, Int. J. Syst. Evol. Micr., 70, 5972–6016, 2020.

Walter, X. A., Picazo, A., Miracle, M. R., Vicente, E., Camacho, A., Aragno, M., and Zopfi, J.: Phototrophic Fe(II)-oxidation in the chemocline of a ferruginous meromictic lake, Front. Microbiol., 5, 713, https://doi.org/10.3389/fmicb.2014.00713, 2014.

Wang, C. F., Fan, X., Zhang, F., Wang, S. Z., Zhao, Y. P., Zhao, X. Y., Zhao, W., Zhu, T. G., Lu, J. L., and Wei, X. Y.: Characterization of humic acids extracted from a lignite and interpretation for the mass spectra, RSC Adv., 7, 20677–20684, https://doi.org/10.1039/C7RA01497J, 2017.

Ward, L. M., Bertran, E., and Johnston, D. T.: Expanded Genomic Sampling of the Desulfobulbales Reveals Distribution and Evolution of Sulfur Metabolisms, Front. Microbiol., 12, 666052, https://doi.org/10.3389/fmicb.2021.666052, 2021.

Weber, K. A., Achenbach, L. A., and Coates, J. D.: Microorganisms pumping iron: Anaerobic microbial iron oxidation and reduction, Nat. Rev. Microbiol., 4, 752–764, 2006.

Weelink, S. A. B., Van Doesburg, W., Saia, F. T., Rijpstra, W. I. C., Röling, W. F. M., Smidt, H., and Stams, A. J. M.: A strictly anaerobic betaproteobacterium *Georgfuchsia toluolica* gen. nov., sp. nov. degrades aromatic compounds with Fe(III), Mn(IV) or nitrate as an electron acceptor, FEMS Microbiol. Ecol., 70, 575–585, 2009.

Weinlich, F. H., Bräuer, K., Kämpf, H., Strauch, G., Tesař, J., and Weise, S. M.: An active subcontinental mantle volatile system in the western Eger rift, Central Europe: Gas flux, isotopic (He, C, and N) and compositional fingerprints, Geochim. Cosmochim. Ac., 63, 3653–3671, 1999.

Wright, M. H., Geszvain, K., Oldham, V. E., Luther, G. W., and Tebo, B. M.: Oxidative formation and removal of complexed Mn(III) by *Pseudomonas* species, Front. Microbiol., 9, 560, https://doi.org/10.3389/fmicb.2018.00560, 2018.

Zerkle, A. L., Jones, D. S., Farquhar, J., and Macalady, J. L.: Sulfur isotope values in the sulfidic Frasassi cave system, central Italy: A case study of a chemolithotrophic S-based ecosystem, Geochim. Cosmochim. Ac., 173, 373–386, 2016.

Paper III

Anaerobic dissolved As(III) removal from metal-polluted waters by cathode-stabilized Fe(III)-oxyhydroxides

Valero A., Jan J., Petrash D. A.

PAPER

Anaerobic dissolved As(III) removal from metal-polluted waters by cathode-stabilized Fe(III)-oxyhydroxides†

Astolfo Valero, iD *[ab] Jiří Jan[a] and Daniel A. Petrash iD [ac]

A bioelectrochemical system (BES) to efficiently induce arsenite scavenging from anoxic waters is yet to be developed. Here we examined to what extent the presence of redox reactive humic substances derivatives and reactive nitrogen species interferes with the bioelectrochemically induced immobilization of As(III) by Fe(III) oxyhydroxides. Insights from extracellular electron transfer to insoluble minerals by a strain of *Geobacter* sp. were acquired and integrated with data from acetate utilization. We furthered our interpretations with *in situ* synchrotron-based analyses of experimentally precipitated biominerals. *Geobacter* sp. cells interacting with cathodes used oxidized humic substance derivatives as electron shuttles which fostered the partial reduction of Fe(III), thus promoting the scavenging of As(III) oxyanions. The oxyanions became immobilized in the reactive surfaces of FeOOH within mineral aggregates, where they were readily oxidized presumably as the result of related Fenton-like reactions. An experiment lacking humic derivatives fueled the formation of bacterial–mineral networks. These networks fostered short-range electron transfer mechanisms that initially promoted biotic amorphous ferrihydrite aggregation. The early ferrihydrite aggregates exhibited a decreased As(III) scavenging capacity. In the presence of both humic derivatives and ammonium, the proposed BES was proven more effective in removing As(III) from solution and despite elevated competing phosphate levels. In the presence of reactive N species alone, stabilization of Fe(III) and microbial attachment promoted Fe(II) scavenging which outcompeted As(III) from the available ligands in the reactive mineral surfaces. Improving mineral stabilization is deemed crucial for direct As(III)-sequestration in BESs. An optimized BES for As-removal would be beneficial not only for sequestering arsenite out of solution in geogenically polluted aqueous systems, but also for addressing the recurrent eutrophication of continental water bodies linked to seasonal phosphate solubilization.

Water impact

A bioelectrochemical system capable of dissolved arsenite removal performs by promoting Fe(III)-oxyhydroxide stabilization under anoxic (ferruginous) conditions. Arsenite is immobilized as arsenate through the involvement of electrochemically enhanced redox-reactive humic substances. They act as alternative electron shuttles during microbial Fe(III) reduction. Since the approach can be reengineered/redesigned to exploit natural microbial electroactive interactions, it has foreseeable relevance for sustainable metalloid decontamination of water bodies.

Introduction

Arsenic (As) could be at relatively high concentrations in aquatic environments exhibiting marked redox boundaries

[a] *Biology Centre of the Czech Academy of Sciences, Institute of Soil Biology and Biogeochemistry, Na Sádkách 7, 370 05 České Budějovice, Czech Republic. E-mail: astolfo.valero@bc.cas.cz*
[b] *University of South Bohemia, Department of Ecosystem Biology, Branisovská 1645/31a, 370 05 České Budějovice, Czech Republic*
[c] *Department of Environmental Geochemistry and Biogeochemistry, Czech Geological Survey, 152 00 Prague 5, Czech Republic*
† Electronic supplementary information (ESI) available. See DOI: https://doi.org/10.1039/d2ew00844k

such as waterlogged soils and sediments,[1,2] aquifers,[3] and meromictic lakes.[4] As toxicity decreases with increasing pH and Eh, as a reflection of its redox-sensitive nature.[5–7] Under anoxic conditions As occurs mainly as the oxyanion arsenite (As(III)), which is more mobile than arsenate (As(v)).[8,9] Although As(v) interferes with oxidative phosphorylation, As(III) is the most toxic As species under environmentally relevant conditions.[5] As(III) bioaccumulates as it has a longer half-life.[10] It readily reacts with thiol functional groups inactivating enzymes and causing protein misfolding and/or aggregation.[5] Observed symptoms of chronic intoxication in mammals include decreased motor coordination, nervous

454 | *Environ. Sci.: Water Res. Technol.*, 2023, **9**, 454–466

55

This journal is © The Royal Society of Chemistry 2023

disorders, respiratory distress, cardiovascular disease and damage to kidneys and the respiratory tract.[5,9]

Due to its large impact on human health, arsenic in groundwater has become a cause of concern in vast regions of South America,[11] Western Africa,[12] and Southern Asia,[13] where an admixture of geogenically As(III)-rich groundwater affects the surficial drinking water supplies. Advances in technological approaches aimed at directly scavenging As(III) from anoxic groundwater would help in mitigating the growing global concern that this metalloid poses. Methods capable of inducing As(III) (co) precipitation within biogenic minerals have been shown feasible for remediation purposes.[14,15] Among such methods are As(III) oxidation to As(v), As(v) co-precipitation and adsorption onto coagulated flocks, ion exchange, adsorption onto various solid media, and membrane filtration. These are, however, energy-intensive and external resource-demanding approaches.[16]

Bioelectrochemical systems (BESs) designed to immobilize metal pollutants by inducing biomineralization reactions on electrodes are among currently emerging, eco-friendly, and sustainable alternatives for direct As(III) removal. BESs rely on the ability of electroactive microorganisms (EAMs) to perform extracellular electron transfer (EET). This is a specialized microbial process that allows EAMs to produce or consume electrical currents by moving electrons to and from extracellular electron acceptors and donors.[17,18] Despite recent developments in BESs for As(III) removal (e.g., ref. 19–21), the role of EET in the abatement is still elusive. In addition, discrete respiration processes that may occur in parallel to EET to also promote aqueous redox transformations of key solid phases (e.g., mineral stabilization) remain unaccounted for (but see ref. 22).

Geobacter species comprise an archetypical group of EAMs capable of harvesting electrical currents from organic compounds. Their metabolic versatility allows them to couple a plethora of alternative extracellular electron donors and acceptors (TEA).[23,24] Among known preferred respiratory pathways of *Geobacter* spp. is the dissimilatory reduction of ferric iron (Fe(III)), which could in turn promote the stabilization of Fe(III) from amorphous hydrous oxyhydroxide precursors to more crystalline phases.[25,26] The more stable Fe(III) oxyhydroxides are known to immobilize As within their crystal arrays.[27–29] We hypothesize that as *Geobacter* spp.—and EAMs in general—mediate in Fe(III) mineral stabilization, they play a still unrecognized role in As(III) scavenging from anoxic waters. The rationale for this working hypothesis is that the microbially mediated stabilization of Fe(III) oxyhydroxides increases the availability of surface sorption sites capable of immobilizing As(III) from solution.[30] In this context, we believe it is important to achieve a broader mechanistic understanding on how the EET from EAM cells to iron minerals could be influenced by an alternative bioutilization of, for example, redox reactive humic substances during Fe(III) reduction.[31–33]

In a ferruginous meromictic lake, Lake Medard, NW Czechia, dissolution and biomineralization reactions encompassing dissolved iron and arsenic are potentially driven by EAMs. The lake bottom water column has an abundance of humic substance derivatives released during lignite degradation in the anoxic sediments.[34] Minor changes in the redox state of the water column affect As speciation and, at times augment the release of As from the sediments.[35] In this model site, arsenic and iron are rapidly cycled between the sediment–water interface and the aqueous redoxcline.[34,36] Another relevant feature that influences the cycling of iron and arsenic in Lake Medard is the coexistence of dissolved inorganic N species.[36] Changes in the dissolved water column N inventory can affect Fe(III) mineral transformations. The N-cycle directly impacts metal(loid) scavenging because the microbial respiration of inorganic nitrate (NO_3^-) and ammonium (NH_4^+) can be coupled to Fe(II) oxidation and Fe-ammox,[25] respectively.

Here we use a BES for modeling the Fe–As mineral dynamics, and the mechanisms by which EAMs indigenous to Lake Medard drive key aqueous redox transformations of iron minerals. Our interest is to explore the utilization of reactive humic substance derivatives as electron shuttles from cells to colloidal ferric iron phases, and to assess the effects that these derivatives have on EET, and, thus, indirectly on As(III) scavenging. For these purposes, we designed a proof-of-concept bioelectrochemical experiment containing Medard-based environmentally relevant concentrations of humic substances and NO_3^- and NH_4^+, here collectively referred to as reactive N species (RNS). To consider the intertwining of Fe(III) mineral stabilization and As(III) scavenging, our experiments evaluated: (i) EET from cells to newly formed Fe(III) minerals; (ii) ferric iron biomineralization and transformations; (iii) the extent by which EET induces As(III) removal from solution associated with secondary Fe(III) oxyhydroxide stabilization; and (iv) the involvement of electroactive bacterial cells colonizing our working electrodes. Results from this work offer insights on factors that depending on particular environmental circumstances need to be weighted when designing a BES system for direct As(III)-sequestration. Implications of our observations for an eventual scaling-up and real-life implementation of a BES for scavenging As(III) in natural systems are discussed. In addition, this study offers insight on generalized microbe–mineral-scale processes that may occur at the reactive surface of organic Fe(III)-mineral aggregates when these are in transit from redox stratified water columns to prevalently anoxic sediment–water interfaces.

Methods

All experimental solutions and sterile growth media were prepared by utilizing chemicals of analytical grade provided by Merck (Germany) or VWR (Germany), and deionized water (18.2 MΩ cm^{-1}, Millipore, Germany). Glassware and materials

were acid-cleaned (HCl, 10% v/v) and sterilized by either autoclaving or UV light. In order to ensure anaerobic conditions, the experimental solutions were purged for 30 minutes with N_2 prior to their use, while all procedures were performed under an N_2 atmosphere ($O_2 < 1.5$ μg L^{-1}) inside an anaerobic chamber (Coy, USA).

Model site

The post-mining Lake Medard (NW Czech Republic, Fig. S1†) is oligotrophic and displays meromictic conditions in its deepest areas. This lake features a dysoxic hypolimnion below ca. 44 to 48 m depth, and a chemically differentiated anoxic ferruginous monimolimnion with high dissolved sulfate concentrations (19 ± 2 mM), but low dissolved hydrogen sulfide contents (<0.3 μM).[36] As in other similar settings, in Lake Medard the internal Fe cycling is largely driven by coupled nitrogen- and sulfur-utilizing species interactions. The planktonic prokaryote community includes a significant abundance of EAMs (among others *Geobacter* spp. and *Rhodoferax* spp.).[34,36] In addition, the anoxic lake sediments exhibit As enrichment into easily reducible and highly crystalline Fe(III) oxyhydroxides.[35]

In November 2019, the redox stratified bottom water column at the central area of Lake Medard was characterized by using a multiparameter sonde (6600 V2-2, YSI, USA). This was followed by bottom water sampling for cation and anion concentration analyses.[34] Results from these analyses guided the preparation of electrolyte solutions featuring environmentally relevant hydrochemistry that considers the measured bottom water dissolved As and Fe concentrations, as well as its conductivity and dissolved acetate and RNS levels. These experimental solutions were used to evaluate the feasibility of a BES for directly sequestering As(III) from the anoxic portion of the Lake Medard bottom water column (Fig. S2†).

Bioelectrocatalysis of Fe(III) oxyhydroxides

Synthetic ferruginous solutions (FS) contained 1200 μM Fe(II), 70 μM Fe(III), as freshly synthesized 2-line ferrihydrite ($5Fe_2O_3 \cdot 9H_2O$) (prepared by following ref. 37), and 10 μM As(III). Dissolved iron and arsenic concentrations were magnified 40× (those measured at the monimolimnion) and were consistent with calculated distribution coefficients between the monimolimnion and sediments (S1.2, Fig. S3†).

To aliquots of the synthetic ferruginous solution described above, we added amendments of 40 μM NO_3^-, 140 μM NH_4^+ and/or 800 μM of humic acids (HAs). Environmentally relevant dissolved concentrations of these species followed the values reported by Petrash et al.[36] The HAs were extracted from a leonardite standard (IHSS, USA) by following Swift.[38] This mineraloid is among the main oxidative breakdown products of lignite.[39] Dissolved breakdown products of lignite are thought to be present in the bottom waters of Lake Medard[34,36] (S1.3, Table S1†). The conductivities of our

experimental solutions were in the range of 7854 ± 335 μS cm^{-1}, also resembling the model lake system. To maintain a circumneutral pH during our experiments we used a phosphate buffer.

Replicate reaction vessels (100 mL, $n = 12$) contained the experimental solutions and a three-electrode setup. This three-electrode setup consisted of an Ag/AgCl 3 M KCl reference electrode (+197 mV *vs.* SHE, Metrohm, Switzerland), and graphite working and counter electrodes (CP Handels, Germany). The graphite electrodes were constructed following Scarabotti et al.[40] and had surface areas of 3.2 and 4.2 cm^2, respectively. All potentials provided hereafter refer to the Ag/AgCl 3 M KCl reference electrode (unless otherwise stated). Assessable Fe–As mineral transformations were fostered by posing the working electrodes at −500 mV by using a multichannel potentiostat (Dropsens μStat 8000, Metrohm, Spain) in chronoamperometric mode, and with currents being recorded every 10 minutes for 48 hours. This electric potential is known to promote both electrotrophic metabolism in *Geobacter* spp.,[41] and reductive dissolution of Fe(III) oxyhydroxides (*e.g.*, ref. 42). The latter being a key process controlling the aqueous As dynamics in our model site.[35]

Three different chronoamperometric assays were performed in triplicate. Biotic assays were performed by inoculating into the reaction vessels actively growing *Geobacter* sp. cells (DSM 11489, S1.1†). To this set of experiments we added 5 mM acetate as an additional carbon source. The inoculated experiments were labeled as follows:

- Experiment A: synthetic ferruginous solutions as described above, amended with RNS and humic substance derivatives extracted from leonardite (biotic FS + HAs + RNS);
- Experiment B: our synthetic ferruginous solutions amended with HAs only (biotic FS + HAs)
- Experiment C: our synthetic ferruginous solution amended with RNS only (biotic FS + RNS).

In addition, a triplicate Experiment D (abiotic FS + HAs + RNS) consisted of an abiotic control of Experiment A.

Samples for dissolved Fe and As concentration analyses were collected at different timespans (0, 1, 4, 12, 24, and 48 hours), filtered (0.45 μm, Whatman®), and acidified (1% v/v) with 2 M trace grade HNO_3. The filters were dried and maintained inside a desiccator under a N_2 atmosphere until solid-phase analyses. In addition, filtered, un-acidified aliquots for acetate, nitrite (NO_2^-), NO_3^-, NH_4^+, and phosphate (PO_4^{3-}) concentration measurements were retrieved at 0, 12, and 24 hours. The samples were freeze-stored (−18 °C) until further analysis.

Chemical analyses

Dissolved Fe and As concentrations from the bioelectrochemical assays were determined by using a Triple Quadrupole ICP-MS (Agilent 8800, USA). The anion contents were determined by using a Dionex ICS-5000 Ion Chromatographer (Thermo Scientific, Germany). The

analytical conditions were described by Petrash *et al.*[34] Both instruments are housed in the BC-CAS in České Budějovice, Czech Republic. Reproducibility of triplicate analyses and an analytical standard measured prior to and after the samples was better than 10% and 20% of the reported values for cations and anions, respectively.

Solid phase analyses

Graphite electrodes were maintained inside a silica desiccator and under a N_2 atmosphere after the shutdown of all electronic connections. Shortly after the end of the experiments, sliced pieces of the graphite electrodes were examined using a field emission JSM 7401-F (JEOL, Japan). We analyzed our working electrodes by scanning electron microscopy (SEM) to obtain insight on the textural and mineral features of surficial precipitates. Spatially resolved synchrotron-based X-ray fluorescence (μ-XRF), angle-resolved diffraction (μ-XRD), and absorption (μ-XAS) were also performed to further characterize synthetic solid phases formed on the surface of the graphite working electrode, and in filtrates from the solution. The latter particles were collected using 0.45 μm quantitative filters (Whatman®, No. 44). The samples were packed and sealed under anoxic conditions and kept so until analyses took place at the MicroXAS beamline (Swiss Light Source, Villigen, Switzerland). At MicroXAS, we determined: (i) the spatial association of Fe and As in the precipitated solid phases; (ii) the mineralogy of the aggregates formed onto electrode surfaces; and (iii) the oxidation state of As and the local bonding environment at the sorption sites of the precipitates. Further information about instrumental and analytical conditions can be found in the ESI† (S1.4).

Statistical analyses

The Shapiro–Wilk test, at the 95% significance level, was used to evaluate the normality of data distribution. Data were normalized by using $\log(x)$ transformation. Statistically relevant differences for each chronoamperometric assay were assessed by *t*-tests ($p < 0.05$) for (i) Fe and As interlinked mineral dynamics and (ii) RNS changes between the different experimental timespans (0, 1, 4, 12, 24, and 48 hours) of each chronoamperometric assay. Data processing was performed with the software R Foundation for Statistical Computing (Vienna, Austria; R Core Team, 2016).

Results

Fe(III) oxyhydroxides bioelectrocatalysis

Cathodic currents were generated for 48 h to induce a reductive milieu with the locus at the cathode surfaces (Fig. 1). The reductive current densities ranged from −10 μA cm^{-2} to −20 μA cm^{-2} (Fig. 1, Exp. A–D). Striking differences in current densities were not observed among biotic and sterile (abiotic) assays. The latter observation points to reactions involving ionic redox species present in solution but not EAM
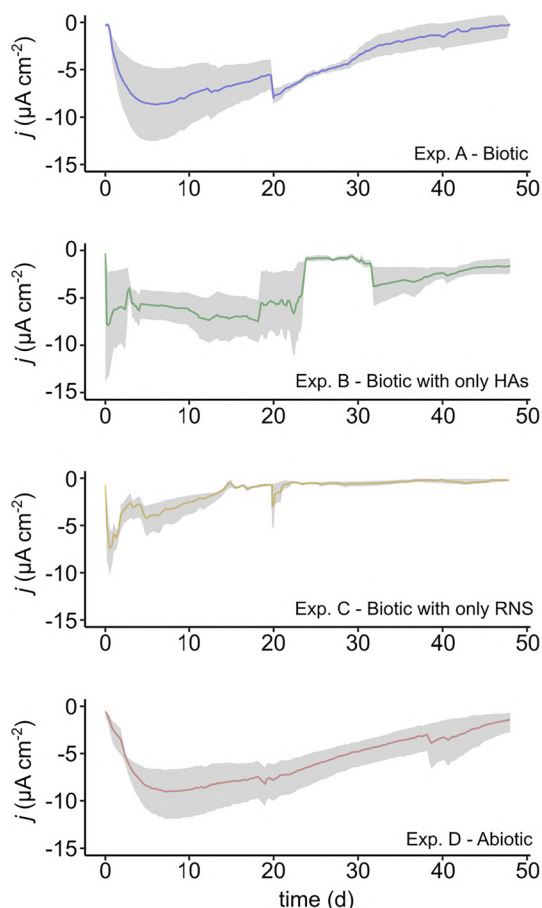
Fig. 1 Cathodic currents recorded after poising the working graphite rod electrodes at −500 mv (*vs.* Ag/AgCl reference electrodes) for 48 h in our discrete chronoamperometric assays, *i.e.*: (1) synthetic ferruginous solutions amended with both reactive nitrogen species (RNS) and humic acid derivatives (HAs; Exp. A); (2) synthetic ferruginous solutions with HAs, but lacking RNS (Exp. B); (3) synthetic ferruginous solutions with RNS and no HAs added (Exp. C); and (4) abiotic control of Exp. A (Exp. D). Colored lines indicate average current densities with grey shadows portraying their standard error.

cells as the main electron sinks.[41] Under our experimental conditions, however, it is difficult to distinguish which specific ionic species were being electrochemically reduced given that the applied electric potential does not only fuel vigorous microbe–electrode interactions,[41] but can also reduce nitrate[43] and/or oxidize HAs[44] also in solution. To shed further light on the nature of redox reactions, we therefore quantified changes in the chemical composition of the solutions during the experiments.

The initial concentrations of ferrous iron (Fe(II)) and As(III), *i.e.*, 1.2 mM and 10 μM, respectively, decreased to <0.4 mM, and <9 μM after a few minutes from the start of the experiments (Table 1). In parallel, the buffering PO_4^{3-} capacity of the solutions decreased between 12% and 40% (Fig. S4†). As the experiments proceeded, however, the Fe–As dynamics at the solutions appeared to have been more strongly controlled by electrochemically induced reactions, and especially by the availability of TEAs other than Fe(III),

Table 1 Dissolved ferrous iron (Fe(II)) and arsenite (As(III)) concentrations, and related standard errors (SE), determined in triplicate experimental solutions for 48 h in our discrete chronoamperometric assays, *i.e.*: (1) synthetic ferruginous solutions amended with both humic acid derivatives (HAs) and reactive nitrogen species (RNS; Exp. A); (2) synthetic ferruginous solutions amended with only HAs (Exp. B); (3) synthetic ferruginous solutions with only RNS (Exp. C); and (4) abiotic control of Exp. A (Exp. D)

Time (h)	Experiment A				Experiment B				Experiment C				Experiment D			
	Fe (mM)	SE	As (μM)	SE	Fe (mM)	SE	As (μM)	SE	Fe (mM)	SE	As (μM)	SE	Fe (mM)	SE	As (μM)	SE
0	0.38	0.03	8.7	0.7	0.34	0.04	9.6	1.1	0.26	0.02	10.7	0.9	0.28	0.03	7.4	0.8
1	0.35	0.05	9.1	0.8	0.08	0.02	8.8	0.4	0.26	0.04	10.2	1.7	0.33	0.03	8.5	0.8
4	0.63	0.03	9.7	0.8	0.04	0.01	10.8	1.8	0.19	0.01	9.8	0.8	0.33	0.03	7.2	0.7
12	0.80	0.01	7.9	0.9	0.07	0.01	9.3	0.4	0.18	0.01	9.6	0.7	0.51	0.05	6.1	0.9
24	0.15	0.01	9.4	1.1	0.07	0.005	9.0	0.3	0.12	0.02	10.1	1.3	0.45	0.04	9.5	0.9
48	0.10	0.002	6.9	0.3	0.13	0.001	10.4	0.9	0.12	0.01	9.7	0.7	0.64	0.06	12.3	1.2
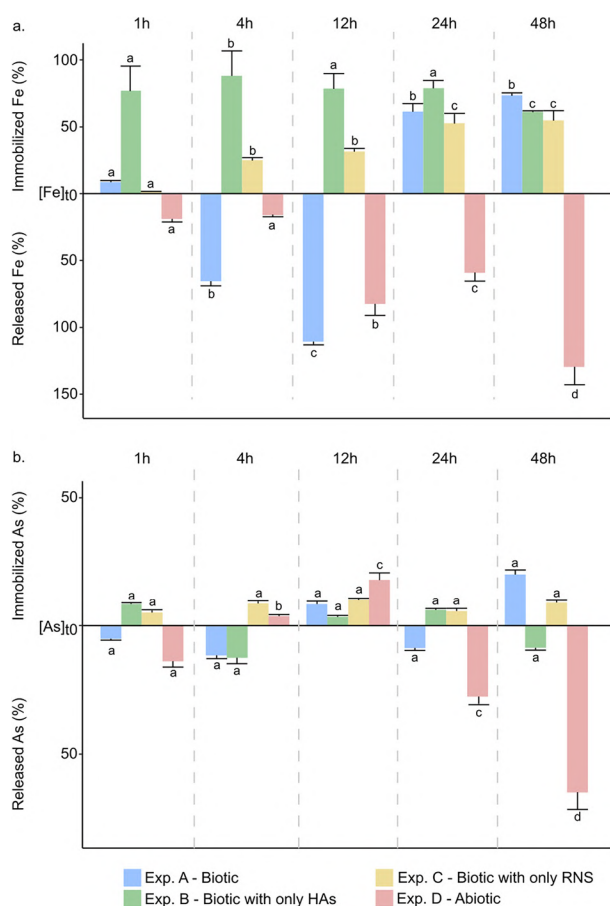
Fig. 2 Iron-linked arsenic transformations (*i.e.*, Fe(III) reductive dissolution and/or Fe(III)-oxyhydroxide precipitation) based on elemental concentrations of (a) iron and (b) arsenic at $t = 0$ h (black solid line). Values above this base-line indicate metal(loid) immobilization and values below the base-line indicate elemental solubilization (%). Concentrations were determined at $t = 1, 4, 12, 24,$ and 48 h during chronoamperometric assays: (1) synthetic ferruginous solutions amended with both RNS and HAs (Exp. A); (2) synthetic ferruginous solutions with HAs, but lacking RNS (Exp. B); (3) synthetic ferruginous solutions with RNS and no HAs added (Exp. C); and (4) an abiotic control of an experiment (Exp. D). Error bars are standard error based on replicate analyses. Statistical differences for experimental timespans (0, 1, 4, 12, 24, and 48 hours) were compared by the *t*-test for each chronoamperometric assay. Equal letters above bars indicate that there was no significant difference ($p > 0.05$), but different letters highlight significant differences ($p < 0.05$).

which may outcompete the latter in non-metabolic binding reactions, for example, HAs derived from leonardite and their quinone derivatives (Fig. 2).

In order to further explore this latter possibility, we evaluated variations in Fe and As contents as our chronoamperometric assays proceed (Fig. 2). This assessment considered the remaining Fe(II) and As(III), *i.e.* <0.4 mM and <9 μM, as the actual starting concentrations. The variations provided insight on the extent of Fe–As immobilization, *i.e.* arsenic coprecipitation with iron-bearing minerals, and/or released back to the solution as the result of reductive Fe(III) dissolution. In inoculated assays containing both RNS and HAs, higher As scavenging was attained within 12 to 48 h; linked to immobilization into newly formed Fe(III) phases (Fig. 2, Exp. A). No significant ($p > 0.05$) dissolved concentration differences were appreciable within this period. Most Fe immobilization occurred shortly after 24 h ($p < 0.05$). Previously, Fe(II) appeared to rather be released. The release of Fe(II) seemed to be fueled by the presence of HAs.[25]

Indeed, after 12 h the biotic assays containing HAs but no RNS showed an up to 18% increase in Fe(II) sourced out of the reductive dissolution of the solid Fe(III) initially immobilized as oxyhydroxide (Fig. 2, Exp. B). These latter experiments also displayed minimum As scavenging (4 to 6%, $p < 0.05$). Conversely, in experiments lacking HAs but containing RNS, dissolved Fe(II) increased by up to 50% at the end of the experiments ($p < 0.05$, Fig. 2, Exp. C). Also in these latter experiments, no striking change in As immobilization was observed and it remained at *ca.* 10% less than the initial value ($p > 0.05$). From these results, we portrayed a key HA role in the observed reductive Fe(III) dissolution. This is a bioinorganic role but not an EAM-mediated since ferrous iron was also released in abiotic control experiments (Fig. 2, Exp. D).

Substrate and reactive nitrogen species utilization

The presence of RNS significantly favors the immobilization of Fe(II) (Fig. 2, Exp. C). This was not an unexpected result since NO_3^- acting as a TEA can sustain EAM–electrode interactions that, in the presence of dissolved Fe(II), could advance our experiments in that direction.[41] To further

458 | *Environ. Sci.: Water Res. Technol.*, 2023, **9**, 454–466

This journal is © The Royal Society of Chemistry 2023

59
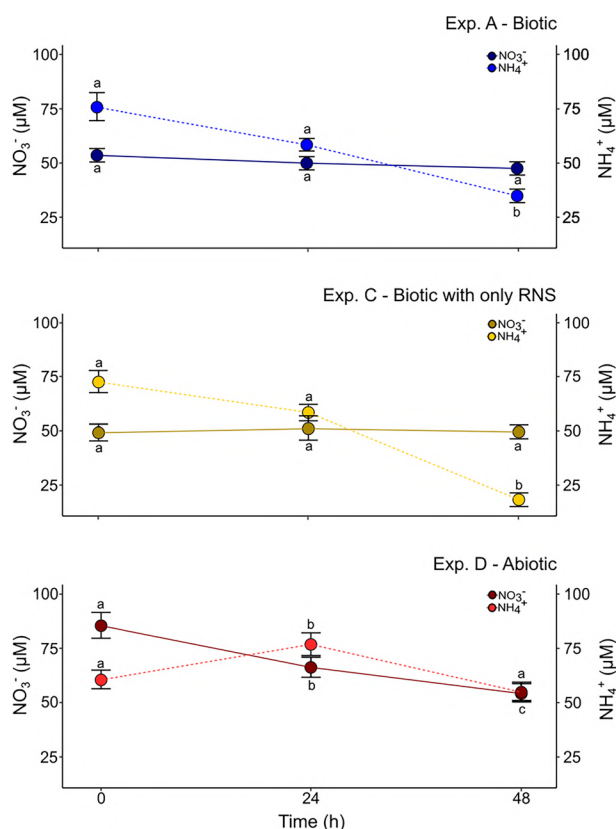
Fig. 3 Reactive nitrogen contents (NO_3^-, solid line; and NH_4^+, dashed line) measured at t = 0, 24, and 48 h as the chronoamperometric assays proceeded: (1) synthetic ferruginous solutions amended with both RNS and HAs (Exp. A); (2) synthetic ferruginous solutions with RNS and no HAs added (Exp. C); and (3) an abiotic control of Exp. A (Exp. D). Experimental/analytical standard errors are shown. Statistical differences for experimental timespans (0, 12, and 24 hours) were compared by the t-test for each chronoamperometric assay. Different letters above bars indicate significant differences ($p < 0.05$), while equal letters show no significant difference ($p > 0.05$).

explore the extent of this response, we quantified changes in RNS concentrations as the experiments proceeded. Contrary to what was anticipated, in biotic experiments the NO_3^- levels remained invariable within analytical error and with no significant differences between them (Fig. 3, Exp. A and C). However, we consistently recorded a sharp decrease in NH_4^+ levels ($p < 0.05$) which could either be indicative of concomitant anoxic ammonium oxidation[45] or point to microbial N-assimilation.[46] The unexpected result probably points to an abiotic reaction leading to dinitrogen (N_2) production at the positively poised counter electrode surfaces because our experimental NH_4^+ contents also decreased significantly in abiotic assays after 24 h (*cf.* ref. 47; Fig. 3, Exp. D). Dinitrogen production is also supported by the fact that all of our chronoamperometric assays showed NO_2^- contents below detection limits (<0.1 μM). Microbial involvement, however, appeared to be somehow needed to avoid any further NO_3^- reduction because non-inoculated assays showed only minor NO_3^- reduction in the initial 24 h (Fig. 3, Exp. D). The EAM-cathode-dissolved Fe(ɪɪ)

interactions, and the presumably concomitant microbial N-utilization drove consumption of between 40 to 90% of acetate added (Fig. S5†). A higher acetate substrate utilization was observed in amendments containing both HAs and RNS.

Characterization of the (bio)mineralization products

The SEM microphotographs of cathodes used in biotic chronoamperometric assays revealed spherical mineral aggregates with sizes ranging from 1 to 10 μm in diameter (Fig. 4a). The minerals were initially associated with the presence of rod-shaped *Geobacter* cells that colonized the electrode surface (Fig. 4b). Although the cells were previously identified to exert no discernible major role as electron sinks, the cathodic potential applied could have induced the same sort of bacterial–electrode interactions previously reported (*e.g.*, ref. 41 and 48). Bioinorganic aggregates in our cathodes are mineral–bacterial cell networks that formed instead of the thick biofilms observed elsewhere, and previously observed in anodes by Kato *et al.*[49] (Fig. 4a′). Mineral aggregation facilitated the production of conductive outer membrane nanowire-like features. These interconnected multiple cells with early formed mineral aggregates dispersed on the electrode surface[50,51] (Fig. 4b′). The nanowire-like features became further mineralized as our experiments proceeded, and, in more advanced stages, the cells ultimately became entombed within dead-cell–mineral (bioinorganic) aggregates (Fig. 4a′).

We evaluated by synchrotron-based μ-XRF the distribution of Fe–As elemental associations in the synthetic bioinorganic aggregates. The μ-XRF maps showed a non-uniform distribution of Fe–As associations on our electrode surfaces, and this elemental association appeared in higher densities in cathodes used in biotic chronoamperometric assays (Fig. S6a†). Replicate As-XANES conducted on our Fe–As elemental hotspots displayed a K-edge peak at *ca.* 11.875 keV (Fig. 5a), and hence can be ascribed to As(v).[52–54] This finding indicates that (i) the initial iron-bound arsenite was oxidized under the experimental anoxic conditions and immobilized within the ensuing bioinorganic aggregates; and (ii) no further As(v) reduction occurred after scavenging from solution despite the prevalent reductive potential applied.

In addition, synchrotron-radiation based angle-resolved X-ray diffraction of the As–Fe elemental hotspots (Fig. S6b and c†) indicated the presence of both poorly crystalline and crystalline oxyhydroxides. The μ-XRD patterns were largely dominated by CuK-equivalent diffraction peaks corresponding to graphite (>wt 90%, Fig. 5b). Despite this graphite dominance that largely hindered identification of other relevant diffraction peaks by overlapping them, 2θ reflections clearly related to the occurrence of poorly crystalline FeOOH were identified. Accordingly, it can be estimated that poorly crystalline FeOOH accounted for up to 7 wt% of total experimental mineralogy (Fig. S7†). Peaks related to crystalline minerals varied in occurrence and

This journal is © The Royal Society of Chemistry 2023

60

Environ. Sci.: Water Res. Technol., 2023, **9**, 454–466 | **459**
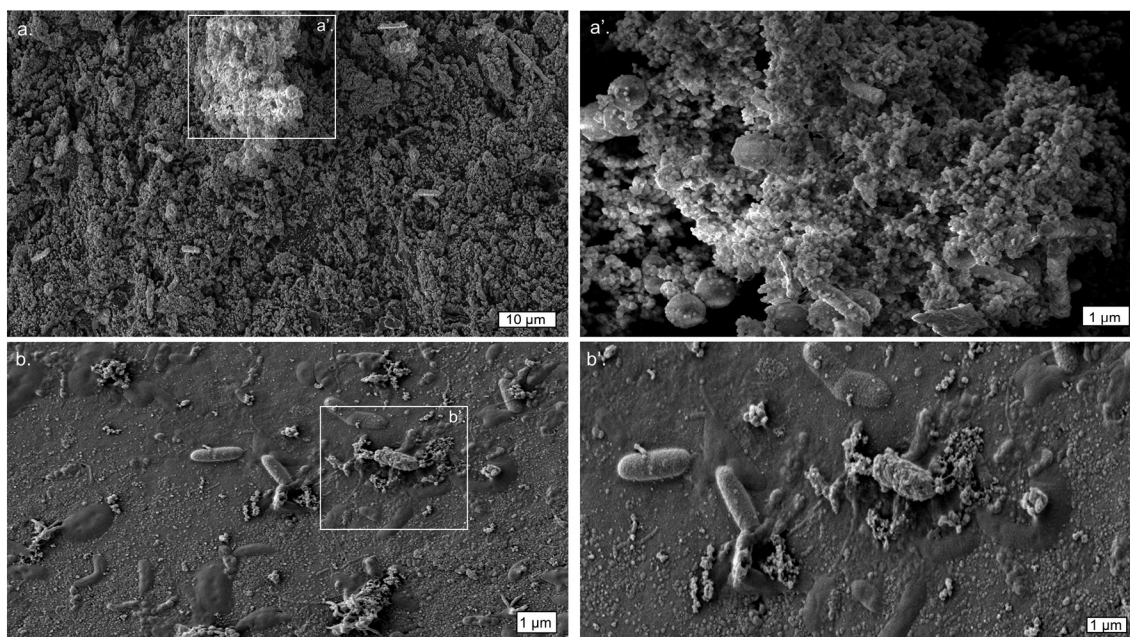
Fig. 4 Representative SEM photomicrographs showing bioinorganic mineral aggregates (a), and electroactive cells (b) colonizing the graphite electrode submerged in synthetic ferruginous solutions inoculated with *Geobacter* spp. Note that a′ and b′ are higher magnification photomicrographs a and b, respectively. SEM analyses revealed cell–mineral networks featuring biomineral aggregates that precipitated in the extracellular environment. The mineralized filamentous features are thought to be FeOOH-entombed nanowires that the electroactive cells used for accessing electrons released from Fe(II)-oxidation.

relative intensities and were only discernible in biotic chronoamperometric assays containing RNS but lacking HAs (Exp. C, Fig. 5b). Contrariwise, only a few crystalline reflections were observed in the sterile experiment, in which the added disordered ferrihydrite was instead reductively dissolved during the whole experimental period (48 h).
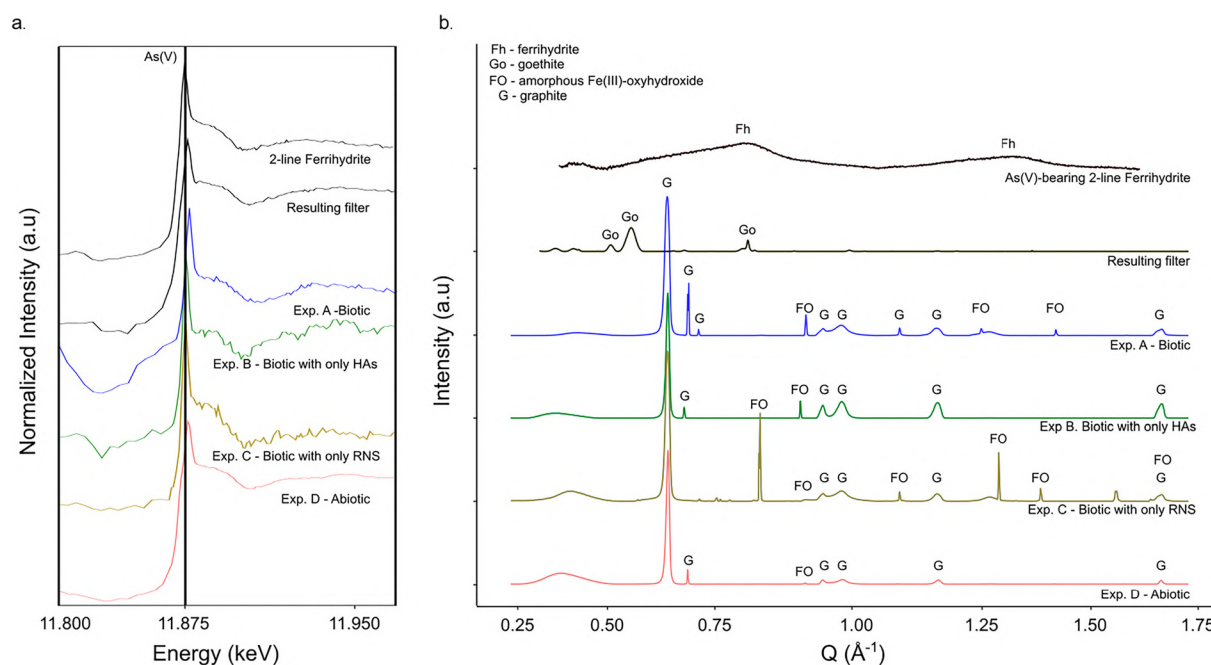
Fig. 5 Comparative normalized synchrotron-radiation based As K-edge XANES spectra (a) and angle-resolved X-ray diffraction patterns (b) from As–Fe elemental hotspots on As(III)-bearing 2-line ferrihydrite as an internal standard, filtrates, and graphite electrode surfaces from different chronoamperometric assays: (1) synthetic ferruginous solutions amended with both RNS and HAs (Exp. A); (2) synthetic ferruginous solutions with HAs, but lacking RNS (Exp. B); (3) synthetic ferruginous solutions with RNS and no HAs added (Exp. C); and (4) an abiotic control of an experiment (Exp. D).

460 | *Environ. Sci.: Water Res. Technol.*, 2023, **9**, 454–466

61

This journal is © The Royal Society of Chemistry 2023

Precipitation of poorly crystalline Fe(III)-bearing minerals on our cathode surfaces is supported by the fact that analogous intensity diffractions at *ca.* 0.8 and 1.4 $Å^{-1}$ are characteristic also in the synthetic As(v)-bearing 2-line ferrihydrite (Fig. 5b). Interestingly, XRD patterns from particles retained in filters differed from those of mineral aggregates at the cathode surfaces. But the presence of such peaks did not allow for unambiguous identification of mineral phases by comparison with the COD and RRUFF databases. The integrated 1D diffraction, however, displayed similarities with the XRD patterns of goethite recently reported by Choi & Oh.[55] Finally, As removal within the presumed goethite-like particles suspended on the synthetic ferruginous solutions is negligible, and the μ-XRF maps of our filters rather exhibited minimum Fe–As elemental hotspots (Fig. S8†).

Discussion

A proof-of-concept bioelectrochemical experiment to induce As(III) removal (*ca.* 30%) from synthetic anoxic (ferruginous) waters containing environmentally relevant dissolved arsenic, RNS and phosphate levels was carried out. Our As(III)-immobilizing BES was inspired by microbial–mineral interactions that couple the Fe–As mineral dynamics described in the model lacustrine system Lake Medard (Fig. S2†).[34–36] In this "natural" aqueous system, slight variations in the redox conditions augmented the affinity of dissolved As for highly redox reactive amorphous Fe(III) oxyhydroxides

that form and are readily transformed in transit between the redoxcline and the sediment–water interface.[35,36]

Data from chronoamperometric assays (*i.e.*, the observed continuous reduction of redox reactive species), coupled with the characterization of bioinorganic aggregates formed on the electrode surfaces (μ-XRF maps of Fe-As elemental hotspots), allowed us to infer that arsenite scavenging in our experiments, and by extrapolation in the model site, proceeds two-fold. First, the negatively poised cathodes—*i.e.*, as surrogates to conductive negatively charged mineral surfaces in the lake—reduced trace levels of dissolved O_2 (*i.e.*, <1.5 μM, data not shown) still available in solution. In the experiments residual O_2 may have existed after purging the flasks and reaction vessels with N_2. This fostered Fenton-type reactions that readily oxidized Fe(II) in solution to fuel the precipitation of poorly crystalline Fe(III) oxyhydroxide nanoparticles at *ca.* t = 0 h (ref. 56 and 57) (Fig. 6a.1). Second, the Fe(III) oxyhydroxides so precipitated sorbed As(III) (AsO_3^{3-}) from solution (*e.g.*, ref. 19 and 53), but this species is readily oxidized to As(v) (AsO_4^{3-}) either by the aforementioned Fenton reactions,[52,58] or as a side result of ensuing oxyhydroxide mineral stabilization (*e.g.*, ref. 27, Fig. 6a.2–3). Importantly, our As K-edge XANES results showed that As(v) was not reduced back to As(III) after mineral immobilization. This result is important as it indicates that our proof-of-concept experiment successfully removed arsenite that was maintained immobilized as the less toxic species arsenate.[59] Fig. 6 depicts the complexity of the (bio)electrochemically induced redox reactions and EET
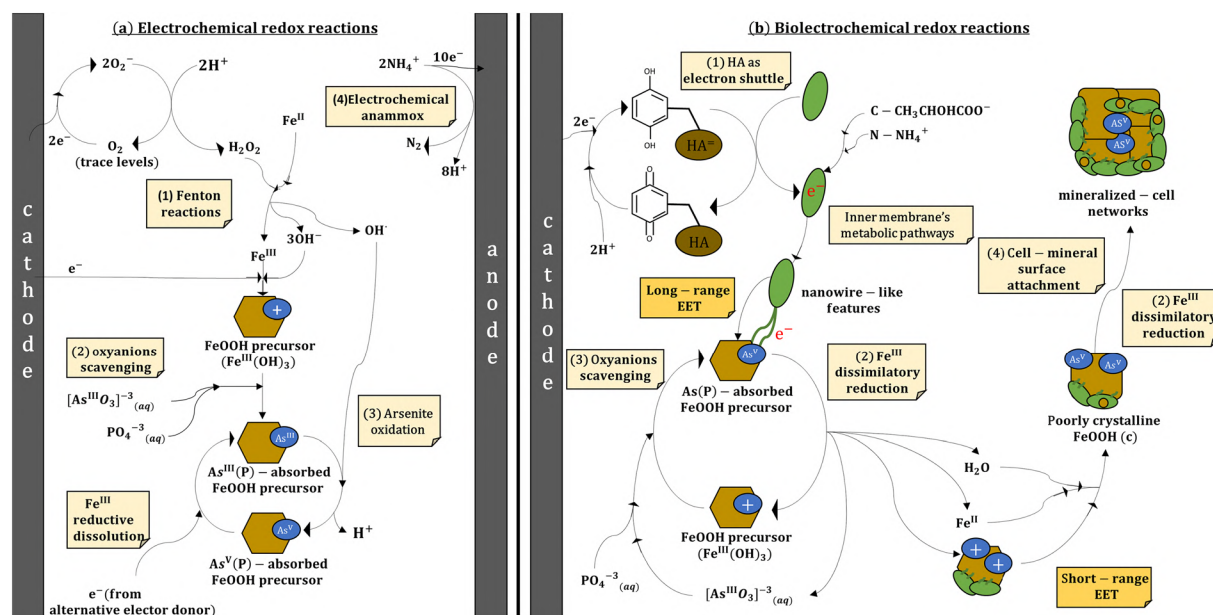
Fig. 6 Scheme illustrating the (a) abiotic redox reactions that occurred at the vicinities of cathodes in all the chronoamperometric assays at t = 0 h, which induced (1) Fe(III)-oxyhydroxide nanoparticle precipitation by Fenton reactions, the As(±P) scavenging from solution into newly formed Fe(III) phases, and (3) the As(III) oxidation by either Fenton reactions or mineral stabilization, as well as (4) possible electrochemical anammox that occurred at the anode. Also displayed are the bioelectrochemically induced redox reactions driven by *Geobacter* sp. to (1) use humic acid derivatives (*e.g.*, quinones) as alternative electron donors, and (2) to perform dissimilatory Fe(III) reduction. These processes ultimately boosted (3) As(v) scavenging from solution and (4) mineral stabilization into cell–mineral networks.

mechanisms at the vicinity of cathodes and *Geobacter* cells during our experiments.

Since dissimilatory Fe(III) reduction is prevalent in most if not all metal-rich redox stratified aqueous environments, an up-scaled version of the proposed BES would be beneficial for low-income communities in underdeveloped countries. They more often comprise those regions where geogenic groundwater As pollution represents a major issue.[11–13] Although As immobilization attained during our chronoamperometric assays (max. *ca.* 30%) was analogous to other batch-type bioelectrochemical approaches (*cf.* ref. 19), the process(es) efficiency must still be improved before foreseeing any eventual scale-up and implementation of BESs to real-life examples of groundwater As(III) pollution. Below we discuss the efficiency shortcomings, and discern possible avenues for further improvement.

Enhancing extracellular electron transfer mechanisms to immobilize As(III)

In an attempt to improve the As(III) scavenging by (bio) electrochemical approaches, Leiva *et al.*[19] mentioned how important it is to achieve a better understanding of extracellular electron transfer mechanisms involved in biomineralization. There remain knowledge gaps on mediated EET pertaining Fe(III) mineral redox transformations on cathodes (see ref. 48). To help in filling some of these gaps and to elaborate on the factors that could enhance As scavenging, we integrated data from chronoamperometric assays, measurable Fe–As biomineralization dynamics on electrode surfaces, and the changes in the RNS in experimental solutions.

In our experiments, the observed degree of stabilization and As(III) scavenging varied depending on whether leonardite-derived HAs, RNS or both were present. Combined, these results point to the need to consider TEA competitiveness, the ability of HAs to act either as electron shuttles or an alternative TEA, and the N source of the system under consideration. Evaluation of RNS levels in biotic chronoamperometric assays pinpoints the fact that the employed *Geobacter* strain did not promote nitrate reduction to ammonium, despite the known functional capacity of these species to use NO_3^- as a TEA,[60] or their ability to use electrodes as the sole source of electrons.[41,61] In addition, a consistent decrease in NH_4^+ contents in solution could be rather linked to direct electrochemically induced N_2 production out of ammonium in solution (Fig. 6a.4). Alternatively, it would suggest that in our BES, N–NH_4^+ would be partly assimilated as a primary N source for bacterial growth.[46]

Highlighted by our results is that leonardite-derived HAs significantly boosted the reductive dissolution of amorphous Fe(III) phases (Fig. 6b.1). This in turn facilitated stabilization to poorly crystalline FeOOH that would have increased the availability of As sorption sites[62] (Fig. 6b.2–3). Thus, leonardite boosted the scavenging of As(III) from

solution too. Although amendments of only leonardite-derived HAs facilitated the stabilization of amorphous Fe(III) oxyhydroxides, they did not generate higher As(III) immobilization than experimental amendments consisting only of RNS. Therefore, the availability of RNS (notably ammonium) seems necessary to promote biotic arsenic scavenging in the presence of HAs. This effect could be related to a need for an additional N-source as has been previously reported for the *Geobacter*-mediated U(VI) reduction, where acetate and ammonium act as C and N sources, respectively.[46] On the other hand, Fe mineral stabilization on cathode surfaces decreased As(III) scavenging in assays only amended with RNS (Exp. C). This result could have been promoted, to some extent, by bioelectrochemical Fe-ammox.[25] It is difficult to discern, however, how solely *Geobacter* cells could have exploited the excess of dissolved NH_4^+ in solution because their specific role in the Fe-ammox processes is yet to be clarified.[63]

The metabolic versatility of *Geobacter* spp. could be a key factor explaining HA utilization but in the absence of anoxic–oxic cycles.[62] Their versatility allows them to exploit electrons released by reducible humic substances for enhancing their dissimilatory Fe(III) reduction capacity,[64,65] and such an ability was likely stimulated by our experimental electric potential (*i.e.*, −500 mV). This causes partial reduction of the oxidized organic radicals comprising the leonardite derivatives (*e.g.*, quinones,[44,66,67] Fig. 6b.1). Quinones are well-known to function as electron shuttles that could enable long-range extracellular electron transfer from EAM outer membranes to Fe(III) oxyhydroxides.[31,68] Thus, as the HAs were electrochemically reduced on the cathodes, their derivatives could be subsequently (re)oxidized while being used as electron shuttles from the cellular envelopes of *Geobacter* sp. to Fe(III)-bearing minerals.

Although As(III) removal was consistently <10% in assays only amended with RNS (*i.e.*, Exp. C), the XRD patterns of these experiments showed crystalline FeOOH phases. Mineral preservation under the reductive potential applied can be linked to poor As(III) scavenging from solution and may result from mineral interactions occurring in the extracellular milieu. Indeed, when leonardite-derived HAs are lacking as suitable redox mediators (shuttles), the biofilms covering our electrode surfaces developed delicate mineral–bacterial networks that resemble the so-called nanowires[51] (Fig. 4b′). The formation of nanowire-like features can thus be thought of as an adaptive response of EAMs that prevents them to waste excessive energy in producing extracellular proteins (c-type cytochromes) for long-range electron transfer within nascent biofilms.[49]

Importantly, cellular attachment to FeOOH mineral surfaces not only decreased the availability of sorption sites but could have also limited further stabilization of early formed amorphous phases,[69] while also reducing the capacity of the amorphous FeOOH precursor to absorb arsenite.[70] Consistent with this interpretation appears to be the lack of

462 | *Environ. Sci.: Water Res. Technol.*, 2023, **9**, 454–466

63

This journal is © The Royal Society of Chemistry 2023

mixed-valence Fe(III,II)-oxyhydroxides in all of our experiments. On the other hand, EAM attachment to mineral surfaces may have operated to prevent further arsenic scavenging because As(V) sorption onto Fe(III) oxyhydroxide could largely be fueled by the presence of an Fe(II)/Fe(III) redox couple.[53] A factor to consider is also that phosphorus oxyanions must have outcompeted their arsenic counterparts for the sorption sites that were available in our experiments.[71] We chose to use a phosphate buffer, however, because in our model site—as in most natural settings featuring toxic As pollution—phosphate concentrations are at least one order of magnitude higher than those of arsenate.[36] Therefore our results are thought to be realistic considering a foreseen application to real-life problems of a to-be-redesigned BES.

Insights from the extracellular electron transfer mechanisms: tools to improve the As-removal bioelectrochemical system

Overall, the BES developed here has advantages for studying complex mineral–EAM interactions because (i) we promoted microbially mediated Fe–As dynamics solely through *Geobacter* interactions with both HAs and cathodes, (ii) the As(III) immobilization does not depend on potentially limited NO_3^--reduction rates, and (iii) our experimental solutions considered environmental relevant Fe and As levels as well as other species that can also be found in anoxic ferruginous water bodies, such as phosphate. In addition, our system can be constructed using low-cost and eco-friendly materials[71,72] while working in an analogous way to already proven technological approaches that are both energy and resource-demanding (*e.g.*, ref. 16 and 74). Future real-life applications of the described BES could consist of (a) a high-volume reactor directly fed-up with As-rich anoxic waters where cathodes would stimulate both microbial–mineral interactions and As(III) scavenging within Fe minerals, and (b) an extraction end where treated water can be recovered under oxic conditions (*e.g.*, see ref. 20). Another related advantage is that a model EAM (*Geobacter* sp.) capable of dissimilatory Fe(III) reduction was used and proven relevant for enhancing As(III) immobilization. In an analogous way, other Fe(III)-reducing EAMs can probably be targeted (*e.g.*, *Rhodoferrax* sp.[67]).

Altogether, our results suggest that by enhancing HA redox reactivity and long-range EET, it is possible to boost the interlinked Fe–As mineral dynamics occurring at Lake Medard and replicated here. Based on this result, we proposed modifications that can be implemented in future bioelectrochemical systems aiming for As(III) removal from polluted aqueous environments. These are:

• To increase the reduction of redox moieties found in the HAs that can serve as redox mediators for Fe(III) mineral phase reductive dissolution by sweeping $E > -500$ mV[44]

• To enhance short-range extracellular electron transfer to Fe(III) nanoparticles by employing electrodes pre-coated with EAMs[72]

• To promote interspecies interactions that could foster Fe-ammox, for example by performing a bioelectrochemical pre-enrichment of both Fe(III)- and N-utilizing microorganisms[73]

• To decrease interferences of other redox-active electrolytes on the targeted reactions occurring on the cathode by employing two-chamber microbial fuel cells.

Finally, our observation could also serve from an ecological perspective to understand how HAs and RNS co-influence microbe–mineral interactions in ferruginous environments, as well as to understand biogeochemical mechanisms involved in particulate As removal in the so-called 'iron snow' that forms at the oxic–anoxic interface of the bottom ferruginous waters. For example:

• HAs as redox mediators could have a fundamental role in regulating the key aqueous iron mineral equilibrium in our model site and analogous systems. This by supporting electrotrophy in bacteria also capable of performing dissimilatory Fe(III)-reduction[34,36]

• Also in the model system, arsenic scavenging after microbially mediated Fe(III) oxyhydroxide stabilization may naturally occur at the surface of organic ferrihydrite aggregates initally formed at the redoxcline but exported to the sediment–water interface where they stabilize

• As immobilization mechanism could be also relevant for PO_4^{3-} that may have outcompeted As-oxyanions for sorption sites on Fe(III) oxyhydroxides[71]

Conclusions

Here we performed a proof-of-concept bioelectrochemical experiment that scavenged As(III) from anoxic ferruginous waters by inducing its co-precipitation with Fe(III). Despite competition of phosphate with arsenite for surficial sorption sites on FeOOH phases, our BES immobilized up to 30% of the dissolved metalloid. The highest arsenite immobilization was attained by enabling *Geobacter* sp. utilization of electrons generated by reducible humic substances which acted also as electron shuttles fostering transformations of Fe(III) oxyhydroxide minerals. Ammonium seems necessary to promote biotic arsenic scavenging in the presence of HAs as redox mediators. A lack of HAs as redox mediators stimulated the formation of EAM–Fe(III) mineral networks with low As-scavenging capacity, but facilitated the anoxic stabilization of amorphous biotic ferrihydrite-like phases. Finally, we observed that long-range EET enhances As(III) immobilization in BESs.

Author contributions

AV: conceptualization, methodology, investigation, data curation, formal analysis, visualization, writing – original draft. JJ: methodology, resources, writing – original draft. DAP: conceptualization, funding acquisition, project administration, resources, supervision, writing – original draft, writing – review & editing.

Conflicts of interest

The authors have no conflicts of interest to declare.

Acknowledgements

References

1 X. Xu, C. Chen, P. Wang, R. Kretzschmar and F. J. Zhao, Control of arsenic mobilization in paddy soils by manganese and iron oxides, *Environ. Pollut.*, 2017, **231**, 37–47.

2 M. Arsic, P. R. Teasdale, D. T. Welsh, S. G. Johnston, E. D. Burton, K. Hockmann and W. W. Bennett, Diffusive Gradients in Thin Films Reveals Differences in Antimony and Arsenic Mobility in a Contaminated Wetland Sediment during an Oxic-Anoxic Transition, *Environ. Sci. Technol.*, 2018, **52**, 1118–1127.

3 K. H. Johannesson, N. Yang, A. S. Trahan, K. Telfeyan, T. J. Mohajerin, S. B. Adebayo, O. A. Akintomide, D. A. Chevis, S. Datta and C. D. White, Biogeochemical and reactive transport modeling of arsenic in groundwaters from the Mississippi River delta plain: An analog for the As-affected aquifers of South and Southeast Asia, *Geochim. Cosmochim. Acta*, 2019, **264**, 245–272.

4 J. R. Lloyd and R. S. Oremland, Microbial Transformations of Arsenic in the Environment: From Soda Lakes to Aquifers, *Elements*, 2006, **2**, 85–90.

5 S. Tamaki and W. T. Frankenberger, Environmental biochemistry of arsenic, *Rev. Environ. Contam. Toxicol.*, 1992, **124**, 79–110.

6 E. Fulladosa, J. C. Murat, M. Martínez and I. Villaescusa, Effect of pH on Arsenate and Arsenite Toxicity to Luminescent Bacteria (Vibrio fischeri), *Arch. Environ. Contam. Toxicol.*, 2004, **46**(2), 176–182.

7 S. K. Tripti and Shardendu, pH modulates arsenic toxicity in Bacillus licheniformis DAS-2, *Ecotoxicol. Environ. Saf.*, 2016, **130**, 240–247.

8 P. L. Smedley and D. G. Kinniburgh, A review of the source, behaviour and distribution of arsenic in natural waters, *Appl. Geochem.*, 2002, **17**, 517–568.

9 A. A. Duker, E. J. M. Carranza and M. Hale, Arsenic geochemistry and health, *Environ. Int.*, 2005, **31**, 631–641.

10 J. P. Buchet, R. Lauwerys and H. Roels, Comparison of the urinary excretion of arsenic metabolites after a single oral dose of sodium arsenite, monomethylarsonate, or dimethylarsinate in man, *Int. Arch. Occup. Environ. Health*, 1981, **48**, 71–79.

11 J. Bundschuh, M. I. Litter, F. Parvez, G. Román-Ross, H. B. Nicolli, J. S. Jean, C. W. Liu, D. López, M. A. Armienta, L. R. G. Guilherme, A. G. Cuevas, L. Cornejo, L. Cumbal and R. Toujaguez, One century of arsenic exposure in Latin America: A review of history and occurrence from 14 countries, *Sci. Total Environ.*, 2012, **429**, 2–35.

12 A. Bretzler, F. Lalanne, J. Nikiema, J. Podgorski, N. Pfenninger, M. Berg and M. Schirmer, Groundwater arsenic contamination in Burkina Faso, West Africa: Predicting and verifying regions at risk, *Sci. Total Environ.*, 2017, **584–585**, 958–970.

13 E. Shaji, M. Santosh, K. V. Sarath, P. Prakash, V. Deepchand and B. V. Divya, Arsenic contamination of groundwater: A global synopsis with focus on the Indian Peninsula, *Geosci. Front.*, 2021, **12**, 101079.

14 P. González-Contreras, J. Weijma and C. J. N. Buisman, Continuous bioscorodite crystallization in CSTRs for arsenic removal and disposal, *Water Res.*, 2012, **46**, 5883–5892.

15 W. Xiu, H. Guo, Q. Liu, Z. Liu, Y. Zou and B. Zhang, Arsenic Removal and Transformation by Pseudomonas sp. Strain GE-1-Induced Ferrihydrite: Co-precipitation Versus Adsorption, *Water, Air, Soil Pollut.*, 2015, **226**(6), 1–14.

16 P. Mondal, S. Bhowmick, D. Chatterjee, A. Figoli and B. van der Bruggen, Remediation of inorganic arsenic in groundwater for safe water supply: A critical assessment of technological solutions, *Chemosphere*, 2013, **92**, 157–170.

17 C. Koch and F. Harnisch, Is there a Specific Ecological Niche for Electroactive Microorganisms?, *ChemElectroChem*, 2016, **3**, 1282–1295.

18 M. O. Yee, J. Deutzmann, A. Spormann and A.-E. Rotaru, Cultivating electroactive microbes—from field to bench, *Nanotechnology*, 2020, **31**, 174003.

19 E. Leiva, E. Leiva-Aravena, C. Rodríguez, J. Serrano and I. Vargas, Arsenic removal mediated by acidic pH neutralization and iron precipitation in microbial fuel cells, *Sci. Total Environ.*, 2018, **645**, 471–481.

20 A. Ceballos-Escalera, N. Pous, P. Chiluiza-Ramos, B. Korth, F. Harnisch, L. Bañeras, M. D. Balaguer and S. Puig, Electro-bioremediation of nitrate and arsenite polluted groundwater, *Water Res.*, 2021, **190**, 116748.

21 L. Wang, Z. Lin, L. Chang, J. Chen, S. Huang, X. Yi, M. Luo and Y. Wang, Effects of anode/cathode electroactive microorganisms on arsenic removal with organic/inorganic carbon supplied, *Sci. Total Environ.*, 2021, **798**, 149356.

22 L. Wang, Z. Lin, S. Liu, D. Fu, Z. Li, Q. Luo, J. Tang, Z. Chen, N. He and Y. Wang, The effect of extracellular electron transfer on arsenic speciation transformation in a soil bioelectrochemical system, *Soil Tillage Res.*, 2020, **204**, 104723.

23 D. R. Lovley, Bug juice: harvesting electricity with microorganisms, *Nat. Rev. Microbiol.*, 2006, **4**(7), 497–508.

24 D. R. Lovley, Electrotrophy: Other microbial species, iron, and electrodes as electron donors for microbial respirations, *Bioresour. Technol.*, 2022, **345**, 126553.

464 | *Environ. Sci.: Water Res. Technol.*, 2023, **9**, 454–466

65

This journal is © The Royal Society of Chemistry 2023

25 E. D. Melton, E. D. Swanner, S. Behrens, C. Schmidt and A. Kappler, The interplay of microbially mediated and abiotic reactions in the biogeochemical Fe cycle, *Nat. Rev. Microbiol.*, 2014, **12**(12), 797–808.

26 L. Shi, H. Dong, G. Reguera, H. Beyenal, A. Lu, J. Liu, H. Q. Yu and J. K. Fredrickson, Extracellular electron transfer mechanisms between microorganisms and minerals, *Nat. Rev. Microbiol.*, 2016, **14**(10), 651–662.

27 F. S. Islam, R. L. Pederick, A. G. Gault, L. K. Adams, D. A. Polya, J. M. Charnock and J. R. Lloyd, Interactions between the Fe(III)-reducing bacterium Geobacter sulfurreducens and arsenate, and capture of the metalloid by biogenic Fe(II), *Appl. Environ. Microbiol.*, 2005, **71**, 8642–8648.

28 C. A. Pearcy, D. A. Chevis, T. J. Haug, H. A. Jeffries, N. Yang, J. Tang, D. A. Grimm and K. H. Johannesson, Evidence of microbially mediated arsenic mobilization from sediments of the Aquia aquifer, Maryland, USA, *Appl. Geochem.*, 2011, **26**, 575–586.

29 B. S. Mirza, S. Muruganandam, X. Meng, D. L. Sorensen, R. R. Dupont and J. E. Mc Lean, Arsenic(V) Reduction in Relation to Iron(III) Transformation and Molecular Characterization of the Structural and Functional Microbial Community in Sediments of a Basin-Fill Aquifer in Northern Utah, *Appl. Environ. Microbiol.*, 2014, **80**, 3198.

30 X. Zhao, Z. Yuan, S. Wang, G. Zhang, S. Qu, Y. Wang, S. Liu, Y. Pan, J. Lin and Y. Jia, The fate of co-existent cadmium and arsenic during Fe(II)-induced transformation of As(V)/Cd(II)-bearing ferrihydrite, *Chemosphere*, 2022, **301**, 134665.

31 L. Klüpfel, A. Piepenbrock, A. Kappler and M. Sander, Humic substances as fully regenerable electron acceptors in recurrently anoxic environments, *Nat. Geosci.*, 2014, **7**(3), 195–200.

32 A.-E. Rotaru, N. R. Posth, C. R. Löscher, E. Vicente, R. P. Cox, J. Thompson, S. W. Poulton and B. Thamdrup, Interspecies interactions mediated by conductive minerals in the sediments of the ferruginous Lake La Cruz, Spain, bioRxiv, 2018, preprint, 366542, DOI: 10.23818/limn.38.10.

33 P. A. Palacios, W. R. Francis and A. E. Rotaru, A Win–Loss Interaction on Fe0 Between Methanogens and Acetogens From a Climate Lake, *Front. Microbiol.*, 2021, **12**, 919.

34 D. A. Petrash, I. M. Steenbergen, A. Valero, T. B. Meador, T. Paces and C. Thomazo, Aqueous system-level processes and prokaryote assemblages in the ferruginous and sulfate-rich bottom waters of a post-mining lake, *Biogeosciences*, 2022, **19**, 1723–1751.

35 K. Umbría-Salinas, A. Valero, J. Jan, J. Borovec, V. Chrastný and D. A. Petrash, Redox-driven geochemical partitioning of metal(loid)s in the iron-rich anoxic sediments of a recently flooded lignite mine pit: Lake Medard, NW Czechia, *J. Hazard. Mater. Adv.*, 2021, **3**, 100009.

36 D. A. Petrash, J. Jan, D. Sirová, N. O. A. Osafo and J. Borovec, Iron and nitrogen cycling, bacterioplankton community composition and mineral transformations involving phosphorus stabilisation in the ferruginous hypolimnion of a post-mining lake, *Environ. Sci.: Processes Impacts*, 2018, **20**, 1414–1426.

37 U. Schwertmann and R. M. Cornell, in *Iron Oxides in the Laboratory*, John Wiley & Sons, Ltd, 2007, pp. 103–112.

38 R. S. Swift, in *Methods of Soil Analysis, Part 3: Chemical Methods*, John Wiley & Sons, Ltd, 2018, pp. 1011–1069.

39 S. Kalaitzidis, S. Papazisimou, A. Giannouli, A. Bouzinos and K. Christanis, Preliminary comparative analyses of two Greek leonardites☆, *Fuel*, 2003, **82**, 859–861.

40 F. Scarabotti, L. Rago, K. Bühler and F. Harnisch, The electrode potential determines the yield coefficients of early-stage Geobacter sulfurreducens biofilm anodes, *Bioelectrochemistry*, 2021, **140**, 107752.

41 K. B. Gregory, D. R. Bond and D. R. Lovley, Graphite electrodes as electron donors for anaerobic respiration, *Environ. Microbiol.*, 2004, **6**, 596–604.

42 K. L. Straub and B. Schink, Ferrihydrite reduction by Geobacter species is stimulated by secondary bacteria, *Arch. Microbiol.*, 2004, **182**(2), 175–181.

43 N. Pous, S. Puig, M. D. Balaguer and J. Colprim, Cathode potential and anode electron donor evaluation for a suitable treatment of nitrate-contaminated groundwater in bioelectrochemical systems, *Chem. Eng. J.*, 2015, **263**, 151–159.

44 J. Duan, Z. Xu, Z. Yang and J. Jiang, Insight to Microbial Fe(III) Reduction Mediated by Redox-Active Humic Acids with Varied Redox Potentials, *Int. J. Environ. Res. Public Health*, 2021, **18**(13), 6807.

45 M. S. M. Jetten, M. Strous, K. T. van de Pas-Schoonen, J. Schalk, U. G. J. M. van Dongen, A. A. van de Graaf, S. Logemann, G. Muyzer, M. C. M. van Loosdrecht and J. G. Kuenen, The anaerobic oxidation of ammonium, *FEMS Microbiol. Rev.*, 1998, **22**, 421–437.

46 P. J. Mouser, A. L. N'Guessan, H. Elifantz, D. E. Holmes, K. H. Williams, M. J. Wilkins, P. E. Long and D. R. Lovley, Influence of heterogeneous ammonium availability on bacterial community structure and the expression of nitrogen fixation and ammonium transporter genes during in situ bioremediation of uranium-contaminated groundwater, *Environ. Sci. Technol.*, 2009, **43**, 4386–4392.

47 B. Qu, B. Fan, S. Zhu and Y. Zheng, Anaerobic ammonium oxidation with an anode as the electron acceptor, *Environ. Microbiol. Rep.*, 2014, **6**, 100–105.

48 N. Heidary, N. Kornienko, S. Kalathil, X. Fang, K. H. Ly, H. F. Greer and E. Reisner, Disparity of Cytochrome Utilization in Anodic and Cathodic Extracellular Electron Transfer Pathways of Geobacter sulfurreducens Biofilms, *J. Am. Chem. Soc.*, 2020, **142**, 5194–5203.

49 S. Kato, K. Hashimoto and K. Watanabe, Iron-Oxide Minerals Affect Extracellular Electron-Transfer Paths of Geobacter spp., *Microbes Environ.*, 2013, **28**, 141–148.

50 D. E. Holmes, Y. Dang, D. J. F. Walker and D. R. Lovley, The electrically conductive pili of Geobacter species are a recently evolved feature for extracellular electron transfer, *Microb. Genomics*, 2016, **2**, e000072.

51 G. Reguera, Harnessing the power of microbial nanowires, *Microb. Biotechnol.*, 2018, **11**, 979–994.

This journal is © The Royal Society of Chemistry 2023

66

Environ. Sci.: Water Res. Technol., 2023, **9**, 454–466 | **465**

52 C. H. Liu, Y. H. Chuang, T. Y. Chen, Y. Tian, H. Li, M. K. Wang and W. Zhang, Mechanism of Arsenic Adsorption on Magnetite Nanoparticles from Water: Thermodynamic and Spectroscopic Studies, *Environ. Sci. Technol.*, 2015, **49**, 7726–7734.

53 J. P. H. Perez, D. J. Tobler, A. N. Thomas, H. M. Freeman, K. Dideriksen, J. Radnik and L. G. Benning, Adsorption and Reduction of Arsenate during the Fe2+-Induced Transformation of Ferrihydrite, *ACS Earth Space Chem.*, 2019, **3**, 884–894.

54 S. Hu, Y. Liang, T. Liu, F. Li, Y. Lu and Z. Shi, Kinetics of As(V) and carbon sequestration during Fe(II)-induced transformation of ferrihydrite-As(V)-fulvic acid coprecipitates, *Geochim. Cosmochim. Acta*, 2020, **272**, 160–176.

55 H. Choi and S. Oh, Abiotic Transient Nitrite Occurrences from Nitrate Reduction through Goethite-Mediated Fe(III)/Fe(II) Cycle with Labile Organic Materials and Ammonia, *Water*, 2020, **12**(4), 1202.

56 C. H. Feng, F. B. Li, H. J. Mai and X. Z. Li, Bio-electro-fenton process driven by microbial fuel cell for wastewater treatment, *Environ. Sci. Technol.*, 2010, **44**, 1875–1880.

57 Z. Lu, D. Chang, J. Ma, G. Huang, L. Cai and L. Zhang, Behavior of metal ions in bioelectrochemical systems: A review, *J. Power Sources*, 2015, **275**, 243–260.

58 W. Ding, J. Xu, T. Chen, C. Liu, J. Li and F. Wu, Co-oxidation of As(III) and Fe(II) by oxygen through complexation between As(III) and Fe(II)/Fe(III) species, *Water Res.*, 2018, **143**, 599–607.

59 M. F. Hughes, B. D. Beck, Y. Chen, A. S. Lewis and D. J. Thomas, Arsenic Exposure and Toxicology: A Historical Perspective, *Toxicol. Sci.*, 2011, **123**, 305–332.

60 D. R. Lovley and E. J. P. Phillips, Novel mode of microbial energy metabolism: organic carbon oxidation coupled to dissimilatory reduction of iron or manganese, *Appl. Environ. Microbiol.*, 1988, **54**, 1472–1480.

61 H. Kashima and J. M. Regan, Facultative nitrate reduction by electrode-respiring Geobacter metallireducens biofilms as a competitive reaction to electrode reduction in a bioelectrochemical system, *Environ. Sci. Technol.*, 2015, **49**, 3195–3202.

62 S. Park, S. H. Kim, H. Chung and K. Nam, Effect of organic substrate and Fe oxides transformation on the mobility of arsenic by biotic reductive dissolution under repetitive redox conditions, *Chemosphere*, 2022, **305**, 135431.

63 L. Wan, H. Liu and X. Wang, Anaerobic ammonium oxidation coupled to Fe(III) reduction: Discovery, mechanism and application prospects in wastewater treatment, *Sci. Total Environ.*, 2022, **818**, 151687.

64 M. Wolf, A. Kappler, J. Jiang and R. U. Meckenstock, Effects of humic substances and quinones at low concentrations on ferrihydrite reduction by Geobacter metallireducens, *Environ. Sci. Technol.*, 2009, **43**, 5679–5685.

65 N. Stern, J. Mejia, S. He, Y. Yang, M. Ginder-Vogel and E. E. Roden, Dual Role of Humic Substances As Electron Donor and Shuttle for Dissimilatory Iron Reduction, *Environ. Sci. Technol.*, 2018, **52**, 5691–5699.

66 G. Ricca, F. Severini, G. di Silvestro, C. M. Yuan and F. Adani, Derivatization and structural studies by spectroscopic methods of humic acids from Leonardite, *Geoderma*, 2000, **98**, 115–125.

67 M. Aeschbacher, M. Sander and R. P. Schwarzenbach, Novel electrochemical approach to assess the redox properties of humic substances, *Environ. Sci. Technol.*, 2010, **44**, 87–93.

68 G. W. Zhou, X. R. Yang, H. Li, C. W. Marshall, B. X. Zheng, Y. Yan, J. Q. Su and Y. G. Zhu, Electron shuttles enhance anaerobic ammonium oxidation coupled to iron(III) reduction, *Environ. Sci. Technol.*, 2016, **50**, 9298–9307.

69 X. Han, E. J. Tomaszewski, J. Sorwat, Y. Pan, A. Kappler and J. M. Byrne, Effect of Microbial Biomass and Humic Acids on Abiotic and Biotic Magnetite Formation, *Environ. Sci. Technol.*, 2020, **54**, 4121–4130.

70 A. Sundman, A. L. Vitzthum, K. Adaktylos-Surber, A. I. Figueroa, G. van der Laan, B. Daus, A. Kappler and J. M. Byrne, Effect of Fe-metabolizing bacteria and humic substances on magnetite nanoparticle reactivity towards arsenic and chromium, *J. Hazard. Mater.*, 2020, **384**, 121450.

71 Y. Gao and A. Mucci, Acid base reactions, phosphate and arsenate complexation, and their competitive adsorption at the surface of goethite in 0.7 M NaCl solution, *Geochim. Cosmochim. Acta*, 2001, **65**, 2361–2378.

72 N. Pous, B. Casentini, S. Rossetti, S. Fazi, S. Puig and F. Aulenta, Anaerobic arsenite oxidation with an electrode serving as the sole electron acceptor: A novel approach to the bioremediation of arsenic-polluted groundwater, *J. Hazard. Mater.*, 2015, **283**, 617–622.

73 T. Bhowmik, S. Sarkar, A. Bhattacharya and A. Mukherjee, A review of arsenic mitigation strategies in community water supplies with insights from South Asia: options, opportunities and constraints, *Environ. Sci.: Water Res. Technol.*, 2022, **8**(11), 2491–2520.

74 Y. Wan, Z. Huang, L. Zhou, T. Li, C. Liao, X. Yan, N. Li and X. Wang, Bioelectrochemical Ammoniation Coupled with Microbial Electrolysis for Nitrogen Recovery from Nitrate in Wastewater, *Environ. Sci. Technol.*, 2020, **54**, 3002–3011.

466 | *Environ. Sci.: Water Res. Technol.*, 2023, **9**, 454–466

67

This journal is © The Royal Society of Chemistry 2023

Paper IV

Enriching electroactive microorganisms from ferruginous lake waters – Mind the sulfate reducers!

Valero, A., Petrash, D.A., Kuchenbuch, A., Korth, B.

Enriching electroactive microorganisms from ferruginous lake waters – Mind the sulfate reducers!

Astolfo Valero [a,b], Daniel A. Petrash [a,c], Anne Kuchenbuch [d], Benjamin Korth [d,*]

[a] Institute of Soil Biology and Biogeochemistry, Biology Centre of the Czech Academy of Sciences, České Budějovice, Czech Republic
[b] Department of Ecosystem Biology, Faculty of Science, University of South Bohemia, České Budějovice, Czech Republic
[c] Department of Environmental Geochemistry and Biogeochemistry, Czech Geological Survey, Prague, Czech Republic
[d] Department of Microbial Biotechnology, Helmholtz Centre for Environmental Research GmbH - UFZ, Leipzig, Germany

ARTICLE INFO

ABSTRACT

Electroactive microorganisms are pivotal players in mineral transformation within redox interfaces characterized by pronounced oxygen and dissolved metal gradients. Yet, their systematic cultivation from such environments remains elusive. Here, we conducted an anodic enrichment using anoxic ferruginous waters from a post-mining lake as inoculum. Weak electrogenicity ($j = \sim5\,\mu A\,cm^{-2}$) depended on electroactive planktonic cells rather than anodic biofilms, with a preference for formate as electron donor. Addition of yeast extract decreased the lag phase but did not increase current densities. The enriched bacterial community varied depending on the substrate composition but mainly comprised of sulfate- and nitrate-reducing bacteria (e.g., *Desulfatomaculum* spp. and *Stenotrophomonas* spp.). A secondary enrichment strategy resulted in different bacterial communities composed of iron-reducing (e.g., *Klebsiella* spp.) and fermentative bacteria (e.g., *Paeniclostridium* spp.). Secondary electron microscopy and energy-dispersive X-ray spectroscopy results indicate the precipitation of sulfur- and iron-rich organomineral aggregates at the anode surface, presumably impeding current production. Our findings indicate that (i) anoxic waters containing geogenically derived metals can be used to enrich weak electricigens, and (ii) it is necessary to specifically inhibit sulfate reducers. Otherwise, sulfate reducers tend to dominate over EAM during cultivation, which can lead to anode passivation due to biomineralization.

1. Introduction

Electroactive microorganisms (EAM) can drive their metabolism by performing extracellular electron transfer (EET), exchanging electrons with insoluble conductive materials such as minerals [1,2] and electrodes [3,4]. EET is conducted by using soluble redox shuttles such as quinones and flavins [5,6] (i.e., mediated EET) or by direct physical contact via multiheme *c*-type cytochromes or nanowires [2,7] (i.e., direct EET). EAM can also directly exchange electrons with other microbial species forming microbial food chains [8] (i.e., direct interspecies electron transfer, DIET).

Studying the EET in *Geobacter sulfurreducens* and *Shewanella oneidensis* has provided insights that have helped decipher the EET mechanisms of other microorganisms. Microorganisms capable of EET have been identified in many different environments and do not exhibit a unitary phylogenetic affiliation but comprise, among others, iron reducers, and acidophilic and neutrophilic iron oxidizers [9,10]. EAM are

commonly enriched using inoculums derived from wastewater and industrial sludges [11,12], soils and sediments [13,14], and groundwater [15,16]. However, EAM can also be cultured by using inoculums derived from tropical and intertidal sediments [17,18], hypersaline lakes [19], or deep-ocean hydrothermal vents [20].

EAM have a widespread occurrence and support vital ecological processes linking biogeochemical cycles and the activity of syntrophic microbial communities [2,21,22]. For example, in dysoxic environments, electroactive Fe(II)-oxidizing bacteria belonging to the *Gallionellaceae* family readily induce Fe(III)-oxyhydroxide precipitation while using nitrate as terminal electron acceptor [22]. On the other hand, by using Fe(III)-oxyhydroxides as terminal electron acceptors while oxidizing organic compounds, members of the *Geobacteraceae* family release Fe(II) back to solution or facilitate the stabilization of mixed-valence Fe(II,III)-oxyhydroxides that can later act as long-term energy sources [2,21]. EAM impact metal solubility by reducing electron acceptors like Cr and U [15,23], or inducing sorption of metals such as Cu

---

* Corresponding author.
   E-mail address: benjamin.korth@ufz.de (B. Korth).

and As through mineral transformations [24,25]. Additionally, they facilitate microbial syntrophy, for example, by reducing oxyhydroxides to conductive minerals like magnetite, aiding DIET to methanogens [26].

Besides the discussed ecological role of EAM, harnessing them in bioelectrochemical systems (BES) offers opportunities for various applications like degradation of organic pollutants, energy production, synthesis of chemicals, bioremediation, and metal recovery (i.e., bio-mining) [27,28]. Biotechnological approaches for biomining address the forecasted shortage of critical transition metals for technological applications [29]. Recent studies showed that EAM indigenous to acid mine drainage facilitate copper recovery from metal-rich solutions [30,31].

Exploring further, yet-to-be-known EAM, unconventional sources for them, and their underlying EET mechanisms can expand (i) our understanding of the role they play in interlinked biogeochemical cycles and (ii) our ability to design novel and more efficient BES for various applications, including biomining [32,33]. Among conceivable sources for unknown EAM are anoxic surficial and ground waters geogenically enriched with metal(oid)s. In those sites, EAM are typically involved in mineral transformations that control the solubility of metal(oid)s [24,34]. Furthermore, anoxic aquatic environments naturally containing dissolved redox mediators, and redox-active mineral particles can stimulate EAM activity [35,36].

One challenge in cultivating unknown EAM and microorganisms, in general, is mimicking the main environmental features of their preferred niche [37]. The variables include salinity, redox potentials, and concentrations of carbon and energy sources [38]. Furthering existing approaches, this study aimed to culture unknown EAM from the ferruginous waters of the meromictic post-mining Lake Medard (North-Western Czech Republic). The bottom water column of Lake Medard is transitional between ferruginous and sulfidic conditions containing redox-reactive humic substances that presumably allocate cryptic interspecies interactions between Fe-, N-, and S-respiring EAM. These microorganisms are considered essential drivers of Fe and Mn biomineralization reactions [36]. Different enrichment conditions were tested to promote the growth of EAM indigenous to Lake Medard. The tested conditions were environmentally relevant and partially mimicked the lake hypolimnetic conditions (e.g., the mixture of volatile fatty acids and the presence of known redox shuttlers, such as humic substances). Planktonic weak electricigens were successfully enriched, producing low currents mainly based on formate oxidation partially coupled to acetogenesis. By performing 16S rRNA amplicon sequencing, several enriched species were identified, supporting the hypothesis that EAM play a role in the aqueous mineral equilibrium in Lake Medard and comparable model systems. However, sulfate reducers dominated the microbial communities, presumably leading to anode passivation. This is due to sulfide accumulation and subsequent abiotic oxidation at the electrode surface, leading to biomineralization that hindered the cultivation of weak electricigens and other EAM.

2. Materials and methods

All used chemicals were of analytical grade and were purchased from Merck KGaA (Germany), Sigma-Aldrich (Germany), and Carl Roth GmbH + Co. KG (Germany). De-ionized water (18.2 MΩ cm^{-1}, Merck Millipore, Germany) was used for preparing all solutions. Glassware and materials were sterilized by autoclaving at 120 °C or soaking with Beckmann solution [39] before use. All experiments were performed in independent biological triplicates, and all potentials reported refer to the standard hydrogen electrode (SHE) by conversion from Ag/AgCl sat. KCl.

2.1. Inoculum – bottom anoxic water from Lake Medard

Lake Medard (50°10′45″N, 12°35′45″E) is a post-mining lake formed after the flooding of an open-cast lignite mine. This oligotrophic lake displays a chemically differentiated, pH-neutral water column (~56 m depth, Fig. S1a) with an anoxic (ferruginous) monimolimnion [40]. In this bottom water, transition metal(loid)s, such as nickel and arsenic, are cycled in association with biological iron and carbon turnover (Fig. S1b and S1c). Cycling of transition metals is probably primarily driven by a microbial community featuring a significant abundance of Fe(II)-oxidizing EAM and dissimilatory Fe(III) reducers. Their peak abundance and diversity are associated with a moderate increase in the bioavailability of volatile fatty acids [36] (e.g., formate and acetate; Fig. S1c).

Water ($n = 2$, 1 L amber laboratory flasks) from the anoxic mon-imolimnion of Lake Medard (~54 m depth, pH = 7.3, and T = 9.7 °C) was collected as previously described [36] and purged within 6 h with 80:20 % N_2:CO_2 gas mixture for 30 min. This was done by using a mechanized gassing-vacuum manifold (25 mL min^{-1}) to ensure anaerobic conditions during storage at 4 °C prior to bioelectrochemical experiments. The planktonic bacterial community at the sampled water column depth is supposed to include a significant abundance of well-known EAM like *Geobacter* spp. and *Rhodoferax* spp. [36,40], as well as other microorganisms capable of Fe(II) oxidation coupled to the reduction of humic substances such as quinones (e.g., *Sideroxydans lithotrophicus*) [41].

2.2. Enrichment of electroactive microorganisms using bioelectrochemical systems

Minimal medium (60 mL, pH = 7.0, DSM 826, German Collection of Microorganisms and Cell Cultures GmbH) was inoculated with Lake Medard's anoxic water (40 mL). The medium contained 0.13 g L^{-1} KCl, 0.31 g L^{-1} NH$_4$Cl, 2.69 g L^{-1} NaH$_2$PO$_4$·H$_2$O, 4.33 g L^{-1} Na$_2$HPO$_4$, 12.5 mL L^{-1} of trace metal solution (DSM 141), and 12.5 mL L^{-1} of vitamin solution (DSM 120). To mimic the volatile fatty acid concentrations from the sampled bottom water [36], acetate and formate (10 mM each) were used as both carbon and electron sources. To improve growth conditions and promote EAM enrichment, yeast extract (1.8 mM), riboflavin (20 μM), or humic acid mixture (50 μM) were added to the minimal medium in a few experiments after > 30 days of cultivation ($n = 12$, Table S1). Anaerobic conditions were obtained by purging 100 mL working volume with 80:20 % N_2:CO_2 gas mixture for 30 min prior to use. Abiotic control experiments were performed by filtering the lake water with sterile syringe filters (0.2 μm, Omnifix, B. Braun Melsungen AG, Germany), while biotic control experiments ($n = 3$) consisted in inoculating BES with Lake Medard's anoxic water (100 mL) but without amending external carbon or electron sources. For secondary enrichment experiments, the planktonic phase was transferred within an anaerobic glove box (95:5 % N_2:H_2 atmosphere, Coy Laboratory Products, Inc., USA) to sterile centrifugation tubes (30 mL, $n = 3$ for each reactor) and centrifuged (10,000g, 4 °C, 2× 10 min). After discarding the supernatant, the cell pellet was resuspended in 30 mL of minimal medium and anaerobically transferred to new reactors.

All experiments were performed in bioelectrochemical systems (BES) consisting of a laboratory bottle (GL 45, 100 mL) featuring a three-electrode setup. Graphite rods ($L = 3$ cm, $d = 0.5$ cm, quality CP-2200, CP-Graphitprodukte GmbH, Germany) pretreated with ultra-sonication (2× 15 min), connected to stainless steel wires ($d = 0.6$ mm, Goodfellow GmbH, Germany), and pierced through butyl stopper were used as working and counter electrodes. These electrodes were constructed and sterilized following Scarabotti et al. [39]. In addition, Ag/AgCl sat. KCl reference electrodes (+197 mV vs. SHE; SE 11, Xylem Analytics GmbH & Co. KG Sensortechnik Meinsberg, Germany) were incorporated. The BES were operated using a multipotentiostat (MPG-2, Bio-Logic Science Instruments, France) in chronoamperometric mode at a working electrode potential of 0.2 V, and the current was recorded every 10 min. Temperature (30 °C) and stirring speed (150 rpm, magnetic stirrer) were continuously controlled. Cyclic voltammetry was

conducted from −0.2 to 0.4 V in different experiments with a scan rate of 1 mV s^{-1}. Fig. S2 provides a schematic representation of the experimental workflow.

2.3. Chemical analyses

Medium samples (1 mL) were collected during enrichment experiments by piercing sterile needles connected to syringes (Omnifix, B. Braun Melsungen AG, Germany), previously purged with 80:20 % N$_2$: CO$_2$ gas mixture, through stoppers. Subsequently, the samples were centrifuged at 6,000g and 4 °C for 10 min, and the supernatant was filtered by PTFE syringe filters (0.2 μm, VWR International GmbH, Germany).

Formate and acetate concentrations were determined by using high-performance liquid chromatography (HPLC, Shimadzu Scientific Instruments, Japan) equipped with a refractive index detector RID-10A, a HiPlex H column (300 × 7.7 mm, 8 mm pore size, Agilent Technologies, USA), and a pre-column (SecurityGuard Cartridge Carbo-H, 4 × 3.0 mm, Phenomenex, USA). The liquid phase was 5 mM sulfuric acid, and samples were run at 50 °C and a flow rate of 0.5 mL min^{-1} for 30 min. Substrate concentration was determined based on a three-point external standard calibration of the peak area for each compound ($R^2 > 0.99$). pH was measured using a pH meter (LAQUAtwin pH-22, HORIBA Advanced Techno, Japan). Samples ($V = 5$ mL, $n = 6$,) from BES amended with yeast extract were also collected for the photometric determination of the chemical oxygen demand (COD). Measurements were conducted using the tube test COD 1500 (REF 985029) of the NANOCOLOR® series (Macherey-Nagel GmbH & Co., KG, Germany) according to the manufacturer's instructions.

2.4. Charge and coulombic efficiencies calculation

Produced Charge (Q_p, C) was obtained by integrating the current (I, A) during anodic enrichments over time (t, s) (Eq. (1).

$$Q_p = \int_0^t I \, dt \tag{1}$$

Theoretical charge production (Q_t, C) was calculated assuming all electrons released from substrate oxidation were transferred to the anode (Eq. (2).

$$Q_{t,i} = (\Delta C_i \times z \times V \times F) \tag{2}$$

ΔC_i is change in acetate or formate concentration (mol L^{-1}), z is number of electrons transferred to the anode (8 and 2 electrons for acetate and formate, respectively), V is working volume of bioelectrochemical reactors (0.1 L), and F is the Faraday constant (96,485 C mol^{-1}).

As yeast extract provides alternative chemically oxidable compounds to the medium, we complementarily calculated Q_t as noted in Eq. (2) but considering the change in COD (i.e., $z = 4$ electrons per O$_2$ molecule).

In addition, coulombic efficiency (CE) was calculated as the ratio of the produced charge (Q_p) and the theoretical charge production (Q_t), as described in Eq. (3) or Eq. (4).

$$CE = \frac{Q_p}{Q_{t,acetate} + Q_{t,formate}} \times 100\% \tag{3}$$

where $Q_{t,acetate}$ and $Q_{t,formate}$ are theoretical charge productions based on acetate and formate consumption, respectively. Alternatively, when acetate was produced rather than microbially utilized, CE was calculated as follows:

$$CE = \frac{Q_p + Q_{t,acetate}}{Q_{t,formate}} \times 100\% \tag{4}$$

2.5. Microbial community analysis of enriched electroactive microorganisms

BES were transferred into an anaerobic glove box to collect biomass samples from solution and working electrodes after stopping enrichment experiments. Planktonic cells were harvested by transferring the remaining solution to sterile centrifugation tubes (30 mL, $n = 3$ for each reactor), centrifuging (10,000g, 4 °C, 2× 10 min), and discarding the resulting supernatant. As biofilm formation was not visually discernible, biomass collection proceeded by collecting whole electrodes in sterile Eppendorf tubes ($n = 3$ per bioelectrochemical enrichment experiment). To directly compare the enrichment cultures with the bacterial community indigenous to Lake Medard's bottom water, 40 mL ($n = 2$) of the inoculum were also treated with the same procedure. Planktonic cells and electrodes were stored at −20 °C prior to genomic DNA extraction. The latter proceeded by using the NucleoSpin® Tissue Kit (Macherey-Nagel GmbH & Co. KG, Germany), and the resulting gDNA yield was quantified by using an Invitrogen Qubit Fluorometer and Qubit dsDNA HS Assay (Thermo Fisher Scientific, USA), according to manufacturer instructions.

To analyze the microbial community composition, the V3-V4 region of the bacterial 16S rRNA genes was amplified using the primers 341f (5′-CCT ACG GGN GGC WGC AG-3′) and 785r (5′-GAC TACHVG GGT ATC TAA KCC-3′) as described by Klindworth et al. [42]. The sequencing library was prepared according to the Illumina 16S Metagenomic Sequencing Library Preparation protocol. PCR reactions were performed with the MyTaq HS Red Mix, 2× (Bioline, Germany). The raw demultiplexed data were processed with the QIIME 2 2019.4 pipeline [43] using the dada2 workflow based on the amplicon sequence variant (ASV) approach [44]. The taxonomic assignment was done using the SILVA 138 reference database [45,46]. Chimera and non-bacterial sequencing reads were removed from the dataset. Further statistical analyses were performed with the R packages phyloseq [47], Ampvis 2 [48], and ggplot2 [49]. Demultiplexed raw sequence data were deposited at the EMBL European Nucleotide Archive (ENA) under the study accession number PRJEB64920.

2.6. Scanning electron microscopy and energy-dispersive X-ray spectroscopy

Scanning electron microscopy (SEM) was performed on representative sampled electrodes from primary and secondary enrichments amended with yeast extract. Electric connections were detached under 95:5 % N$_2$:H$_2$ atmosphere, and electrodes were stored in sterile Eppendorf tubes inside an anaerobic glove box (Coy Laboratory Products, Inc., USA) before analysis. Photos of electrode surfaces were obtained by employing a MIRA3 field emission scanning electron microscope (FEG-SEM, Tescan, Brno, Czech Republic). Imaging proceeded by operating the instrument at 15.0 kV and 17 mm working distance for magnifications ranging from 5000× to 30,000×. The elemental composition of the surface was analyzed by field emission scanning electron microscopy (Zeiss Merlin VP Compact, Carl Zeiss Microscopy, Oberkochen, Germany) in combination with an energy dispersive X-ray spectrometer (Bruker Quantax X-Flash, Bruker Nano GmbH, Germany). In order to achieve effective ionization of 3D metals, an electron acceleration voltage of 18 kV was chosen. For each sample, five fields-of-view were randomly selected and X-ray spectra were acquired. Using the Bruker Esprit software, the bremsstrahlung background was removed from the spectra, and the relative concentration of the detected chemical elements was determined.

3. Results and discussion

3.1. Anodic enrichment

We enriched EAM from the monimolimnion of Lake Medard using

one-chamber BES. An anode potential of 0.2 V (versus SHE) was applied as preliminary experiments showed it to be more suitable than 0 V and 0.4 V (Fig. S3, Table S1). However, the experiments exhibited a rather erratic and hardly reproducible current production and, thus, growth of EAM. This is illustrated by the presentation of results from only 12 out of a total of > 40 experiments (Table S1) in the present manuscript (Fig. 1) as obtained current densities (j) varied considerably. The first experiments were conducted only with acetate as energy and carbon source. From these, only one replicate exhibited low electroactivity, reaching 1 $\mu A\ cm^{-2}$ after ca. 50 days of cultivation (Fig. S4). Therefore, the following experiments were performed using acetate and formate (10 mM each) as energy and carbon sources (Fig. 1a). Although considerable amounts of acetate (42 ± 10 %) and formate (95 ± 7 %) were consumed in the second set of experiments (Table S2), the initial j was consistently low (<2 $\mu A\ cm^{-2}$) during > 10 days of cultivation (i.e., 1st batch cycle). Simultaneous addition of 10 mM acetate and 10 mM formate led to an increase in j, reaching 4-6 $\mu A\ cm^{-2}$ during the 2nd batch cycle. While the measured current generation conclusively indicates weak EAM activity, as evidenced by the negligible current in the abiotic controls (<0.01 $\mu A\ cm^{-2}$, Fig. S5) and control experiments with only lake water (Fig. S6), this activity was not sustained. Notably, a second organic substrate addition did not lead to an increase in current production. Instead, it resulted in the accumulation of acetate and formate, suggesting a change in microbial activity or substrate utilization dynamics.

To distinguish the contribution of biofilm and planktonic cells to the current production, electrodes and planktonic cells were separated in additional experiments. By doing so, a working electrode was transferred to laboratory bottles with fresh medium in an anaerobic glove box, and the old medium was equipped with a new set of electrodes. In this experiment, planktonic cells showed an electrogenic response that reached a current density comparable to the original BES for media containing acetate, acetate and formate, and additional yeast extract (for each experiment $n = 1$, Fig. S7). In contrast, the transferred electrodes exhibited considerably lower current densities, indicating that planktonic cells were the main contributor to current production.

Nevertheless, a low level of electrogenicity, substantially higher than abiotic controls (Fig. S5), could also be attributed to microbial cells attached to the transferred electrodes as they exhibit a stable j of ca. 0.4 $\mu A\ cm^{-2}$ during the whole experimental time.

Following this observation, a method [50] for enriching EAM was performed. In these secondary enrichment experiments, new BES ($n = 3$) with planktonic cells anaerobically harvested from one replicate of primary enrichment experiments (replicate R1, Fig. 1a). Compared to primary enrichments, a more rapid current increase was observed after 3-4 days, indicating a successful EAM selection (Fig. 1b). j reached similar values compared to primary enrichment experiments. However, current production also did not recover after substrate addition indicating a time-dependent inhibition of electrogenicity (Fig. S8a,b).

To facilitate EAM enrichments, a new set of experiments was conducted by amending the medium with yeast extract (1.8 mM). Yeast extract can act as electroactivity enhancer by providing redox shuttles such as flavins and further carbon and electron sources [51,52]. Yeast addition considerably reduced the lag phase to 5–6 days but similar maximum current densities (j_{max}) were obtained in the first batch cycle (5.2 ± 1.2 $\mu A\ cm^{-2}$; Fig. 1c); while formate (98 ± 3 %) and acetate (36 ± 26 %) were consumed (Table S2). This observation was confirmed during secondary enrichment experiments with yeast extract-amended medium (i.e., $n = 3$, inoculated with R1 from primary enrichments, Fig. 1c) decreasing the lag phase to ca. 3 days in the case of two replicates, while j was similar (Fig. 1d). Nevertheless, EAM activity and current production were also not maintained using the yeast extract-amended medium. Addition of acetate and formate (10 mM each) only resulted in the occurrence of short peaks ($j_{max} = 25\ \mu A\ cm^{-2}$ for a few hours), while substrate consumption was lower than during primary enrichments (Table S2). Surprisingly, few BES showed acetate production (Table S2 and section 3.2). All experiments showed final pH values that ranged from 6.8 to 7.2. For a few yeast-amended experiments (Table S1), riboflavin (20 μM) and humic acids (50 μM) were added to the medium to improve mediated EET capabilities (e.g., [53,54]).
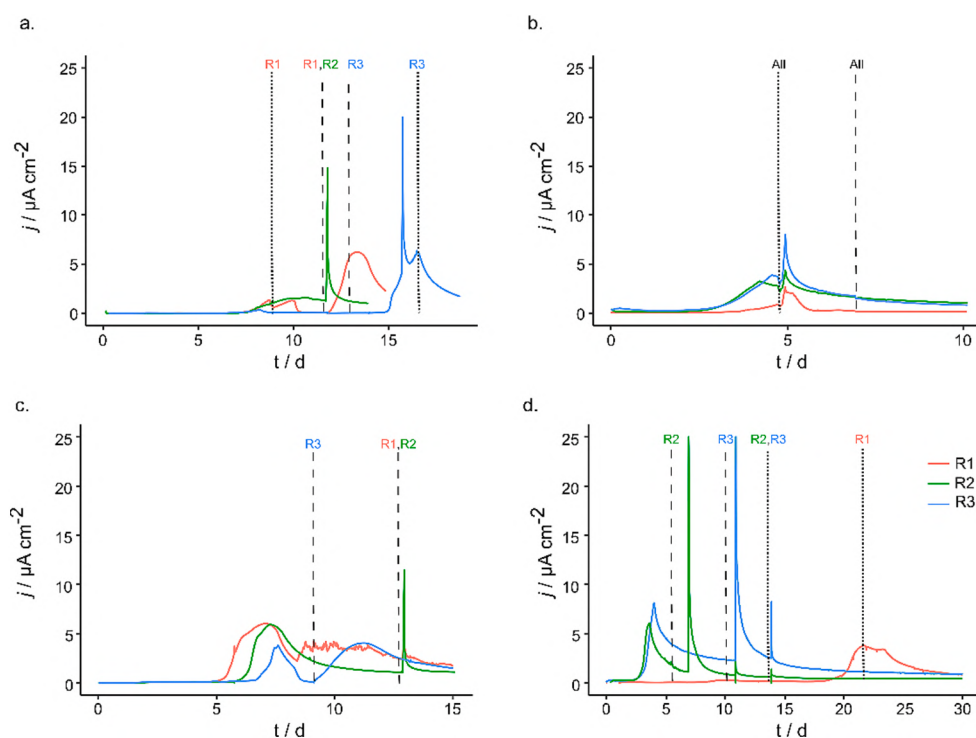
Fig. 1. Current densities during primary (a, c) and secondary (b, d) anodic enrichments ($n = 3$) of electroactive microorganisms by using ferruginous water from the monimolimnion of Lake Medard as inoculum. Medium contained acetate and formate (a, b) or additional yeast extract (c, d). Sharp current peaks were observed after sampling events followed by substrate addition (dashed lines), alternative sample collection, or cyclic voltammetry (dotted lines).

However, no significant *j* increase was observed (Fig. S8c, d).

In summary, obtaining reproducible cultivation results presented a significant challenge, a phenomenon frequently observed in studies focusing on enriching weak electricigens and other EAM [32,33]. Considering the low temperature (<10 °C) and low substrate availability (acetate <80 nM, formate <40 nM) in the sampled water column, a low microbial abundance in the inoculum was expected, which likely restricted bioelectrochemical cultivation approaches. Considering also the experimental parameters that can be varied (e.g., substrate amount and composition, one-chamber or-two-chamber systems, and different anode potential) in a more comprehensive study, the limitations of the used BES (i.e., 100 mL lab bottles) become apparent and call for reliable high-throughput methods [55–57]. Further experimental considerations might be needed to increase electric current output, such as (i) increasing the surface area of working electrodes (e.g., by using carbon felt) [17] or (ii) adding redox mediators (e.g., AQDS) [58]. These alternatives, however, could also bring additional challenges, such as masking the signal of redox pairs during cyclic voltammetry (CV) or increasing capacitive currents [32]. In addition, experiments with weak electricigens and high surface electrodes need to be accompanied by appropriate and sufficient abiotic control experiments to allow discrimination of the expected low current output compared to the increased reaction area for abiotic electrochemical reactions.

CV was performed to obtain information about the electrochemical properties of the enriched microbiome. However, similar to chronoamperometric cultivation, the interpretation of results was challenging as the electrochemical response was not reproducible. Especially the experiments with formate and acetate showed high anodic current peaks between 0.0 V and 0.2 V during turnover conditions being significantly higher than j_{max} during chronoamperometric cultivation (Fig. 2a, b). This indicates no steady-state conditions during CV

(Fig. S9). Nevertheless, these oxidative peaks were likely related to microbial activity as they were not observed in abiotic controls experiments (Fig. S10). It must be noticed that the redox reactions seemed to be irreversible because no reductive peaks were observed (Fig. 2 and Fig. S9). We speculate that the lack of reductive peaks was caused by the dissimilatory reduction of sulfate and reactive Fe(III), followed by their precipitation on the anode surface [59] (see section 3.4). These biomineralization reactions were primarily influenced by the high proportion of these reactants (16 mM sulfate and 32 μM Fe) in the inoculum [36,60]. Based on previous reports [59], the produced sulfide and reduced iron species could be reoxidized at more positive potentials but to an electrochemical inert derivate, thus leaving the electrode surface passivated and preventing further EET reactions [59]. The similarity of voltammograms recorded at turnover (Fig. 2c) and non-turnover (Fig. S11) conditions with yeast-amended medium indicates that redox compounds within the yeast extract interfere with redox signals from EAM.

3.2. Charge balance and coulombic efficiency

For calculating charge balances, all electron sources (acetate, formate, yeast extract) and sinks (current, acetate formation) were considered and converted to charge equivalents (Fig. 2). The overall produced charge was small as compared to the consumed substrate in all replicates leading to low coulombic efficiencies (*CE*) ranging from 0.1 to 5.3 %, both in primary and secondary enrichments (Table S2). Likely, the high concentration of sulfate in the inoculum (ca. 16 mM) and the applied cultivation conditions (e.g., 10 mM acetate and formate) led to the emergence of sulfate reducers lowering *CE* (see also sections 3.3 to 3.5). However, low *CE* has also been described as a common feature of weak electricigens, which are known for developing successful surviving
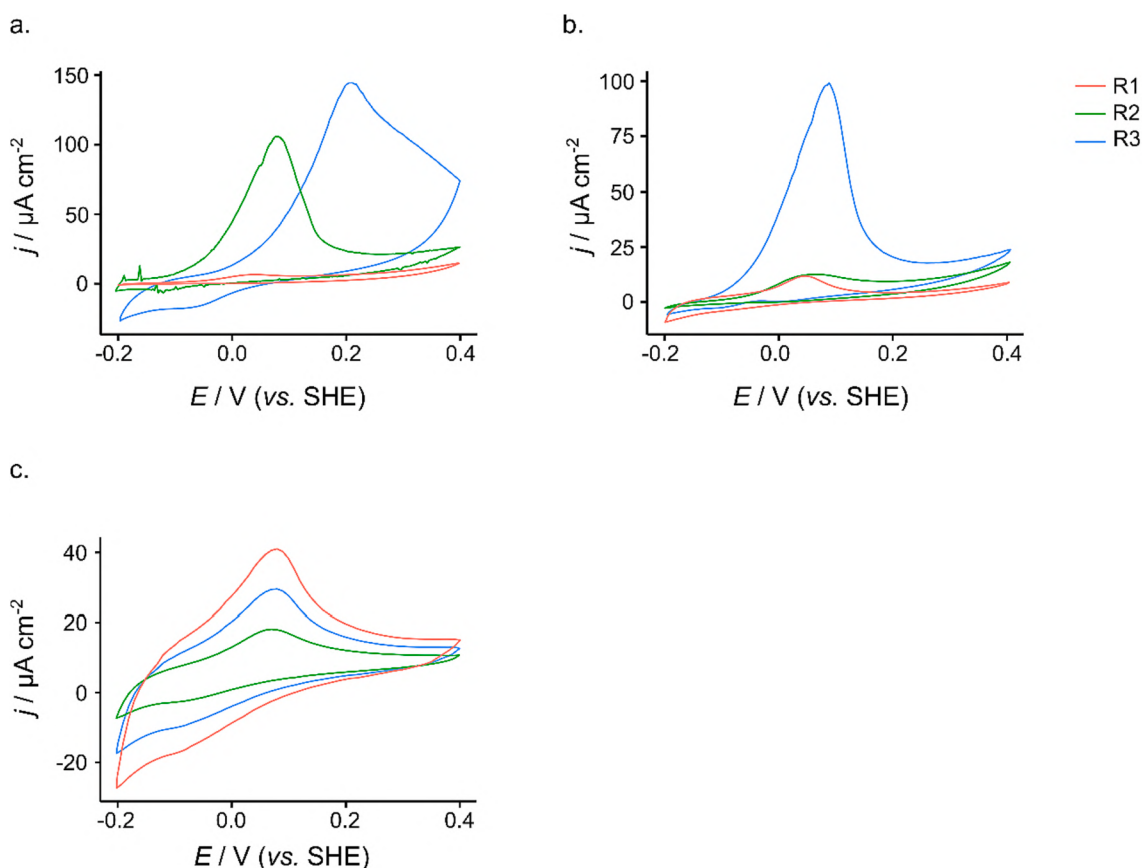
Fig. 2. Cyclic voltammograms recorded during turnover conditions of primary and secondary anodic enrichments with acetate and formate as carbon and electron source (a, b), and primary enrichments with yeast extract-amended medium (c). Scan rate was 1 mV s^{-1} and only 3rd cycles are shown.

strategies to deal with detrimentally evolving growth conditions [32,33]. One replicate was an exception (Fig. 3a, R2), with a high *CE* of 84.1 %. The high *CE* was associated with considerable acetate production accompanied by formate consumption in the second batch cycle. Acetogenesis was more often observed for the enrichments with yeast extract (Fig. 3 a,b). These exhibited highly variable *CE* ranging between 1.0 and 261.9 %, and 12.3 to 154.7 % for primary and secondary enrichments, respectively (Table S2). EET involving formate dehydrogenase has been well described for the facultative anaerobe *Shewanella oneidensis*, a model EAM that prefers planktonic growth and thrives in many redox-stratified environments [54,61,62]. However, neither is *Shewanella* described to produce acetate based on formate utilization nor was it detected by bacterial 16S rRNA amplicon sequencing (section 3.3).

In one-chamber BES, the consumption of cathodically produced hydrogen can lead to *CE* greater than 100 % [63]. However, in our experiments, this effect is unlikely, because the current production contributes minimally to the overall charge balance and is insignificant when considering the charges required for acetogenesis (Fig. 3). As the *CE* calculations are solely based on formate and acetate consumption, yeast extract compounds could have contributed to the observed high *CE* accompanied by acetogenesis. To verify this assertion, chemical oxygen demand (COD) measurements were performed capturing all oxidizable organic compounds in solution. However, for replicates showing a significant acetate production, COD consumption did not exceed the formate consumption normalized to charge equivalents (Fig. S12, Table S3). These results indicate that acetogenesis was product of fermentation processes rather than the consequence of adding yeast extract to the mineral medium. As the counter electrodes exhibited potentials ranging from -1.0 to -0.6 V (vs. SHE, Fig. S13), cathodically produced hydrogen may have also played a role in acetogenesis.

3.3. Analysis of the microbial community composition

Bacterial 16S rRNA amplicon sequencing was performed to analyze the bacterial community composition of enrichment experiments.

Previous research showed that *Geobacter* spp., a well-known Fe(III)-reducing bacteria, occurs in the sampled anoxic waters [36,40]. However, members of the *Geobacteraceae* family were not identified in the inoculum. Instead, *Ferribacterium* spp. (26.0 ± 7.6 %) and *Rhodoferax* spp. (28.8 ± 10.1 %) dominated the microbial community. Interestingly, *Ferribacterium* spp. were not previously quantified at the lake microbiome; while *Rhodoferrax* spp. were predominant only in the microaerophilic zone of the water column, and with relative abundances decreasing significantly towards the anoxic monimolimnion [36,40]. Differences of our results with previous bacterial 16S rRNA amplicon sequencing could be related to unaccounted changes in the bacterial community composition due to seasonal variability, storage before inoculation of experiments [64], or method bias when processing 16S rRNA amplicon sequencing data [65].

Although Fe(III)-reducing bacteria dominated the inoculum, the applied enrichment strategy resulted in a more diverse community. Acetate and formate mainly promoted the growth of sulfate-reducing bacteria (*Desulfatomaculum* spp., 61.7 ± 7.5 % relative amplicon abundance). Also, species capable of Fe(III) reduction (e.g., *Klebsiella* spp., 7.8 ± 3.0 %) and bacteria already observed in anodic BES (e.g., *Aquabacterium* spp., a known nitrate-reducer, 18.8 ± 9.6 %) were detected. In contrast, addition of yeast extract decreased the dominance of sulfate-reducing bacteria (*Desulfotomaculum* spp., 31.9 ± 18.8 %) but enhanced growth of bacteria belonging to the gram-negative genus *Stenotrophomonas* (26.6 ± 15.3 %), and *Klebsiella* (42.9 ± 40.0 %) which also comprises known EAM [6,66].

Whereas some EAM are known for mediated EET to insoluble conductive materials (e.g., species of *Klebsiella* [6,67]) and likely contributed to current production, other genera were previously enriched only under cathodic conditions (e.g., species of *Desulfotomaculum* and *Desulfosporosinus* [68,69]). This led to doubts about their role in anodic enrichments. Preliminary insights could be drawn from their ability to perform acetogenesis [69,70] as observed in enrichments with yeast extract (section 3.2), but further research is needed to explore their actual function in anodic BES. Although the sulfate concentration was moderate in the reactor volume (i.e., <7.0 mM, mainly originating from
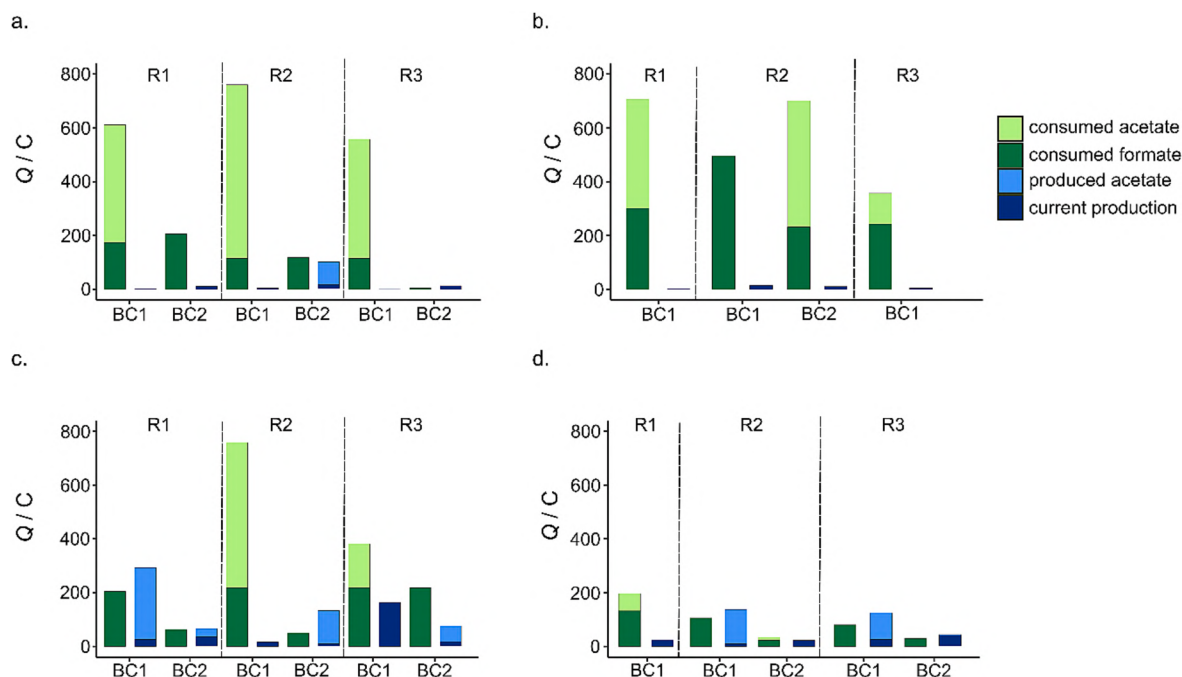
Fig. 3. Comparison between the experimental charge (Q) produced by electroactive microorganisms (■) and the theoretical charge based on the utilization of formate and acetate (■) during primary (a, c) and secondary (b, d) anodic enrichments ($n = 3$, R1-R3). Medium contained an acetate and formate mixture as electron source (a, b), alternatively, yeast extract was amended to medium (c, d). Charge production was delimitated by batch cycles (BC, i.e., substrate consumption indicated by current decay).

the anoxic water used as inoculum [36,40]; Fig. S1), the produced sulfide can likely be reoxidized at the applied anode potential [71] leading to continuous recycling of sulfate which promoted the growth of sulfate reducers together with the high availability of organic substrates. Apparently, sulfate reducers outcompeted EAM under these conditions suggesting the relevance of using specific inhibitors for sulfate-reduction, like adenosine-5′-phosphosulfate in furthering cultivation approaches as inhibition by high formate concentrations does not apply for all sulfate-reducers [72,73].

No gDNA could be extracted from secondary enrichment experiments amended with formate and acetate, but it was obtained from BES amended with yeast extract. In those BES, and contrary to our expectations of further enriching the dominant species of primary enrichment experiments [74], the microbial community considerably differed from the proceeding enrichment (Fig. 4). Two replicates of the BES containing yeast were dominated by the fermentative electricigen *Paeniclostridium* spp. [75] (76.7 ± 4.7 %) [70]. A high occurrence of *Stenotrophomonas* spp. (up to 54.1 %) was observed for the other replicate. Sufficient biomass formation at electrodes allowing amplicon sequencing only occurred in two replicates with yeast amendment, and the microbial composition of the biofilm resembled the community in the planktonic phase (Fig. S14).

Interestingly, the one replicate with only acetate as the substrate that displayed a slowly increasing current production (Fig. S4) was dominated by the Fe(III)-reducer *Geothrix* spp. (Fig. S14; 71.6 %). Species of *Geothrix* are described as slow-growing bacteria that thrive by oxidizing fatty acids (e.g., acetate and lactate) and conducting mediated EET to Fe(III)-oxyhydroxides and electrodes [5,76].

3.4. Characterization of anode surfaces

Electrode passivation during cultivation of EAM can result from the formation of insulating precipitates at the electrode surface. To investigate this possibility, a few anodes were anaerobically sampled, stored after cultivation, and analyzed with scanning emission microscopy (SEM) and energy-dispersive X-ray spectroscopy (EDX). For all tested enrichment conditions, the analyses clearly displayed fossilized rod-shaped cells of different lengths embedded within aggregates of microcrystalline mineral nanoparticles (Fig. 5a-c). These aggregates apparently precipitated during initial stages of biofilm formation and were absent from blank electrodes (Fig. 5e). EDX analyses of the precipitates mainly highlighted sulfur accumulation (12.2 ± 5.5 %, normalized to atom weight) in all enrichments, but also increased amounts of iron (1.9 ± 0.1 %), and phosphorus (1.3 ± 0.1 %).

Other trace metals like cobalt and manganese were also detected (Fig. S15 and Table S4). Accumulation of these redox-active elements was likely the product of biomineralization reactions because the observed microbial-mineral textures were absent at the surface of blank anodes with negligible elemental contents other than carbon from graphite electrodes (Fig. S15 and Table S4). Other than sorption, sulfur and iron precipitation were likely promoted by the metabolic capabilities of the detected sulfate reducers (e.g., *Desulfotomaculum* and *Desulfosporosinus* [23,69,70,77]). Sulfide oxidation could had also contributed to anode passivation by inducing iron-coprecipitation with zero-valent sulfur within the bioinorganic aggregates. In primary enrichment experiments, sulfur and iron precipitations were likely facilitated by their high concentrations in the inoculum (Fig. S1), followed by alteration of their oxidation states during CV [59]. Although lake water was not used in secondary enrichment experiments, EDX analysis showed a substantially higher fraction of iron and sulfur at the electrode (Table S4) suggesting that the transferred cell pellet contained sufficient amounts of these elements to passivate electrodes. For instance, sulfate-reducing bacteria are known to mineralize zero-valent sulfur [78]. However, biomineralization probably affected BES by decreasing the number of attachment sites for EAM and redox-active sites for mediated EET [79].

3.5. Enriching electroactive microorganisms from ferruginous lake water

The experiments were designed to enrich electroactive microorganisms, however, most of the enrichment cultures were dominated by sulfate-reducing microorganisms. Although, a certain genetic potential for microbial sulfate reduction at bottom waters of Lake Medard was recently highlighted [36], the extent of dominance was not expected as
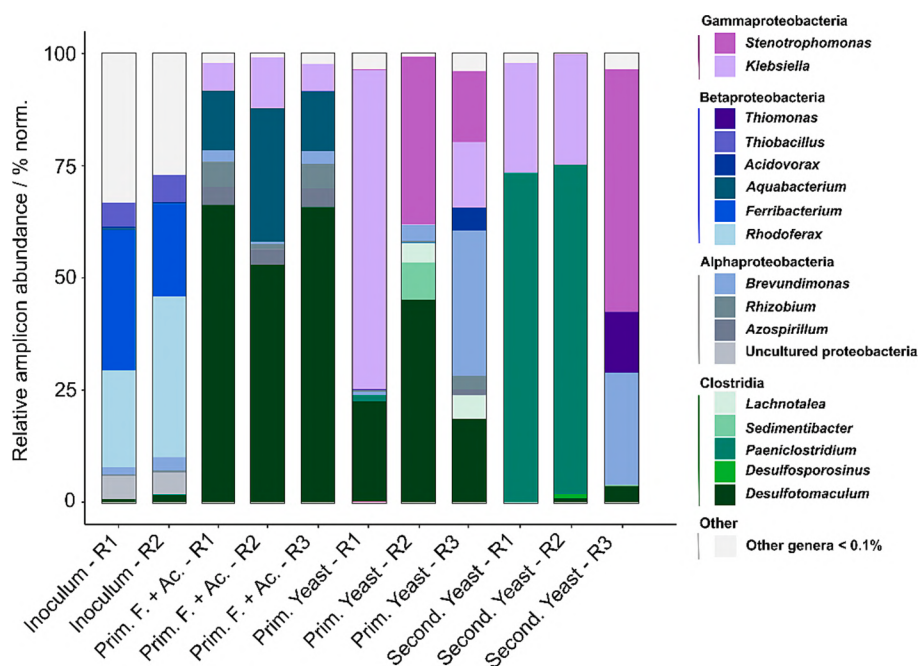
Fig. 4. Microbial community analysis, based on the genus level, of the planktonic phase from primary (prim.) and secondary (second.) anodic enrichments and inoculum by performing bacterial 16S rRNA amplicon sequencing. The medium contained acetate and formate (F + Ac) or was additionally amended with yeast extract (Yeast).
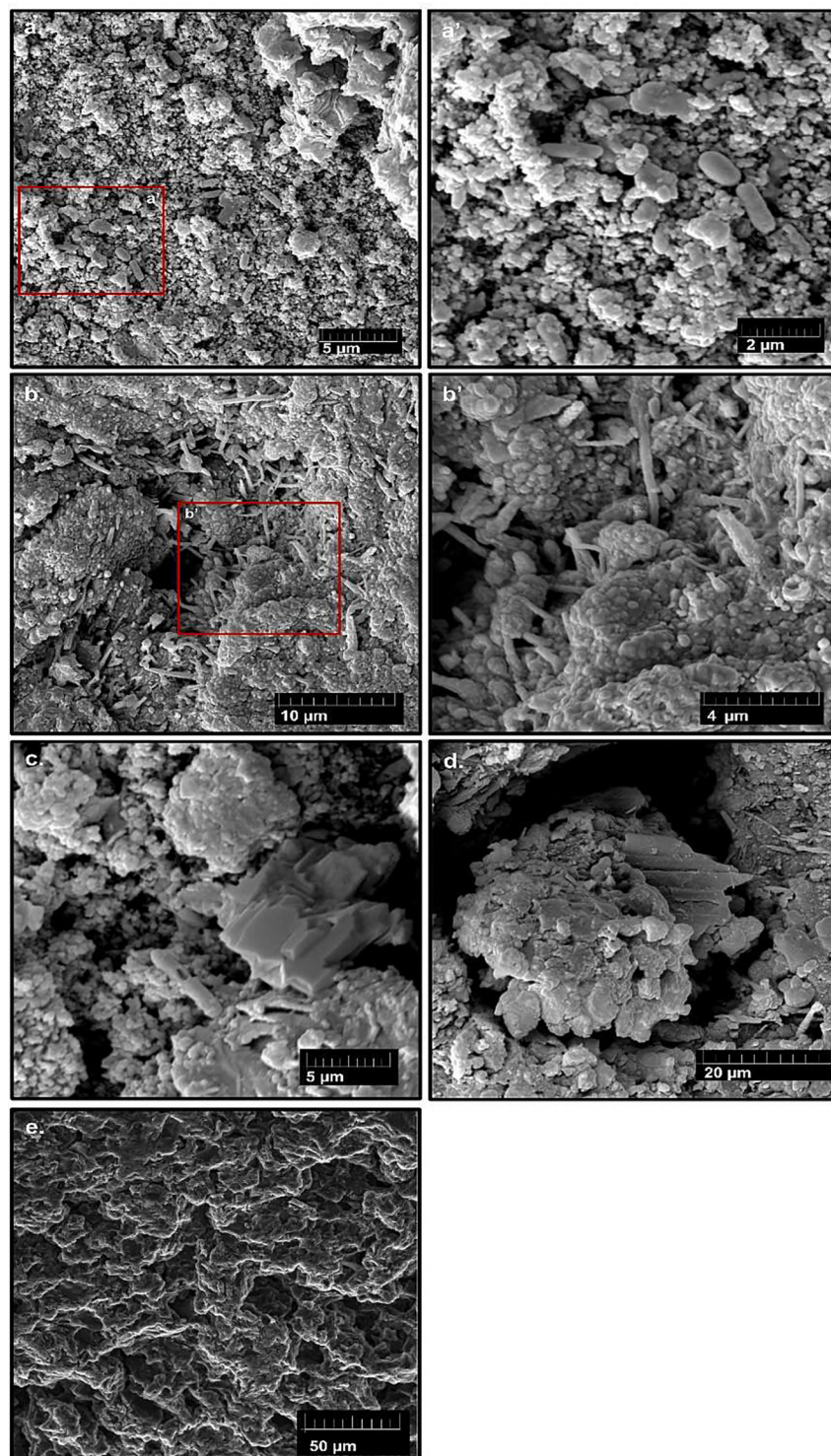
Fig. 5. Scanning electron microscopy photos portraying inorganic precipitates with embedded microorganisms and extracellular polymeric substances on the surface of working electrodes from primary (a) and secondary (b) enrichments amended with yeast extract. Microbial activity at the anode surface stimulated the precipitation of microcrystalline minerals, in both primary (c) and secondary (d) enrichments, that were absent at the surface of control anodes (e). a' and b' represent higher magnifications of a and b, respectively.

the abundance of microorganisms related to sulfur metabolism was low in the inoculum (1 % of *Desulfatomaculum* spp. (sulfate reducer) and ca. 5 % of *Thiobacillus* spp. (sulfide oxidizer), Fig. 4). Apparently, sulfate-reducing metabolisms are limited in the bottom waters of Lake Medard by the low amounts of available carbon and energy sources (e.g., <80 nM acetate and <40 nM formate, Fig. S1) which was no longer the case during anodic enrichments. Based on thermodynamics, Fe(III)-

reducing metabolisms ($E^{0'}(Fe^{3+}/Fe^{2+}) = 0.77$ V) are clearly favored over sulfate reducers ($E^{0'}(SO_4^{2-}/HS^-) = -0.22$ V) for biochemical standard conditions, however, it is also assumed that the energy harvest of EAM and other metal-respiring microorganisms is limited compared to microorganisms using soluble terminal electron acceptors [80,81].

Co-occurrence of Fe(III)-reducing and sulfate-reducing

microorganisms is observed in many anoxic habitats where iron reducers seemingly have a slight advantage due to their higher affinity for organic substrates [82–85]. However, pH and abiotic reactions also contribute to this complex interplay [86]. For example, the use of one-chamber BES resulted in an availability of cathodically produced hydrogen that likely supported the growth of sulfate reducers capable of hydrogenotrophy. Moreover, 'cryptic sulfur cycles', often occurring in sediment or aquatic environments, involves a series of subtle transformations of sulfur compounds, where sulfur is repeatedly oxidized and reduced, often through interactions with Fe(III)-oxyhydroxides [87]. This results in the formation and consumption of various sulfur intermediates without significant net changes in sulfur's oxidation state [88,89].

The anode potential of 0.2 V might have permitted abiotic sulfide oxidation to sulfur (Supplementary Material 1). However, estimating the contribution of sulfide oxidation to current production in BES is challenging due to sulfur being repeatedly oxidized and reduced. Continuous sampling and measuring of several sulfur species would have been required. However, assuming that sulfate is completely reduced (i.e., resulting in 6 mM sulfide based on 40 % v/v inoculum with a sulfate content of ca. 16 mM, Fig. S1), a charge of 124 C can be calculated based on complete re-oxidation to elemental sulfur which would have represented a substantial fraction of the total charge of many experiments (Fig. 3).

Future research efforts using as inoculum water from Lake Medard or other ferruginous anoxic waters bearing substantial dissolved sulfate levels should avoid the emergence of sulfate reducers in order to successfully enrich weak electricigens and other EAM. This could be achieved by (i) removing the sulfate from the inoculum by anaerobic centrifugation, filtration, or chemical precipitation, or (ii) adding selective inhibitors for sulfate reduction (e.g., adenosine-5′-phosphosulfate).

4. Conclusions

By using anoxic ferruginous waters from a post-mining lake as inoculum for anodic enrichments of electroactive microorganisms (EAM) and different variations of carbon and electron source (only acetate, acetate and formate, and additional yeast extract), only small amounts of current were generated. The enriched bacterial communities were diverse and rarely showed clear patterns. For instance, *Geothrix* was only enriched in one replicate with acetate. Well-known EAM were rarely detected despite the inoculum contained substantial amounts of Fe(III)-reducing bacteria. Instead, sulfate- and nitrate-reducing bacteria dominated the enrichments, while Fe(III)-reducers represented a relatively small share. Current production predominantly depended on the consumption of formate by planktonic cells instead of biofilms attached to anodes. A charge balance analysis hinted that formate consumption was potentially coupled to acetogenesis in some experiments, which is rarely described [90,91].

Cyclic voltammetry, scanning emission microscopy, and energy-dispersive X-ray spectroscopy results indicate the irreversible formation of microcrystalline nanoparticles at the anode surface, leading to its passivation. The high share of detected sulfate reducers also suggests their contribution to this electrode passivation together with the electrochemical oxidation of sulfide. Therefore, selective inhibitors for sulfate reduction (e.g., adenosine-5′-phosphosulfate) should be used in attempts to enrich EAM from sulfate-rich lakes like Medard. Alternatively, chemical sulfate precipitation and anaerobic centrifugation or filtration could be applied to provide a sulfate-free inoculum to enrich weak electricigens and other EAM from anoxic ferruginous waters or similar habitats. Future experiments could be performed with two-chamber systems avoiding hydrogen crossover, which is also a preferred substrate of many sulfate reducers. Besides the screening of further short-chain fatty acids as carbon and energy sources, different anode potentials should also be in the focus of future experimental

efforts. Together with the number of replicates required to obtain reproducible results, this indicates the demand for high-throughput methods to enrich weak electricigens and other EAM. Despite the assumption that the not maintained current production is a result of non-conductive precipitates at the anode and outcompetition of EAM by sulfate reducers, the low current generation and the lack of typical EAM in the community analysis indicate the enrichment of weak electricigens, which shifted from sulfur (e.g., *Desulfotomaculum* spp.) and nitrogen (e.g., *Aquabacterium* spp.)-based metabolism to an alternative electrogenic pathway (see [33] and references therein).

Consequently, these bacteria could drive relevant mineral transformations based on formate oxidation and interlink Fe, S, N, and P cycles as observed in the redox-stratified water column of Lake Medard and ferruginous analogs. The detected microorganisms *Desulfotomaculum* spp., *Klebsiella* spp., and *Geothrix* spp. hold potential for powering BES designed for metal recovery because respective close relatives perform dissimilatory Fe(III) reduction [5,6,23,67,76], which can drive the biomineralization of oxyhydroxides, phosphates, and sulfides [25]. Overall, our study clearly shows that cultivation conditions need further optimization, and specific inhibitors for sulfate reducers should be used to explore the biomineralization reactions in Lake Medard or comparable environments, and to enrich weak electricigens and other EAM aiming at recovering critical metals from naturally and anthropogenically metal-enriched waters.

CRediT authorship contribution statement

Astolfo Valero: Writing – original draft, Methodology, Investigation, Formal analysis, Data curation. **Daniel A. Petrash:** Writing – review & editing, Supervision, Project administration, Funding acquisition, Conceptualization. **Anne Kuchenbuch:** Writing – review & editing, Visualization, Methodology, Investigation. **Benjamin Korth:** Writing – review & editing, Methodology, Supervision, Conceptualization.

Declaration of competing interest

The authors declare the following financial interests/personal relationships which may be considered as potential competing interests: Daniel A. Petrash reports financial support was provided by Czech Science Foundation. Astolfo Valero reports financial support was provided by German Academic Exchange Service.

Data availability

Data will be made available on request.

Acknowledgements

Appendix A. Supplementary material

Supplementary data to this article can be found online at https://doi.org/10.1016/j.bioelechem.2024.108661.

References

[1] S. Kato, K. Hashimoto, K. Watanabe, Microbial interspecies electron transfer via electric currents through conductive minerals, PNAS 109 (2012) 10042–10046, https://doi.org/10.1073/PNAS.1117592109.

[2] L. Shi, H. Dong, G. Reguera, H. Beyenal, A. Lu, J. Liu, H.Q. Yu, J.K. Fredrickson, Extracellular electron transfer mechanisms between microorganisms and minerals, Nature Reviews Microbiology 14 (2016) 651–662, https://doi.org/10.1038/nrmicro.2016.93.

[3] D.R. Lovley, Bug juice: harvesting electricity with microorganisms, Nature Reviews Microbiology 4 (2006) 497–508, https://doi.org/10.1038/nrmicro1442.

[4] D.R. Lovley, Electrotrophy: Other microbial species, iron, and electrodes as electron donors for microbial respirations, Bioresour. Technol. 345 (2022) 126553, https://doi.org/10.1016/J.BIORTECH.2021.126553.

[5] M.G. Mehta-Kolte, D.R. Bond, Geothrix fermentans secretes two different redox-active compounds to utilize electron acceptors across a wide range of redox potentials, Appl. Environ. Microbiol. 78 (2012) 6987–6995, https://doi.org/10.1128/AEM.01460-12.

[6] X. Li, L. Liu, T. Liu, T. Yuan, W. Zhang, F. Li, S. Zhou, Y. Li, Electron transfer capacity dependence of quinone-mediated Fe(III) reduction and current generation by Klebsiella pneumoniae L17, Chemosphere. 92 (2013) 218–224, https://doi.org/10.1016/J.CHEMOSPHERE.2013.01.098.

[7] D.R. Lovley, D.J.F. Walker, Geobacter Protein Nanowires, Front. Microbiol. 10 (2019) 2078, https://doi.org/10.3389/FMICB.2019.02078.

[8] D.R. Lovley, Syntrophy Goes Electric: Direct Interspecies Electron Transfer, Annu. Rev. Microbiol. 71 (2017) 643–664, https://doi.org/10.1146/Annurev-Micro-030117-020420.

[9] N. Chabert, O. Amin Ali, W. Achouak, All ecosystems potentially host electrogenic bacteria, Bioelectrochemistry 106 (2015) 88–96, https://doi.org/10.1016/J.BIOELECHEM.2015.07.004.

[10] C. Koch, F. Harnisch, Is there a specific ecological niche for electroactive microorganisms? ChemElectroChem 3 (2016) 1282–1295, https://doi.org/10.1002/CELC.201600079.

[11] J. Kan, L. Hsu, A.C.M. Cheung, M. Pirbazari, K.H. Nealson, Current production by bacterial communities in microbial fuel cells enriched from wastewater sludge with different electron donors, Environ. Sci. Tech. 45 (2011) 1139–1146, https://doi.org/10.1021/ES102645V.

[12] D. Sun, D. Call, A. Wang, S. Cheng, B.E. Logan, Geobacter sp. SD-1 with enhanced electrochemical activity in high-salt concentration solutions, Environ. Microbiol. Rep. 6 (2014) 723–729, https://doi.org/10.1111/1758-2229.12193.

[13] A. Cabezas, B. Pommerenke, N. Boon, M.W. Friedrich, Geobacter, anaeromyxobacter and anaerolineae populations are enriched on anodes of root exudate-driven microbial fuel cells in rice field soil, Environ. Microbiol. Rep. 7 (2015) 489–497, https://doi.org/10.1111/1758-2229.12277.

[14] C. Armato, D. Ahmed, V. Agostino, D. Traversi, R. Degan, T. Tommasi, V. Margaria, A. Sacco, G. Gilli, M. Quaglio, G. Saracco, T. Schilirò, Anodic microbial community analysis of microbial fuel cells based on enriched inoculum from freshwater sediment, Bioprocess Biosyst. Eng. 42 (2019) 697–709, https://doi.org/10.1007/S00449-019-02074-0.

[15] K.B. Gregory, D.R. Lovley, Remediation and recovery of uranium from contaminated subsurface environments with electrodes, Environ. Sci. Tech. 39 (2005) 8943–8947, https://doi.org/10.1021/ES050457E.

[16] M. Wei, F. Harnisch, C. Vogt, J. Ahlheim, T.R. Neue, H.H. Richnowa, Harvesting electricity from benzene and ammonium-contaminated groundwater using a microbial fuel cell with an aerated cathode, RSC Adv. 5 (2014) 5321–5330, https://doi.org/10.1039/C4RA12144A.

[17] L.E. Doyle, P.Y. Yung, S.D. Mitra, S. Wuertz, R.B.H. Williams, F.M. Lauro, E. Marsili, Electrochemical and genomic analysis of novel electroactive isolates obtained via potentiostatic enrichment from tropical sediment, J. Power Sources 356 (2017) 539–548, https://doi.org/10.1016/J.JPOWSOUR.2017.03.147.

[18] C. Li, C.E. Reimers, Y. Alleau, Using oxidative electrodes to enrich novel members in the desulfobulbaceae family from intertidal sediments, Microorganisms. 9 (2021) 2329, https://doi.org/10.3390/MICROORGANISMS9112329.

[19] S. Yadav, R. Singh, S.S. Sundharam, S. Chaudhary, S. Krishnamurthi, S.A. Patil, Geoalkalibacter halelectricus SAP-1 sp. nov. possessing extracellular electron transfer and mineral-reducing capabilities from a haloalkaline environment, Environ. Microbiol. 24 (2022) 5066–5081, https://doi.org/10.1111/1462-2920.16200.

[20] S. Kawaichi, T. Yamada, A. Umezawa, S.E. McGlynn, T. Suzuki, N. Dohmae, T. Yoshida, Y. Sako, N. Matsushita, K. Hashimoto, R. Nakamura, Anodic and cathodic extracellular electron transfer by the filamentous bacterium Ardenticatena maritima 110S, Front. Microbiol. 9 (2018) 315537, https://doi.org/10.3389/FMICB.2018.00068.

[21] E.E. Roden, Microbial iron-redox cycling in subsurface environments, Biochem. Soc. Trans. 40 (2012) 1249–1256, https://doi.org/10.1042/BST20120202.

[22] C. Bryce, N. Blackwell, C. Schmidt, J. Otte, Y.M. Huang, S. Kleindienst, E. Tomaszewski, M. Schad, V. Warter, C. Peng, J.M. Byrne, A. Kappler, Microbial anaerobic Fe(II) oxidation – Ecology, mechanisms and environmental implications, Environ. Microbiol. 20 (2018) 3462–3483, https://doi.org/10.1111/1462-2920.14328.

[23] B.M. Tebo, A.Y. Obraztsova, Sulfate-reducing bacterium grows with Cr(VI), U(VI), Mn(IV), and Fe(III) as electron acceptors, FEMS Microbiol. Lett. 162 (1998) 193–198, https://doi.org/10.1111/J.1574-6968.1998.TB12998.X.

[24] C.A. Pearcy, D.A. Chevis, T.J. Haug, H.A. Jeffries, N. Yang, J. Tang, D.A. Grimm, K. H. Johannesson, Evidence of microbially mediated arsenic mobilization from

sediments of the Aquia aquifer, Maryland, USA, Appl. Geochem. 26 (2011) 575–586, https://doi.org/10.1016/J.APGEOCHEM.2011.01.015.

[25] J.M. Zachara, R.K. Kukkadapu, J.K. Fredrickson, Y.A. Gorby, S.C. Smith, Biomineralization of Poorly Crystalline Fe(III) Oxides by Dissimilatory Metal Reducing Bacteria (DMRB), Geomicrobiol. J. 19 (2010) 179–207, https://doi.org/10.1080/01490450252864271.

[26] A.E. Rotaru, F. Calabrese, H. Stryhanyuk, F. Musat, P.M. Shrestha, H.S. Weber, O.L. O. Snoeyenbos-West, P.O.J. Hall, H.H. Richnow, N. Musat, B. Thamdrup, Conductive particles enable syntrophic acetate oxidation between geobacter and methanosarcina from coastal sediments, MBio 9 (2018) e00226–18, https://doi.org/10.1128/MBIO.00226-18.

[27] F. Harnisch, U. Schröder, From MFC to MXC: chemical and biological cathodes and their potential for microbial bioelectrochemical systems, Chem. Soc. Rev. 39 (2010) 4433–4448, https://doi.org/10.1039/C003068F.

[28] U. Schröder, F. Harnisch, L.T. Angenent, Microbial electrochemistry and technology: terminology and classification, Energy Environ. Sci. 8 (2015) 513–519, https://doi.org/10.1039/C4EE03359K.

[29] K. Binnemans, P.T. Jones, T. Müller, L. Yurramendi, Rare Earths and the Balance Problem: How to Deal with Changing Markets? J. Sustain. Metall. 4 (2018) 126–146, https://doi.org/10.1007/S40831-018-0162-8.

[30] C. Ai, Z. Yan, S. Hou, X. Zheng, Z. Zeng, C. Amanze, Z. Dai, L. Chai, G. Qiu, W. Zeng, Effective Treatment of Acid Mine Drainage with Microbial Fuel Cells: An Emphasis on Typical Energy Substrates, Minerals 10 (2020) 443, https://doi.org/10.3390/MIN10050443.

[31] L. Zhang, H. Zhao, H. Hou, G. Zou, G. Gu, G. Qiu, Galvanic biomining: a low-carbon hydrometallurgical process for efficient resource recovery and power generation, ACS Sustain. Chem. Eng. 11 (2023) 4040–4048, https://doi.org/10.1021/ACSSUSCHEMENG.2C05784.

[32] L.E. Doyle, E. Marsili, Weak electricigens: A new avenue for bioelectrochemical research, Bioresour. Technol. 258 (2018) 354–364, https://doi.org/10.1016/J.BIORTECH.2018.02.073.

[33] K. Aiyer, L.E. Doyle, Capturing the signal of weak electricigens: a worthy endeavour, Trends Biotechnol. 40 (2022) 564–575, https://doi.org/10.1016/J.TIBTECH.2021.10.002.

[34] B.S. Mirza, S. Muruganandam, X. Meng, D.L. Sorensen, R.R. Dupont, J.E. Mc Lean, Arsenic(V), reduction in relation to Iron(III) transformation and molecular characterization of the structural and functional microbial community in sediments of a basin-fill aquifer in Northern Utah, Appl. Environ. Microbiol. 80 (2014) 3198, https://doi.org/10.1128/AEM.00240-14.

[35] J. Sánchez-España, I. Yusta, A. Ilin, C. van der Graaf, I. Sánchez-Andrea, Microbial Geochemistry of the Acidic Saline Pit Lake of Brunita Mine (La Unión, SE Spain), Mine Water Environ. 39 (2020) 535–555, https://doi.org/10.1007/S10230-020-00655-0.

[36] D.A. Petrash, I.M. Steenbergen, A. Valero, T.B. Meador, T. Paces, C. Thomazo, Aqueous system-level processes and prokaryote assemblages in the ferruginous and sulfate-rich bottom waters of a post-mining lake, Biogeosciences 19 (2022) 1723–1751, https://doi.org/10.5194/BG-19-1723-2022.

[37] I.D. Puspita, Y. Kamagata, M. Tanaka, K. Asano, C.H. Nakatsu, Are Uncultivated bacteria really uncultivable? Microbes Environ. 27 (2012) 356, https://doi.org/10.1264/JSME2.ME12092.

[38] E.J. Stewart, Growing unculturable bacteria, J. Bacteriol. 194 (2012) 4151–4160, https://doi.org/10.1128/JB.00345-12.

[39] F. Scarabotti, L. Rago, K. Bühler, F. Harnisch, The electrode potential determines the yield coefficients of early-stage Geobacter sulfurreducens biofilm anodes, Bioelectrochemistry 140 (2021) 107752, https://doi.org/10.1016/J.BIOELECHEM.2021.107752.

[40] D.A. Petrash, J. Jan, D. Sirová, N.O.A. Osafo, J. Borovec, Iron and nitrogen cycling, bacterioplankton community composition and mineral transformations involving phosphorus stabilisation in the ferruginous hypolimnion of a post-mining lake, Environ. Sci. Process Impacts. 20 (2018) 1414–1426, https://doi.org/10.1039/c8em00328a.

[41] A. Jain, A. Coelho, J. Madjarov, C.M. Paquete, J.A. Gralnick, Evidence for quinol oxidation activity of ImoA, a novel NapC/ NirT family protein from the neutrophilic Fe(II)-oxidizing bacterium sideroxydans lithotrophicus ES-1, MBio 13 (2022), https://doi.org/10.1128/MBIO.02150-22.

[42] A. Klindworth, E. Pruesse, T. Schweer, J. Peplies, C. Quast, M. Horn, F.O. Glöckner, Evaluation of general 16S ribosomal RNA gene PCR primers for classical and next-generation sequencing-based diversity studies, Nucleic Acids Res. 41 (2013) e1–e, https://doi.org/10.1093/NAR/GKS808.

[43] E. Bolyen, J.R. Rideout, M.R. Dillon, N.A. Bokulich, C.C. Abnet, G.A. Al-Ghalith, H. Alexander, E.J. Alm, M. Arumugam, F. Asnicar, Y. Bai, J.E. Bisanz, K. Bittinger, A. Brejnrod, C.J. Brislawn, C.T. Brown, B.J. Callahan, A.M. Caraballo-Rodríguez, J. Chase, E.K. Cope, R. Da Silva, C. Diener, P.C. Dorrestein, G.M. Douglas, D. M. Durall, C. Duvallet, C.F. Edwardson, M. Ernst, M. Estaki, J. Fouquier, J. M. Gauglitz, S.M. Gibbons, D.L. Gibson, A. Gonzalez, K. Gorlick, J. Guo, B. Hillmann, S. Holmes, H. Holste, C. Huttenhower, G.A. Huttley, S. Janssen, A. K. Jarmusch, L. Jiang, B.D. Kaehler, K. Bin Kang, C.R. Keefe, P. Keim, S.T. Kelley, D. Knights, I. Koester, T. Kosciolek, J. Kreps, M.G.I. Langille, J. Lee, R. Ley, Y. X. Liu, E. Loftfield, C. Lozupone, M. Maher, C. Marotz, B.D. Martin, D. McDonald, L.J. McIver, A.V. Melnik, J.L. Metcalf, S.C. Morgan, J.T. Morton, A.T. Naimey, J. A. Navas-Molina, L.F. Nothias, S.B. Orchanian, T. Pearson, S.L. Peoples, D. Petras, M.L. Preuss, E. Pruesse, L.B. Rasmussen, A. Rivers, M.S. Robeson, P. Rosenthal, N. Segata, M. Shaffer, A. Shiffer, R. Sinha, S.J. Song, J.R. Spear, A.D. Swafford, L. R. Thompson, P.J. Torres, P. Trinh, A. Tripathi, P.J. Turnbaugh, S. Ul-Hasan, J.J. J. van der Hooft, F. Vargas, Y. Vázquez-Baeza, E. Vogtmann, M. von Hippel, W. Walters, Y. Wan, M. Wang, J. Warren, K.C. Weber, C.H.D. Williamson, A.

D. Willis, Z.Z. Xu, J.R. Zaneveld, Y. Zhang, Q. Zhu, R. Knight, J.G. Caporaso, Reproducible, interactive, scalable and extensible microbiome data science using QIIME 2, Nat. Biot. 37 (2019) 852–857, https://doi.org/10.1038/s41587-019-0209-9.

[44] B.J. Callahan, P.J. McMurdie, M.J. Rosen, A.W. Han, A.J.A. Johnson, S.P. Holmes, DADA2: High-resolution sample inference from Illumina amplicon data, Nat. Methods 13 (2016) 581–583, https://doi.org/10.1038/nmeth.3869.

[45] P. Yilmaz, L.W. Parfrey, P. Yarza, J. Gerken, E. Pruesse, C. Quast, T. Schweer, J. Peplies, W. Ludwig, F.O. Glöckner, The SILVA and "All-species Living Tree Project (LTP)" taxonomic frameworks, Nucleic Acids Res 42 (2014) D643–D648, https://doi.org/10.1093/NAR/GKT1209.

[46] M.R. McLaren, Silva SSU taxonomic training data formatted for DADA2 (Silva version 138), (2020). doi: 10.5281/ZENODO.3731176.

[47] P.J. McMurdie, S. Holmes, phyloseq: An R Package for Reproducible Interactive Analysis and Graphics of Microbiome Census Data, PLoS One 8 (2013) e61217, https://doi.org/10.1371/journal.pone.0061217.

[48] K.S. Andersen, R.H. Kirkegaard, S.M. Karst, M. Albertsen, ampvis2: an R package to analyse and visualise 16S rRNA amplicon data, BioRxiv. (2018) 299537, https://doi.org/10.1101/299537.

[49] H. Wickham, ggplot2 Elegant Graphics for Data Analysis, Use r! Series, Springer, New York, 2016, 10.1007/978-0-387-98141-3.

[50] A. Baudler, S. Riedl, U. Schröder, Long-term performance of primary and secondary electroactive biofilms using layered corrugated carbon electrodes, Front. Energy Res. 2 (2014) 30, https://doi.org/10.3389/FENRG.2014.00030.

[51] M. Masuda, S. Freguia, Y.F. Wang, S. Tsujimura, K. Kano, Flavins contained in yeast extract are exploited for anodic electron transfer by Lactococcus lactis, Bioelectrochemistry 78 (2010) 173–175, https://doi.org/10.1016/J.BIOELECHEM.2009.08.004.

[52] E.T. Sayed, Y. Saito, T. Tsujiguchi, N. Nakagawa, Catalytic activity of yeast extract in biofuel cell, J. Biosci. Bioeng. 114 (2012) 521–525, https://doi.org/10.1016/J.JBIOSC.2012.05.021.

[53] M. Wolf, A. Kappler, J. Jiang, R.U. Meckenstock, Effects of humic substances and quinones at low concentrations on ferrihydrite reduction by Geobacter metallireducens, Environ. Sci. Tech. 43 (2009) 5679–5685, https://doi.org/10.1021/ES803647R.

[54] S.J. Fuller, D.G.G. McMillan, M.B. Renz, M. Schmidt, I.T. Burke, D.I. Stewart, Extracellular electron transport-mediated fe(iii) reduction by a community of alkaliphilic bacteria that use flavins as electron shuttles, Appl. Environ. Microbiol. 80 (2014) 128–137, https://doi.org/10.1128/AEM.02282-13.

[55] A. Kuchenbuch, R. Frank, J.V. Ramos, H.G. Jahnke, F. Harnisch, Electrochemical microwell plate to study electroactive microorganisms in parallel and real-time, Front. Bioeng. Biotechnol. 9 (2022) 821734, https://doi.org/10.3389/FBIOE.2021.821734.

[56] W. Miran, W. Huang, X. Long, G. Imamura, A. Okamoto, Multivariate landscapes constructed by Bayesian estimation over five hundred microbial electrochemical time profiles, Patterns 3 (2022) 100610, https://doi.org/10.1016/j.patter.2022.100610.

[57] T.R. Molderez, A. Prévoteau, F. Ceyssens, M. Verhelst, K. Rabaey, A chip-based 128-channel potentiostat for high-throughput studies of bioelectrochemical systems: Optimal electrode potentials for anodic biofilms, Biosens. Bioelectron. 174 (2021) 112813, https://doi.org/10.1016/J.BIOS.2020.112813.

[58] C.M. Martinez, X. Zhu, B.E. Logan, AQDS immobilized solid-phase redox mediators and their role during bioelectricity generation and RR2 decolorization in air-cathode single-chamber microbial fuel cells, Bioelectrochem 118 (2017) 123–130, https://doi.org/10.1016/J.BIOELECHEM.2017.07.007.

[59] S.M. de Smit, C.J.N. Buisman, J.H. Bitter, D.P.B.T.B. Strik, Cyclic voltammetry is invasive on microbial electrosynthesis, ChemElectroChem 8 (2021) 3384–3396, https://doi.org/10.1002/CELC.202100914.

[60] B.G. Ateya, F.M. AlKharafi, A.S. Al-Azab, Electrodeposition of sulfur from sulfide contaminated brines, Electrochem. Solid St. 6 (2003) C137, https://doi.org/10.1149/1.1599686.

[61] N.J. Kotloski, J.A. Gralnick, Flavin electron shuttles dominate extracellular electron transfer by Shewanella oneidensis, MBio 4 (2013) 553–565, https://doi.org/10.1128/MBIO.00553-12.

[62] A.L. Kane, E.D. Brutinel, H. Joo, R. Maysonet, C.M. VanDrisse, N.J. Kotloski, J.A. Gralnick, Formate metabolism in Shewanella oneidensis generates proton motive force and prevents growth without an electron acceptor, J. Bacteriol. 198 (2016) 1337–1346, https://doi.org/10.1128/JB.00927-15.

[63] B. Korth, J. Kretzschmar, M. Bartz, A. Kuchenbuch, F. Harnisch, Determining incremental coulombic efficiency and physiological parameters of early stage Geobacter spp. enrichment biofilms, PLoS One 15 (2020) e0234077, https://doi.org/10.1371/journal.pone.0234077.

[64] Y. Wang, X. Li, Y. Chi, W. Song, Q. Yan, J. Huang, Changes of the Freshwater Microbial Community Structure and Assembly Processes during Different Sample Storage Conditions, Microorganisms. 10 (2022) 1176, https://doi.org/10.3390/MICROORGANISMS10061176.

[65] J.T. Jeske, C. Gallert, Microbiome analysis via OTU and ASV-based pipelines—a comparative interpretation of ecological data in WWTP systems, Bioengineering 9 (2022) 146, https://doi.org/10.3390/BIOENGINEERING9040146.

[66] K. Venkidusamy, M. Megharaj, Identification of electrode respiring, hydrocarbonoclastic bacterial strain Stenotrophomonas maltophilia MK2 highlights the untapped potential for environmental bioremediation, Front. Microbiol. 7 (2016) 229962, https://doi.org/10.3389/FMICB.2016.01965.

[67] L. Yu, S. Wang, Q. wen Tang, M. yue Cao, J. Li, K. Yuan, P. Wang, W. wei Li, Enhanced reduction of Fe(III) oxides and methyl orange by Klebsiella oxytoca in

presence of anthraquinone-2-disulfonate, Appl. Microbiol. Biotechnol. 100 (2016) 4617–4625, https://doi.org/10.1007/S00253-016-7281-6.

[68] A. Angelov, S. Bratkova, A. Loukanov, Microbial fuel cell based on electroactive sulfate-reducing biofilm, Energy Convers. Manag. 67 (2013) 283–286, https://doi.org/10.1016/J.ENCONMAN.2012.11.024.

[69] V. Agostino, A. Lenic, B. Bardl, V. Rizzotto, A.N.T. Phan, L.M. Blank, M.A. Rosenbaum, Electrophysiology of the Facultative Autotrophic Bacterium Desulfosporosinus orientis, Front. Bioeng. Biotechnol. 8 (2020) 538436, https://doi.org/10.3389/FBIOE.2020.00457.

[70] T. Aüllo, A. Ranchou-Peyruse, B. Ollivier, M. Magot, Desulfotomaculum spp. and related gram-positive sulfate-reducing bacteria in deep subsurface environments, Front. Microbiol. 4 (2013) 58161, https://doi.org/10.3389/FMICB.2013.00362.

[71] S. Dai, B. Korth, L. Schwab, F. Aulenta, C. Vogt, F. Harnisch, Deciphering the fate of sulfate in one- and two-chamber bioelectrochemical systems, Electrochim. Acta 408 (2022) 139942, https://doi.org/10.1016/J.ELECTACTA.2022.139942.

[72] M.K. Stoeva, J.D. Coates, Specific inhibitors of respiratory sulfate reduction: Towards a mechanistic understanding, Microbiology. 165 (2019) 254–269, https://doi.org/10.1099/MIC.0.000750.

[73] L. Voskuhl, D. Brusilova, V.S. Brauer, R.U. Meckenstock, Inhibition of sulfate-reducing bacteria with formate, FEMS Microbiol. Ecol. 98 (2022) fiac003, https://doi.org/10.1093/FEMSEC/FIAC003.

[74] S. Riedl, R.K. Brown, S. Klöckner, K.J. Huber, B. Bunk, J. Overmann, U. Schröder, Successive conditioning in complex artificial wastewater increases the performance of electrochemically active biofilms treating real wastewater, ChemElectroChem 4 (2017) 3081–3090, https://doi.org/10.1002/CELC.201700929.

[75] J. Dorazco-Delgado, J.H. Serment-Guerrero, S.M. Fernández-Valverde, M.C. Carreño-De-león, J.C. Gómora-Hernández, Voltage production and simultaneous municipal wastewater treatment in microbial fuel cells performed with Clostridium strains, Rev. Mex, Ing. Quim. 20 (2021) IA2325, https://doi.org/10.24275/RMIQ/IA2325.

[76] J.D. Coates, D.J. Ellis, C.V. Gaw, D.R. Lovley, Geothrix fermentans gen. nov., sp. nov., a novel Fe(III)-reducing bacterium from a hydrocarbon-contaminated aquifer, Int J Syst Bacteriol 49 (1999) 1615–1622, https://doi.org/10.1099/00207713-49-4-1615.

[77] D. Bertel, J. Peck, T.J. Quick, J.M. Senko, Iron transformations induced by an acid-tolerant Desulfosporosinus species, Appl. Environ. Microbiol. 78 (2012) 81–88, https://doi.org/10.1128/AEM.06337-11.

[78] S.L. Hockin, G.M. Gadd, Linked redox precipitation of sulfur and selenium under anaerobic conditions by sulfate-reducing bacterial biofilms, Appl. Environ. Microbiol. 69 (2003) 7063–7072, https://doi.org/10.1128/AEM.69.12.7063-7072.2003.

[79] D. Nosek, T. Mikołajczyk, A. Cydzik-Kwiatkowska, Anode modification with Fe2O3 affects the anode microbiome and improves energy generation in microbial fuel cellS powered by wastewater, Int. J. Environ. Res. Public Health 20 (2023) 2580, https://doi.org/10.3390/IJERPH20032580.

[80] L.J. Bird, V. Bonnefoy, D.K. Newman, Bioenergetic challenges of microbial iron metabolisms, Trends Microbiol. 19 (2011) 330–340, https://doi.org/10.1016/J.TIM.2011.05.001.

[81] B. Korth, F. Harnisch, Spotlight on the energy harvest of electroactive microorganisms: The impact of the applied anode potential, Front. Microbiol. 10 (2019) 452764, https://doi.org/10.3389/FMICB.2019.01352.

[82] D.R. Lovley, E.J.P. Phillips, Competitive mechanisms for inhibition of sulfate reduction and methane production in the zone of ferric iron reduction in sediments, Appl. Environ. Microbiol. 53 (1987) 2636–2641, https://doi.org/10.1128/AEM.53.11.2636-2641.1987.

[83] L.C. Wunder, D.A. Aromokeye, X. Yin, T. Richter-Heitmann, G. Willis-Poratti, A. Schnakenberg, C. Otersen, I. Dohrmann, M. Römer, G. Bohrmann, S. Kasten, M.W. Friedrich, Iron and sulfate reduction structure microbial communities in (sub-) Antarctic sediments, ISME J 15 (2021) 3587–3604, https://doi.org/10.1038/s41396-021-01014-9.

[84] M. Barlett, K. Zhuang, R. Mahadevan, D. Lovley, Integrative analysis of Geobacter spp. and sulfate-reducing bacteria during uranium bioremediation, Biogeosciences 9 (2012) 1033–1040, https://doi.org/10.5194/BG-9-1033-2012.

[85] F.H. Chapelle, D.R. Lovley, Competitive exclusion of sulfate reduction by Fe(III)-reducing bacteria: a mechanism for producing discrete zones of high-iron ground water, Groundwater 30 (1992) 29–36, https://doi.org/10.1111/J.1745-6584.1992.TB00808.X.

[86] J.M. Paper, T.M. Flynn, M.I. Boyanov, K.M. Kemner, B.R. Haller, K. Crank, A.M. Lower, Q. Jin, M.F. Kirk, Influences of pH and substrate supply on the ratio of iron to sulfate reduction, Geobiology 19 (2021) 405–420, https://doi.org/10.1111/GBI.12444.

[87] S.W. Poulton, M.D. Krom, R. Raiswell, A revised scheme for the reactivity of iron (oxyhydr)oxide minerals towards dissolved sulfide, Geochim. Cosmochim. Acta 68 (2004) 3703–3715, https://doi.org/10.1016/J.GCA.2004.03.012.

[88] B.B. Jørgensen, A.J. Findlay, A. Pellerin, The biogeochemical sulfur cycle of marine sediments, Front. Microbiol. 10 (2019) 436320, https://doi.org/10.3389/FMICB.2019.00849.

[89] C.M. Hansel, C.J. Lentini, Y. Tang, D.T. Johnston, S.D. Wankel, P.M. Jardine, Dominance of sulfur-fueled iron oxide reduction in low-sulfate freshwater sediments, ISME J 9 (2015) 2400–2412, https://doi.org/10.1038/ismej.2015.50.

[90] Y. Yao, B. Fu, D. Han, Y. Zhang, H. Liu, Formate-dependent acetogenic utilization of glucose by the fecal acetogen clostridium bovifaecis, Appl. Environ. Microbiol. 86 (2020) e01870-20, https://doi.org/10.1128/AEM.01870-20.

[91] J. Moon, J. Dönig, S. Kramer, A. Poehlein, R. Daniel, V. Müller, Formate metabolism in the acetogenic bacterium Acetobacterium woodii, Environ. Microbiol. 23 (2021) 4214–4227, https://doi.org/10.1111/1462-2920.15598.

3. Conclusion and future prospects

Geochemical characterization of the uppermost layers of the anoxic sediment pile highlighted that redox conditions of the water column affect the partitioning of iron, manganese and other bioactive metal(loid)s such as arsenic. Metal(loid)s are released to the bottom waters by reductive dissolution of pre-existing authigenic iron mineral phases (e.g., oxyhydroxides and siderite). Considering that the anoxic sediment pile is enriched in metal(loid)s (e.g., arsenic, vanadium, and lanthanides), insights from Paper I suggest that siderophile elements can be continuously imported to the sediment-water interface under current reductive conditions of the water column. This could also alter the dynamic of other elements or compounds not evaluated in this research, but of know redox reactivity such as fulvic acids. Insights from Paper II demonstrated that concentration gradients of siderophile elements are also influenced by microbially-mediated mineral transformations of ferric and manganic species. They serve as substrate for metal dissimilatory reduction, which favour the prevalence of ferruginous conditions in the monimolimnion of Lake Medard. Hence, electroactive iron-reducers (e.g., *Geobacter* and *Rhodoferax* spp.) drive the overlapped cycle of iron and other elements (e.g., phosphorus and arsenic) in the anoxic water column by performing the dissimilatory reduction and stabilization of ferric and manganic organomineral aggregates exported from the redoxcline after their precipitation by iron oxidizer–nitrate reducer organisms (e.g., *Gallionella* spp.). Thereby, it can be inferred that the niche-differentiated electroactive microbiome of Lake Medard can substantially impact on iron biomineralization in the monimolimnion as stated in the first work hypothesis (see section 1.4).

Further mechanistic insights on how electroactive metabolisms impact iron mineral transformations were gained by applying controlled electric potentials in bioelectrochemical systems capable to induce microbe-mineral interactions (Papers III & IV). Bioelectrochemical experiments demonstrated that electrodes poised at redox potentials akin sinking mineral aggregates in Lake Medard fuel EET in the anoxic ferruginous waters. Electrotophy or electrogenesis relying on the metabolization of labile carbon sources and assimilation of ammonia, can also be enhanced by the gradients of these species in the water column depth. Interestingly, an increment of the content of labile carbon sources (e.g., formate) stimulated both the switch to an electroactive lifestyle in nitrate- (*Stenotrophomonas* spp.) and sulphate-reducers (*Desulfatomaculum* spp.) and the occurrence of microbial sulphate reduction, a metabolism restrained in the monimolimnion of Lake Medard by the low amounts of metabolizable carbon sources. Such adaptiveness to the available electron sources and sinks suggests that biomineralization involving iron and siderophile elements is driven by interspecies interactions. This further support the stated in the first work hypothesis (see section 1.4).

In the presence of conductive particles, reactive nitrogen species and humic substance derivatives – as it occurs in the anoxic bottom waters – electroactive iron-reducers showed a preference for electron shuttlers over nitrate as alternative terminal electron acceptors (Paper III). Similarly, the amendment of flavin-type compounds as electron shuttlers seemed key to enhance microbial EET when using Lake Medard water as inoculum. Therefore, the fact that redox mediators can enable a shift to electroactive metabolism under ferruginous anoxic conditions agrees with the stated in the second work hypothesis (see topic 1.4). Microbial EET also induced the biomineralization of organomineral aggregates on the surface of electrodes. They often entombed the microbial cells and displayed an enrichment in iron, sulphur, and other trace metal(loid)s. Biomineralization and concomitant changes on the solubility of siderophile

elements depended on the availability of alternative electron sources and sinks. Paper III showed that the presence of both humic substance derivatives and reactive nitrogen species boosted the formation of aggregates of amorphous Fe(III)-oxyhydroxides with high capacity to scavenge oxyanions from anoxic ferruginous waters. In contrast, absence of humic substances derivatives fostered the formation of extensive microbe-mineral networks entombing the cells, which induced the stabilization of Fe(III)-oxyhydroxides with low capacity to sequester oxyanions. Accordingly, insights from Paper III support the third work hypothesis (see section 1.4) as chemolithotrophic iron(III) respiration involving humic substances affect the dynamics of dissolved oxyanions. However, it does not further facilitate the stabilization of Fe(III)-oxyhydroxides. A mechanistic scheme can be found in Figure 4.
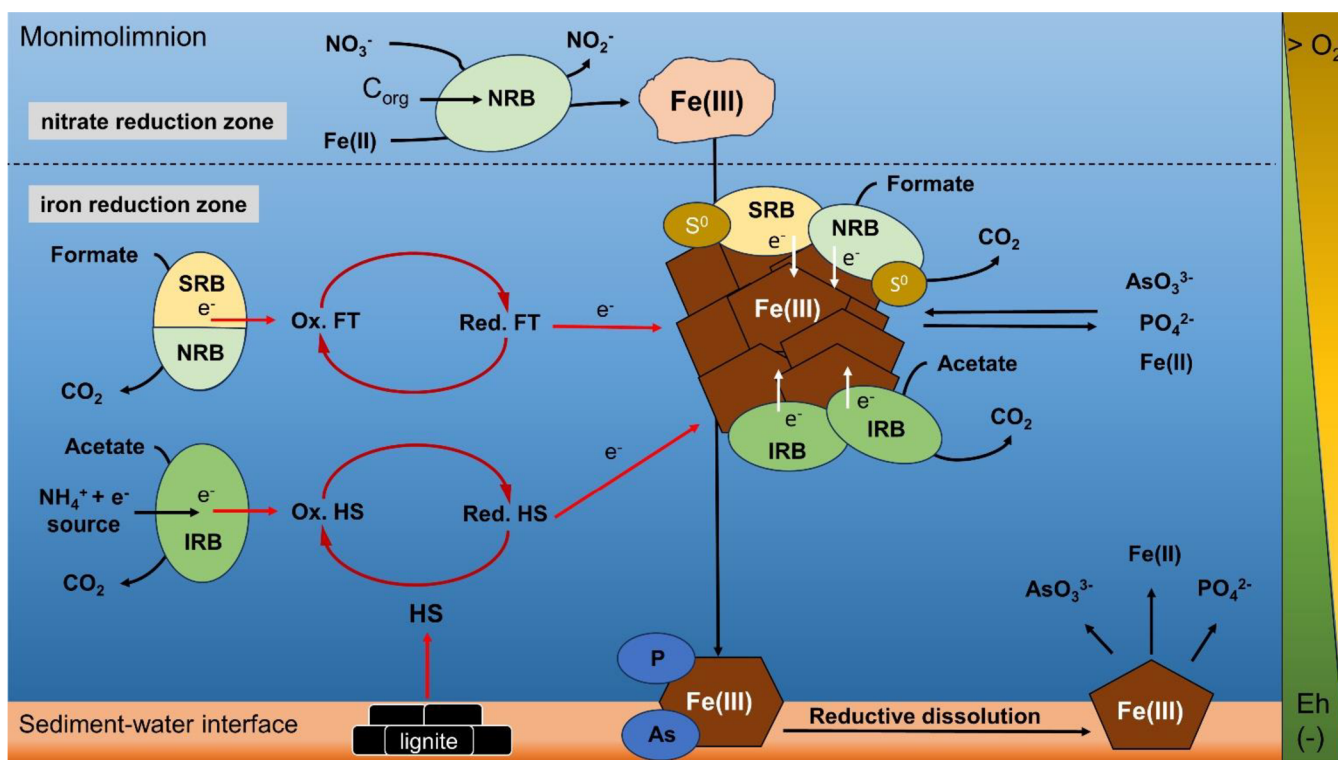

Figure 4. Scheme depicting how electroactive species affect the linked biogeochemical cycling of nutrients and metals under environmental gradients of dissolved oxygen (O_2) and redox potential (Eh) in the anoxic ferruginous monimolimnion of Lake Medard. Direct electron transfer (white arrows) and mediated electron transfer (red arrows), by re-oxidable flavin-type compounds (FT) and humic substance derivatives (HS), allow nitrate-reducers (NRB), sulphate-reducers (SRB), and iron-reducers (IRB) to drive iron mineral transformation in aggregates in transit from the hypolimnion to the sediment-water interface (brown polygons).

Insights on how the presence of alternative electron sources and sinks affects iron biomineralization were gained by studying organomineral aggregates accumulated on the surface of electrodes. These aggregates are described to resemble the organic ferrihydrite aggregates initially formed at the redoxcline but exported to the sediment-water interface of our model site. Metal(loid)s immobilization occurred at the reactive surfaces of amorphous iron mineral aggregates and was mediated by both model and non-conventional EAM. Consequently, mechanistic insights from this research could expand the role of EAM in iron biomineralization in metal-rich redox interfaces with strong selective competition and several electron sources and sinks.

In addition, results from this study could be pertinent to design novel bioelectrotechnologies aiming to recover or remove siderophile elements from redox-stratified environments, within iron minerals, with high metal loads. Initial considerations can be drawn from Papers III and IV, but future research and engineering efforts would benefit from the following recommendations:

- Bioelectrochemical systems using anoxic ferruginous waters bearing high levels of dissolved sulphate may avoid the emergence of sulphate reducers in order to successfully enrich EAM by amending inhibitors for sulphate reduction (e.g., adenosine-5′ phosphosulfate).

- Using two-chamber bioelectrochemical systems (i.e., independent cathodic and anodic compartments separated by ionic exchange membranes) could enhance both electrotophy and electrogenesis without undesired interference of alternative electron sinks and sources (e.g., dihydrogen, sulphate, and traces of dissolved oxygen)

- Occurrence of interspecies interactions (e.g., Fe-ammox or methanogenesis) by using Lake Medard as inoculum in cathodic chambers could benefit microbe-mineral interactions as observed under anodic conditions. Such interactions can be stimulated by applying higher cathodic potentials that increase the reactivity of humic substances (i.e., > -300 mV *vs*. SHE)

- In order to augment microbe-electrode interactions of non-conventional EAM, alternative procedures, such as using carbon felt, iron oxides coating or increasing the surface area, may be tested when constructing working electrodes.

4.   References

Aiyer K. and Doyle L. E. (2022) Capturing the signal of weak electricigens: a worthy endeavour. *Trends Biotechnol* **40**, 564–575.

Armato C., Ahmed D., Agostino V., Traversi D., Degan R., Tommasi T., Margaria V., Sacco A., Gilli G., Quaglio M., Saracco G. and Schilirò T. (2019) Anodic microbial community analysis of microbial fuel cells based on enriched inoculum from freshwater sediment. *Bioprocess Biosyst Eng* **42**, 697–709.

Benzerara K., Miot J., Morin G., Ona-Nguema G., Skouri-Panet F. and Férard C. (2011) Importance, mécanismes et implications environnementales de la biominéralisation par les microorganismes. *Comptes Rendus - Geoscience* **343**, 160–167.

Berg J. S., Jézéquel D., Duverger A., Lamy D., Laberty-Robert C. and Miot J. (2019) Microbial diversity involved in iron and cryptic sulfur cycling in the ferruginous, low-sulfate waters of Lake Pavin. *PLoS One* **14**, e0212787.

Bertel D., Peck J., Quick T. J. and Senko J. M. (2012) Iron transformations induced by an acid-tolerant Desulfosporosinus species. *Appl Environ Microbiol* **78**, 81–88.

Borch T., Masue Y., Kukkadapu R. K. and Fendorf S. (2007) Phosphate imposed limitations on biological reduction and alteration of ferrihydrite. *Environ Sci Technol* **41**, 166–172.

Bryce C., Blackwell N., Schmidt C., Otte J., Huang Y. M., Kleindienst S., Tomaszewski E., Schad M., Warter V., Peng C., Byrne J. M. and Kappler A. (2018) Microbial anaerobic Fe(II) oxidation – Ecology, mechanisms and environmental implications. *Environ Microbiol* **20**, 3462–3483.

Chabert N., Amin Ali O. and Achouak W. (2015) All ecosystems potentially host electrogenic bacteria. *Bioelectrochemistry* **106**, 88–96.

Clément J. C., Shrestha J., Ehrenfeld J. G. and Jaffé P. R. (2005) Ammonium oxidation coupled to dissimilatory reduction of iron under anaerobic conditions in wetland soils. *Soil Biol Biochem* **37**, 2323–2328.

Cosmidis J. and Benzerara K. (2022) Why do microbes make minerals? *Comptes Rendus - Geoscience* **354**, 1–

39.

Doyle L. E., Yung P. Y., Mitra S. D., Wuertz S., Williams R. B. H., Lauro F. M. and Marsili E. (2017) Electrochemical and genomic analysis of novel electroactive isolates obtained via potentiostatic enrichment from tropical sediment. *J Power Sources* **356**, 539–548.

Erable B., Vandecandelaere I., Faimali M., Delia M. L., Etcheverry L., Vandamme P. and Bergel A. (2010) Marine aerobic biofilm as biocathode catalyst. *Bioelectrochemistry* **78**, 51–56.

Fuller S. J., McMillan D. G. G., Renz M. B., Schmidt M., Burke I. T. and Stewart D. I. (2014) Extracellular electron transport-mediated fe(iii) reduction by a community of alkaliphilic bacteria that use flavins as electron shuttles. *Appl Environ Microbiol* **80**, 128–137.

Harnisch F. and Freguia S. (2012) A Basic Tutorial on Cyclic Voltammetry for the Investigation of Electroactive Microbial Biofilms. *Chem Asian J* **7**, 466–475.

He S., Lau M. P., Linz A. M., Roden E. E. and McMahon K. D. (2019) Extracellular Electron Transfer May Be an Overlooked Contribution to Pelagic Respiration in Humic-Rich Freshwater Lakes. *mSphere* **4**.

Helton A. M., Ardón M. and Bernhardt E. S. (2015) Thermodynamic constraints on the utility of ecological stoichiometry for explaining global biogeochemical patterns. *Ecol Lett* **18**, 1049–1056.

Hidalgo D., Sacco A., Hernández S. and Tommasi T. (2015) Electrochemical and impedance characterization of Microbial Fuel Cells based on 2D and 3D anodic electrodes working with seawater microorganisms under continuous operation. *Bioresour Technol* **195**, 139–146.

Jiang Y. Bin, Zhong W. H., Han C. and Deng H. (2016) Characterization of electricity generated by soil in microbial fuel cells and the isolation of soil source exoelectrogenic bacteria. *Front Microbiol* **7**, 1776.

Kappler A., Bryce C., Mansor M., Lueder U., Byrne J. M. and Swanner E. D. (2021) An evolving view on biogeochemical cycling of iron. *Nature Reviews Microbiology 2021 19:6* **19**, 360–374.

Kappler A., Thompson A. and Mansor M. (2023) Impact of Biogenic Magnetite Formation and Transformation on Biogeochemical Cycles. *Elements* **19**, 222–227.

Kato S., Hashimoto K. and Watanabe K. (2012) Microbial interspecies electron transfer via electric currents through conductive minerals. *Proc Natl Acad Sci U S A* **109**, 10042–10046.

Kawaichi S., Yamada T., Umezawa A., McGlynn S. E., Suzuki T., Dohmae N., Yoshida T., Sako Y., Matsushita N., Hashimoto K. and Nakamura R. (2018) Anodic and cathodic extracellular electron transfer by the filamentous bacterium Ardenticatena maritima 110S. *Front Microbiol* **9**, 315537.

Klüpfel L., Piepenbrock A., Kappler A. and Sander M. (2014) Humic substances as fully regenerable electron acceptors in recurrently anoxic environments. *Nature Geoscience 2014 7:3* **7**, 195–200.

Koch C. and Harnisch F. (2016a) Is there a Specific Ecological Niche for Electroactive Microorganisms? *ChemElectroChem* **3**, 1282–1295.

Koch C. and Harnisch F. (2016b) What is the essence of microbial electroactivity? *Front Microbiol* **7**, 229845.

Korth B. and Harnisch F. (2019) Spotlight on the energy harvest of electroactive microorganisms: The impact of the applied anode potential. *Front Microbiol* **10**, 452764.

Kotloski N. J. and Gralnick J. A. (2013) Flavin electron shuttles dominate extracellular electron transfer by Shewanella oneidensis. *mBio* **4**, 553–565.

Lambrecht N., Wittkop C., Katsev S., Fakhraee M. and Swanner E. D. (2018) Geochemical Characterization of Two Ferruginous Meromictic Lakes in the Upper Midwest, USA. *J Geophys Res Biogeosci* **123**, 3403–3422.

Logan B. E., Rossi R., Ragab A. and Saikaly P. E. (2019) Electroactive microorganisms in bioelectrochemical systems. *Nature Reviews Microbiology 2019 17:5* **17**, 307–319.

Lovley D. R. (2012) Electromicrobiology. *https://doi.org/10.1146/annurev-micro-092611-150104* **66**, 391–409.

Lovley D. R. (2022) Electrotrophy: Other microbial species, iron, and electrodes as electron donors for microbial respirations. *Bioresour Technol* **345**, 126553.

Lovley D. R. and Holmes D. E. (2021) Electromicrobiology: the ecophysiology of phylogenetically diverse electroactive microorganisms. *Nature Reviews Microbiology 2021 20:1* **20**, 5–19.

Lovley D. R. and Phillips E. J. P. (1988) Novel Mode of Microbial Energy Metabolism: Organic Carbon Oxidation Coupled to Dissimilatory Reduction of Iron or Manganese. *Appl Environ Microbiol* **54**, 1472–1480.

Lovley D. R. and Walker D. J. F. (2019) Geobacter Protein Nanowires. *Front Microbiol* **10**, 2078.

Marsili E., Baron D. B., Shikhare I. D., Coursolle D., Gralnick J. A. and Bond D. R. (2008) Shewanella secretes flavins that mediate extracellular electron transfer. *Proc Natl Acad Sci U S A* **105**, 3968–3973.

Melton E. D., Swanner E. D., Behrens S., Schmidt C. and Kappler A. (2014) The interplay of microbially mediated and abiotic reactions in the biogeochemical Fe cycle. *Nature Reviews Microbiology 2014 12:12* **12**, 797–808.

Meysman F. J. R., Cornelissen R., Trashin S., Bonné R., Martinez S. H., van der Veen J., Blom C. J., Karman C., Hou J. L., Eachambadi R. T., Geelhoed J. S., Wael K. De, Beaumont H. J. E., Cleuren B., Valcke R., van der Zant H. S. J., Boschker H. T. S. and Manca J. V. (2019) A highly conductive fibre network enables centimetre-scale electron transport in multicellular cable bacteria. *Nature Communications 2019 10:1* **10**, 1–8.

Muehe E. M., Scheer L., Daus B. and Kappler A. (2013) Fate of arsenic during microbial reduction of biogenic versus abiogenic As-Fe(III)-mineral coprecipitates. *Environ Sci Technol* **47**, 8297–8307.

Palacios P. A., Francis W. R. and Rotaru A. E. (2021) A Win–Loss Interaction on Fe0 Between Methanogens and Acetogens From a Climate Lake. *Front Microbiol* **12**, 919.

Petrash D. A., Jan J., Sirová D., Osafo N. O. A. and Borovec J. (2018) Iron and nitrogen cycling, bacterioplankton community composition and mineral transformations involving phosphorus stabilisation in the ferruginous hypolimnion of a post-mining lake. *Environ Sci Process Impacts* **20**, 1414–1426.

Rotaru A. E., Calabrese F., Stryhanyuk H., Musat F., Shrestha P. M., Weber H. S., Snoeyenbos-West O. L. O., Hall P. O. J., Richnow H. H., Musat N. and Thamdrup B. (2018) Conductive Particles Enable Syntrophic Acetate Oxidation between Geobacter and Methanosarcina from Coastal Sediments. *mBio* **9**.

Rotatru A.-E., Posth N. R., Löscher C. R., Miracle M. R., Vicente E., Cox R. P., Thompson J., Poulton S. W. and Thamdrup B. (2019) Interspecies interactions mediated by conductive minerals in the sediments of the Iron rich Meromictic Lake La Cruz, Spain. *Limnetica* **38**, 21–40.

Sánchez-España J., Yusta I., Ilin A., van der Graaf C. and Sánchez-Andrea I. (2020) Microbial Geochemistry of the Acidic Saline Pit Lake of Brunita Mine (La Unión, SE Spain). *Mine Water Environ* **39**, 535–555.

Schröder U., Harnisch F. and Angenent L. T. (2015) Microbial electrochemistry and technology: terminology and classification. *Energy Environ Sci* **8**, 513–519.

Shi L., Dong H., Reguera G., Beyenal H., Lu A., Liu J., Yu H. Q. and Fredrickson J. K. (2016) Extracellular electron transfer mechanisms between microorganisms and minerals. *Nature Reviews Microbiology 2016 14:10* **14**, 651–662.

Sundman A., Vitzthum A. L., Adaktylos-Surber K., Figueroa A. I., van der Laan G., Daus B., Kappler A. and Byrne J. M. (2020) Effect of Fe-metabolizing bacteria and humic substances on magnetite nanoparticle reactivity towards arsenic and chromium. *J Hazard Mater* **384**, 121450.

Taillefert M., Beckler J. S., Carey E., Burns J. L., Fennessey C. M. and DiChristina T. J. (2007) Shewanella putrefaciens produces an Fe(III)-solubilizing organic ligand during anaerobic respiration on insoluble Fe(III) oxides. *J Inorg Biochem* **101**, 1760–1767.

Tebo B. M. and Obraztsova A. Y. (1998) Sulfate-reducing bacterium grows with Cr(VI), U(VI), Mn(IV), and Fe(III) as electron acceptors. *FEMS Microbiol Lett* **162**, 193–198.

Tremblay P. L., Aklujkar M., Leang C., Nevin K. P. and Lovley D. (2012) A genetic system for Geobacter metallireducens: role of the flagellin and pilin in the reduction of Fe(III) oxide. *Environ Microbiol Rep* **4**, 82–88.

Wang H., Lu L., Mao D., Huang Z., Cui Y., Jin S., Zuo Y. and Ren Z. J. (2019) Dominance of electroactive microbiomes in bioelectrochemical remediation of hydrocarbon-contaminated soils with different textures. *Chemosphere* **235**, 776–784.

Yee M. O., Deutzmann J., Spormann A. and Rotaru A.-E. (2020) Cultivating electroactive microbes—from field to bench. *Nanotechnology* **31**, 174003.

5.   *Curriculum vitae*

MSc. Astolfo Valero

02.02.1993 – Venezuela
astolfo.valero@bc.cas.cz

Education

2020 – 2024 | **PhD in Hydrobiology** – University of South Bohemia (USB), České Budějovice, Czech Republic.
Thesis: "*The role of electroactive organisms in biomineralization reactions involving transition metals, nitrogen, and humic substances under suboxic/anoxic conditions*". Advisor: MSc. Daniel Petráš, PhD.

2017 – 2019 | **MSc in Chemical Oceanography** – Federal University of Rio Grande (FURG). Rio Grande, Brazil.
Thesis: "*Trace metals potential availability in sediments of shipyard areas in southeastern and southern Brazil*". Advisor: Dr. Prof. Mônica Wallner-Kersanach

2010 – 2016 | **Bc in Geochemistry** – Central University of Venezuela (UCV). Caracas, Venezuela.

Research Experience

2019 – Current | **Research assistant** at Bioelectrochemistry and biomineralization laboratory, Organic Geochemistry research group – Institute of Soil Biology and Biogeochemistry, Czech Academy of Sciences (BC CAS). České Budějovice, Czech Republic.

2022 | **Short research stay** (3 months) at Bioelectrotechnology WG – Helmholtz Centre for Environmental Research (UFZ). Leipzig, Germany

Mentoring

2020 | Co-advisor of the undergraduate thesis of Bc. Thayna Pedroso Peterle – Oceanology undergraduate programme, Federal University of Rio Grande (FURG). Rio Grande, Brazil.
Thesis: "*Pollution and ecological risk assessment of trace metals in sediments of shipyard areas at Southeastern and Southern Brazil*"

Grants/Awards

2022 | **Best poster presentation by a Graduate Student** – 8th Global Conference of the International Society for Microbial Electrochemistry and Technology (ISMET8).
2022 | **Short-term research scholarship #91820787** – German Academic Exchange Service (DAAD).

Peer-reviewed publications

Valero, A., Petrash, D.A., Kuchenbuch, A., Korth, B. Enriching electroactive microorganisms from ferruginous lake waters – Mind the sulfate reducers! *Bioelectrochemistry* 157, 108661. DOI: 10.1016/j.bioelechem.2024.108661

López-Hernández D., Morales L., Umbría-Salinas K., **Valero A.**, Meléndez W., & López-Contreras A. C, N and P contributions to sediments of two Venezuelan coastal lagoons and their relationships with the adsorption of P. *Under review at Clean - Soil Air Water.*

Petrash D. A., Thomazo C., **Valero A.**, Valdés J. J., Umbría-Salinas K., Meador T. B., Konhauser K. O. Elemental dynamics and interactions in a carbonate-buffered, sulfatic, and ferruginous lake. *Under review at Journal of Geophysical Research – Biogeosciences.*

Valero A., Umbría-Salinas K., Morales L., Meléndez W., López-Contreras A., López-Hernández D. Iron and manganese geochemical partitioning and its impact on phosphorus adsorption in two coastal lagoons at the Caribbean Sea. *In preparation for Oceanologia*

Valero A., Jan J. & Petrash D. A. Anaerobic dissolved As(III) removal from metal-polluted waters by cathode-stabilized Fe(III)-oxyhydroxides. *Environmental Sciences: Water Research & Technology.* DOI: 10.1039/D2EW00844K

Petrash D. A., Steenbergen I. M., **Valero A.**, Meador T. B., Pačes T., Thomazo C. Aqueous system-level processes and prokaryote assemblages in the ferruginous and sulfate-rich bottom waters of a post-mining lake. *Biogeosciences* 19, 1723–1751. DOI: 10.5194/bg-19-1723-2022

Osafo N. O. A., Jan J., **Valero A.**, Porcal P., Petrash D. A., Borovec J.. Organic matter character as a critical factor determining the fate and stability of its association with iron in sediments. *Journal of Soils and Sediments* 22, 1865–1875. DOI: 10.1007/s11368-022-03207-x

Umbría-Salinas K. M., **Valero A.**, Jan J., Borovec J., Chrastný V., Petrash D. A. Redox-driven geochemical partitioning of metal(loid)s in the iron-rich anoxic sediments of a recently flooded lignite mine pit: Lake Medard, NW Czechia. *Journal of Hazardous Matererials Advances* 100009. DOI: 10.1016/j.hazadv.2021.100009

Umbría-Salinas K. M., **Valero A.**, Wallner-Kersanach M., de Andrade C. F., Yabe M. J. S., Wasserman J. C., Kuroshima K. N., Zhang H. Labile metal assessment in water by Diffusive Gradients in Thin Films in shipyards on the Brazilian subtropical coast. *Science of the Total Environment* 775, 145184. DOI: 10.1016/j.scitotenv.2021.145184

Umbría-Salinas K. M., **Valero A.**, Martins S. E., Wallner-Kersanach M. Copper ecological risk assessment using DGT technique and PNEC: A case study in the Brazilian coast. *Journal of Hazardous Matererials* 403, 123918. DOI: 10.1016/j.jhazmat.2020.123918

Valero A., Umbría-Salinas K. M., Wallner-Kersanach M., de Andrade C. F., Yabe M. J. S., Contreira-Pereira L., Wasserman J. C., Kuroshima K. N., Zhang H. Potential availability of trace metals in sediments in southeastern and southern Brazilian shipyard areas using the DGT technique and chemical extraction methods. *Science of the Total Environment* 710, 136216. DOI: 10.1016/j.scitotenv.2019.136216

International scientific conferences

Valero A., Petrash D. A., Harnisch F., Korth B. Enrichment of electroactive formate-utilizing bacteria from ferruginous lake waters. 8th International Society for Microbial Electrochemistry and Technology Global Conference.

Petrash D. A., Steenbergen I. M., **Valero A.**, Meador T. B., Lalonde S. V., Thomazo C. Disentangling the overlapping zonation of dissimilatory iron and sulfate reduction in a carbonate-buffered sulfate-rich and ferruginous lake water column. EGU General Assembly 2022. DOI: 10.5194/egusphere-egu22-183

Valero A., Umbría-Salinas K., Jan J., Borovec J., Petrash D. A. Using ferruginous lake waters as source of Fe-metabolizing electroactive bacteria to produce biomodified electrodes and induce Fe-bearing nano-particles precipitation. Goldschmidt virtual conference 2021. DOI: 10.7185/gold2021.5621

Umbría-Salinas K., **Valero A.**, Jan J., Chrastný V., Petrash D. A. Rare Earths partitioning in a ferruginous/dysoxic geochemical disequilibrium zone. Goldschmidt virtual conference 2021. DOI: 10.7185/gold2021.3751

Petrash D. A., **Valero A.**, Meador T. B., Jan J., Thomazo C. The unbalanced Fe and S biogeochemical budgets in the ferruginous and sulfate-rich waters of a post-mining lake. Goldschmidt virtual conference 2021. DOI: 10.7185/gold2021.3049

Valero A., Umbría-Salinas K., Jan J., Borovec J., Petrash D. A.. As enrichment in Fe-reactive phases in sediments of the meromictic and ferruginous post-mining Lake Medard, Czech Republic. 2nd International (online) Conference on Contaminated Sediments.

Astolfo Valero
České Budějovice
April 2024

6.   *Appendix*

6.1.   *Consent of the copyright holders of Chapter III*

ROYAL SOCIETY OF CHEMISTRY

Permission Request Form for RSC Material

To request permission to use material from material published by The Royal Society of Chemistry (RSC), please complete and return this form.

From: Name: Astolfo Valero   E-mail: astolfo.valero@bc.cas.cz

Address: Branišovská 1645/31a. 370 05 České Budějovice, Czech Republic

I am preparing the following work for publication:

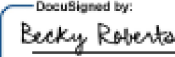|	
Article/Chapter Title	
Journal/Book Title	PhD. Thesis: The role of electroactive organisms in biomineralization reactions involing transition metals, nitrogen and humic substances under anoxic conditions
Editor/Author(s)	Valero A.
Publisher	Faculty of Science, University of South Bohemia

I would very much appreciate your permission to use the following material:

Journal/Book Title	Environmental Science: Water Research & Technology
Article/Chapter Title	Anaerobic dissolved As(III) removal from metal-polluted waters by cathode-stabilized Fe(III)-oxyhydroxides
RSC Editor/Author(s)	Valero A., Jan J., Petrash D, A,
DOI	https://doi.org/10,1039/D2EW00844K
Year of Publication	2023
Description of Material	
Page(s)	454 – 466

I will acknowledge the original source as specified at the https://rsc.li/permissions,

Signed: _____   Date: 20.03.2024

The Royal Society of Chemistry hereby grants permission for the use of the material specified above in the work described and in all subsequent editions of the work for distribution throughout the world, in all media including electronic and microfilm, You may use the material in conjunction with computer-based electronic and information retrieval systems, grant permissions for photocopying, reproductions and reprints, translate the material and to publish the translation, and authorise document delivery and abstracting and indexing services, Please note that if the material specified above or any part of it appears with credit or acknowledgement to a third party then you must also secure permission from that third party before reproducing that material. The Royal Society of Chemistry is a signatory to the STM Guidelines on Permissions (available on request).

Signed: *Becky Roberts*   Date: 20/3/2024 | 3:09 PM GMT